An Isopycnal Numerical Model

for the Simulation of Fluid Mud Dynamics

DISSERTATION

zur Erlangung des akademischen Grades zum Doktor der Ingenieurwissenschaften (Dr.-Ing.) an der Fakultät für Bauingenieur- und Vermessungswesen der Universität der Bundeswehr München

von Dipl.-Ing. Denise Wehr

Hamburg, Februar 2012

Vorwort / Preface

Durch die zunehmende Vertiefung der Bundeswasserstraßen im Küstenbereich hat sich in den Ästuaren eine erhebliche Verschlickung entwickelt, der nur mit sehr aufwendigen und kostspieligen Unterhaltungsmaßnamen entgegengewirkt werden kann. Vor allem die Tideems weist in großen Bereichen kein reines Meerwasser mehr auf, sondern führt eine so hohe Feststofffracht aus kohäsiven Sedimenten mit sich, dass trübe Flüssigschlicke gebildet werden. Zur Evaluierung von Lösungsstrategien für diese Problematik benötigt die wasserbauliche Systemanalyse Simulationsmodelle, mit denen man auch die Dynamik von Flüssigschlicken modellieren kann. Hierfür haben die Bundesanstalt für Wasserbau und das Institut für Wasserwesen der Universität der Bundeswehr München das Projekt MudSim beim ‚Kuratorium für Forschung im Küsteningenieurwesen' (KFKI) des BMBF beantragt. Es beinhaltete
a) die Entwicklung eines rheologischen Modells für Flüssigschlicke aus rheometrischen Messungen am Institut für Wasserwesen der Universität der Bundeswehr und
b) die Entwicklung eines numerischen Modells zur Simulation der Flüssigschlickdynamik an der Bundesanstalt für Wasserbau in Hamburg.
Die Untersuchungen des Teilprojekts MudSim-A haben gezeigt, dass es möglich ist, das Fließverhalten von Flüssigschlicken zu erklären und die Rheologie von Flüssigschlicken hinreichend genau zu parametrisieren. Dargestellt werden die Ergebnisse dieses Teilprojekts in den Mitteilungen des Instituts für Wasserwesen der Universität der Bundeswehr München, Heft 111/2011. Die Ergebnisse der Modellentwicklung für die Simulation von Flüssigschlickdynamiken des Teilprojektes MudSim-B sind in der vorliegenden Schrift beschrieben.

In Ihrer hier vorliegenden Dissertationsschrift beschreibt Frau Dr.-Ing. Denise Wehr wie man die Flüssigschlickdynamik mit einem isopyknischen Ansatz diskretisieren kann. Frau Wehr konnte hiermit zeigen, dass es möglich ist, viele Details, wie z.B. die Ausbreitung von internen Wellen zu simulieren. Frau Dr.-Ing. Wehr hat damit einen wichtigen Meilenstein auf dem Weg zur integrierten Simulation eines Ästuars gesetzt, dessen Gezeitendynamik in weiten Bereichen durch turbulente Strömungen geprägt ist, in manchen Bereichen aber auch Flüssigschlickzonen aufweist.

München, im Februar 2012 — Prof. Dr.-Ing. Andreas Malcherek

Abstract

The progressive extension and development of coastal waterways has led to an increase in siltation and formation of fluid mud in sections of estuarine shipping channels, ports and port approaches over the past decades. The need for a better understanding and a profound knowledge of fluid mud dynamics has increased so that it is necessary to develop new maintenance strategies and renaturation measures in estuaries as well as optimize existing ones. Numerical simulations contribute to the evaluation of such strategies. For that reason, the aim of this thesis is to enable the numerical simulation of fluid mud dynamics.

Fluid mud forms by building up a structure of aggregates in regions in which there is an increasing accumulation of cohesive sediments. Although the water content of the high-concentration suspension can be very high, the flow behavior changes from Newtonian to non-Newtonian. However, most of the current established hydrodynamic numerical models solve the shallow water equations with a Newtonian assumption. A standard numerical model approach for the Reynolds-averaged Navier-Stokes equations is therefore extended in this thesis to cover the simulation of non-Newtonian behavior. The developments are based on an existing numerical model in isopycnal coordinates. A vertical resolution by isopycnal layers - layers of constant density - is pursued as the flow can be strongly stratified in systems of high-concentration suspensions. In addition, sharp density gradients characterize the transitional area of fluid mud and water body. The isopycnal discretization enables a vertically resolved simulation of the velocity and density distribution inside the fluid mud body. The isopycnal layers interact due to momentum transfer, mass transfer and interfacial shear stresses. Advective and gravitational transport, mixing and settling of cohesive sediment suspensions are realized by changes in the isopycnal layer thicknesses as each layer represents a suspension with a specific sediment concentration. The vertical transport rates are determined by parameterizations of transport subprocesses and lead to variations in the layer thicknesses. The rheology of fluid mud is dominated by the break-up and recovery of the internal structure in response to shear impact (non-Newtonian behavior). A time- and space-dependent rheological viscosity is therefore introduced into the internal stress terms for the simulation of the rheological behavior of fluid mud.

Applications to schematic and realistic model domains demonstrate the abilities and performance of the extended isopycnal numerical model for the simulation of fluid mud dynamics such as simulation of fluid mud influenced by tidal currents.

Zusammenfassung

In den letzten Jahrzehnten hat der fortschreitende Ausbau von Seeschifffahrtsstraßen zu einer Zunahme der Verschlickung und Entstehung von Flüssigschlick in Bereichen der ästuarinen Schifffahrtstraßen, Häfen und Hafeneinfahrten geführt. Der Bedarf an fundierten Kenntnissen über die Flüssigschlickdynamik wächst, um neue Unterhaltungsstrategien und Renaturierungsmaßnahmen in Ästuaren zu entwickeln und bestehende zu optimieren. Numerische Modelle dienen als Werkzeug zur Beurteilung dieser Strategien und Maßnahmen. Ziel der vorliegenden Arbeit ist daher, die numerische Simulation der Dynamik von Flüssigschlick zu ermöglichen.
Flüssigschlick entsteht in Bereichen erhöhter Akkumulation von kohäsiven Sedimenten. Diese bilden Aggregate und führen zum Aufbau einer inneren Struktur, mit der sich das Fließverhalten der hochkonzentrierten Schlicksuspension von Newtonschen zu nicht-Newtonschen Verhalten verändert. Die derzeit etablierten hydrodynamischen Modelle lösen die Flachwassergleichungen unter der Annahme eines Newtonschen Fluides. In der vorliegenden Arbeit wird daher ein herkömmliches numerisches Verfahren für die Reynolds-gemittelten Navier-Stokes Gleichungen für die Simulation von nicht-Newtonschen Verhalten erweitert.

Die Entwicklungen für die Simulation der Flüssigschlickdynamik bauen auf einem bestehenden isopyknischen numerischen Modell auf. Eine vertikale Auflösung durch Isopyknen - Schichten gleicher Dichte - ist in dieser Arbeit eingesetzt worden, um stark geschichtete Strömungen in Gewässern mit hochkonzentrierten Suspensionen zu realisieren. Insbesondere die Grenzschicht zwischen Flüssigschlick- und Wasserkörper ist durch einen ausgeprägten Dichtesprung gekennzeichnet. Die isopyknische Diskretisierung ermöglicht die Dichte- und Strömungsverteilung im Flüssigschlickkörper vertikal aufzulösen. Die isopyknischen Schichten interagieren durch Impulsaustausch, Massenaustausch und Schubspannungen an den Grenzflächen. Jede Isopykne repräsentiert eine Suspension mit entsprechender Sedimentkonzentration. Advektion und gravitationeller Transport, Durchmischung und Absetzen kohäsiver Schwebstoffsuspensionen wird durch Änderungen der Schichtdicke der Isopyknen realisiert. Die vertikalen Transportraten zwischen den isopyknischen Schichten werden durch Parametrisierungen der Transportteilprozesse bestimmt. Die Rheologie von Flüssigschlick wird durch Aufbrechen und Neubildung der internen Struktur in Reaktion auf einwirkende Scherkräfte dominiert (nicht-Newtonsches Verhalten). Das rheologische Verhalten wird im numerischen Modell durch eine zeit- und ortsabhängige rheologische Viskosität umgesetzt, die in den Termen der inneren Spannungen der Impulsgleichung berücksichtigt wird.

Anwendungen auf schematische und realistische Modellgebiete verdeutlichen die Möglichkeiten und Leistungsfähigkeit des weiterentwickelten isopyknischen numerischen Modells für die Simulation der Flüssigschlickdynamik. Weiterhin zeigen die Modellanwen-

dungen, dass die Entwicklung von Flüssigschlick im tidebeeinflussten System mit diesem Modellverfahren simuliert werden kann.

der Bundeswehr
Universität München

Fakultät für Bauingenieur- und Vermessungswesen

Thema der Dissertation:	An Isopycnal Numerical Model for the Simulation of Fluid Mud Dynamics
Verfasser:	Denise Wehr
Promotionsausschuss:	
Vorsitzender:	Univ.-Prof. Dr. rer. nat. habil. Thomas Apel Universität der Bundeswehr München Institut für Mathematik und Bauinformatik Professur für Mathematik
1. Berichterstatter:	Univ.-Prof. Dr.-Ing. habil. Andreas Malcherek Universität der Bundeswehr München Institut für Wasserwesen Professur für Hydromechanik und Wasserbau
2. Berichterstatter:	Prof. Ordinario Vincenzo Casulli University of Trento Department of Civil and Environmental Engineering
Tag der Einreichung:	24.10.2011
Tag der Prüfung:	19.01.2012
Mit der Prüfung erlangter akademischer Grad:	Doktor der Ingenieurwissenschaften (Dr.-Ing.)

Danksagung / Acknowledgment

Diese Arbeit entstand während der Bearbeitung des KFKI-Forschungsvorhabens *MudSim-B - Numerische Simulation der Dynamik von Flüssigschlick* (Förderkennzeichen: 03 KIS 067), welches durch das Bundesministerium für Bildung und Forschung (BMBF) gefördert wurde. Die Untersuchungen zu dieser Arbeit habe ich an der Bundesanstalt für Wasserbau - Abteilung Wasserbau im Küstenbereich - in Hamburg und in Zusammenarbeit mit dem Institut für Wasserwesen der Universität der Bundeswehr München durchgeführt. Großer Dank gilt daher Herrn Prof. Dr.-Ing Andreas Malcherek und Herrn Dr.-Ing Harro Heyer für die Initiierung und Anregung zu dieser Forschungsarbeit.

Besonders bei meinem Doktorvater, Prof. Dr.-Ing Andreas Malcherek, möchte ich mich herzlich bedanken für die konstruktiven, motivierenden Diskussionen und der ansteckenden Freude an immer wieder neuen Forschungsaspekten, für die hilfreichen Hinweise im richtigen Moment und für die vielen spontanen Gespräche, die trotz der Entfernung Hamburg-München immer möglich waren.

I would like to thank my second supervisor, Prof. Vincenzo Casulli, for many inspiring and valuable discussions on isopycnals, for providing the hydrodynamic isopycnal code on which I could base my work on, and for the time I could spend in Trento for my research work. I always returned to Hamburg with new ideas and good advices for my work.

Bei Prof. Dr. rer. nat. Thomas Apel bedanke ich mich für die Übernahme des Vorsitzes des Prüfungsausschusses für meine Promotion.

Herrn Dr.-Ing Harro Heyer und Herrn Holger Rahlf bin ich dankbar für den Freiraum zum Forschen, der es mir ermöglicht hat in einem erfahrenen Kollegenkreis und in einer technisch hervorragend ausgestatteten Umgebung promovieren zu können.

Ganz herzlich bedanken möchte ich mich bei Herrn Dr.-Ing. Günther Lang für die Betreuung meiner Arbeit in der BAW, die Unterstützung, die vielen hilfreichen Gespräche und wertvollen Anregungen.
Ebenfalls herzlich bedanken möchte ich mich bei Herrn Dr.-Ing. Holger Weilbeer für die Unterstützung und ideenreichen, motivierenden Gespräche.

Meinen Kollegen Ingrid Holzwarth, Frank Kösters, Holger Weilbeer und Günther Lang danke ich für das Lesen von Abschnitten meiner Arbeit und für die hilfreichen Anmerkungen.

Meinem Münchener Kollegen und MudSim-Projektpartner Hanno Cha danke ich für die gute und produktive Zusammenarbeit.

Dank gilt auch meiner engagierten *Tecplotterin* und studentischen Hilfskraft Johanna Scharnhorst.

Vielen Dank an meine Kollegen in der BAW und in der UniBw München: es macht einfach Spaß mit so tollen Kollegen zusammenzuarbeiten.

Meinen Eltern danke ich dafür, dass sie mich auf meinem Ausbildungsweg in allen meinen Entscheidungen unterstützt haben und mich ermutigt haben neue Wege zu gehen.

Ganz besonderer Dank gilt meinem Mann Andres für den Rückhalt, die notwendige Ablenkung und seine einfach großartige Unterstützung.

Hamburg, im Februar 2012 Denise Wehr, geb. Knoch

Contents

List of Figures

List of Tables

1 Introduction

1.1 Motivation and Objectives

Fluid mud (hyperconcentrated mud suspension) is a suspension consisting of mineral particles, organic substances, water and in some cases small amounts of gas. The fraction of clay particles is accountable for the specific flow behavior of fluid mud because of the cohesive properties of the clay particles. Cohesive sediments in water are transported by turbulent currents whereas in regions of quiescent flow or during periods of low currents, e.g. during slack water in tidal currents, the particles settle and accumulate on the bottom. Then fluid mud forms where there is an adequate supply of suspended matter. Fluid mud describes a state in which mud is capable of flowing in spite of very high concentrations of suspended matter in the range of several 10 g/L (see Table 1 on Page 8). The flow behavior of fluid mud depends on the shear state and can be described as viscoelastic with a yield stress. By comparison, water is characterized as an ideal viscous Newtonian fluid. Fluid mud, being a non-Newtonian fluid, is therefore governed by a different rheology than clear water. The investigation and process description of highly concentrated suspensions is of relevance to many fields of work. Besides fluid mud formation in coastal areas and estuaries, many of the issues are similar to those in fields such as sewage sludge treatment [Mori et al., 2006; Novarino et al., 2010] or the production and processing of bentonite [Heinz, 2006] suspensions, cement or concrete [Banfill, 2003; Roussel, 2007].

Naturally occurring mud provides nutrients for organisms in waters as mud exhibits a relatively high content of organic substances. However, mud becomes an unwanted material when it accumulates, deposits and consolidates. In many estuarine waters and harbors in particular, the mud budget has been greatly affected by infrastructure projects over the past few decades. The increasing siltation of harbor basins, harbor access channels and parts of shipping channels leads to an increase in the level of maintenance requirements and, as a consequence, to higher costs. Depending on its contaminant load, dredged material is also expensive to redistribute in the water or to dump on landfill sites. Another issue is the determination of the nautical depth where the presence of fluid mud in waterways needs to be considered. Hence, an almost stationary fluid mud layer may be navigable in spite of a high concentration of solids if the vessel overcomes its yield stress [Wurpts, 2005].

A profound understanding of the process of the formation, development and transport of fluid mud and the description of its rheological behavior is needed in order to enable construction work, maintenance work and activities aimed at reducing siltation to be evaluated, planed and optimized. Today, the required detailed investigations and prognoses of the behavior and reaction of water systems are supported by numerical

modeling.
The numerical modeling of estuaries is carried out by means of three-dimensional models which take account of physical processes such as the suspended sediment transport, salt transport, density-induced currents, turbulence. These conventional models are based on the assumption of a Newtonian fluid. However, highly concentrated mud suspensions exhibit a distinctly non-Newtonian behavior. Therefore, in this thesis a module for the simulation and prediction of the dynamics of fluid mud is developed. An existing numerical method has been extended to include an approximation of the inner stresses in a non-Newtonian fluid and by considering a parameterized approach for the description of the specific rheological behavior of fluid mud. In addition, major subprocesses of the fluid mud transport are taken into account by parameterizations in the model.
There is usually a strong density gradient at the transition between a fluid mud layer and the body of water above it. This transitional zone is known as a lutocline. The two fluid layers exhibit very different flow behaviors and interact by means of the shear forces acting in the boundary layer. A common approach is therefore to model the fluid mud as a two-dimensional, depth-averaged layer. Processes such as the formation and resuspension of fluid mud lead to changes in the density gradient and to the development of a system with multiple layers. An isopycnal approach, in which the mud suspensions are resolved three-dimensionally by means of layers of constant density, has been chosen in this research work to improve the resolution of such mechanisms.

This thesis expands an existing numerical method of modeling the dynamics of fluid mud. The fundamental properties and flow behavior of fluid mud are described in Sections 2.1 and 2.2 respectively of Section 2 while the main processes governing the dynamics of fluid mud are discussed in Section 2.3. This is followed by an introduction to the general mathematical description of the movement of fluids in Section 2.4. Section 2.5 provides an overview and evaluation of existing numerical methods of modeling fluid mud.

The conceptual principles of the numerical model are developed in Section 3 and are based on the description of the dynamics, the rheology of fluid mud and the overview of existing methods of modeling. This is followed by the presentation of the isopycnal numerical method and how it has been extended to include the modeling of vertical transport processes in Section 4. Section 5 deals with the functionality of the model which is illustrated by examples of tests and verifications. The application of two sectional models of the Ems estuary in Section 6 illustrates how the method can be applied to complex estuary systems. The thesis concludes with a discussion of the results and by identifying possible future developments and those aspects in which further research is required.

1.2 Motivation und Zielsetzung

Flüssigschlick (*fluid mud*, *hyperconcentrated mud suspension*) ist eine Suspension bestehend aus mineralischen Partikeln, organischen Stoffen, Wasser und teilweise auch geringen Anteilen von Gasen. Ein wesentlicher Bestandteil dieser Suspensionen ist der erhebliche Anteil an Tonpartikeln, die kohäsive Eigenschaften aufweisen. Dieser kohäsive Anteil ist maßgeblich für das Fließverhalten des Flüssigschlicks verantwortlich. Kohäsive Sedimente werden im Gewässer durch turbulente Strömungen transportiert. In strömungsberuhigten Gebieten und zu Phasen beruhigter Strömung, z.B. während der Kenterungsphasen in Tideströmungen, sinken die Partikel zu Boden und akkumulieren dort. Bei ausreichendem Schwebstoffangebot entstehen hier Flüssigschlickschichten. Diese Schlickschichten befinden sich in einem fließfähigen Zustand, obwohl die Schwebstoffkonzentratrationen sehr hoch werden können im Bereich von einigen 10 g/L (siehe Tabelle 1 auf Seite 8). Das Fließverhalten von Flüssigschlick ist abhängig vom Scherzustand und kann als viskoelastisch mit einer Fließgrenze (*yield stress*) beschrieben werden. Im Vergleich dazu wird Wasser als ein ideal viskoses Newtonsches Fluid charakterisiert. Daher unterliegt Flüssigschlick als nicht-Newtonsches Fluid einer anderen Rheologie als Wasser. Die Untersuchung und Prozessbeschreibung von hochkonzentrierten Suspensionen umfasst viele Bereiche. Neben dem Flüssigschlickvorkommen in Ästuaren und Küstengewässern sind Fragestellungen der Behandlung von Klärschlämmen [Mori et al., 2006; Novarino et al., 2010] oder auch Herstellung und Verarbeitung von Bentonit-Suspensionen [Heinz, 2006], Zement oder Beton [Banfill, 2003; Roussel, 2007] vergleichbar.

Natürlich vorkommender Schlick bietet Organismen in Gewässern ein Nährstoffangebot aufgrund der hohen organischen Bestandteile. Schlick wird jedoch zu einem unerwünschten Material, wenn er verstärkt akkumuliert, sich ablagert und konsolidiert. Insbesondere in vielen ästuarinen Wasserstraßen und Hafenanlagen haben Infrastrukturmaßnahmen der letzten Jahrzehnte zu einer starken Beeinflussung des Schlickhaushaltes geführt. Die zunehmende Verschlickung in Häfen, Hafenzufahrten und auch in Fahrrinnenabschnitten geht mit einem erhöhten Unterhaltungsbedarf und damit auch erhöhten Kostenaufwand einher. Die Umlagerung im Gewässer oder Verbringung auf Deponien des gebaggerten Materials kann je nach Schadstoffbelastung ebenfalls kostenintensiv werden. Eine weitere Fragestellung bezüglich des Flüssigschlickvorkommens in Wasserstraßen ist die Ermittlung der nautischen Tiefe. Obgleich Flüssigschlick sehr hohe Konzentrationen aufweist, kann er bei entsprechender Belastung fließfähig bleiben. So kann eine fast ruhende Flüssigschlickschicht trotz hoher Feststoffkonzentration schiffbar sein, wenn ihre Fließgrenze vom fahrenden Schiff überschritten wird [Wurpts, 2005].

Vertieftes Prozessverständnis über die Entstehung, Entwicklung und des Transportes sowie der Beschreibung des rheologischen Fließverhaltens von Flüssigschlick ist erfor-

derlich um Fragestellungen zu Bau- und Unterhaltungsmaßnahmen zu beantworten und Methoden zur Verminderung der Verschlickung des Systems zu entwickeln. Diese Maßnahmen bedürfen detaillierter Untersuchungen und Prognosen zum Systemverhalten eines Gewässers, welche heute durch den Einsatz von numerischen Modellen unterstützt werden.
Numerische Modellierung von Ästuaren erfolgt mit dreidimensionalen Modellen, die Schwebstofftransport, Salztransport, dichteinduzierten Strömung, Turbulenz usw. berücksichtigen. Diese konventionellen Modelle basieren auf der Annahme eines Newtonschen Fluides. Hochkonzentrierte Schlicksuspensionen verhalten sich jedoch deutlich nicht-Newtonsch. In der vorliegenden Arbeit wird daher ein Modellbaustein zur Simulation und Prognose der Dynamik von Flüssigschlick entwickelt. Ein bestehendes numerisches Verfahren wird durch eine Approximation für die inneren Spannungen eines nicht-Newtonschen Fluides erweitert und es wird ein parametrisierter Ansatz zur Beschreibung des spezifischen rheologischen Verhaltens von Flüssigschlick integriert. Wesentliche Teilprozesse des Schlicktransportes sind über Parametrisierungen im Modell realisiert worden.
Eine sich gebildete Flüssigschlickschicht im Gewässer weist meist einen starken Dichtesprung zum darüber liegenden Wasserkörper auf. Dieser Übergangsbereich wird als Lutokline bezeichnet. Die beiden Fluidschichten haben ein grundverschiedenes Fließverhalten und interagieren über Scherkräfte an der Grenzfläche. Daher ist ein häufig gewählter Ansatz den Flüssigschlick als einen zweidimensionalen tiefengemittelten Layer zu modellieren. Prozesse wie die Entstehung und Resuspension von Flüssigschlick wirken sich in einer Änderung des Dichtegradienten und der Entwicklung eines Mehrschichtensystems aus. Um diese Mechanismen besser auflösen zu können, wird in der vorliegenden Arbeit ein isopyknischer Ansatz verfolgt, der Schlicksuspensionen durch Schichten gleicher Dichte dreidimensional auflöst.

Im Rahmen dieser Arbeit ist ein vorhandenes numerisches Modellverfahren für die Modellierung der Dynamik von Flüssigschlick erweitert worden. In Kapitel 2 werden die grundlegenden Eigenschaften (Abschnitt 2.1) und das Fließverhalten von Flüssigschlick (Abschnitt 2.2) beschrieben. In einem weiteren Abschnitt werden die wesentlichen Prozesse, die die Dynamik von Flüssigschlick bestimmen, erläutert (Abschnitt 2.3). Darauf folgt eine Einführung für die allgemeine mathematische Beschreibung der Bewegung von Flüssigkeiten in Abschnitt 2.4. Ein Überblick über vorhandene numerische Modellverfahren zur Simulation von Flüssigschlick wird in Abschnitt 2.5 gegeben und bewertet. Auf Basis der Beschreibung der Dynamik und der Rheologie von Flüssigschlick sowie der Übersicht vorhandener Modellverfahren werden in Kapitel 3 die konzeptionellen Grundlagen für das numerische Modell entwickelt. Danach erfolgt die Darstellung des isopyknischen, numerischen Modellverfahrens und dessen Erweiterungen zur Modellierung von vertikalen Transportprozessen in Kapitel 4. In Kapitel 5 wird die Funktionalität des

Modells anhand von schematischen Testbeispielen und Verifikationsbeispielen dargelegt. Die Modellierung von zwei Ausschnittsmodellen des Emsästuars, dargestellt in Kapitel 6, gibt einen Eindruck über die Anwendbarkeit des Verfahrens für komplexe Ästuarsysteme. Abschließend werden die Ergebnisse der Arbeit diskutiert und Perspektiven für Weiterentwicklungen sowie zukünftiger Forschungsbedarf aufgezeigt.

2 Properties, Processes and Mathematical Description of Fluid Mud Dynamics

2.1 Fluid Mud Properties

Natural mud suspensions or fluid mud basically consist of water and mineral grains with a mean diameter ranging from 1 μm to 10 μm. They also contain small concentrations of organic components, which vary greatly according to the season, and gas. These two minor components are not considered in this work.
The solid particles are mostly clay (particle size <2 μm) and silt (particle size <63 μm). Additionally, colloids with a particle diameter of around 0.1 μm form a sub-fraction of the clay fraction. The inorganic particles consist of different types of mineral (clay minerals, quartz, silicates) and their distribution is site-specific. Other comparable suspensions such as industrial water-debris mixtures, cement and bentonite often contain coarser grain sizes than colloidal clay suspensions. Estuarine mud suspensions have a high clay content which significantly influences their rheological behavior.

Coussot [1997] indicates three fundamental physical parameters which have an effect on the rheology of mud suspensions: the concentration described by the solid volume concentration, the grain size distribution and the ion concentration (natural clay suspensions are cation-saturated and have a pH of around 7).
The solid volume concentration is defined by the relationship between the volumes of the two components, water (index w) and solids content (index s):

$$\phi_s = \frac{V_s}{V_s + V_w}. \tag{2.1.1}$$

The relation between the solid volume concentration ϕ_s and the solid mass concentration c_s is

$$c_s = \phi_s \varrho_s \tag{2.1.2}$$

and in terms of density, the bulk density is defined by

$$\varrho = \varrho_w + \left(1 - \frac{\varrho_w}{\varrho_s}\right) c_s = \phi_s \varrho_s + (1 - \phi_s)\, \varrho_w. \tag{2.1.3}$$

The particle density is approximately ϱ_s=2650 kg/m^3 and the water density ϱ_w=1000 kg/m^3.

In mud suspensions a distinction can generally be made between the different interactions of the constituents [Coussot, 1997]:

- water molecule interactions
- colloidal interactions of particles <10 μm such as van der Waals attraction, double-layer interaction, Born repulsion

- friction or collision between particles >10 μm

The weight of clay particles is small enough so that even Brownian motion keeps them in suspension. Moreover, clay particles have a negative charge on their surface so that they repel each other. These electrical repulsive forces are neutralized by ambient water ions or by organic polymers. Colliding clay particles stick to each other, forming aggregates or flocs. This is the cohesive property of clay particles. Cohesion is the most important mechanism governing the behavior of mud suspensions. The flocs that have formed can now settle under the action of gravity. They may be disrupted under shear impact and then re-aggregate with decreasing shear if the attractive forces are stronger than the repulsive forces. This process of the break-up and aggregation of the flocs is known as flocculation. A more detailed description of these mechanisms is given by McAnally and Mehta [2001] and Dankers [2006] amongst others.
Fluid mud is formed by such aggregates which hinder each other in settling as their concentration increases. Under quiescent conditions the aggregates form a granular structure, also known as a gel. A strong density gradient arises between the hyperconcentrated mobile or static mud at the bottom and the water body above. This gradient is known as the lutocline. An additional characteristic is that below the lutocline the flow behavior is non-Newtonian and laminar. Ross and Mehta [1989] indicates that lutoclines form if the concentration exceeds 10 kg/m^3 (ϱ =1006.2 kg/m^3).
However, it is difficult to define a characteristic concentration or bulk density of fluid mud. The concentration is dependent on several constituents of the aggregates and can be site-specific. Different concentration ranges can be found in the literature. Some of them are shown in Table 1.

A more detailed description of estuarine muds is given by Winterwerp and van Kesteren [2004], Coussot [1997] and Ross [1988].

Soulsby (2000) in Whitehouse et al. [2000]		flocculated suspension, 0.01–3 kg/m^3	fluid mud, 3–100 kg/m^3	consolidating settled bed, 50–100 kg/m^3
Winterwerp [1999]	low-concentration mud suspension, several 0.01 kg/m^3 to a few 0.1 kg/m^3	high-concentration mud suspension, few 0.1 kg/m^3 to few 1 kg/m^3	fluid mud, several 10 kg/m^3 to 100 kg/m^3	
van Rijn [2005] revised from Bruens (2003)	dilute mud suspension, 0–10 kg/m^3		fluid mud, 10–300 kg/m^3	consolidated mud, >300 kg/m^3

Table 1: *Overview of mud suspension concentrations.*

2.2 Rheology of Suspensions

2.2.1 Introduction to Rheology

Rheology is the science of the deformation and flow behavior of materials ranging from ordinary liquids to elastic solids. This general definition of rheology was drawn up by Bingham. Today, the term 'rheology' is mainly used to denote the study of complex fluids. Thus Oswald [2009] establishes the term 'rheophysics' which describes the study of arbitrary types of material (gaseous, liquid, solid materials or materials between liquid and solid). In the present paper the term rheology is used with its original meaning.

There are two different rheological approaches. The macroscopic approach comprises the mechanics of continuous media, based on macroscopic physics such as Newton's Law and the first and second principles of thermodynamics. The structure of a material is characterized by its average appearance and is described by constitutive laws. The relationship between stress and strain/deformation is one of the most applied laws. This relationship can be measured and adopted for model approaches.
The microscopic approach identifies the rheological phenomena on its microscopic structure scale. Thus, the rheological description varies with the scale of the structure and the material. Changes in the particle interactions during flow are examples of such microscopic mechanisms.
In the following, the macroscopic rheological approach is primarily applied and the focus is on the rheology of fluids.

2.2.2 Fluid Flow Behavior

A fluid can be characterized according to its behavior under the action of external pressure or shear stress. The first type of behavior distinguishes between compressibility and incompressibility depending on whether a fluid element reacts to the applied pressure or not. Most of the time, fluids can be considered as incompressible, whereas gases are compressible media. This assumption is used to set up the continuity equation for a fluid element. The influence of shearing on a continuous fluid element is more important. The shear stress can be expressed by different rheological constitutive laws. They describe the fluid behavior due to flow curves (shear stress τ_{ij} versus shear rate $\dot{\gamma}_{ij} = \frac{\partial u_i}{\partial x_j}$), which is illustrated in Figure 1. There are two elementary fluid behaviors, known as the Newtonian and the non-Newtonian fluid behavior respectively. A Newtonian fluid is defined by the linear dependence of the two parameters shear rate and shear stress, with viscosity as the constant of proportionality. Newtonian fluids are homogeneous and isotropic, for example water. The viscosity of the materials in simple

shear (one-dimensional shear) is defined as

$$\mu = \frac{\tau}{\dot{\gamma}}. \tag{2.2.1}$$

In the following, this viscosity is also denoted as rheological viscosity μ_r in contrast to the turbulent viscosity in hydrodynamics. Non-Newtonian fluids have a non-linear flow curve and/or can have a yield stress τ_y. The reaction of these complex fluids to shear impact may be time-dependent. Not only may they exhibit viscous behavior but, such as solids, they may additionally have elastic characteristics - these are viscoelastic fluids. The rheology of non-Newtonian suspensions and especially of mud suspensions is described in the following section. The suspensions are assumed to be homogeneous and are treated as a continuum.

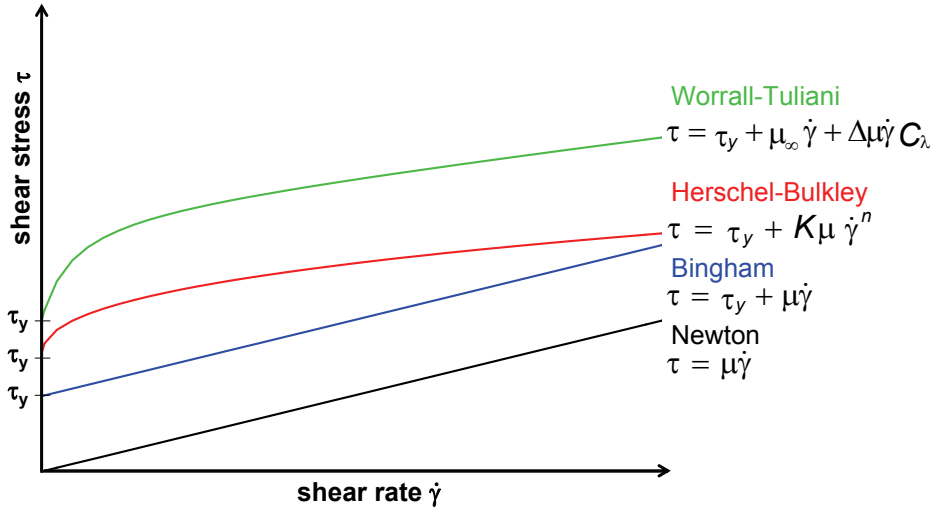

Figure 1: *Rheological constitutive laws.*
They describe the behavior of a material under influence of shear impact. The simplest constitutive law is that of a Newtonian fluid with a constant viscosity. Some materials have to overcome a specific stress, the yield stress τ_y, to deform. The yield stress and other parameters of the constitutive laws can be determined by rheological measurements.

2.2.3 Rheological Characteristics of Suspensions

In terms of the rheological viscosity of non-Newtonian fluids (complex fluids such as suspensions) a distinction can be made between the following basic types of shear behavior [Chhabra and Richardson, 2008; Coussot, 1997]:

- time-independent fluid behavior
  - shear-thinning
  - shear-thickening

  - viscoplastic / yield-stress fluids

- time-dependent fluid behavior
  - thixotropy

- viscoelastic behavior

The rheological viscosity in shear-thinning materials decreases with increasing shear rate: $\frac{d\mu}{d\dot{\gamma}} < 0$. Such materials include, for example, mud suspensions, blood and yoghurt. Shear-thinning is a phenomenon which results from phase transitions or changes in the particle structure.
Shear-thickening leads to increasing viscosity with an increasing shear rate: $\frac{d\mu}{d\dot{\gamma}} > 0$. Shear-thickening or dilatant materials are, for example, certain granular, water-silicium or clay suspensions. These two behaviors are qualitatively illustrated in Figure 2.

A yield stress τ_y can also be observed for many shear-thinning fluids. The characteristic behavior of such fluids is realized with the constitutive laws by Hershel-Bulkley and Worrall-Tuliani (see Figure 1). The critical shear stress in the fluid has to be exceeded in order for the fluid to begin flowing or deforming. Examples of yield stress fluids are fresh concrete, greases, mud, lavas, paint, inks, filled polymers and foodstuffs such as molten chocolate or toothpaste. These kinds of suspension form a continuous matrix of bonded particles as long as the shear impact is below the yield stress. If the yield stress is exceeded, the bonds break and the fluid starts to move.
The simplest constitutive approach to describing a yield stress fluid is the Bingham model, illustrated in Figure 1, which is a linear function with a yield stress. When the yield stress is exceeded, the fluid reacts as a Newtonian fluid. Such fluids are known as Bingham-plastic or viscoplastic fluids whereas yield stress fluids with a non-linear flow curve are known as yield-pseudoplastic fluids.

Thixotropic materials change their behavior with time under constant shear conditions. The rheological viscosity changes with time $\frac{d\mu}{dt} \neq 0$. Thixotropy describes the destruction and recovery of the granular matrix and flocs with time as these processes do not take place immediately. As the shear stress increases, interior bonds crack to support a new shear strain state. Only a lower shear stress might then be needed to conserve this shear state owing to the bonds breaking up. It requires time and the absence of the shear stresses, or a reduction of such stresses, to rebuild the structural bonds. Clay-water mixtures and paints are typical thixotropic and shear-thinning suspensions.

The last characteristic is viscoelasticity. The behavior of viscoelastic fluids is dependent on the time of the shear impact. They react elastically in the same way as a solid when subject to brief impacts and in the same way as a purely viscous fluid under continuous shear.

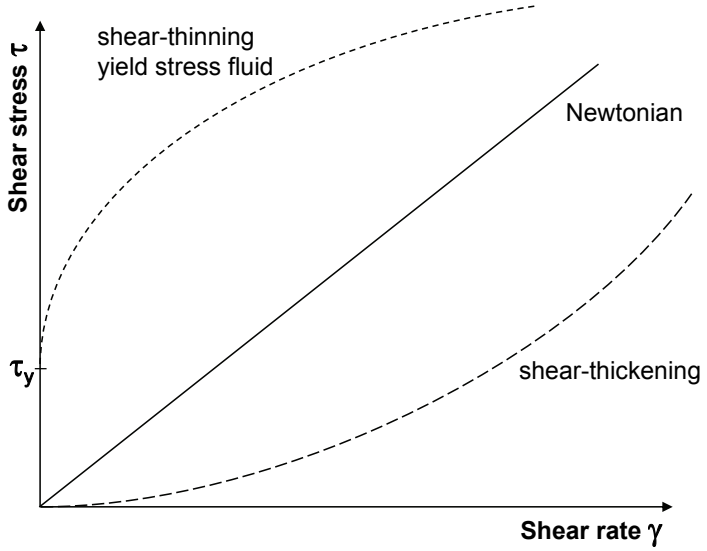

Figure 2: *Shear-thickening and shear-thinning behavior (redrawn from Coussot [1997]). The viscosity decreases with increasing shear rate of a shear-thinning material and shear-thickening behavior leads to an increase of the viscosity with an increase of the shear rate.*

The two latter types of behavior, thixotropy and viscoelasticity, are both related to a characteristic time of the phenomenon. That time has to be considered during observation of such behavior.

2.2.4 Rheological Behavior of Fluid Mud

Fluid Mud contains a considerably large amount of clay. Therefore, the cohesive properties of clay dominate the rheological behavior of mud suspensions.
High-concentration mud suspensions can be characterized as shear-thinning, thixotropic, viscoelastic, yield stress fluids. However, these characteristics do not necessarily affect the behavior of fluid mud in all flow conditions and for every mud consistency. Understanding the rheological behavior of fluid mud is essential for the simulation of its (laminar) flow and transport.
In mud suspensions in which clay particles predominate shear-thinning is mainly induced by the break-up of flocs and/or the orientation of the particles or aggregates. These effects are illustrated in Figure 3. Worrall and Tuliani [1964] derived a constitutive approach with a structural parameter to consider the degree of aggregation and to which break-up of the flocs occurred. Toorman [1997] and Wurpts [2005] analyzed the Worrall-Tuliani model. They found out that the flow curves of colloidal soils and cohesive suspended sediments match observations very well as long as they contain a great deal of clay and only a small amount of organic substances. More details on the constitutive law and parameterizations of the model are given in Section 3.4.
Hyper-concentrated mud suspensions behave elastically at low deformations (low shear impact) below the yield stress. Rheological measurements require different methods to

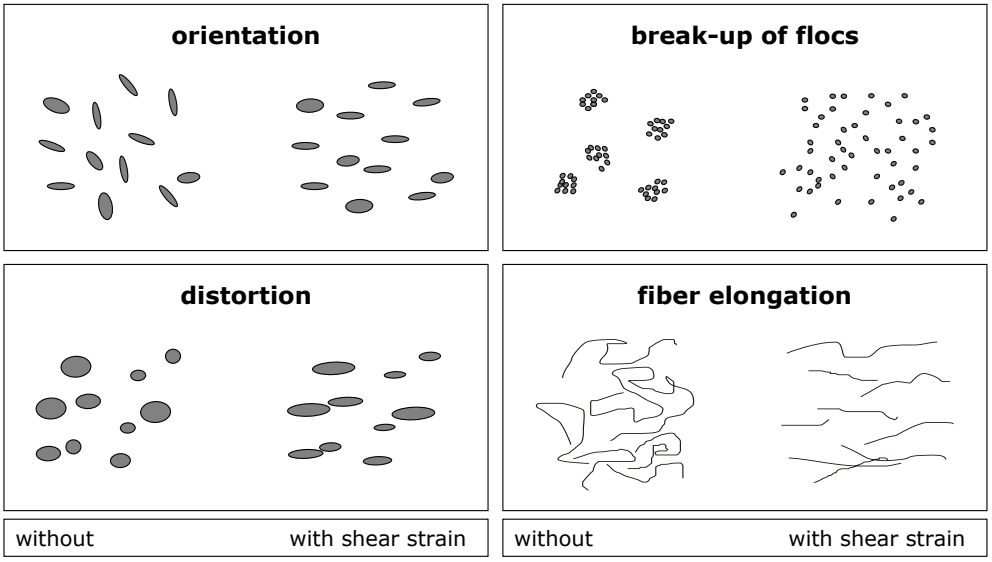

Figure 3: *Particle structures under shear impact (modified from Brummer [2006]).*
Spherical particles can orientate or distort under impact of shear to minimize the resistance against the shear impact. The bonds of flocs break-up and fibers elongate under impact of shear. These processes can lead to shear-thinning behavior of a material.

analyze behavior. For viscoplastic behavior the fluid deformation is measured under a permanent shear impact with increasing shear stress whereas, for elastic behavior, the deformation is measured under oscillating shear.
Fluid mud is approximated as a one-phase fluid, which implies that settling has to be negligible during the rheological measurements.

2.3 Fluid Mud Dynamics

The most important fluid mud transport processes and fluid mud dynamics are described below and are based on a review of the available literature. Further details can be found in McAnally et al. [2007a], McAnally et al. [2007b], Mehta et al. [1989], Whitehouse et al. [2000], Wan and Wang [1994], Winterwerp and van Kesteren [2004] and van Kessel [1997].

2.3.1 Formation of Fluid Mud

Fluid mud formation is related to the amount of cohesive material available in the water body. Cohesive material is transported into the system in different ways, for example by land erosion, elutriation and shore erosion. The fine material is transported downstream in rivers.
Fluid mud occurs in coastal regions in the turbidity maximum zone of estuaries, shores, on mud flats and in harbors. Fluid mud forms layers ranging from a few decimeters to

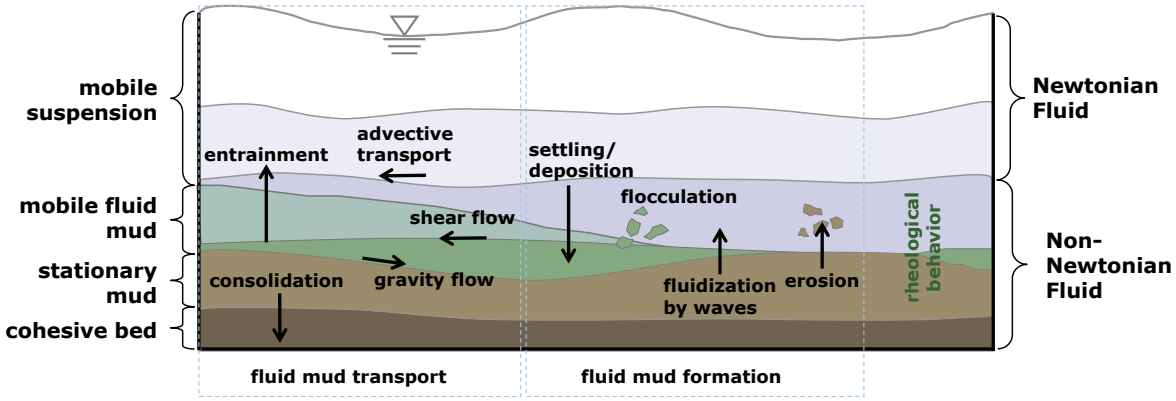

Figure 4: *Significant physical processes for fluid mud dynamics.*
In this scheme the cohesive sediment concentration increases from surface to bottom. The left side shows transport processes of mud suspensions. The right side shows processes which contribute to the formation of fluid mud. The physical processes are dependent on the rheological behavior.

several meters in thickness.
The formation of fluid mud is a combination of the settling and flocculation of suspended cohesive material and the fluidization of mud deposits by waves. Additionally, the erosion of consolidated mud enriches the cohesive suspended load in the water system. The formation and transport processes are illustrated in Figure 4. The transport processes are further described in the Sections 2.3.2 and 2.3.3. Once fluid mud is formed, it is mainly transported by advection due to currents or waves, shear flow and gravity-driven currents. Vertical transport occurs due to the entrainment of fluid mud into the water body above. This results in the fluid mud being resuspended.
Furthermore, fluid mud settles during decelerating or slack currents where the capacity to carry particles or flocs is reduced. This is often a temporary mechanism as in tidal currents. If the decelerated currents continue in the long term the fluid mud consolidates as seen in harbor basins and on river banks.

Flocculation

Flocculation covers the processes of the aggregation and break-up of flocs. Aggregates or flocs consist mainly of cohesive material and smaller amounts of organic material, other sediment particles, nutrients and a great amount of water. Owing to their high water content, their density may be only slightly higher than the density of water, resulting in very low settling velocities.
The state of dispersion and aggregation of flocs depends on the balance between attractive and repulsive forces. Aggregates form due to cohesive forces, collision and polymeric bonding of the solid particles. Collision supports aggregation and is induced by turbulent flow and the increasing concentration of suspended matter. Brownian mo-

tion also leads to collision. Another mechanism for the build-up of aggregates results from particles with higher settling velocities overtaking those with lower velocities.
Although turbulent flow leads to aggregation, strong turbulent flow causes the break-up of the aggregates as the repulsive forces overcome the attractive forces.
Turbulence affects the flocculation process while the process of the formation of fluid mud influences turbulence. The generated aggregates settle due to hindered settling to the bottom and the vertical concentration profile increases downwards. This stratification attenuates the turbulence in the regions of high concentrations, allowing fluid mud to form.
In tidal currents, the flocculation process and the resulting suspended sediment transport is strongly coupled to the intensity of turbulence, buoyancy destruction and the vertical suspended sediment concentration profile [Winterwerp, 2011].

2.3.2 Horizontal Transport Processes of Fluid Mud

Shear Flow

The advective flow of fluid mud can be caused by currents and waves. Currents above a fluid mud layer can force the fluid mud to flow owing to interfacial friction (shear flow), while stronger boundary layer flow leads to entrainment of fluid mud into the water body (by exceeding the fluid resistance). If the oscillating currents of wind waves impact the mobile mud layer, they induce a movement of the fluid mud layer parallel to the direction of wave propagation. This type of transport occurs in shallow waters in shelf regions, for example.

Gravity Flow

Density-driven currents are referred to as density flow, gravity flow or turbidity flow. In general, density flows are currents caused by gravity forces having an effect on any density differences in a fluid. Gravity flow describes down-slope movement of a suspension due to the impact of gravity. Mobile mud can be transported by gravity flow whereas turbidity currents describe density currents of suspensions with solid particles. Such suspensions are not necessarily fluid mud.

In this case, McAnally et al. [2007b] distinguishes between three kinds of gravity flow:

1. non-turbulent, laminar down-slope fluid mud flow
2. turbulent down-slope fluid mud flow where the turbulence is induced by the mud suspension itself
3. gravity flow induced by the flow of the ambient suspension or waves.

The internal shear strength of the fluid mud has to be exceeded in order for gravity flow to be initiated and is characterized by the yield stress.
If neither currents nor waves act on a hyper-concentrated layer (case 1. or 2.) the bottom slope has to be steep enough to enable the gravitational force to overcome the yield strength. The flow regime changes from laminar to turbulent flow with increasing slope and increasing internal shear. McAnally et al. [2007a] concluded that a slope of less than one degree leads to laminar gravity currents in the fluid mud.
If the down-slope turbidity current of a fluid mud layer exceeds the critical shear stress for erosion, the mud layer is enriched with additional sediment load from the bottom, which in turn accelerates the velocity of the layer. This is referred to as auto-suspending turbidity flow [Scully et al., 2002; Wright et al., 2001]. However, dissipative turbidity flow decelerates the fluid mud movement due to the denser suspension mixing with the less concentrated suspension at the interface. The interfacial mixing leads to decreasing concentration of the fluid mud layer. In nature, gravity flow exhibits both mechanisms, auto-suspending and dissipative turbidity, concurrently.
The presence of high ambient turbulent currents (case 3.) leads to an increase in the internal resistance of the fluid mud layer and decelerates the gravity current. However, at the same time, the turbulent shear forces keep the fluid mud mobile.

2.3.3 Vertical Transport Processes of Fluid Mud

The vertical processes of mud suspensions and stationary mud depend on the condition, sediment concentration and impact on the mud. They describe the transition from dilute to high-concentration suspensions and then to mud beds. In terms of mobility, the processes transform mud suspensions from mobile to stationary conditions and vice versa. This is shown in Figure 5.

Settling

Settling is a process influenced by the gravity force acting on the particles or aggregates, the viscous drag of the ambient fluid and the interaction of the aggregates [Mehta et al., 1989]. Therefore, the settling velocity of particles and aggregates depends on their density, size, shape and the ambient fluid properties.
The settling velocity and formation of fluid mud itself depend on the size, density, shape and strength of the flocs. Formulations for the settling velocity which consider these aspects are often based on the approximation that flocs are self-similar entities.
The settling velocity of aggregates ranges from around 10^{-5} m/s to 10^{-2} m/s [McAnally et al., 2007a].
In general, the settling velocity increases with increasing concentration. At very high suspended matter concentrations the settling velocity decreases due to inhibiting aggre-

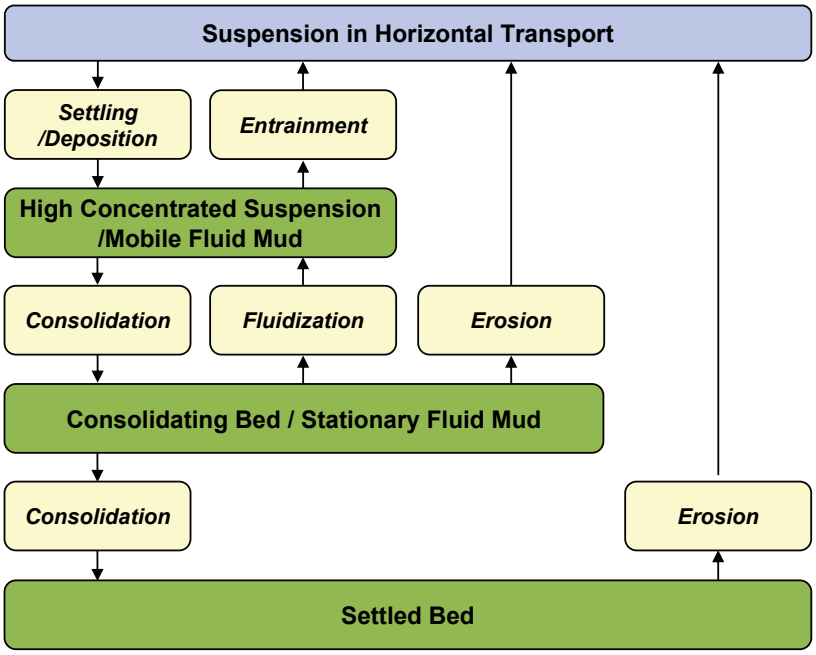

Figure 5: *Vertical transport processes for cohesive sediments (modified according to Mehta et al. [1989]).*
The vertical transport processes (yellow panels) depend on the rheological condition and sediment concentration. They transfer a dilute suspension of cohesive material in horizontal transport (blue panel) to a high-concentration suspension/mobile fluid mud to stationary fluid mud and to consolidated mud bed (green panel) and vice versa.

gates (hindered settling). This starts at concentrations of around 5-10 kg/m^3 [Mehta et al., 1989] which is also the range in which fluid mud is generated. With increasing contact between the aggregates the settling process is replaced more and more by consolidation. The concentration at this point is defined as the gelling concentration.

Entrainment

Entrainment describes the transition from a highly concentrated suspension to a suspension with a lower concentration as a result of turbulent mixing (mobilization of fluid mud).
There are two different entrainment cases [McAnally et al., 2007a; Kranenburg, 1994]:

1. Considering a turbulent mixed water layer above a nearly quiescent fluid mud layer. Turbulent eddies will cause the fluid mud to become mixed with the water layer.

2. The water layer is assumed to be static, while the fluid mud layer is turbulent. The fluid mud layer moves between a lower rigid bed layer and a water layer. If the mud suspension allows sufficiently high Reynolds numbers the shear stresses at these boundaries will cause turbulence and water will be entrained in the fluid mud layer.

The first case is the most frequently observed case, whereas the second case is a phenomenon observed particularly in estuaries. During slack water, the water layer may be far slower than the inertial flowing mud suspension layer or even static. In both entrainment cases, the thickness of the water layer decreases and that of the mud layer increases with simultaneously decreasing concentration. The turbulent mixing involves turbulence damping due to stratification effects. The stratification of a fluid and the turbulence structure of the flow can be characterized by the gradient Richardson number Ri

$$Ri = -\frac{g\frac{\partial \varrho}{\partial z}}{\varrho\left(\frac{\partial u}{\partial z}\right)^2} \tag{2.3.1}$$

where z is the height above the bottom, ρ is the suspension density and u the current speed at depth z. As the density gradient increases, the turbulence is damped and the flow reaches a laminar state. At a Ri-value between 0.1 and 0.3 the turbulence is totally damped by stratification [Whitehouse et al., 2000].
Additionally, the Ri-number may be an indicator of interfacial mixing (initiation of entrainment). Whitehouse et al. [2000] reports, for example, that entrainment occurs at Ri-numbers lower than around 10. In this case, the bulk Richardson number, which is a discretized form of the gradient Ri-number, is applied

$$Ri_* = \frac{(\varrho_w - \varrho_{mud})}{\varrho_{mud}} \frac{gH_{mud}}{(u_w - u_{mud})^2}. \tag{2.3.2}$$

This equation considers a two-layer system comprising a water layer (index w) and a fluid mud layer (index mud). The degree of stratification can be classified as:

$$\begin{aligned} Ri &< \frac{1}{4} \text{ instable stratification} \\ Ri &> \frac{1}{4} \text{ stable stratification} \end{aligned} \tag{2.3.3}$$

Entrainment approaches for the determination of entrainment rates are presented in Section 3.6.

Fluidization of Mud Deposits by Waves

Fluidization is the process of transition from consolidated cohesive bed to fluid mud under the impact of waves.
At first, the distribution of the resultant stresses in suspensions and mud beds has to be studied, see Figure 6. Fluid mud deposits or consolidated mud beds are regarded as solids in which the aggregates are in contact with each other, forming a soil matrix with fluid-filled pores. The total load is supported by the soil matrix and the pore water. This is described by the total normal stress σ. The effective normal stress $\sigma^{'}$ is the load supported by the granular structure. u_p is the pore water pressure. They are related with $\sigma^{'} = \sigma - u_p$. The pore pressure is the sum of the hydrostatic pressure p_h and the

excess pore pressure Δu_p: $u_p = \Delta u_p + p_h$. In mobile suspensions or fluid mud there is no permanent contact between the aggregates and the entire load is supported by the fluid phase. The effective normal stress is then zero and $\sigma = p_h$. Both, the aggregates and the pore water, support the load as the contact between the aggregates increases and a granular structure is formed. The effective normal stress will then increase.
Fluidization occurs in freshly consolidated mud beds. Whereas the material is increasingly eroded as consolidation progresses. Additionally, a low permeability of the mud bed supports fluidization.

Waves cause oscillating pressure gradients in the pore water, progressively weakening the grain structure. As a result, the pore water will start to flow. If the upward velocity is pronounced enough, the aggregate bonds will break up. The excess pore pressure increases as the effective stress decreases. If the effective stress approaches zero the mud bed is transformed from a solid to a fluid with a specific viscosity. This is the fluidization process. The reaction of the mud bed is both elastic and viscous. The elasticity restores the initial condition of the mud bed after impact whereas the viscous behavior responds in a dissipative manner. It attenuates the wave action and the amplitude of the waves propagating over the fluid mud. Moreover, modeling of this

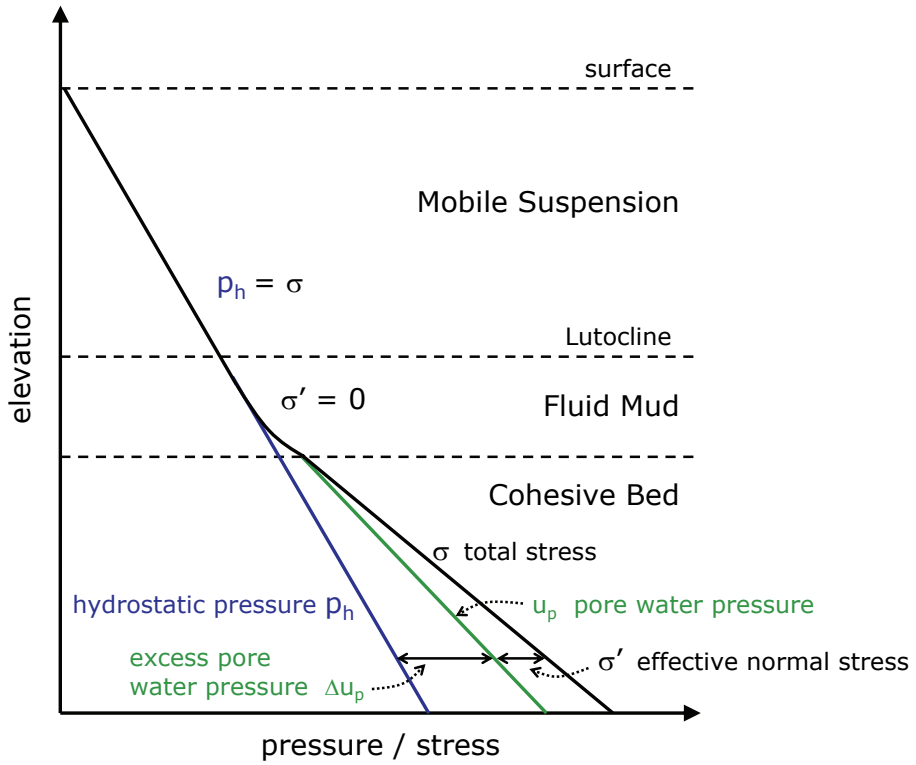

Figure 6: *Scheme of the vertical stress profile from mobile suspension to fluid mud and to cohesive bed (modified from Ross and Mehta [1990]).*
The total stress inside the cohesive bed is the sum of hydrostatic pressure, excess pore water pressure and the effective normal stress. The first two quantities represent the load supported by the pore water. The latter results from the load supported by the granular structure.

process needs to describe the viscoelastic behavior.
Once the mud bed is fluidized it can easily be entrained or transported due to shear and gravitational forces.

Research on the understanding, description and modeling of wave attenuation over a fluid mud bed and fluidization due to wave action is being carried out by several research groups e.g. Mehta [1996], Jain and Mehta [2009], Foda and Hunt [1993] and Soltanpour and Haghshenas [2009].

Consolidation

As the suspended matter concentration increases, the aggregates hinder each other in settling which generates fluid mud. The gelling concentration then is reached at which the aggregates are in contact with each other. Now the aggregates form a granular structure with water-filled pores. Consolidation begins of this soil structure if the fluid mud becomes stationary. The weight of the overlying water column is supported by the granular matrix and the pore water. The load causes the pore water to escape and the soil matrix to densify, resulting in a reduction in the volume of the cohesive bed - the primary consolidation. Secondary consolidation then begins with the full dewatering of the pores. Sorting of the aggregates starts to allow further reduction of the interstitials. Moreover, the elevation of the lutocline decreases during the consolidation process. Consolidation of cohesive material is a relatively slow process compared with the other transport processes that have been mentioned and takes place on a time scale ranging from hours to years. By contrast, consolidation in sandy beds occurs immediately, the pore water escapes and the grains are rearranged. Owing to the slowness of this process, fresh deposits are easily entrained or eroded again. Accordingly, the degree of consolidation gives information about the erodibility of the cohesive bed [Lick and McNeil, 2001]. The evolution of strength in dependence to the effective stress of the cohesive bed is studied by Merckelbach [2000]. The indicator for the strength or resistance against erosion is the yield stress of the consolidated cohesive bed.
Numerical modeling of consolidation rates can be considered as a settling velocity. A combined formulation for consolidation and hindered settling by means of the density is described by Toorman and Berlamont [1993], for example. Parameterizations are gained from settling column experiments.

2.3.4 Fluid Mud Dynamics under Tidal Flow

The formation and transport of fluid mud in estuaries and coastal regions is forced by tidal conditions. Estuarine fluid mud most commonly develops in the maximum turbidity zone. Depending on the tidal phase, the mud settles during slack water and is

mobilized or entrained by highly turbulent ebb and flood velocities. Fluid mud is present only during certain hydrological events or during low current tidal phases as determined by the hydrological situation and on the availability of mud in the estuary. This is the case in the Weser Estuary, for example, or in wide areas during all tidal stages, as in the Ems Estuary. Schrottke et al. [2006] observed that, in the Weser, fluid mud may occur in the troughs of dunes in the turbidity zone. In the Ems Estuary fluid mud layers of several meters in thickness appear in the maximum turbidity zone, especially during ebb tide, due to the tidal asymmetry. For example, this was observed during a field survey in 2009 (see Figure 7). Figure 8 shows a lutocline detected during flood tides where internal waves are observed.

Mud suspensions settle and are deposited on the bottom during slack water. As flood or ebb currents increase the mud deposits are then eroded and the fluid mud or mobile mud is entrained into the water body (see Figure 9). Depending on the intensity of the currents, the fluid mud may become totally mixed into with the water body. In phases of moderately turbulent currents, fluid mud is generated owing to flocculation processes and hindered settling of the flocs and a sharp lutocline forms. The mud concentration is so high below the lutocline that the flow behavior differs from that in the water column (see Section 2.2.4). Vertical fluid mud transport processes during a tide period are dominated by the settling and formation of fluid mud as well as by entrainment, particularly in deep channels.
A typical phenomenon observed in estuaries is the decoupled flow of the water body and fluid mud layer. The fluid mud has a more inertial flow than water. The currents in the water body are nearly zero at the beginning of slack water but the fluid mud is still moving. However, once the mud movement stagnates, the shear forces of the main flow have to overcome the resistance of the mud to force the fluid mud to flow.
The estuarine system may be influenced hydrodynamically by the fluid mud when the thickness of the layers reaches a certain thickness and the fluid mud covers wide areas. The strong density stratification results in turbulence damping in the region of the water-fluid mud interface and finally leads to a reduced bottom friction.
Fluid mud deposits on river banks or mud flats can move down slope due to gravitational forcing. Gravity flow may move fluid mud to the deepest parts of an estuary such as the shipping channels as well as over great distances in the longitudinal direction of estuaries. The near-bed transport of cohesive sediments in the form of fluid mud layers is associated with significantly higher transport rates than the transport in suspension in the water body above. The knowledge about gravity flow of fluid mud can be used most effectively for maintenance purposes in harbor basins [Wurpts, 2005].

In consolidated mud, the cohesive forces and the density of the granular structure increase so that high impacts, for example waves or ship-induced waves, are required for re-mobilization. Ship-induced waves are more likely to cause erosion at the river

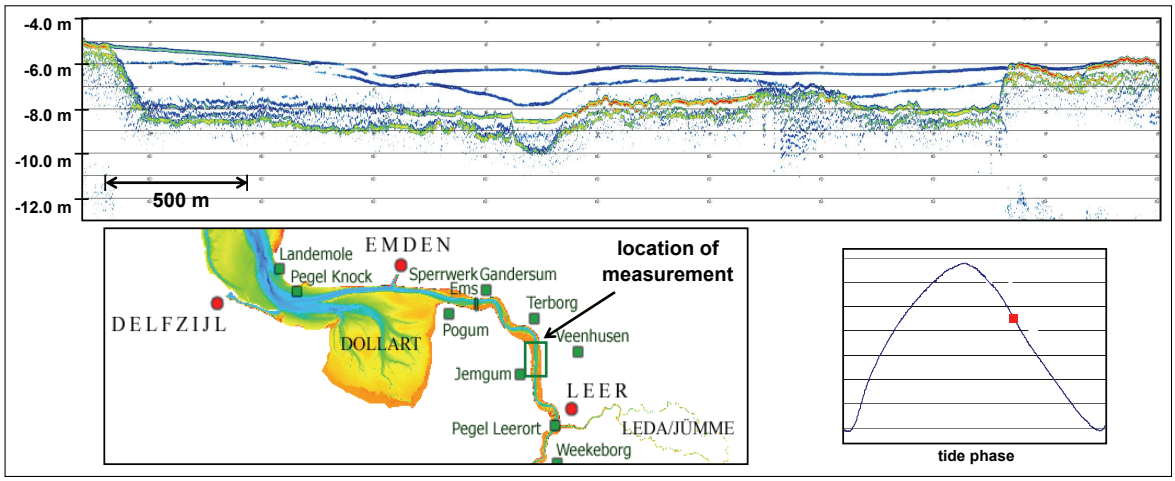

Figure 7: *Multi-layer system of fluid mud detected due to sediment echo sounder measurements (parametric sub-bottom profiler for shallow water) during ebb tide.*
The longitudinal section is located between Terborg and Leer in the lower Ems Estuary. Blue lines indicate strong density gradients and the horizon in red to yellow indicates the sediment bed. The field survey was carried out in July 2009 by the Federal Waterways Engineering and Research Institute (BAW).

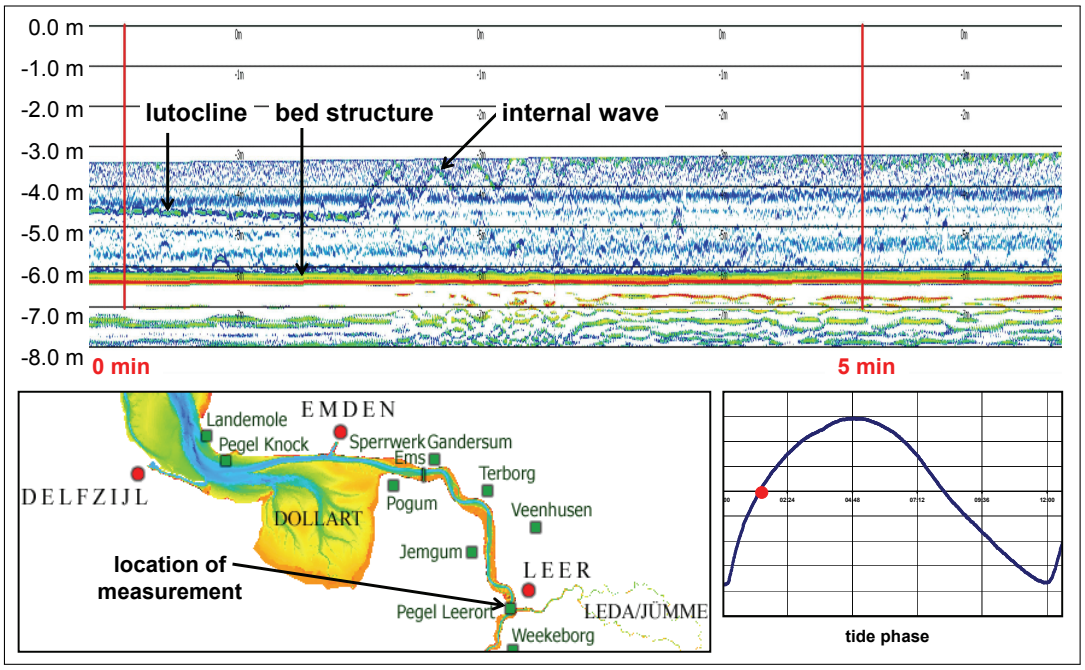

Figure 8: *Fluid mud detected due to sediment echo sounder measurements (parametric sub-bottom profiler for shallow water) in the Ems Estuary during flood tide.*
The observations show a time series at a position near Leerort where the measured data begins at -3.0 m below water surface. The lutocline remains at about -4.5 m water depth at the beginning and then an internal wave is initiated. The field survey was carried out in June 2011 by the Federal Waterways Engineering and Research Institute (BAW)).

banks. Impacts by waves need wide areas such as tidal flats or shorelines where the waves have enough fetch to develop. The oscillatory currents act on the mud deposits which are fluidized and softened owing to their viscoelastic behavior.

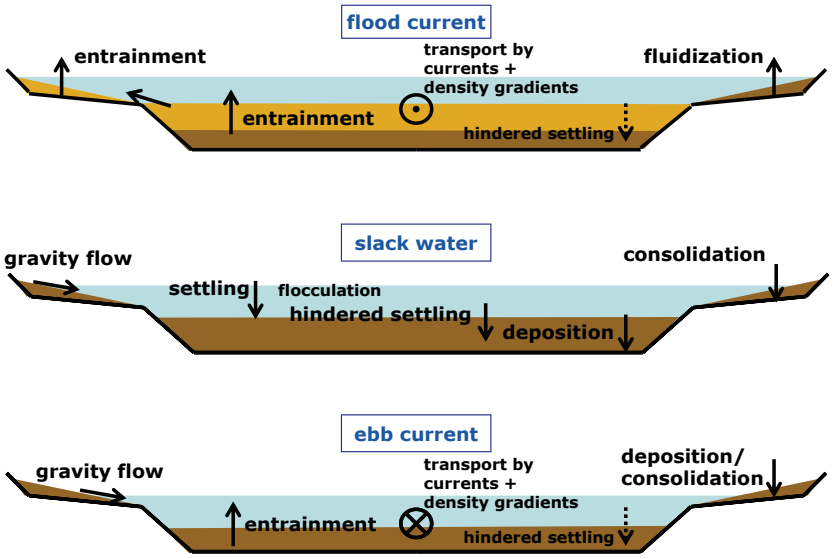

Figure 9: *Scheme of dominant physical processes in a tide influenced cross-section. High flood currents lead to entrainment and mobilization of fluid mud. The mobile suspensions are transported upstream of the river. Fluidization occurs in shallow water regions due to impact of waves. Settling, aggregation and deposition are dominant processes during slack water. Fluid mud is forming. Mobile mud layer flow downslope even at very small slopes due to gravity forces. The fluid mud is entrained again with increasing velocities during ebb tide. Suspended mud particles are transported in areas of low currents like the tidal flats during flood. They deposit and accumulate here during slack water. They can be remobilized by ebb currents or by waves.*

2.4 Mathematical Description of Fluid Movement

2.4.1 Basic Equations of Motion - Cauchy's Equations of Motion

Cauchy's equations of Motion describe the flow of materials with any flow behavior. They are based on the Principle of Momentum for a collection of particles [Malvern, 1969]. This principle says:

1. The total momentum of a given mass of particles changes with time and is determined by a rate.

2. The rate of momentum is equal to a vector sum of all external forces, which act on the given mass of particles.

3. The precondition for this principle is Newton's Third Law, where action and reaction determine the internal stresses.

To find a mathematical formulation for the first statement, a given mass of a medium with a specific Volume V and a specific surface S is considered. The change of mo-

mentum ($\varrho \mathbf{u} V$) with time is expressed with

$$\frac{d}{dt}\int_V \varrho \mathbf{u} dV, \tag{2.4.1}$$

and also represents the acceleration of the mass (ϱV) with the density ϱ and the velocity vector $\mathbf{u}$. The external forces are represented by a surface force $\mathbf{s}$ (force per surface area) and a body force $\mathbf{b}$ (force per mass). Both forces act on the considered mass. They can be formulated with

$$\int_S \mathbf{s} dS \text{ and } \int_V \varrho \mathbf{b} dV. \tag{2.4.2}$$

The momentum balance is set up where the change of momentum equals the external forces

$$\frac{d}{dt}\int_V \varrho \mathbf{u} dV = \int_S \mathbf{s} dS + \int_V \varrho \mathbf{b} dV. \tag{2.4.3}$$

Changing the formulation in rectangular coordinates and replacing the external force per surface with the stress tensor ($s_i = \tau_{ji} n_i$), the divergence theorem can be applied

$$\int_S \tau_{ji} n_i dS = \int_V \frac{\partial \tau_{ji}}{\partial x_i} dV \tag{2.4.4}$$

with n_i as the i-th component of the normal vector. These transformations result in the momentum balance

$$\int_V \varrho \frac{du_i}{dt} dV = \int_V \frac{\partial \tau_{ji}}{\partial x_i} dV + \int_V \varrho b_i dV \tag{2.4.5}$$

and lead to **Cauchy's Equations of Motion** with reduction of the integrals

$$\boxed{\varrho \frac{du_i}{dt} = \frac{\partial \tau_{ji}}{\partial x_j} + \varrho b_i} \tag{2.4.6}$$

The pressure can be extracted from the external body forces and replaced with

$$b_i = -\frac{1}{\varrho}\frac{\partial p}{\partial x_i} + f_i. \tag{2.4.7}$$

Dividing by density, a more common form known for fluid dynamics results

$$\frac{du_i}{dt} = -\frac{1}{\varrho}\frac{\partial p}{\partial x_i} + \frac{1}{\varrho}\frac{\partial \tau_{ji}}{\partial x_j} + f_i \tag{2.4.8}$$

in index notation or in vector notation

$$\boxed{\frac{D\mathbf{u}}{Dt} = -\frac{1}{\varrho} grad p + \frac{1}{\varrho} div \boldsymbol{\tau} + \mathbf{f}} \tag{2.4.9}$$

where $\mathbf{f}$ is the external force vector normalized by density, p is the total pressure and $\boldsymbol{\tau}$ is the stress tensor. The fully written Cauchy equations have the following form

$$\begin{aligned}
\frac{\partial u}{\partial t} + u\frac{\partial u}{\partial x} + v\frac{\partial u}{\partial y} + w\frac{\partial u}{\partial z} &= -\frac{1}{\varrho}\frac{\partial p}{\partial x} + \frac{1}{\varrho}\left(\frac{\tau_{xx}}{\partial x} + \frac{\tau_{yx}}{\partial y} + \frac{\tau_{zx}}{\partial z}\right) + f_x \\
\frac{\partial v}{\partial t} + u\frac{\partial v}{\partial x} + v\frac{\partial v}{\partial y} + w\frac{\partial v}{\partial z} &= -\frac{1}{\varrho}\frac{\partial p}{\partial y} + \frac{1}{\varrho}\left(\frac{\tau_{xy}}{\partial x} + \frac{\tau_{yy}}{\partial y} + \frac{\tau_{zy}}{\partial z}\right) + f_y \\
\frac{\partial w}{\partial t} + u\frac{\partial w}{\partial x} + v\frac{\partial w}{\partial y} + w\frac{\partial w}{\partial z} &= -\frac{1}{\varrho}\frac{\partial p}{\partial z} + \frac{1}{\varrho}\left(\frac{\tau_{xz}}{\partial x} + \frac{\tau_{yz}}{\partial y} + \frac{\tau_{zz}}{\partial z}\right) + f_z
\end{aligned} \tag{2.4.10}$$

After deriving the equations of motion, the components of motion are examined in Section 2.4.2, which than leads to a more detailed discussion of the stresses in Section 2.4.3.

2.4.2 Decomposition of Motion

There are four different kinds of motion: translation, rotation, non deformable volume change and deformation with consistent volume. The decomposition of motion was introduced by Stokes and evaluated in Lamb [1932] and Malcherek [2001]. In the array of motion a specific point is defined by $\mathbf{x} = (x, y, z)$ and an infinitely close point is given by $\mathbf{x} + d\mathbf{x} = (x + dx, y + dy, z + dz)$. If the movement of a considered element is only translation, the array of motion can be described by

$$\mathbf{u}(\mathbf{x} + d\mathbf{x}) = \mathbf{u}(\mathbf{x}). \tag{2.4.11}$$

The pure rotation has the following form

$$\begin{aligned} \mathbf{u}(\mathbf{x} + d\mathbf{x}) &= \frac{1}{2} rot\mathbf{u} \times d\mathbf{x} \\ &= \frac{1}{2} \begin{pmatrix} \frac{\partial w}{\partial y} - \frac{\partial v}{\partial z} \\ \frac{\partial u}{\partial z} - \frac{\partial w}{\partial x} \\ \frac{\partial v}{\partial x} - \frac{\partial u}{\partial y} \end{pmatrix} \cdot \begin{pmatrix} \partial x \\ \partial y \\ \partial z \end{pmatrix} = \frac{1}{2} \begin{pmatrix} \frac{\partial^2 u}{\partial z^2} - \frac{\partial^2 w}{\partial xz} - \frac{\partial^2 v}{\partial xy} + \frac{\partial^2 u}{\partial y^2} \\ \frac{\partial^2 v}{\partial x^2} - \frac{\partial^2 u}{\partial xy} - \frac{\partial^2 w}{\partial yz} + \frac{\partial^2 v}{\partial z^2} \\ \frac{\partial^2 w}{\partial y^2} - \frac{\partial^2 v}{\partial yz} - \frac{\partial^2 u}{\partial xz} + \frac{\partial^2 w}{\partial x^2} \end{pmatrix} \cdot \end{aligned} \tag{2.4.12}$$

The motion of pure non deformable volume change is

$$\mathbf{u}(\mathbf{x} + d\mathbf{x}) = \frac{1}{3} div\mathbf{u}\mathbf{E}d\mathbf{x} = \frac{1}{3} \begin{pmatrix} \partial x \left(\frac{\partial u}{\partial x} + \frac{\partial v}{\partial y} + \frac{\partial w}{\partial z} \right) \\ \partial y \left(\frac{\partial u}{\partial x} + \frac{\partial v}{\partial y} + \frac{\partial w}{\partial z} \right) \\ \partial z \left(\frac{\partial u}{\partial x} + \frac{\partial v}{\partial y} + \frac{\partial w}{\partial z} \right) \end{pmatrix} \tag{2.4.13}$$

with the unit matrix $\mathbf{E}$. Finally, the deformation with conserved volume can be determined by

$$\begin{aligned} \mathbf{u}(\mathbf{x} + d\mathbf{x}) &= \left(\mathbf{D} - \frac{1}{3} div\mathbf{u}\mathbf{E} \right) d\mathbf{x} \\ &= \left[\frac{1}{2} \begin{pmatrix} 2\frac{\partial u}{\partial x} & \frac{\partial u}{\partial y} + \frac{\partial v}{\partial x} & \frac{\partial u}{\partial z} + \frac{\partial w}{\partial x} \\ \frac{\partial u}{\partial y} + \frac{\partial v}{\partial x} & 2\frac{\partial v}{\partial y} & \frac{\partial v}{\partial z} + \frac{\partial w}{\partial y} \\ \frac{\partial u}{\partial z} + \frac{\partial w}{\partial x} & \frac{\partial v}{\partial z} + \frac{\partial w}{\partial y} & 2\frac{\partial w}{\partial z} \end{pmatrix} - \begin{pmatrix} \frac{1}{3} div\mathbf{u} & 0 & 0 \\ 0 & \frac{1}{3} div\mathbf{u} & 0 \\ 0 & 0 & \frac{1}{3} div\mathbf{u} \end{pmatrix} \right] \cdot \begin{pmatrix} \partial x \\ \partial y \\ \partial z \end{pmatrix} \end{aligned} \tag{2.4.14}$$

with the deformation rate tensor

$$\mathbf{D} = \frac{1}{2} \left(\frac{\partial u_i}{\partial x_j} + \frac{\partial u_j}{\partial x_i} \right) = \frac{1}{2} \left(\nabla \mathbf{u} + \nabla \mathbf{u}^T \right). \tag{2.4.15}$$

This leads to the total vector field of motion in combination of the four kinds of motion

$$\mathbf{u}\left(\mathbf{x}+d\mathbf{x}\right)=\mathbf{u}(\mathbf{x})+\frac{1}{2}rot\mathbf{u}\times d\mathbf{x}+\frac{1}{3}div\mathbf{u}\mathbf{E}d\mathbf{x}+\left(\mathbf{D}-\frac{1}{3}div\mathbf{u}\mathbf{E}\right)d\mathbf{x}. \tag{2.4.16}$$

The assumption of an incompressible fluid only allows a volume change combined with a deformation. Thus, the term for non deformable volume change is set to zero

$$\frac{1}{3}div\mathbf{u}\mathbf{E}d\mathbf{x}=0, \tag{2.4.17}$$

and it results in the volume conservation equation (equation of continuity)

$$div\mathbf{u}=0. \tag{2.4.18}$$

For incompressible fluids it follows

$$\mathbf{u}\left(\mathbf{x}+d\mathbf{x}\right)=\mathbf{u}(\mathbf{x})+\frac{1}{2}rot\mathbf{u}\times d\mathbf{x}+\mathbf{D}d\mathbf{x}. \tag{2.4.19}$$

This formulation leads to the internal stresses of a medium with progressive assumptions. It can be assumed that rotational motion of the entire element as well as the translation and movement of this element in space has no influence on the internal stresses. So the equation is reduced by two additional terms. Adding now the dynamic viscosity μ $[kg/(m\cdot s)]$ as a proportional constant results in

$$\boldsymbol{\tau}=2\mu\mathbf{D} \tag{2.4.20}$$

the tensor of internal stresses.
In the next section properties and abilities of the stress tensor are discussed.

2.4.3 The Total Stress Tensor

The total stress tensor $\boldsymbol{\sigma}$ describes internal and external stresses such as water pressure, thermodynamical stresses, internal shear stresses, etc. Commonly the stress tensor of the Navier-Stokes equations considers hydrostatic pressure, atmospheric pressure, internal stresses and friction at the boundaries. The total stress tensor of the Cauchy equations of motion is defined as follows

$$\boldsymbol{\sigma}=-p\mathbf{E}+\boldsymbol{\tau}. \tag{2.4.21}$$

The terms of internal viscous stresses of the Cauchy equations (2.4.9) (second terms of the left side) denote the general expression for internal stresses with

$$\frac{1}{\varrho}div\boldsymbol{\tau}=\frac{1}{\varrho}div\begin{bmatrix}\tau_{xx} & \tau_{xy} & \tau_{xz}\\ \tau_{yx} & \tau_{yy} & \tau_{yz}\\ \tau_{zx} & \tau_{zy} & \tau_{zz}\end{bmatrix}. \tag{2.4.22}$$

Figure 10 shows the orientation of the stress components in three-dimensional space. Subsequently, the mathematical description of the internal stresses of incompressible Newtonian and non-Newtonian fluids will be described, which is presented in detail, for example, by Malvern [1969] and Chhabra and Richardson [2008].

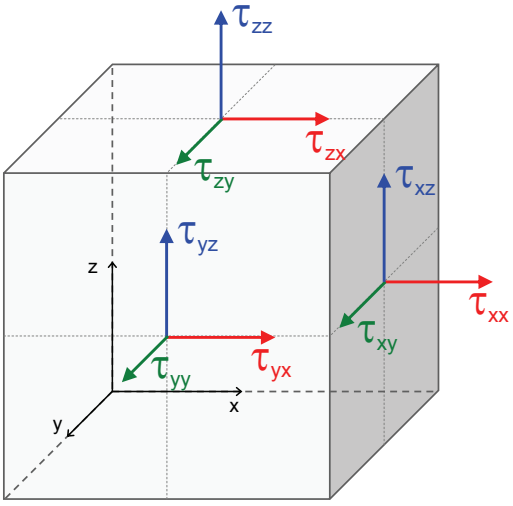

Figure 10: *Shear stress components at the cross-sections of a Cartesian system.*

2.4.4 Internal Stress Tensor of a Newtonian Incompressible Fluid

The shear stress tensor of an isotropic and homogeneous Newtonian fluid is described by the deformation rate tensor $\mathbf{D} = \frac{1}{2}\left(\nabla\mathbf{u} + \nabla\mathbf{u}^T\right)$ times the dynamic viscosity μ. In Newtonian fluids, the viscosity is assumed to be constant. Hence the divergence of the stress tensor is $div\left(2\mu\mathbf{D}\right) = 2\mu div\mathbf{D}$. The generation of the divergence of the stress tensor leads to the formulation

$$\frac{\mu}{\varrho} div\left(\nabla\mathbf{u} + \nabla\mathbf{u}^T\right) = \frac{\mu}{\varrho}\begin{bmatrix} 2\frac{\partial}{\partial x}\left(\frac{\partial u}{\partial x}\right) + \frac{\partial}{\partial y}\left(\frac{\partial u}{\partial y} + \frac{\partial v}{\partial x}\right) + \frac{\partial}{\partial z}\left(\frac{\partial u}{\partial z} + \frac{\partial w}{\partial x}\right) \\ \frac{\partial}{\partial x}\left(\frac{\partial u}{\partial y} + \frac{\partial v}{\partial x}\right) + 2\frac{\partial}{\partial y}\left(\frac{\partial v}{\partial y}\right) + \frac{\partial}{\partial z}\left(\frac{\partial v}{\partial z} + \frac{\partial w}{\partial y}\right) \\ \frac{\partial}{\partial x}\left(\frac{\partial u}{\partial z} + \frac{\partial w}{\partial x}\right) + \frac{\partial}{\partial y}\left(\frac{\partial v}{\partial z} + \frac{\partial w}{\partial y}\right) + 2\frac{\partial}{\partial z}\left(\frac{\partial w}{\partial z}\right) \end{bmatrix}. \quad (2.4.23)$$

For incompressible fluids the continuity equation (2.4.18) is used to reduce the mixed derivative terms from the stress tensor. Some restructuring of the stress tensor makes that clear

$$\frac{1}{\varrho} div\boldsymbol{\tau} = \frac{\mu}{\varrho}\begin{bmatrix} \frac{\partial}{\partial x}\left(\frac{\partial u}{\partial x} + \frac{\partial v}{\partial y} + \frac{\partial w}{\partial z}\right) + \left(\frac{\partial^2 u}{\partial x^2} + \frac{\partial^2 u}{\partial y^2} + \frac{\partial^2 u}{\partial z^2}\right) \\ \frac{\partial}{\partial y}\left(\frac{\partial u}{\partial x} + \frac{\partial v}{\partial y} + \frac{\partial w}{\partial z}\right) + \left(\frac{\partial^2 v}{\partial x^2} + \frac{\partial^2 v}{\partial y^2} + \frac{\partial^2 v}{\partial z^2}\right) \\ \frac{\partial}{\partial z}\left(\frac{\partial u}{\partial x} + \frac{\partial v}{\partial y} + \frac{\partial w}{\partial z}\right) + \left(\frac{\partial^2 w}{\partial x^2} + \frac{\partial^2 w}{\partial y^2} + \frac{\partial^2 w}{\partial z^2}\right) \end{bmatrix}. \quad (2.4.24)$$

By applying the continuity equation $\frac{\partial u}{\partial x} + \frac{\partial v}{\partial y} + \frac{\partial w}{\partial z} = 0$ the following form of the stress tensor is obtained

$$\frac{1}{\varrho} div\boldsymbol{\tau} = \frac{\mu}{\varrho}\begin{bmatrix} \frac{\partial^2 u}{\partial x^2} + \frac{\partial^2 u}{\partial y^2} + \frac{\partial^2 u}{\partial z^2} \\ \frac{\partial^2 v}{\partial x^2} + \frac{\partial^2 v}{\partial y^2} + \frac{\partial^2 v}{\partial z^2} \\ \frac{\partial^2 w}{\partial x^2} + \frac{\partial^2 w}{\partial y^2} + \frac{\partial^2 w}{\partial z^2} \end{bmatrix}. \quad (2.4.25)$$

This leads to a decoupled system of the x, y, z-components of the viscous stress terms, because the x-component of the stress terms consists only of derivatives of the x-velocity and the y-component of the stress terms consists only of derivatives of the

y-velocity and so on. The three-dimensional stress terms have the form of a parabolic diffusion equation with the constant viscosity (diffusive) coefficient $\frac{\mu}{\varrho}$.

Navier-Stokes Equations

Now, the Navier-Stokes equations can be derived from Cauchy's equations of motion (2.4.10) by substitution of the general stress tensor with the incompressible Newtonian stress tensor (2.4.25) and by applying mass conservation

$$\begin{aligned}
\frac{\partial u}{\partial t}+u\frac{\partial u}{\partial x}+v\frac{\partial u}{\partial y}+w\frac{\partial u}{\partial z} &= -\frac{1}{\varrho}\frac{\partial p}{\partial x}+\frac{\mu}{\varrho}\left(\frac{\partial^2 u}{\partial x^2}+\frac{\partial^2 u}{\partial y^2}+\frac{\partial^2 u}{\partial z^2}\right)+f_x \\
\frac{\partial v}{\partial t}+u\frac{\partial v}{\partial x}+v\frac{\partial v}{\partial y}+w\frac{\partial v}{\partial z} &= -\frac{1}{\varrho}\frac{\partial p}{\partial y}+\frac{\mu}{\varrho}\left(\frac{\partial^2 v}{\partial x^2}+\frac{\partial^2 v}{\partial y^2}+\frac{\partial^2 v}{\partial z^2}\right)+f_y \\
\frac{\partial w}{\partial t}+u\frac{\partial w}{\partial x}+v\frac{\partial w}{\partial y}+w\frac{\partial w}{\partial z} &= -\frac{1}{\varrho}\frac{\partial p}{\partial z}+\frac{\mu}{\varrho}\left(\frac{\partial^2 w}{\partial x^2}+\frac{\partial^2 w}{\partial y^2}+\frac{\partial^2 w}{\partial z^2}\right)+f_z \\
\frac{\partial u}{\partial x}+\frac{\partial v}{\partial y}+\frac{\partial w}{\partial z} &= 0. \qquad (2.4.26)
\end{aligned}$$

2.4.5 Internal Stress Tensor of a Non-Newtonian Fluid

According to Section 2.4.4, the divergence of the stress tensor is developed for a non-Newtonian fluid with a variable kinematic rheological viscosity $\nu = f\left(\mathbf{x}, \left|\frac{\partial u}{\partial x}\right|\right)$ determined by constitutive laws, examples see Figure 1. The assumption for the rheological viscosity in tensor formulation is given in Section 3.5. Now the viscosity has to be derived, too

$$div\left(\nu\mathbf{D}\right)=\begin{bmatrix}
\frac{\partial}{\partial x}\left(\nu\left(\frac{\partial u}{\partial x}+\frac{\partial u}{\partial x}\right)\right)+\frac{\partial}{\partial y}\left(\nu\left(\frac{\partial u}{\partial y}+\frac{\partial v}{\partial x}\right)\right)+\frac{\partial}{\partial z}\left(\nu\left(\frac{\partial u}{\partial z}+\frac{\partial w}{\partial x}\right)\right) \\
\frac{\partial}{\partial x}\left(\nu\left(\frac{\partial u}{\partial y}+\frac{\partial v}{\partial x}\right)\right)+\frac{\partial}{\partial y}\left(\nu\left(\frac{\partial v}{\partial y}+\frac{\partial v}{\partial y}\right)\right)+\frac{\partial}{\partial z}\left(\nu\left(\frac{\partial v}{\partial z}+\frac{\partial w}{\partial y}\right)\right) \\
\frac{\partial}{\partial x}\left(\nu\left(\frac{\partial u}{\partial z}+\frac{\partial w}{\partial x}\right)\right)+\frac{\partial}{\partial y}\left(\nu\left(\frac{\partial v}{\partial z}+\frac{\partial w}{\partial y}\right)\right)+\frac{\partial}{\partial z}\left(\nu\left(\frac{\partial w}{\partial z}+\frac{\partial w}{\partial z}\right)\right)
\end{bmatrix} \qquad (2.4.27)$$

unfortunately, the continuity equation cannot be extracted anymore.

In this work, non-Newtonian fluid behavior will be transformed on a hydrodynamic numerical approach based on the Navier-Stokes equations (2.4.10), which are valid for incompressible Newtonian fluids. Comparing the Newtonian (2.4.25) and the non-Newtonian three-dimensional stress components (2.4.27), their appearance differs essentially. The solution algorithm for the equations of motion is influenced by them. The Newtonian stress tensor contains only linear terms $\frac{\mu}{\varrho}\frac{\partial^2 u_i}{\partial x_i^2}$, whereas the non-Newtonian tensor includes also non-linear terms $\frac{\partial}{\partial x_i}\left(\nu\frac{\partial u_i}{\partial x_j}\right)$, where ν is a non-negative function of the derivatives $\frac{\partial u_i}{\partial x_i}$. The partial differential character of the tensor changes from parabolic to hyperbolic because of the non-linear stress terms. Moreover, the stress terms of the directions x, y, z are strongly coupled by the mixed derivatives such as

$\frac{\partial u_i}{\partial x_i \partial x_j}$, but also by the presence of all three components of the velocity vector. All these aspects change the character of the solution system.

With the aim to improve existing and approved hydrodynamic numerical models for the simulation of fluid mud dynamics, suitable approximations has to be identified. Otherwise the solution algorithm of the numerical model has to be changed significantly.

In Section 3.3 a closer look on the importance of the particular stress components is given by a dimensional analysis and an approximation will be derived for application to shallow water hydrodynamics.

2.5 Outline of Numerical Methods for the Simulation of Fluid Mud

Numerical models are a way of predicting fluid mud dynamics. They have to solve the governing equations of motion adapted to fluid mud movement. There are different concepts for simulating the transport, flow behavior and development of fluid mud in a hydrodynamic model environment. In principle, the following different types of conceptual model for the numerical simulation of fluid mud dynamics exist:

- three-dimensional models with different discretization schemes
  - in x, y, z-coordinates (Cartesian)
  - in x, y, σ-coordinates
  - in x, y, ϱ-coordinates (isopycnal models)
- two-phase models
- single-layer fluid mud models

In the following, the approaches of numerical models that have been developed in recent years are presented. The suitability of their application to fluid mud dynamics in coastal areas as well as their limitations are summarized and assessed.

The numerical differential models on Cartesian grids solve the conservation of mass and momentum equation for fluid mud in three or fewer dimensions. The fluid mud behavior is simulated by the rheological correlation between shear stress and deformation rate in form of a parametrization which is used instead of the Newtonian stress tensor.

A two-dimensional laterally-averaged model (2DV) for the simulation of fluid mud dynamics was developed by Yan and Hayter [1994]. The model includes a hydrodynamic module with a turbulence model and a cohesive sediment transport module simulating low-concentration suspensions as well as fluid mud. The following transport processes are considered: advection, dispersion, aggregation, settling, re-entrainment, erosion,

deposition, bed formation and bed-consolidation. Fluid mud is described by its Bingham plastic behavior with an additional yield stress term in the momentum equations. Density is treated as a time-dependent quantity. As only a few results were presented, further applications and validation of the model would be needed for an assessment of the predictability of fluid mud dynamics.

Le Hir et al. [2001] developed a continuous approach for the simulation of the water column with cohesive sediments and fluid mud and a progressive transition to the bottom sediment. The processes under consideration leading to the formation of high-concentration layers are stratification-induced turbulence damping, settling and the viscous behavior of mud. The rheological viscosity is determined as a function of shear and concentration. This is implemented in form of a one-dimensional vertical model (SAM-1DV).

Teeter presented a three-dimensional, curvilinear, hydrodynamic model in Cartesian coordinates (CH3DZ) [Teeter and Johnson, 2005a,b] which includes cohesive suspended sediment transport and a fluid mud module (CH3DZ-FM). The hydrodynamic model is fully coupled with a sediment module of a layered bed structure in which deposition through hindered settling, erosion of consolidated mud and entrainment are considered. The movement of the fluid mud is forced by gravitational effects on slopes and density-dependent yield stress. Fluid mud specific properties are applied by exceeding a specific density threshold. The rheological behavior is described by a viscoplastic approach with a yield stress.

Another three-dimensional model for the simulation of fluid mud was developed by Guan et al. [2005] based on the generalized σ-coordinate Princeton Ocean Model (POM). The horizontal discretization is defined by curvilinear grids and the vertical discretization by σ-layers which have a higher resolution near the bottom with respect to fluid mud layers. The hydrodynamic model includes a sediment transport module covering deposition and erosion. The non-Newtonian fluid mud behavior is considered by a rheological viscosity approach. The turbulence model used considers eddy viscosity damping with increasing sediment stratification. Compared with observations, this approach underpredicted vertical mixing. Therefore, they introduced an additional term for vertical viscosity which takes account of mixing due to internal waves riding on the lutocline and represents a parameterized approach to the entrainment of fluid mud. After a sensitivity study, they remark that the 3D-model results are very sensitive to the parameterized processes and more process-based studies are necessary.

The second type of numerical model are the two-phase models. They solve the conservation of mass and the momentum equations for the fluid as well as for the sediment phase by considering interactions of those phases. A two-phase model approach which includes fluid mud properties was established by Hsu et al. [2007]. The model considers boundary layer transport, gravity-driven sediment transport, the interaction between

turbulence and sediment concentration and sediment granular rheology. Son and Hsu [2009] extends it to include dynamic flocculation processes. They infer from studies on fluid mud dynamics that one of the important processes is the turbulence damping of the carrier fluid due to sediment density stratification. The approach is able to simulate dilute as well as high-concentration suspensions. It was not possible to simulate the mobilization of mud from the bed. The two-phase equations are simplified to reduce the computational effort. Some of the simplifications apply the mean flow velocity to the sediment phase and neglect the acceleration terms.

The transitional zone between fluid mud and the overlying water body is characterized by a sharp density gradient, the lutocline. Below the lutocline, the flow behavior is non-Newtonian. It is possible to assume a strong stratified flow of two layers. Therefore, there are some numerical approaches which approximate the fluid mud as a single layer between the water body and the consolidated bed. A model of this type has been incorporated in the Delft3D software package described in Winterwerp et al. [2002] and in the user manual of Deltares [2010]. The water and fluid mud layer interact only as a result of interfacial shear stresses. The water body can be simulated in two or three dimensions and a depth-averaged simulation is used for the fluid mud layer. The sediment concentration of the fluid mud layer is taken as constant and does not vary with time or space. The fluid mud behavior is described as a Bingham plastic fluid but with constant yield stress. The model was applied in an investigation of dredging activities in a tide-influenced river. Another single-layer model, named FLUIDMUDFLOW-2D was developed by H.R. Wallingford [Crapper and Ali, 1997]. However, it does not include the specific rheological characteristics of fluid mud. The single-layer models are not able to reproduce the vertical density and velocity distribution of fluid mud. Vertical transport processes such as hindered settling or entrainment result in a vertical density distribution which could not be resolved sufficiently with the single-layer approach.

2.5.1 Evaluation of the Numerical Methods

The main purpose of the numerical model will be its application to investigations in coastal regions, estuaries and harbors. These are complex topographical domains influenced by three-dimensional physical processes. One- or two-dimensional numerical models are not sufficient in such cases.
The fluid mud thickness covers only a few decimeters compared to the total water depth of several meters. The high-concentration suspensions only reach thicknesses of one or more meters in mud transport dominated estuaries and rivers. Vertical density distributions of mud suspensions not only vary due to horizontal processes but also mainly due to vertical transport processes such as hindered settling, consolidation, entrainment and resuspension of mud suspensions. In other words, the transitions between dilute

suspension, high-concentration suspension, mobile fluid mud, freshly consolidated fluid mud and consolidated fluid mud must be reproduced. Predictive numerical simulations thus require sufficiently resolved processes.

Accordingly, a single-layer model is very limited in simulating these processes. Cartesian grid resolutions with z-planes or with σ-layers require high vertical resolutions in the range of centimeters for the reproduction of density distribution and vertical velocity profiles within the fluid mud. Another solution is to use an adaptive vertical grid resolution to take account of simulation accuracy in the mud layers which depends on the particle concentration and results in fine resolutions at high concentrations. However, large domains are usually investigated, in particular in coastal regions and estuaries where the computational effort can rapidly increase due to grid refinement.

The 3D isopycnal model approach has its advantages in such cases. Within this model concept, the vertical domain is divided into layers of constant density, the ϱ-layers or isopycnal layers. The vertical discretization is thus matched automatically to the density distribution (described in more detail in Section 3.2). This conceptual model is able to reproduce the density distribution and changes with considerably low discretization effort.

Fluid mud does not necessarily appear in the entire investigation area. This means that the appearance and disappearance of fluid mud should be possible. The z- and σ-layers are always active, even though with a very small thickness in case of the σ-layers. The isopycnal layer can be active with a definite thickness or inactive with a thickness equal to zero. However, the layers do not have to be active or inactive at the same time over the entire model domain. Within the scope of this thesis, the isopycnal model approach is used and extended to include the simulation of fluid mud dynamics.

Fluid mud can be described as a viscoplastic fluid e.g. as a non-ideal Bingham fluid. The rheological behavior changes with time and depends on the cohesive sediment concentration and shear/deformation rate, to name the most important parameters [McAnally et al., 2007a; Toorman, 1997]. There are times of sharp as well as of smooth transitions between different rheological stages in stratified systems. If the fluid mud behavior is described by a constant density and a constant yield stress it only represents one specific rheological state. The isopycnal concept leads to a continuous approach for stratified flow with arbitrary concentration profiles. Accordingly, the characterization of the flow behavior should be based on a continuous formula. It is this conceptual model that is considered in this thesis.

The concept and fundamental properties of the developed and extended model for the simulation of fluid mud dynamics are evaluated in Section 3.

3 Conceptual Model

3.1 Basic Concept and Properties of the Model

Fluid mud and dilute suspensions differ fundamentally in their specific rheological behavior (Section 2.2). Hydrodynamic numeric simulations consider the flow behavior due to the stress terms of the momentum equations.

The momentum conservation of every viscoelastic material can be described by Cauchy's equation of motion given as

$$\frac{du_i}{dt} = \frac{1}{\varrho}\frac{\partial \sigma_{ji}}{\partial x_j} + f_i \tag{3.1.1}$$

which is described and derived in Section 2.4.1. The rheological behavior is characterized by the first term on the right side containing the stress tensor σ_{ji}. This term is equal to $-\partial p_i/\partial x_i + \partial \tau_{ji}/\partial x_j$ for incompressible fluids. For Newtonian fluids, the internal stresses (Section 2.4.4) are given as

$$\tau_{ij} = \mu \left(\frac{\partial u_i}{\partial x_j} + \frac{\partial u_j}{\partial x_i} \right) \tag{3.1.2}$$

Therefore, the Navier-Stokes equations used for hydrodynamic simulation are a special case of the Cauchy equations. The same applies to the Reynolds-averaged Navier-Stokes equations which are obtained by choosing the shear stress tensor as

$$\tau_{ij} = (\mu_t + \mu_{mol}) \left(\frac{\partial u_i}{\partial x_j} + \frac{\partial u_j}{\partial x_i} \right) \tag{3.1.3}$$

where μ_t is the turbulent and μ_{mol} the molecular dynamic viscosity. A possible realization of the general rheological fluid behavior in a numerical model is the introduction of the rheological viscosity μ_r which can be determined according to different constitutive laws, see Section 2.2.1. Thus, the form of the shear stress tensor of the Navier-Stokes or the Reynolds-averaged Navier-Stokes equations does not change:

$$\tau_{ij} = \mu_r \left(\frac{\partial u_i}{\partial x_j} + \frac{\partial u_j}{\partial x_i} \right). \tag{3.1.4}$$

It is therefore possible to use conventional 3D-codes applied to river or coastal engineering as well as for the simulation of fluid mud dynamics. Based on a dimensional analysis, the important components of the internal stress tensor are identified in Section 3.3 which demonstrates a suitable approximation of the non-Newtonian stresses for fluid mud. Later on this is adapted to the numerical model presented in Section 4.

Consequently, a rheological approach has to be identified to describe the flow behavior in a mud-water system qualitatively and quantitatively. The rheological behavior in terms of the rheological viscosity μ_r might be dependent on [Mehta, 1991; Berlamont et al., 1993; Coussot, 1997]:

- suspended matter concentration starting from clear water up to sediment bed
- flow shear rates ranging from zero to those for highly turbulent motion
- size distribution of the suspended matter
- temperature and salinity of the water body
- biochemical behavior of the suspended material (flocculation, organic polymer formation)

In this thesis, it is assumed that the rheological approach is sufficiently described by two indicators: the bulk density, which is proportional to the suspended matter concentration, and the flow shear rate, whose formulation indicates a Newtonian or a non-Newtonian fluid. The applied rheological model and corresponding parameterizations are presented in Section 3.4.

The suspended matter concentration is not only an important parameter for determining the rheology, but also it is used for the numerical discretization scheme. A high-concentration benthic layer often has a sharp density gradient at the transition to a layer of lower concentration, known as the lutocline. Therefore, the numerical model should be able to reproduce a highly stratified flow. Conventional three-dimensional hydrodynamic models require a very fine vertical resolution in order to reproduce sharp density gradients and their movement. This can result in a high computational effort because the entire domain is based on the same vertical grid spacing. There are other methods of domain decomposition or dynamic grid refinement but they are not necessarily more efficient.

A fluid mud body and the overlying water body behave very differently and interact at their interface. Therefore, some numerical approaches simulate the fluid mud as a single-layer coupled with a hydrodynamic model (described in Section 2.5). However, fluid mud is not stable all of the time, especially in tidal currents. The development of fluid mud results mostly in a change of the solid concentration which can hardly be reproduced with a single layer model with one specific density and rheological state.

This thesis pursues an isopycnal numerical approach in which discretization follows the physical parameter bulk density which directly relates to the suspended matter concentration. Thus, a change in stratification is accompanied by a change in the discretization. The vertical discretization due to isopycnals, layers of constant density, is described in Section 3.2.

A 3D hydrodynamic isopycnal model of this type has been adapted for the simulation of fluid mud dynamics in this thesis. A detailed description of the numerical model and the extensions is given in Section 4. The advection-diffusion equation for suspended load transport is not solved here; the classic hydrodynamic momentum equations in

an isopycnal discretization scheme are solved instead. Every density layer represents a homogeneous suspension with a specific rheological behavior. The numerical model covers the entire water column from free surface to stationary bed. Mud suspension transport is realized due to changing thicknesses of the density layers. The rheological approach is applied to the entire water column. Therefore, the resulting viscosity in the numerical model is the sum of the rheological and turbulent viscosity. An advanced turbulence model with damping due to stratification effects is not implemented in the numerical model as turbulence modeling is not one of the objectives of this work. Thus, the turbulent viscosity is kept simple here and set to a constant value for each density layer.

In addition to the fundamental determination of the flow behavior the fluid mud dynamics are described by transport processes (Figure 4). Gravity flow is solved due to the pressure term of the momentum equation which considers density differences. Shear flow is caused by vertical, interfacial shear stresses at the isopycnal interface (interfacial momentum transfer). The vertical transport processes induce mass fluxes at the isopycnal interfaces, thus changing the state of stratification. An approach for the vertical mass transfer in an isopycnal system is derived in Section 4.3. This approach enables density layers to vary in thickness by applying settling fluxes or mixing fluxes. A settling velocity approach with hindered settling is implemented for the formation of fluid mud (Section 3.7). Consolidation is not considered owing to the fact that the applications presented later cover only a few days and are therefore not in the time range in which consolidation of mud occurs. Entrainment (Section 3.6) is introduced for the mobilization and mixing of fluid mud due to shear impact. Fluidization due to wave impact is not considered here as coupling with a wave model is not the aim of this work.
Most of these processes are transformation or exchange processes from dilute suspensions to high-concentration layers to mobile fluid mud layers and up to stationary layers or vice versa, which can be realized due to interfacial mass fluxes. The basis for including those transport processes is established by developing and implementing the mathematical approach for diapycnal mass transfer. Additional mechanisms can be introduced into the isopycnal numerical model in the same way as for the settling and entrainment approach.

3.2 Vertical Resolution due to Isopycnals

The discretization scheme has to be able to reproduce sharp density gradients as well as to form three-dimensional concentration profiles. A z-layer-based model needs a very high resolution near the river bed to represent sharp density gradients. The bottom depth can vary highly with the increasing model domain and leads to a vertical resolution in the range of centimeters or decimeters over large areas. This increases

the computational effort. By comparison, σ-layers have the advantage of following the topology of the model domain and they guarantee a high near-bed resolution. However, similar to z-layered discretization, the high resolution covers the entire model domain and increases the computational effort. A discretization with ϱ-layers enables the resolution due to physical phenomena rather than due to geographical conditions to be adapted. This kind of discretization is defined by layers of constant density - the isopycnal layers - whose thickness changes due to physical processes. The interfaces of the layers always define a density gradient. The density is related to the concentration of a suspension, therefore changes in the sediment transport regime automatically have an impact on the discretization. Such an appropriate discretization concept will be applied in this thesis.

Sharp density gradients can be resolved by a few layers only based on the predefined density differences between the layers. Thus, the smaller the density differences, the thinner the layer for a specific density gradient is, see Figure 11. The maximum number of isopycnal layers in the model domain and the density classes of the layers are predefined. Isopycnal approaches are often used for oceanographic problems where density-driven currents are dominant.
According to the isopycnal principle the constraint

$$\boxed{\frac{\partial \varrho_m}{\partial t} = 0} \tag{3.2.1}$$

has to be satisfied, where ϱ_m is the density of the m-th isopycnal layer and stable

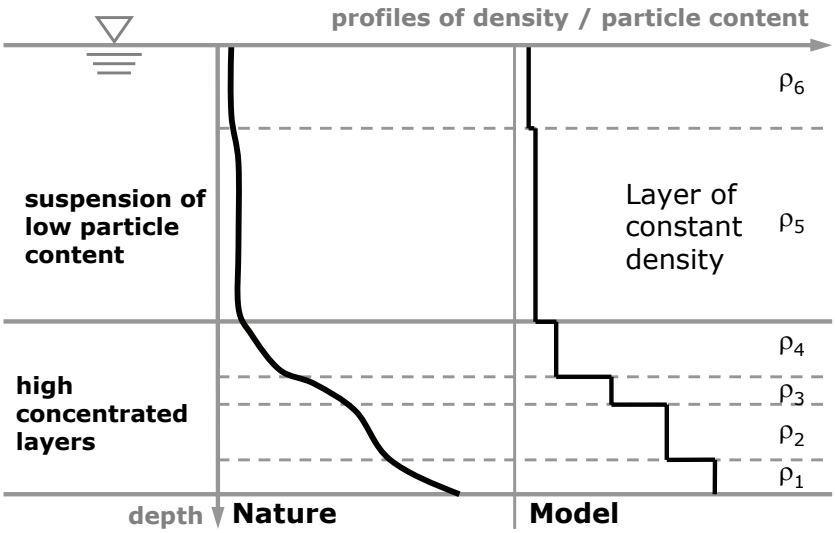

Figure 11: *Scheme of the isopycnal approach.*
In an isopycnal model the vertical density profile is described by layers of constant density. In this case, every layer represents a suspension of a specific sediment concentration. Their thickness varies according to physical processes.

stratification also has to be guaranteed. The bulk density is given by

$$\varrho = \varrho_w + \left(1 - \frac{\varrho_w}{\varrho_s}\right) c_s \tag{3.2.2}$$

with the dry density of the sediments ϱ_s, the water density ϱ_w and the volumetric sediment concentration c_s.

3.3 Approximation for the Internal Stresses for High-concentrated Mud Suspensions

The non-Newtonian stress tensor is described in Section 2.4.5 and it is shown that the partial differential character of the tensor differs significantly from the Newtonian stress tensor. The relevant terms have therefore been derived for the internal stresses of the Navier-Stokes equations.

The internal viscous stress terms of a non-Newtonian fluid are examined by dimensional analysis. The velocity and length variables are replaced by dimensionless expressions

$$\hat{x} = \frac{x}{L}; \quad \hat{u} = \frac{u}{U}; \quad \hat{y} = \frac{y}{L}; \quad \hat{v} = \frac{v}{U}; \quad \hat{z} = \frac{z}{H}; \quad \hat{w} = \frac{w}{W}; \tag{3.3.1}$$

where both horizontal lengths are characterized by the same length L. The horizontal velocities are represented by the same characteristic velocity U. Their vertical components are classified by H and W. The variables of the three internal stress components of Equation (2.4.27) are replaced by the dimensionless characteristics

$$\frac{U}{L^2}\left[2\frac{\partial}{\partial\hat{x}}\left(\nu\frac{\partial\hat{u}}{\partial\hat{x}}\right) + \frac{\partial}{\partial\hat{y}}\left(\nu\left(\frac{\partial\hat{u}}{\partial\hat{y}} + \frac{\partial\hat{v}}{\partial\hat{x}}\right)\right)\right] + \frac{\partial}{\partial\hat{z}}\left(\nu\left(\frac{U}{H^2}\frac{\partial\hat{u}}{\partial\hat{z}} + \frac{W}{LH}\frac{\partial\hat{w}}{\partial\hat{x}}\right)\right) \tag{3.3.2a}$$

$$\frac{U}{L^2}\left[\frac{\partial}{\partial\hat{x}}\left(\nu\left(\frac{\partial\hat{u}}{\partial\hat{y}} + \frac{\partial\hat{v}}{\partial\hat{x}}\right)\right) + 2\frac{\partial}{\partial\hat{y}}\left(\nu\frac{\partial\hat{v}}{\partial\hat{y}}\right)\right] + \frac{\partial}{\partial\hat{z}}\left(\nu\left(\frac{U}{H^2}\frac{\partial\hat{v}}{\partial\hat{z}} + \frac{W}{LH}\frac{\partial\hat{w}}{\partial\hat{y}}\right)\right) \tag{3.3.2b}$$

$$\frac{\partial}{\partial\hat{x}}\left(\nu\left(\frac{U}{LH}\frac{\partial\hat{u}}{\partial\hat{z}} + \frac{W}{L^2}\frac{\partial\hat{w}}{\partial\hat{x}}\right)\right) + \frac{\partial}{\partial\hat{y}}\left(\nu\left(\frac{U}{LH}\frac{\partial\hat{v}}{\partial\hat{z}} + \frac{W}{L^2}\frac{\partial\hat{w}}{\partial\hat{y}}\right)\right) + 2\frac{W}{H^2}\frac{\partial}{\partial\hat{z}}\left(\nu\frac{\partial\hat{w}}{\partial\hat{z}}\right) \tag{3.3.2c}$$

Further transformation of the characteristic factors leads to

$$\frac{U}{L^2}\left[2\frac{\partial}{\partial\hat{x}}\left(\nu\frac{\partial\hat{u}}{\partial\hat{x}}\right) + \frac{\partial}{\partial\hat{y}}\left(\nu\left(\frac{\partial\hat{u}}{\partial\hat{y}} + \frac{\partial\hat{v}}{\partial\hat{x}}\right)\right)\right] + \frac{\partial}{\partial\hat{z}}\left(\nu\left(\frac{U}{H^2}\frac{\partial\hat{u}}{\partial\hat{z}} + \frac{U}{L^2}\frac{\partial\hat{w}}{\partial\hat{x}}\right)\right) \tag{3.3.3a}$$

$$\frac{U}{L^2}\left[\frac{\partial}{\partial\hat{x}}\left(\nu\left(\frac{\partial\hat{u}}{\partial\hat{y}} + \frac{\partial\hat{v}}{\partial\hat{x}}\right)\right) + 2\frac{\partial}{\partial\hat{y}}\left(\nu\frac{\partial\hat{v}}{\partial\hat{y}}\right)\right] + \frac{\partial}{\partial\hat{z}}\left(\nu\left(\frac{U}{H^2}\frac{\partial\hat{v}}{\partial\hat{z}} + \frac{U}{L^2}\frac{\partial\hat{w}}{\partial\hat{y}}\right)\right) \tag{3.3.3b}$$

$$\frac{\partial}{\partial\hat{x}}\left(\nu\left(\frac{U}{LH}\frac{\partial\hat{u}}{\partial\hat{z}} + \frac{UH}{L^3}\frac{\partial\hat{w}}{\partial\hat{x}}\right)\right) + \frac{\partial}{\partial\hat{y}}\left(\nu\left(\frac{U}{LH}\frac{\partial\hat{v}}{\partial\hat{z}} + \frac{UH}{L^3}\frac{\partial\hat{w}}{\partial\hat{y}}\right)\right) + 2\frac{U}{LH}\frac{\partial}{\partial\hat{z}}\left(\nu\frac{\partial\hat{w}}{\partial\hat{z}}\right) \tag{3.3.3c}$$

by applying the relation $\frac{U}{H} = \frac{W}{H}$ obtained from the dimensionless continuity equation [Malcherek, 2001]

$$\frac{U}{L}\left(\frac{\partial u}{\partial x} + \frac{\partial v}{\partial y}\right) + \frac{W}{H}\frac{\partial w}{\partial z} = 0. \tag{3.3.4}$$

Finally, the characteristic factors can be expressed in terms of the length only

$$\frac{1}{L^2}\left[2\frac{\partial}{\partial \hat{x}}\left(\nu\frac{\partial \hat{u}}{\partial \hat{x}}\right) + \frac{\partial}{\partial \hat{y}}\left(\nu\left(\frac{\partial \hat{u}}{\partial \hat{y}} + \frac{\partial \hat{v}}{\partial \hat{x}}\right)\right)\right] + \frac{\partial}{\partial \hat{z}}\left(\nu\left(\frac{1}{H^2}\frac{\partial \hat{u}}{\partial \hat{z}} + \frac{1}{L^2}\frac{\partial \hat{w}}{\partial \hat{x}}\right)\right) \tag{3.3.5a}$$

$$\frac{1}{L^2}\left[\frac{\partial}{\partial \hat{x}}\left(\nu\left(\frac{\partial \hat{u}}{\partial \hat{y}} + \frac{\partial \hat{v}}{\partial \hat{x}}\right)\right) + 2\frac{\partial}{\partial \hat{y}}\left(\nu\frac{\partial \hat{v}}{\partial \hat{y}}\right)\right] + \frac{\partial}{\partial \hat{z}}\left(\nu\left(\frac{1}{H^2}\frac{\partial \hat{v}}{\partial \hat{z}} + \frac{1}{L^2}\frac{\partial \hat{w}}{\partial \hat{y}}\right)\right) \tag{3.3.5b}$$

$$\frac{\partial}{\partial \hat{x}}\left(\nu\left(\frac{1}{LH}\frac{\partial \hat{u}}{\partial \hat{z}} + \frac{H}{L^3}\frac{\partial \hat{w}}{\partial \hat{x}}\right)\right) + \frac{\partial}{\partial \hat{y}}\left(\nu\left(\frac{1}{LH}\frac{\partial \hat{v}}{\partial \hat{z}} + \frac{H}{L^3}\frac{\partial \hat{w}}{\partial \hat{y}}\right)\right) + 2\frac{1}{LH}\frac{\partial}{\partial \hat{z}}\left(\nu\frac{\partial \hat{w}}{\partial \hat{z}}\right). \tag{3.3.5c}$$

An additional assumption is necessary before the dimensionless parameters are analyzed. The objective is the simulation of fluid mud dynamics. It is assumed that turbulence is totally damped due to stratification in high concentration flow or at least the turbulent viscosity is negligible compared to the rheological viscosity. Turbulence becomes important in the transition area between fluid mud and water body for the calculation of the correct shear force in this area. However, this is a subject of research itself (e.g. interaction between rheology and turbulence) and goes beyond the scope of this thesis. Therefore, the turbulent viscosity is neglected so that only viscous internal stresses are considered, but being aware that the internal shear will be underestimated in the non-laminar flow regions.

The rheological viscosity is not a directional quantity. A material can be sheared in one or more directions. As long as the absolute value of the shear rate vector or tensor remains the same, then the viscous response will be the same. The movement of a fluid mud layer in a horizontal direction dominates the movement in a vertical direction. The variation of the velocity over the vertical is higher than in the horizontal direction. This also results from the interpretation of the characteristic length. The characteristic horizontal length L represents the horizontal extent of the fluid mud layer which may be around several hundred meters. A fluid mud layer thickness ranges from decimeters to about 1 m which describes the vertical characteristic length H. Consequently, it can be stated that $L \gg H$. Therefore, the viscous stress terms containing the horizontal velocity derivatives $\frac{\partial^2 u}{\partial z^2}$ and $\frac{\partial^2 v}{\partial z^2}$ in z-direction have the strongest impact on the fluid behavior. The terms of the derivatives $\frac{\partial^2 w}{\partial x^2}$ and $\frac{\partial^2 w}{\partial y^2}$ have the least influence.

Now that the significant internal stresses are identified with regard to the problem of interest. The non-Newtonian fluid behavior can be transferred to a numerical model based on the Navier-Stokes equations which assume the incompressibility approximation

and a Newtonian fluid. The viscous terms are given by

$$\text{x-component:} \quad \frac{\partial}{\partial x}\left(\nu\frac{\partial u}{\partial x}\right)+\frac{\partial}{\partial y}\left(\nu\frac{\partial u}{\partial y}\right)+\frac{\partial}{\partial z}\left(\nu\frac{\partial u}{\partial z}\right) \tag{3.3.6a}$$

$$\text{y-component:} \quad \frac{\partial}{\partial x}\left(\nu\frac{\partial v}{\partial x}\right)+\frac{\partial}{\partial y}\left(\nu\frac{\partial v}{\partial y}\right)+\frac{\partial}{\partial z}\left(\nu\frac{\partial v}{\partial z}\right) \tag{3.3.6b}$$

$$\text{z-component:} \quad \frac{\partial}{\partial x}\left(\nu\frac{\partial w}{\partial x}\right)+\frac{\partial}{\partial y}\left(\nu\frac{\partial w}{\partial y}\right)+\frac{\partial}{\partial z}\left(\nu\frac{\partial w}{\partial z}\right) \tag{3.3.6c}$$

for the Navier-Stokes equations. The dimensional analysis shows that these terms are the most important for high-concentration flow such as for shallow water hydrodynamics. Therefore, the same terms will be applied as an approximation for the description of the non-Newtonian fluid (mud) behavior. A full description of the non-Newtonian behavior would require all terms of the stress tensor, including the non-linear terms. However, it would be a problem to solve the equations of motions by considering the non-linear viscous terms. This approximation for the non-Newtonian stress tensor allows to adopt the rheological behavior of fluid mud on a conventional hydrodynamic model.

3.4 Rheological Approach for Mud Suspensions

The velocity distribution of highly concentrated mud suspensions is inevitably subjected to the modeling of the rheological behavior. A brief introduction on the rheology of mud suspensions is given in Section 2.2. The way to a parameterized rheological model presented in this section is based on the investigations of Malcherek and Cha [2011]. The rheological model implemented in the numerical model is a parameterized form of the Worrall-Tuliani model [Worrall and Tuliani, 1964]

$$\tau = \tau_y + \mu_\infty \dot{\gamma} + \Delta\mu \dot{\gamma} c_\lambda, \tag{3.4.1}$$

which is discussed in detail by Toorman [1997, 1994] for cohesive suspensions. The viscosity μ_∞ is the asymptotic value for $\dot{\gamma} \to \infty$ at the structural state of full breakdown of the structure and $\Delta\mu$ is the viscosity at a specific degree of structure. The first two terms of this model have the form of the Bingham model with the yield stress τ_y and the linear dependence of shear rate and viscosity (viscoplastic behavior). The third term accounts for time-dependent changes in the structure due to the structural parameter c_λ. Depending on the shear impact, aggregates can break-up and recover in the mud suspension but such mechanisms occur gradually and not immediately (thixotropic behavior). The structural parameter ranges between one and zero:

$$c_\lambda = \begin{cases} 1 & \text{maximum degree of aggregation} \\ 0 & \text{complete break-up of aggregation} \end{cases} \tag{3.4.2}$$

and is depicted in Figure 12. The rate of change c_λ under shear impact is given by

$$\frac{dc_\lambda}{dt} = c_{aggr}\,(1 - c_\lambda) - c_{break}\dot{\gamma}c_\lambda. \tag{3.4.3}$$

The parameters c_{break} and c_{aggr} are empirical constants for the break-up and re-/ aggregation of flocs respectively. The first term is not dependent on the shear impact whereas the break-down of aggregates (second term) increases with increasing shear rate.

One solution of the differential equation can be gained from the equilibrium state where break-up and recovery of aggregates are at equilibrium (no change with time $\frac{dc_\lambda}{dt} = 0$). A formulation for c_λ then results in

$$c_\lambda = \frac{c_{aggr}}{c_{break}\dot{\gamma} + c_{aggr}}. \tag{3.4.4}$$

This leads to the first order shear stress formulation for the equilibrium structural state

$$\begin{aligned} \tau &= \tau_y + \mu_\infty\dot{\gamma} + \Delta\mu\dot{\gamma}\frac{c_{aggr}}{c_{break}\dot{\gamma} + c_{aggr}} \\ \text{or} \quad \tau &= \tau_y + \mu_\infty\dot{\gamma} + \Delta\mu\dot{\gamma}\frac{1}{\frac{c_{break}}{c_{aggr}}\dot{\gamma} + 1}. \end{aligned} \tag{3.4.5}$$

where the yield stress is independent of the structural parameter [Toorman, 1997]. This implies for rheological measurements that the shear stress has to be increased slowly enough and continuously so that the aggregate bonds are in equilibrium with the applied shear rate.

Consequently, rheological measurements are required to determine the four parameters (τ_y, μ_∞, $\Delta\mu$ and the relation of $\frac{c_{break}}{c_{aggr}}$) in relation to the solid volume concentration.

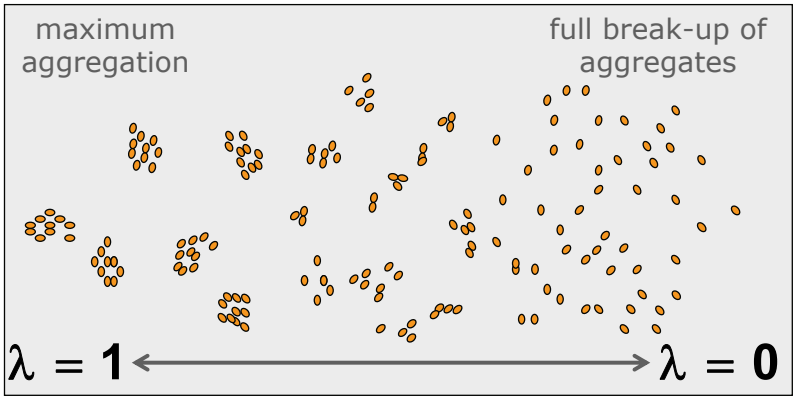

Figure 12: *Aggregation and break-up of flocs.*
The maximum degree of aggregation is defined with $\lambda = 1$ and $\lambda = 0$ indicates the state where all particle bonds are broken.

3.4.1 Rheological Measurement of Fluid Mud Samples

Rheological measurements of estuarine muds were carried out by Malcherek and Cha [2011]. They developed parameterizations for the Worrall-Tuliani model based on these measurements which is presented in this and the following section.
Ten fluid mud samples were taken from different locations in the estuaries Ems and Weser. These samples had to be prepared for the rheological measurements by sieving out particles >63 μm because the rheological measuring device is not capable of measuring sandy material. Besides, measuring the suspensions containing only the clayey and silty fractions reduces the dependence on the sediment particle distribution. Sand-mud mixtures are highly complex suspensions due to the different properties of the constituents.
The following additional analyses of the samples were carried out:

- grain size distribution determined with a laser diffraction particle size distribution analyzer,
- determination of the ignition loss and
- determination of the dry density with a special device for fine particles and powders which measures the volume by gas (helium) displacement under temperature-controlled conditions.

The resulting grain size analysis of the Ems and Weser samples showed almost no fractions smaller than 1 μm. The median grain size of the samples was in the range of 10 μm with a very small fraction of clay-sized particles. The coefficient of uniformity ranged from 2.48 to 3.19. A material/soil can be characterized by the uniformity coefficient in the classes (EN ISO 14688-2, 2004): C_U >15 multi-graded, C_U =6-15 medium-graded and <6 even-graded. Therefore, the grain size distribution can be characterized as even-graded. All samples exhibited very similar results in terms of the uniformity and the mean grain size and because of that a dependence of the rheological behavior on the grain size distribution can be neglected. The organic content determined due to the loss on ignition was about 7% and the dry density was in the range of 2,524 and 2,625 kg/m^3.

The aim of the rheological measurements is to find a qualitative and quantitative relation between the viscosity and the shear rate in dependence on the solid volume concentration. Thus, four different concentrated suspensions were prepared from the dried samples with the sediment volume concentrations 5.5%, 7%, 8.5% and 10%.

The used rheometer was a *MCR 51-Rheometer* from *Anton Paar*. This rheometer can be applied under several conditions and configurations. Important features are the kind of shear impact on the sample (controlled shear stress or shear rate, oscillation or

rotation) while the measuring device is a rotating plate to plate or conus to plate system and the temperature is adjustable. The minimum possible angular rate is 10^{-5}/min under controlled shear stress conditions and 10^{-3}/min under controlled shear rate conditions. The measurements were set-up with a plate to plate configuration under controlled shear stress conditions and at a constant temperature of 20°C.

The yield stress (critical stress for initiation of movement/deformation) can be determined from rheological measurements. Chhabra and Richardson [2008] indicate that the existence of a true yield stress is often uncertain because no yield stress may exist at very small shear rates but very high viscosities may do so. It is mostly assumed an apparent yield stress, which is dependent on the range of the rheological measurement. Additionally, the measured data fitted to different rheological models will lead to different yield stresses.
Berlamont et al. [1993] report from literature review about different methods for the yield stress determination: apparent yield stress resulting from least squares fitting of a rheological model, evaluation of the residual yield stress from controlled shear rate measurements (with meanwhile recovery between the shear stages) by extrapolation of the flow curve or rheological measurement under controlled shear stress conditions.
Nowadays, the rheometers have become more precise and can be used for very low shear stresses which has led to progress in the yield stress evaluation [Barnes, 2000; Chhabra and Richardson, 2008]. The controlled shear stress method is more appropriate than the controlled shear rate method for the evaluation of the yield stress because the structure of the sample is be better preserved during the testing period (one stage of shear/stress).
The controlled shear stress method applies a shear stress on the sample which increases incrementally. The progression to a next shear stress state is approached very slowly to keep an equilibrium state of aggregation. The yield stress is then evaluated by extrapolation of the data to the point of zero shear rate. This method was applied in the studies of Malcherek and Cha [2011]. The rheological measurements have led to flow curves and their related yield stress for every sample of the different concentrated suspensions. Figure 13 shows an example of the resulting flow curves and the viscosity curve of one sample. An increasing yield stress proportional to the volume concentration can be observed. After initiation of movement the shear rate increases only slightly with rising shear stress. The mud suspensions are a shear thinning material in which the aggregates bonds slowly break-up during the first stage described. At a certain shear stress the structure is destroyed entirely. This point of shear stress is reached later with increasing concentration. The second stage now begins in which even low advancing shear stresses lead to large deformations (small gradient in the flow curve). The viscosity-shear rate relation behaves accordingly and the viscosity decreases with the progressive shear impact. The gap due to structural breaking also becomes apparent.

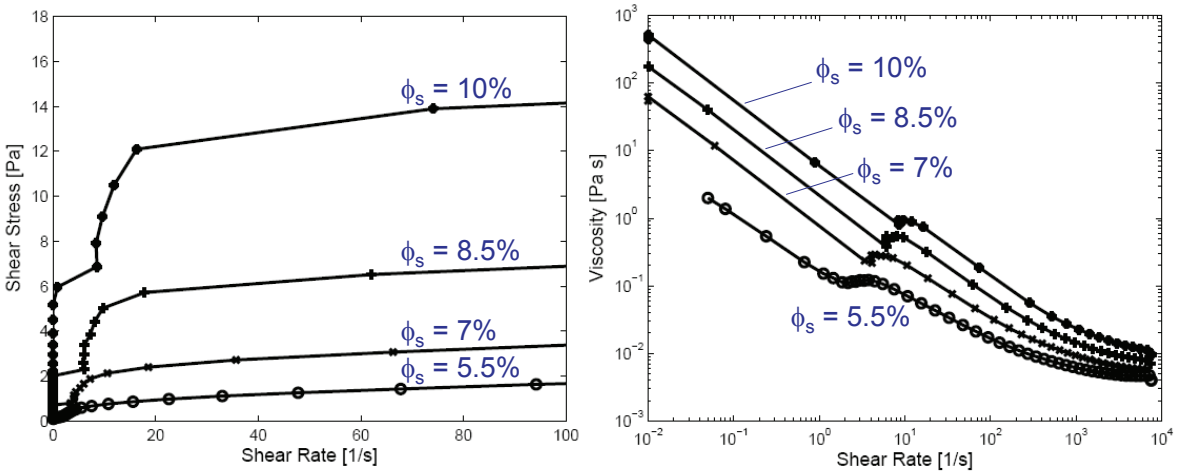

Figure 13: *Example of the results of rheological measurements - flow curve and viscosity curve with logarithmic scale (modified from Malcherek and Cha [2011]).*
The rheological measurements have been carried out for four different degrees of dilution for each sample (sediment volume concentrations 5.5%, 7%, 8.5% and 10%). The flow curves show an increasing yield stress with increasing sediment volume concentration indicated by the initiation of deformation (left panel). The viscoosity decreases with increasing shear rates due to break-up of flocs (right panel).

In a next step these measured data were converted into parameterizations as a function of the solid volume concentration.

3.4.2 Parameterization of the Worrall-Tuliani Model for Mud Suspensions

The parameterizations identified by [Malcherek and Cha, 2011] were based on rheological analysis by taking all ten samples into account as the rheological approach should be as generally valid as possible. Nevertheless, these parameterizations should still be understood as a result of these special mud samples. Other sampling campaigns might get different results with the same method.

The four parameters identified above (τ_y, μ_∞, $\Delta\mu$ and $\frac{c_{break}}{c_{aggr}}$) are given in relation to the solid volume content. The yield stress is exponentially dependent on the volume concentration

$$\tau_y = a_1 \phi_s^{b_1} \tag{3.4.6}$$

which is a relation according to Migniot [1989]. The viscosity μ_∞ defines the viscosity for a completely destroyed structure which ranges from the minimum value, the viscosity of clear water ($\mu_0 = 0.001$ Pa s), to increasing magnitudes depending on the particle content. This viscosity is defined by

$$\mu_\infty = \mu_0 exp\left(b_2 \phi_s\right). \tag{3.4.7}$$

The viscosity $\Delta\mu$ for a specific degree of structure is a linear function of ϕ_s

$$\Delta\mu = a_2\phi_s. \tag{3.4.8}$$

Finally, the relation of the structural parameters is expressed by a non-linear function

$$\frac{c_{break}}{c_{aggr}} = c_{struc} = a_3\phi_s^{-b_3}. \tag{3.4.9}$$

Accordingly, the Worrall-Tuliani model in terms of the predefined parameters results in

$$\tau = a_1\phi_s^{b_1} + \mu_0 exp\left(b_2\phi_s\right)\dot{\gamma} + a_2\phi_s\dot{\gamma}\frac{1}{a_3\phi_s^{-b_3}\dot{\gamma}+1}. \tag{3.4.10}$$

This formulation is adjusted to the measured data due to surface fitting for all samples. The surface fitting relates the shear stress to two parameters: the solid volume concentration and the shear rate. An example of surface fitting is illustrated in Figure 14. The resulting empirical parameters are

$$\begin{aligned} a_1 &= 7021\,\text{Pa} \\ b_1 &= 4.245 \\ a_2 &= 0.8358\,\text{Pa}\cdot\text{s} \\ b_2 &= 14.69 \\ a_3 &= 0.02193\,\text{s} \\ b_3 &= 0.5808 \end{aligned} \tag{3.4.11}$$

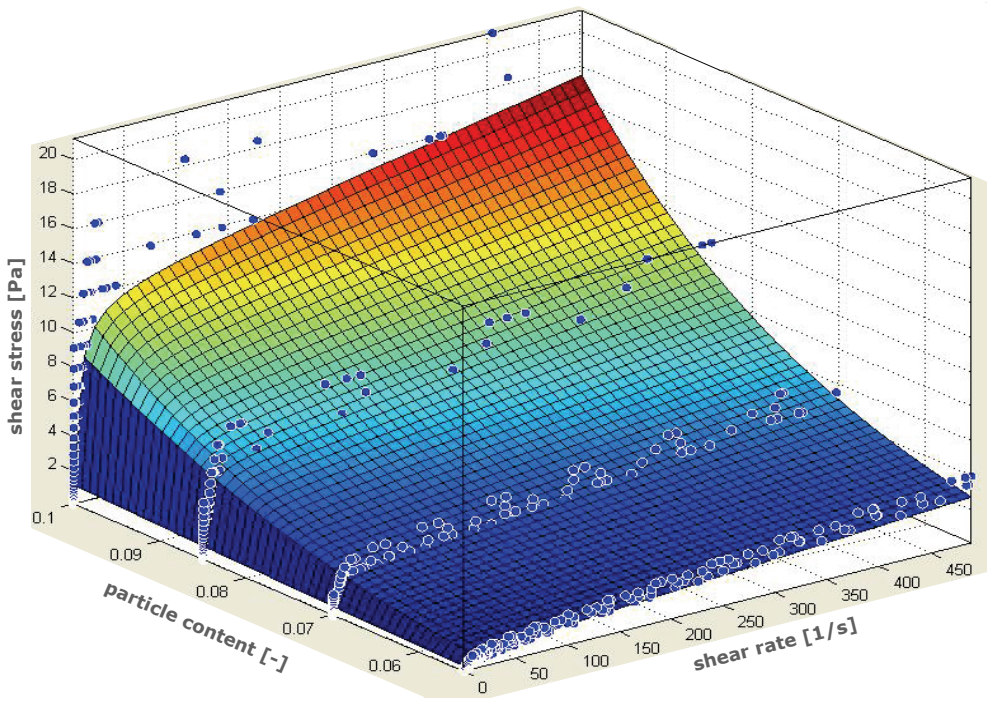

Figure 14: *Parameterization due to surface fitting (modified from Malcherek and Cha [2011]). The shear stress is parameterized as a function of the particle content and the shear rate.*

and were presented in Knoch and Malcherek [2011]. The fully parametrized formulation according to Worrall-Tuliani then leads to

$$\tau = 7021\,\mathrm{Pa}\,\phi_s^{4.245} + \mu_0 \exp\left(14.69\phi_s\right)\dot{\gamma} + \frac{0.8358\,\mathrm{Pa}\cdot\mathrm{s}\,\phi_s\dot{\gamma}}{0.02193\,\mathrm{s}\,\phi_s^{-0.5808}\dot{\gamma}+1}. \quad (3.4.12)$$

Accordingly, the rheological viscosity has the following form

$$\mu_r = \frac{7021\,\mathrm{Pa}\,\phi_s^{4.245}}{\dot{\gamma}} + \mu_0 \exp\left(14.69\phi_s\right) + \frac{0.8358\,\mathrm{Pa}\cdot\mathrm{s}\,\phi_s}{0.02193\,\mathrm{s}\,\phi_s^{-0.5808}\dot{\gamma}+1}. \quad (3.4.13)$$

The parameterized rheological model describes the shear-thinning behavior and viscoplastic behavior of a mud suspension qualitatively and quantitatively as a function of the solid volume concentration or the bulk density respectively. This approach represents a continuous formulation from clear water to a high concentrated suspension. For a particle concentration equal to zero the rheological viscosity is reduced to the viscosity μ_0 of clear water and behaves as a Newtonian fluid (Figure 17 for ϱ =1,000 kg/m^3).
In the following, the parameterized quantities used to describe the behavior of mud suspensions are shown as a function of the bulk density, because the isopycnal numerical model characterizes the mud suspensions in dependence on the bulk density. The yield stress increases exponentially with the increasing bulk density of the mud suspension, see Figure 15. The next diagram shows flow curves for different bulk densities (Figure 16). In this case, the shear rate (intensity) is chosen ranging from 0 to 100 s^{-1} which is a range recommended by Berlamont et al. [1993] to study sedimentological applications. Shear rate intensities occur in the range of 0–10 s^{-1} within the fluid mud body, whereas in turbulent flow the shear intensity may become much higher. There can be observed a stronger increase in the shear stress in the low shear rate range than in the higher shear rate range. At the beginning, the structure of the material is able to endure higher stresses but this ability decreases with the break-up of the structure due to increasing shear impact.
The rheological viscosity is shown in Figure 17 as a function of the shear rate and for different bulk densities. The shear-thinning behavior of fluid mud is represented accordingly by the decreasing rheological viscosity with increasing shear rates. Again the rheological viscosity decreases rapidly in the low shear rate range with increasing shear. The internal structure breaks up during the shear period where the viscosity decreases strongly. With the complete break-up of the aggregates the viscosity curve progresses asymptotically to a specific viscosity magnitude.

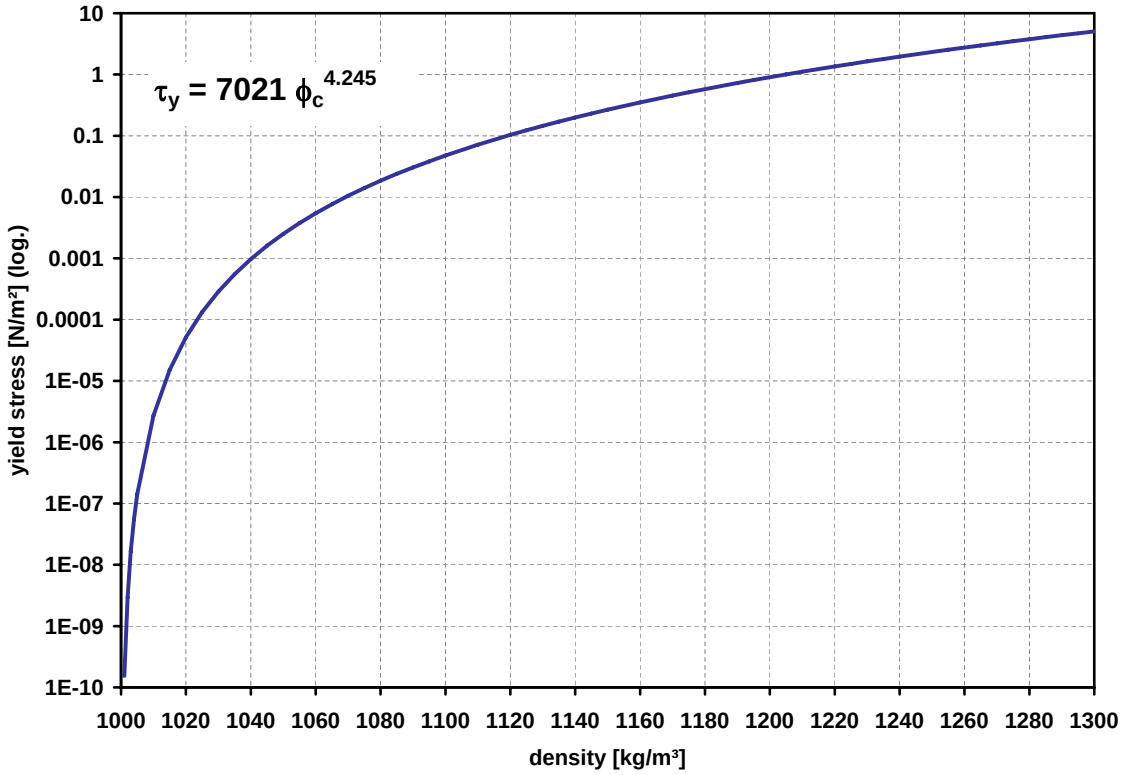

Figure 15: *Yield stress as a function of the bulk density according to the parameterized Worrall-Tuliani model.*

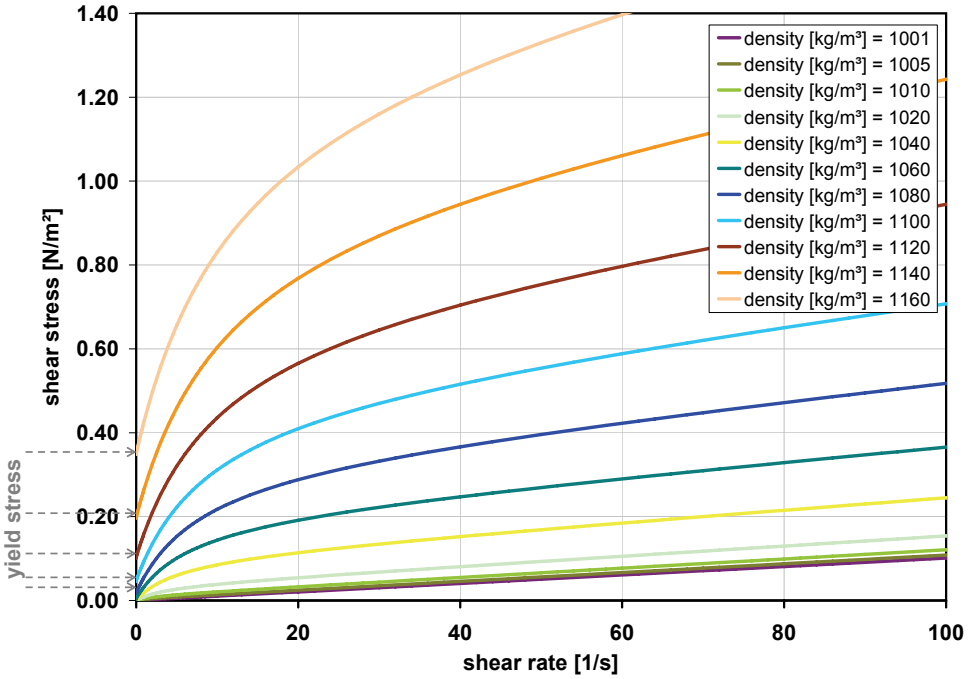

Figure 16: *Flow curves for different bulk densities according to the parameterized Worrall-Tuliani model.*
The shear stress increases with increasing bulk density and shear rate. The initiation of deformation is described by the yield stress which increases according to the bulk density.

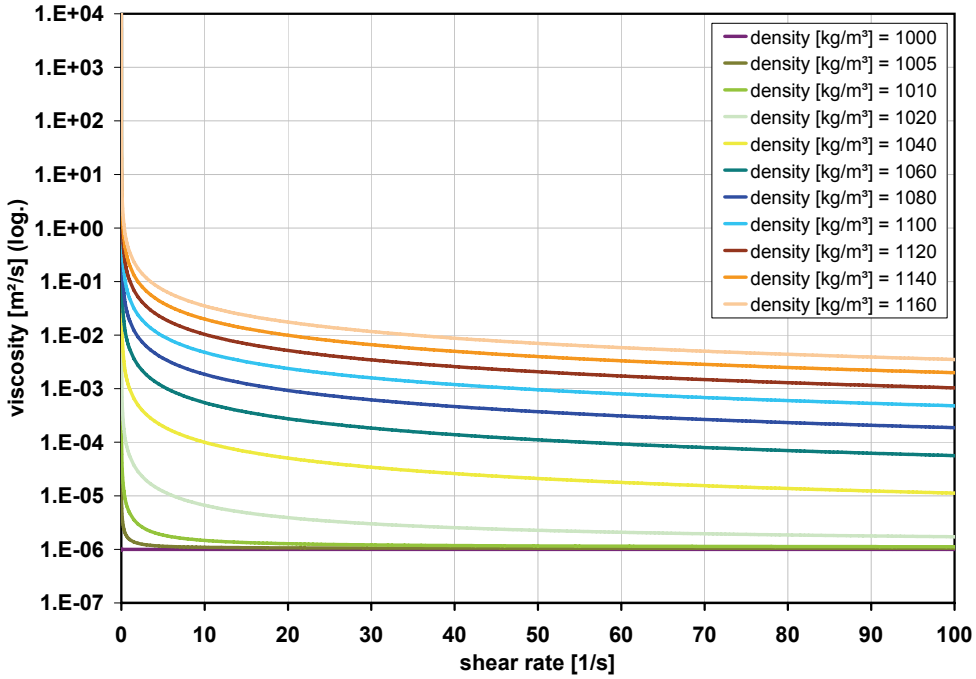

Figure 17: *Rheological viscosity-shear rate relation for different bulk densities according to the parameterized Worrall-Tuliani model.*
The viscosity decreases with break-up of the internal structure caused by an increasing shear rate. The viscosity of clear water remains constant and it indicates Newtonian behavior.

3.5 Rheological Viscosity in Three-dimensional Flow

The rheological constitutive laws shown in Section 2.2 consider a medium under simple shear such as the laminar Couette flow in x-direction. In this case, the velocity u decreases linearly with depth, the shear stress tensor reduces to the component τ_{xz} and the deformation rate tensor to $\dot{\gamma}_{xz}$, respectively. The rheological viscosity is described by the ratio of the shear stress intensity and shear rate intensity. The rheological viscosity is then given by

$$\mu_r = \frac{|\tau_{xz}|}{|\dot{\gamma}_{xz}|} \tag{3.5.1}$$

where the shear rate component $\dot{\gamma}_{xz}$ is equal to $\frac{\partial u}{\partial z}$. All three quantities are scalar values. The shear rate depends on the stress state. However, in three dimensions both are described by a tensor, see Equation (2.4.15). An isotropic and homogeneous fluid is assumed. Therefore, the viscosity of an infinitely small volume is the same in all spatial directions and it is represented by a scalar value. In other words, the viscosity does not depend on the direction of the shear, but on the magnitude or shear intensity. Thus, in three-dimensions the scalar viscosity has to be a function of the magnitudes of the shear stress and shear rate tensor. A three-dimensional approach for the rheological viscosity will be derived in this section.
The general constitutive law $\boldsymbol{\sigma} = \mathbf{F}(\mathbf{D})$ of an **isotropic** material behaves **invariant** for

volume conserving and orthogonal coordinate transformations which means the material behavior is independent from the direction of deformation but depends on its magnitude. The tensor function $\mathbf{F}(\mathbf{D})$ for a non-linear viscous fluid (non-Newtonian) is defined with [Fredrickson, 1964; Robertson, 2008]

$$\mathbf{F}(\mathbf{D}) = \mu_0\mathbf{E} + \mu_1\mathbf{D} + \mu_2\mathbf{D}^2. \tag{3.5.2}$$

where $\mu_i\,(i = 0, 1, 2)$ are scalar material functions of the invariants of $\mathbf{D}$. The fluid is assumed to have no memory such as viscoplastic materials in contrast to viscoelastic materials.
It follows a detailed consideration on the invariants of symmetric 2nd-order tensors including the shear stress and shear rate tensor. Invariants of a tensor have following properties [Bronstein et al., 1997]:

- An invariant of a tensor is a function of tensor components whose scalar value does not change with rotation of the coordinate system. Examples for these components are the trace and the determinant of a tensor.
- Invariants are independent of the chosen Cartesian coordinate system.
- Any function of the three principal invariants (see Equation (3.5.3) below) are an invariant itself.
- A tensor is invariant, in contrdiction to a tensor invariant, if the tensor components do not change their value by rotation of the coordinate system (rotational invariance) or translation (translational invariance) of the origin.

The three principal invariants of a 2nd-order and symmetric tensor $\mathbf{B}$ are given by [Prager, 1961; Malvern, 1969; Fredrickson, 1964]:

$$\mathbb{I}_B = \mathrm{tr}(\mathbf{B}) = b_{ii} = b_{11} + b_{22} + b_{33} \tag{3.5.3a}$$

$$\begin{aligned}\mathbb{II}_B &= \frac{1}{2}\left[(\mathrm{tr}(\mathbf{B}))^2 - \mathrm{tr}\left(\mathbf{B}^2\right)\right] = \frac{1}{2}\left[\mathbb{I}_B^2 - \mathrm{tr}\left(\mathbf{B}^2\right)\right] = \frac{1}{2}\left[b_{ii}^2 - b_{ij}b_{ji}\right] \\ &= \frac{1}{2}\left[(b_{11}+b_{22}+b_{33})^2 - \left(b_{11}^2+b_{22}^2+b_{33}^2\right) - 2\left(b_{12}^2+b_{13}^2+b_{23}^2\right)\right] \\ &= b_{11}b_{22} + b_{22}b_{33} + b_{11}b_{33} - \left(b_{12}^2+b_{13}^2+b_{23}^2\right)\end{aligned} \tag{3.5.3b}$$

$$\begin{aligned}\mathbb{III}_B &= \det(\mathbf{B}) \\ &= b_{11}b_{22}b_{33} + 2b_{12}b_{13}b_{23} - b_{11}b_{23}^2 - b_{22}b_{13}^2 - b_{33}b_{12}^2\end{aligned} \tag{3.5.3c}$$

with $b_{ij} = b_{ji}$. Additionally, the third invariant $\mathbb{III}_B$ can be written as a function of the trace of the tensor $\mathbf{B}$ [Oliveira and Pinho, 1998]

$$\mathbb{III}_B = \frac{1}{6}\left[(\mathrm{tr}(\mathbf{B}))^3 - 3\mathrm{tr}(\mathbf{B})\,\mathrm{tr}\left(\mathbf{B}^2\right) + 2\mathrm{tr}\left(\mathbf{B}^3\right)\right] \tag{3.5.4}$$

and the three terms are given by

$$\begin{aligned}(\mathrm{tr}\,(\mathbf{B}))^3 &= b_{ii}^3 = (b_{11}+b_{22}+b_{33})^3 \\ &= \left(b_{11}^2+b_{22}^2+b_{33}^2\right)(b_{11}+b_{22}+b_{33}) \\ &+ 2\left[b_{11}^2(b_{22}+b_{33})+b_{22}^2(b_{11}+b_{33})+b_{33}^2(b_{11}+b_{22})+3b_{11}b_{22}b_{33}\right]\end{aligned} \tag{3.5.5a}$$

$$\begin{aligned}\mathrm{tr}\,(\mathbf{B})\,\mathrm{tr}\left(\mathbf{B}^2\right) &= b_{ii}b_{ij}b_{ji} \\ &= (b_{11}+b_{22}+b_{33})\left[\left(b_{11}^2+b_{22}^2+b_{33}^2\right)+2\left(b_{12}^2+b_{13}^2+b_{23}^2\right)\right]\end{aligned} \tag{3.5.5b}$$

$$\begin{aligned}\mathrm{tr}\left(\mathbf{B}^3\right) &= b_{ij}b_{jl}b_{li} \\ &= \left(b_{11}^3+b_{22}^3+b_{33}^3\right) \\ &+ 3\left[(b_{11}+b_{22})\,b_{12}^2+(b_{11}+b_{33})\,b_{13}^2+(b_{22}+b_{33})\,b_{23}^2\right] \\ &+ 6b_{12}b_{13}b_{23}.\end{aligned} \tag{3.5.5c}$$

It follows that the scalar material functions of Equation (3.5.2) are expressed in terms of the three principal invariants of the deformation rate tensor: $\mu_i\left(\mathbb{I}_D, \mathbb{II}_D, \mathbb{III}_D\right)$. The dependence on the tensor invariants can be further simplified for incompressible (constant density) materials. The first invariant of the shear rate tensor becomes zero, and the second and third invariant can be written in reduced form

$$\mathbb{I}_D = \mathrm{tr}\,(\mathbf{D}) = \nabla\mathbf{u} = 0 \tag{3.5.6a}$$

$$\mathbb{II}_D = -\frac{1}{2}\mathrm{tr}\left(\mathbf{D}^2\right) = -\frac{1}{2}\dot{\gamma}_{ij}\dot{\gamma}_{ji} \tag{3.5.6b}$$

$$\mathbb{III}_D = \frac{1}{3}\mathrm{tr}\left(\mathbf{D}^3\right) = \dot{\gamma}_{ij}\dot{\gamma}_{jl}\dot{\gamma}_{li}. \tag{3.5.6c}$$

In the general constitutive equation (3.5.2) μ_i depends now only on $\mathbb{II}_D$ and $\mathbb{III}_D$. Furthermore, the first term can be expressed with $\mu_0\mathbf{E} = -p\mathbf{E}$ and only the deviatoric stress $\boldsymbol{\tau}$ is considered in the following (see Equation (2.4.21)). Accordingly, the deviatoric rate of deformation is equal to the rate of deformation for incompressible fluids. The constitutive equation results now in

$$\boldsymbol{\tau} = \mu_1\left(\mathbb{II}_D, \mathbb{III}_D\right)\mathbf{D} + \mu_2\left(\mathbb{II}_D, \mathbb{III}_D\right)\mathbf{D}^2 \tag{3.5.7}$$

which describes a Reiner-Rivlin fluid [Graebel, 2007]. The first term contains the (rheological) viscosity of the units $N \cdot s/m$. In the second term the material parameter μ_2 has the unit $N \cdot s^2/m$. According to Robertson [2008] and [Graebel, 2007] any Reiner-Rivlin fluid can be well described by using the following reduced form

$$\boldsymbol{\tau} = \mu_1\left(\mathbb{II}_D, \mathbb{III}_D\right)\mathbf{D} \quad \text{for} \quad \mu_1 \geq 0 \tag{3.5.8}$$

which is called the constitutive equation of a **generalized Newtonian fluid**. Consequently, the rheological viscosity can be expressed by a function of the second and third invariant of the shear rate tensor: $\mu_r\left(\mathbb{II}_D, \mathbb{III}_D\right) = \mu_1\left(\mathbb{II}_D, \mathbb{III}_D\right)$.

In one-dimensional or laminar two-dimensional flow the third invariant vanishes with $\det(\mathbf{D}) = 0$ or $\dot{\gamma}_{ij}\dot{\gamma}_{jl}\dot{\gamma}_{li} = 0$. In three-dimensional flow conditions such as turbulent flow the third determinant does not vanish except for time-averaged quantities [Oliveira and Pinho, 1998].

Most of the rheological measurements are carried out in one- or two-dimensional shear. The dependence of the viscosity on the third invariant can therefore not be quantified [Robertson, 2008]. The influence of the third invariant is difficult to measure and to the knowledge of the author there are no data available for high concentrated cohesive suspensions to determine the relationship between μ_r and $\mathbb{III}_D$. Thus, the third invariant is neglected in the following. A general tensor formulation of the shear stress for non-Newtonian fluids can be written as [Malvern, 1969; Robertson, 2008; Graebel, 2007]

$$\boldsymbol{\tau} = \mu_r(\mathbb{III}_D)\,\mathbf{D}. \tag{3.5.9}$$

The second invariant of the deformation rate tensor expressed in terms of the velocity gradients results in

$$\begin{aligned}\mathbb{III}_D &= -2\left(\left(\frac{\partial u}{\partial x}\right)^2 + \left(\frac{\partial v}{\partial y}\right)^2 + \left(\frac{\partial w}{\partial z}\right)^2\right) \\ &\quad - \left(\frac{\partial u}{\partial y} + \frac{\partial v}{\partial x}\right)^2 - \left(\frac{\partial u}{\partial z} + \frac{\partial w}{\partial x}\right)^2 - \left(\frac{\partial v}{\partial z} + \frac{\partial w}{\partial y}\right)^2.\end{aligned} \tag{3.5.10}$$

This expression reduces for two-dimensional flow in the xz-plane with velocities $u(z) \neq 0$ and $v = w = 0$ to $\mathbb{III}_D = -(\partial u/\partial z)^2$. This results in the same formulation of the rheological viscosity as shown in the example at the beginning of this section. The simple shear example is now evaluated for an ideal plastic fluid, the Bingham fluid, to derive later the rheological viscosity as a function of $\mathbb{III}_D$ for different approaches of the material behavior. A Bingham fluid in simple shear starts to move once the shear stress intensity $|\tau_{xz}|$ exceeds the yield stress τ_y. This is the one-dimensional yield condition $\tau_y \geq |\tau_{xz}|$ for $\dot{\gamma}_{xz} = 0$. Thus, the constitutive relation for a Bingham fluid is given by

$$|\tau_{xz}| = \tau_y + 2\mu_B\,|\dot{\gamma}_{xz}| \tag{3.5.11}$$

for one-dimensional shear. After exceeding the yield stress the fluid behaves like a Newtonian fluid with a constant viscosity μ_B, the Bingham viscosity. The one-dimensional rheological viscosity formulation then results in

$$\mu_r = \frac{|\tau_{xz}|}{|\dot{\gamma}_{xz}|} = \frac{\tau_y}{|\dot{\gamma}_{xz}|} + 2\mu_B \tag{3.5.12}$$

by taking the intensities of the shear stress and shear rate into account.

Von Mises proposed a yield condition for an ideal plastic and incompressible material [Prager, 1961]

$$\tau_y^2 \geq \mathbb{III}_\tau = -\frac{1}{2}\tau_{ij}\tau_{ji} \quad \text{for} \quad \mathbf{D} = 0 \tag{3.5.13}$$

which is valid for three-dimensional shear. The shear stress intensity is determined by the second invariant of the shear stress tensor $\mathbb{III}_\tau$. Based on this and by considering the von Mises yield condition, an approach for plastic material behavior for arbitrary deformation rates or shear rates is depicted [Prager, 1961; Malvern, 1969]

$$2\mu_B\dot{\gamma}_{ij} = \begin{cases} 0 & \text{for} \quad 1 - \frac{\tau_y}{\sqrt{|\mathbb{III}_\tau|}} < 0 \\ \tau_{ij}\left(1 - \frac{\tau_y}{\sqrt{|\mathbb{III}_\tau|}}\right) & \text{for} \quad 1 - \frac{\tau_y}{\sqrt{|\mathbb{III}_\tau|}} \geq 0 \end{cases} . \tag{3.5.14}$$

The Equation (3.5.14) for non zero deformation is squared

$$4\mu_B^2\dot{\gamma}_{ij}^2 = \tau_{ij}^2\left(1 - \frac{\tau_y}{\sqrt{|\mathbb{III}_\tau|}}\right)^2 \quad \text{for} \quad \mathbf{D} \neq 0. \tag{3.5.15}$$

This leads to a formulation in terms of the second invariants:

$$4\mu_B^2\mathbb{III}_D \;=\; \mathbb{III}_\tau\left(1 - \frac{\tau_y}{\sqrt{|\mathbb{III}_\tau|}}\right)^2 = \left(\sqrt{|\mathbb{III}_\tau|} - \tau_y\right)^2 \tag{3.5.16}$$

with $\dot{\gamma}_{ij}\dot{\gamma}_{ij} = 2\mathbb{III}_D$ and $\tau_{ij}\tau_{ij} = 2\mathbb{III}_\tau$. Finally, the viscosity is given by

$$\mu_r = \frac{\boldsymbol{\tau}}{\mathbf{D}} = \frac{\tau_y}{\sqrt{|\mathbb{III}_D|}} + 2\mu_B \tag{3.5.17}$$

for the three-dimensional case. Different expressions for the rheological viscosity can be developed in accordance with rheological constitutive laws:

$$\mu_r\left(\mathbb{III}_D\right) = \frac{\tau_y}{\sqrt{|\mathbb{III}_D|}} + 2\mu_B \qquad \text{for a Bingham fluid} \tag{3.5.18a}$$

$$\mu_r\left(\mathbb{III}_D\right) = \frac{\tau_y}{\sqrt{|\mathbb{III}_D|}} + K\sqrt{|\mathbb{III}_D|}^{(b-1)} \qquad \text{for a generalized Newtonian power-law fluid} \tag{3.5.18b}$$

$$\mu_r\left(\mathbb{III}_D\right) = \frac{\tau_y}{\sqrt{|\mathbb{III}_D|}} + 2^b K\sqrt{|\mathbb{III}_D|}^{(b-1)} \qquad \text{for a Herschel-Bulkley fluid} \tag{3.5.18c}$$

$$\mu_r\left(\mathbb{III}_D\right) = \frac{\tau_y}{\sqrt{|\mathbb{III}_D|}} + 2\mu_\infty + \frac{\Delta\mu}{\frac{C_{break}}{C_{aggr}}\sqrt{|\mathbb{III}_D|} + 1} \qquad \text{for a Worrall-Tuliani fluid.} \tag{3.5.18d}$$

The empirical parameter K is the consistency coefficient. The empirical exponent b denotes the flow index. The dynamic viscosity μ_∞ describes the viscosity at fully broken structure. The second invariant of the Worrall-Tuliani approach is located in the denominator in particular. The term $\sqrt{|\mathbb{III}_D|}$ represents the intensity of the shear rate

independently of the direction of action. Multiplied by the empirical constant $\frac{C_{break}}{C_{aggr}}$, this term describes the break-up of aggregates with increasing shear forces.

The flow regime of a river or estuary is dominated by vertical gradients of horizontal velocity. Thus, a sufficient approximation for $\mathbb{III}_D$ is obtained by neglecting derivatives of the vertical velocity component because the horizontal velocity gradients are much greater than the vertical velocity gradients. In addition, the horizontal derivatives of the horizontal velocity components are very small. Using these assumptions, the shear rate intensity expression reduces to

$$\mathbb{III}_D = -\left[\left(\frac{\partial u}{\partial z}\right)^2 + \left(\frac{\partial v}{\partial z}\right)^2\right]. \tag{3.5.19}$$

Accordingly, the rheological viscosity of a Worrall-Tuliani fluid in three-dimensional flow results in

$$\mu_r = \frac{\tau_y}{\sqrt{\left|\left(\frac{\partial u}{\partial z}\right)^2 + \left(\frac{\partial v}{\partial z}\right)^2\right|}} + 2\mu_\infty + \frac{\Delta\mu c_{aggr}}{c_{break}\sqrt{\left|\left(\frac{\partial u}{\partial z}\right)^2 + \left(\frac{\partial v}{\partial z}\right)^2\right|} + c_{aggr}}. \tag{3.5.20}$$

The effect of turbulence is modeled with a comparable approach for the turbulent viscosity. For example, the mixing length model describes the turbulent viscosity with

$$\mu_t = \frac{l_m}{\varrho}\sqrt{|\mathbb{III}_D|} = \frac{l_m}{\varrho}\sqrt{\left|\left(\frac{\partial u}{\partial z}\right)^2 + \left(\frac{\partial v}{\partial z}\right)^2\right|} \tag{3.5.21}$$

as a function of the shear rate intensity and the mixing length l_m [Malcherek, 2001; Schlichting and Gersten, 1997]. Similarly, the shear rate intensity is approximated by vertical gradients of horizontal velocity, because they express the maximum shearing.

Therefore, the effect of increasing turbulence or increasing rheological viscosity is the same in the Navier-Stokes equations, i.e. damping of the current velocity. However, with regard to the diffusion of suspended particles, the level of mixing is increased by turbulence but reduced by an increase of rheological viscosity.

If the rheological behavior of fluid mud becomes similar to a plastic solid (e.g. consolidated mud) then also the other components of the second shear rate invariant can become significant. Furthermore, the third invariant should be taken into account in the function of the viscosity.

3.6 Mobilization of Mud Suspensions

The mobilization processes of fluid mud depend on the condition and concentration of the mud as well as on the impact on it, see Section 2.3 and in detail McAnally et al. [2007a], Kranenburg [1994] and Mehta et al. [1989]. While erosion refers to

the mobilization of consolidated mud beds, entrainment is the transition from a higher concentrated layer to a layer of lower concentration. The latter one is also known as resuspension or redispersion. Both are induced by shear flow velocities and turbulent forces. Fluidization describes the transition of consolidated mud to mobile mud due to wave impact. Wave impact is most effective in shallow water, e.g. mud flats and along the shoreline. The simulation of fluidization requires additional coupling to a wave module, which is beyond the scope of this thesis. Entrainment is the process of vertical mixing which is the focus of this thesis. In particular, fluid mud under the influence of tidal currents is vertically transported by entraining processes.

Entrainment can be considered in different ways depending on the conceptual approach of the numerical fluid mud model. Most approaches need parameterizations which are functions of the degree of density stratification characterized by the Richardson number. Vertical turbulent mixing is damped by the stratification at the lutocline, but the breaking of internal waves and entrainment lead to vertical mixing. This vertical exchange at the lutocline can be realized by an additional vertical viscosity term, which is described by Guan et al. [2005] in a three-dimensional σ-layer model, for example. In numerical models with discrete fluid mud layers, which are either single-layer models coupled with a hydrodynamic model or an isopycnal model, an entrainment mass flux has to be defined for the exchange between the fluid mud and the overlying layer. In an isopycnal approach with constant density layers, both the water layer and the fluid mud layer will decrease, but a third layer of lower concentration will occur in between. Some entrainment flux approaches are presented below.

McAnally et al. [2007a] suggests different approaches for the dimensionless entrainment coefficient E for the first entrainment case

$$E = \frac{\Phi^{ent}}{u_{*,wm}} \tag{3.6.1}$$

where $u_{*,wm}$ is the friction velocity at the interface of fluid mud and water layer and $\Phi^{ent} = dH/dt$ is the entrainment rate. It was observed that, with increasing stratification, the entrainment coefficient decreases because turbulence becomes less dominant in stratified flows. The degree of stratification is expressed by the Richardson number. The entrainment coefficient can be formulated as a function of the bulk Richardson number Ri_*

$$Ri_* = \frac{(\varrho_w - \varrho_{mud})}{\varrho_0} \frac{gH_w}{u_{*,wm}^2} \tag{3.6.2}$$

with the reference density ϱ_0, the depth H_w and the density of the upper water layer ϱ_w. The reference density is set equal to ϱ_w. In the following, the index w is used for the water layer, mud for the fluid mud layer and wm for the interface of both layers. Different entrainment coefficients are proposed as a function of the bulk Richardson

number [McAnally et al., 2007a]

$$E = f\left(Ri_*\right)^{-\frac{1}{2}} \quad \text{or} \quad E = f\left(Ri_*\right)^{-\frac{1}{4}}. \tag{3.6.3}$$

An entrainment rate expression based on the turbulent kinetic energy equation was developed by Kranenburg and Winterwerp [1997]. This is a solution for the first entrainment case with a two-layer system comprising a mixed water layer above a quiescent fluid mud layer (entraining fluid mud into the turbulent water body above, see Section 2.3.3). Mud is entrained into the water layer due to shear. The turbulent kinetic energy equation is integrated over the depth of the turbulent mixed layer and results in:

$$\begin{aligned} 0 &= \underbrace{C_q \frac{d}{dt}\left(H_w u_w \frac{dH}{dt}\right)}_{(I)} - \underbrace{2C_s\left(u_{*,wm}^2 - u_{*,y}^2\right)\left(u_w - u_{wm}\right)}_{(II)} \\ &- \underbrace{C_s \frac{dH}{dt}\left[\left(u_w - u_{wm}\right)^2 - C_y u_{*,y}^2\right]}_{(II)} - \underbrace{C_s\left(u_*^2 - u_{*,y}^2\right)\left(u_w - u_{wm}\right)}_{(III)} \\ &- \underbrace{C_\sigma\left[\left(u_*^3 + u_{*,wm}^3\right)^{2/3} - u_{*,y}^2\right]\left(u_*^3 + u_{*,wm}^3\right)^{1/3}}_{(IV)} \\ &+ \underbrace{\frac{dH}{dt}\frac{gH_w}{\varrho_w}\frac{\left(\varrho_s - \varrho_w\right)}{\varrho_s}\left(c_{mud} - c_w\right)}_{(V)}. \end{aligned} \tag{3.6.4}$$

The sidewall effects and settling are neglected here. C_q, C_s, C_y and C_σ are empirical constants. The shear velocities are $u_{*,wm}$ at the interface of water and fluid mud and u_* of the main flow at the free surface. The suspended sediment concentration is denoted by c and a related index. The terms of the integrated turbulent kinetic energy equation are

(I) the storage term which is only important in weakly stratified flow,

(II) the shear production term at the interface,

(III) the shear production term at the free surface of the upper layer,

(IV) the stirring term including turbulent viscous effects,

(V) the buoyancy term described as a function of the Ri_*-number.

The strength of the fluid mud layer is taken into account by the yield stresses shear velocity $u_{*,y}^2$. The turbulent viscous effects are expressed by the relation $\frac{u_{wm}}{u_w}$. If turbulence is insignificant u_{wm} tends to zero. In case of turbulence is dominant, u_{wm} reaches the value of u_w.

For soft mud beds, the term of coefficient C_y can be neglected because it is very small compared with the buoyancy term. However, it should be included if erosion of consolidated fluid mud occurs. The first case of non-consolidated muds and a strong

stratified flow is now considered. The storage term is set to zero. Then the entrainment rate is given by

$$\Phi^{ent} = \frac{dH}{dt} = \left(C_s \left(u_w - u_{wm}\right) \left[2\left(u_{*,wm}^2 - u_{*,y}^2\right) + \left(u_*^2 - u_{*,y}^2\right)\right] + C_\sigma \left[\left(u_*^3 + u_{*,wm}^3\right)^{\frac{2}{3}} - u_{*,y}^2\right] \left(u_*^3 + u_{*,wm}^3\right)^{\frac{1}{3}} \right) \left(-C_s \left(u_w - u_{wm}\right)^2 + \frac{gH_w}{\varrho_r} \frac{\left(\varrho_s - \varrho_r\right)}{\varrho_s} \left(c_{wm} - c_w\right) \right)^{-1}. \tag{3.6.5}$$

Further simplification can be achieved by neglecting the shear production term (III) at the free surface. It results in the entrainment rate according to Winterwerp et al. [2002]

$$\Phi^{ent} = \frac{2C_s \left(u_w - u_{wm}\right) \left\langle u_{*,wm}^2 - u_{*,y}^2 \right\rangle + C_\sigma \left\langle \left(u_*^3 + u_{*,wm}^3\right)^{\frac{2}{3}} - u_{*,y}^2 \right\rangle \left(u_*^3 + u_{*,wm}^3\right)^{\frac{1}{3}}}{C_s \left(u_w - u_{wm}\right)^2 + gH_w \frac{\left(\varrho_{mud} - \varrho_w\right)}{\varrho_w}}. \tag{3.6.6}$$

where the terms in angular brackets are set to zero if they become negative. When multiplied by the sediment concentration of the fluid mud layer $c_{mud} = \varrho_s \frac{\varrho_{mud} - \varrho_w}{\varrho_s - \varrho_w}$ the mass entrainment rate is obtained. The empirical constants were determined in experiments by Winterwerp and Kranenburg [1997] and Kranenburg and Winterwerp [1997] and can be set to $C_q = 5.6$, $C_s = 0.25$ and $C_\sigma = 0.42$.

The shear velocity of the interface can be described as a function of a friction parameter f_{wm} with

$$u_{*,wm}^2 = f_{wm} \left(u_w - u_{mud}\right)^2 \tag{3.6.7}$$

or as a function of the viscosity

$$u_{*,wm}^2 = \nu_{wm} \left(\nu_t, \nu_r\right) \frac{\partial u}{\partial z} = \nu_{wm} \left(\nu_t, \nu_r\right) \frac{u_w - u_{mud}}{\Delta z}. \tag{3.6.8}$$

where $u_{*,y}^2$ represents the strength of the fluid mud layer and indicates therefore a critical shear stress.

The yield stresses shear velocity is defined as

$$u_{*,y}^2 = \frac{\tau_y}{\varrho_{mud}}. \tag{3.6.9}$$

The yield stress is determined as a function of the mud concentration with the parameterized Worrall-Tuliani model (3.4.12). This is the critical shear stress velocity for entrainment.

The entrainment rate approach of Equation (3.6.6) is analyzed in Figure 18. The entrainment rate is a function of the shear velocity difference $\left(u_{*,wm}^2 - u_{*,y}^2\right)$ (with $u_* = 0$), the velocity difference $\left(u_w - u_{wm}\right)$ (with $u_{wm} = u_{mud}$ the mean fluid mud velocity) and

the water layer depth H_w. However, the entrainment rate is not dependent on the fluid mud layer depth. The top diagram shows the entrainment intensity $H_{mud,\Delta t}/H_{mud,0}$ (depth after the time period Δt / initial depth) versus the velocity quotient u_{mud}/u_w for different velocities of the water layer. The entrained amount increases with increasing interfacial shear or decreasing velocity quotient u_{mud}/u_w. The bottom diagram shows the relationship between entrainment rate and water layer depth for different velocity differences of the adjacent layers. The entrainment rate decreases with reducing water layer depth. The entrainment rate curve runs asymptotically with increasing water layer depth.

The following entrainment approach assumes the second entrainment case (entraining water into the fluid mud body below, see Section 2.3.3). A parameterized approach for the entrainment rate of fluid mud was introduced by Whitehouse et al. [2000]

$$\Phi^{ent} = \frac{C_f u_{mud}}{(1+63Ri_*^2)^{\frac{3}{4}}} = C_f u_{mud}\left(1+63\left(\frac{(\varrho_w-\varrho_{mud})}{\varrho_w}\frac{gH_{mud}}{(u_{mud}-u_w)^2}\right)^2\right)^{-\frac{3}{4}} \tag{3.6.10}$$

and, based on comparisons with filed data, he recommends setting the coefficient C_f in the order of magnitude 1.0. In this case, the bulk Richardson number is defined as a function of the fluid mud layer depth H_{mud}. Whitehouse et al. [2000] recommend that entrainment only takes place for $Ri_* < 10$. Furthermore, the entrainment rate becomes very small for $Ri_* > 10$.

An additional threshold is introduced for this entrainment case to take the rheological behavior into account. The fluid mud resistance against entrainment can be specified by the yield stresses shear velocity $u_{*,y}^2$ (Equation (3.6.9)). Entrainment is thus initiated if $|u_{*,wm}| > |u_{*,y}|$ with the interfacial shear velocity $u_{*,wm}$.

The entrainment rate Φ^{ent} is a function of the fluid mud layer depth H_{mud}, the difference of the velocities of the adjacent water and fluid mud layer $(u_w - u_{mud})$ and the mean velocity of the fluid mud layer. Their relationship is analyzed in the diagrams of Figure 19. The top diagram shows the relationship between the fluid mud layer depth quotient $H_{mud,\Delta t}/H_{mud,0}$ (depth after the time period Δt / initial depth) and the velocity quotients u_w/u_{mud} for different velocities of the water layer. No entrainment occurs for $H_{mud,\Delta t}/H_{mud,0} = 1$. The entrainment intensity increases with increasing mean velocity of the fluid mud layer and decreasing velocity quotient. The bottom diagram represents the entrainment rate versus the fluid mud layer depth for different velocity differences $(u_{mud} - u_w)$. The entrainment rate increases with the difference of the velocity which describes the shear impact at the water-fluid mud interface. In addition, the entrainment rate decreases asymptotically with increasing fluid mud layer depth.

Both approaches include parameterizations, which make the simulation results rather

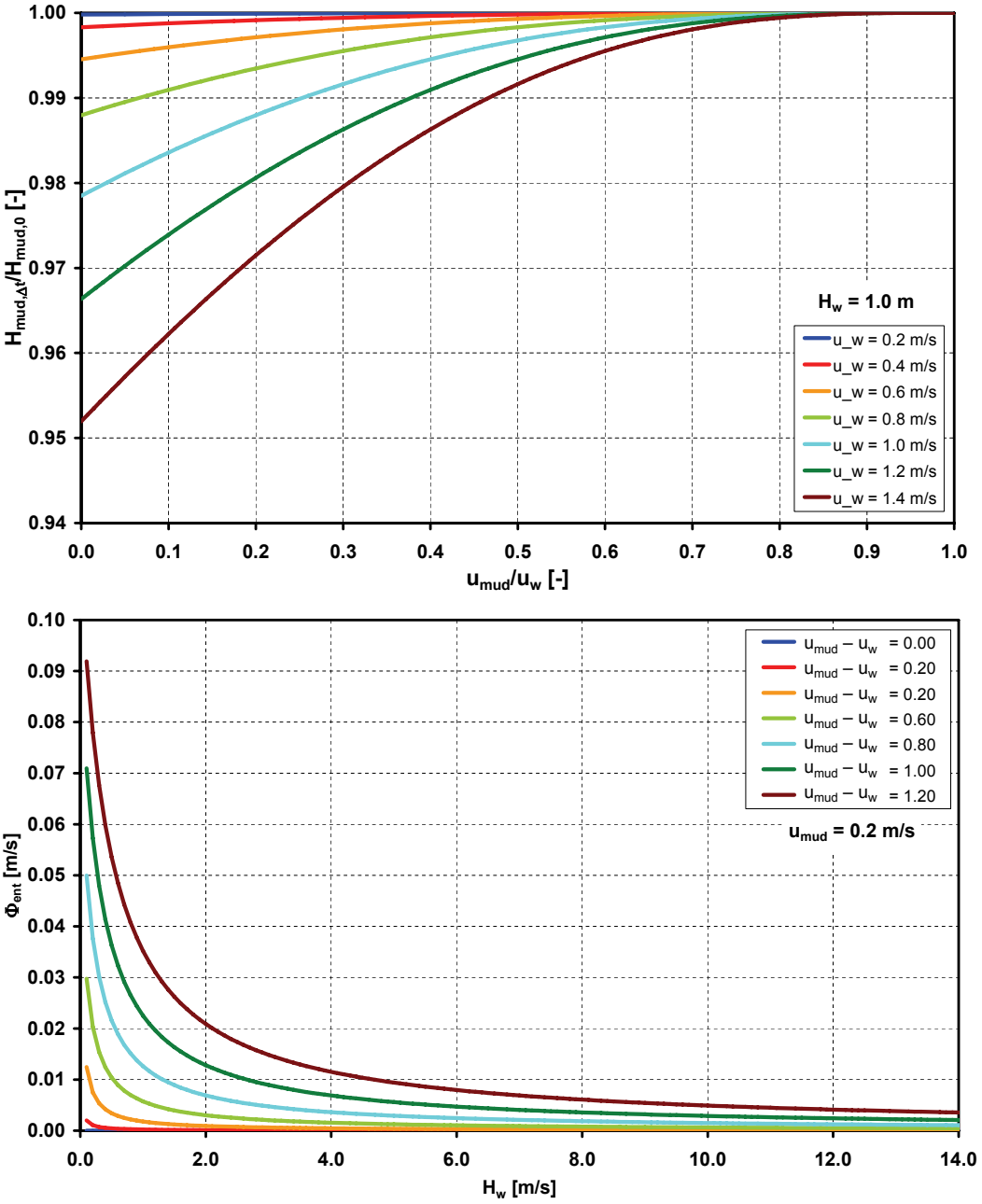

Figure 18: *Analysis of the entrainment model according to Winterwerp et al. [2002]. The top diagram shows the relationship of the quotient of the fluid mud layer depth $H_{mud,\Delta t}/H_{mud,0}$ and the velocity quotient u_{mud}/u_w for different mean velocities of the water layer. The bottom diagram shows the entrainment rate versus the water layer depth. The entrainment rate increases with increasing shear or differences of the velocity. Moreover, the entrainment rate decreases asymptotically with the water layer depth.*

sensitive to the chosen parameters. Therefore, advanced calibration and comparison with field data are needed. At present, the isopycnal numerical model introduced in Section 4 does not include a sophisticated turbulence model which considers turbulence damping by sediment concentration, for example. Thus, the driving force for entrainment - turbulence in the overlying water column - will be underestimated.

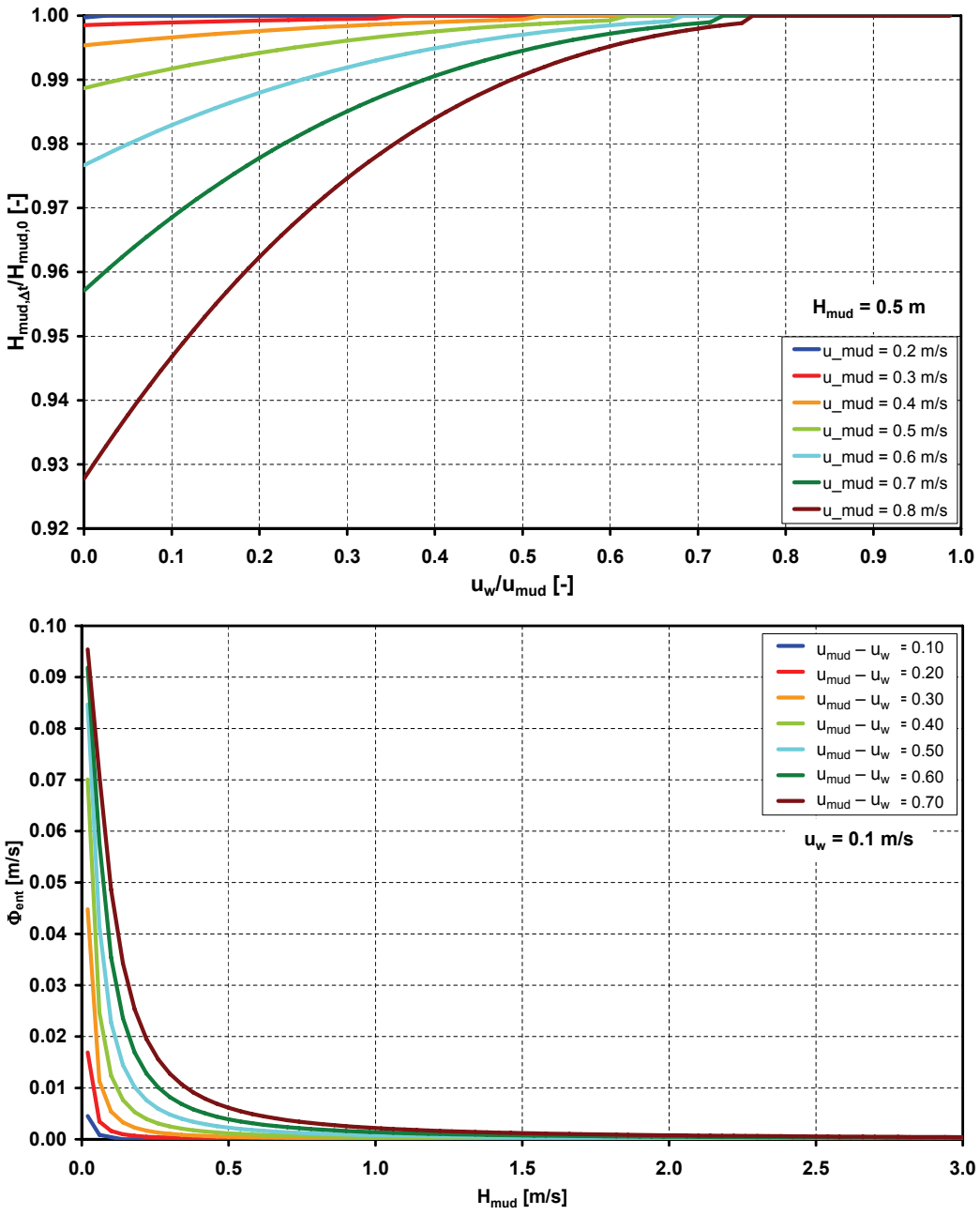

Figure 19: *Analysis of the entrainment model according to Whitehouse et al. [2000]. The top diagram shows the relationship of the quotient of the fluid mud layer depth $H_{mud,\Delta t} / H_{mud,0}$ and the velocity quotient u_w / u_{mud} for different mean velocities of the fluid mud layer. The bottom diagram shows the entrainment rate versus the fluid mud layer depth. The entrainment rate increases with increasing shear or differences of the velocity. Moreover, the entrainment rate decreases asymptotically with the fluid mud layer depth.*

3.7 Settling of Mud Suspensions

There are various approaches to determining the settling velocity of cohesive sediments. The settling velocity is dependent on the state of flocculation (floc size), the specific weight of the particle or floc, the suspended matter concentration and cohesive forces, to name a few of the parameters. The settling velocity can be expressed as a function of the particle concentration c_s to consider the flocculation process. This can be done in a simplified manner with the power law

$$w_{s,p} = k c_s^m \tag{3.7.1}$$

with the empirical coefficients k and m. This parameterization for settling is implemented in the numerical model by setting the empirical coefficients $k = 0.00024$ and $m = 1.17$ according to Schulze [1990]. The approach results in a settling velocity that increases with the concentration.
Further aspects of flocculation and their dependence on turbulence can be taken into account with an additional term introduced by van Leussen [1994] and Malcherek [1995]

$$w_s = w_{s,p} \frac{1 + aG}{1 + bG^2} \tag{3.7.2}$$

with the empirical parameters a and b and the dissipation parameter $G = \sqrt{\epsilon/\nu}$ which represents the turbulent state. The turbulent dissipation rate ϵ can be determined, for example, from a two-equation k-ϵ-turbulence model. The progressive break-up of flocs due to increasing turbulence is considered with an increase of G, resulting in a decreasing settling velocity. This approach is not applied in the following studies as an advanced turbulence model has not yet been implemented.

Another aspect of flocculation is hindered settling. As the concentration increases, the flocs impede each other in the settling process, thus reducing their average settling velocity.
Winterwerp and van Kesteren [2004] specified the following settling velocity formula with regard to hindered settling

$$w_s = w_{s,p} \frac{(1 - \phi_*)^n (1 - \phi_s)}{(1 - 2.5\phi_f)} \tag{3.7.3}$$

where the background settling velocity can be determined by the power law, $\phi_s = c_s/\varrho_s$ is the solid volume concentration of primary particles, $\phi_* = \min[1, \phi_f]$ is the threshold for consolidation, the exponent n accounts for non-linear effects and $\phi_f = c_s/\phi_{gel}$ is the solid volume concentration of mud flocs.
The parameter ϕ_f is dependent on the gelling concentration ϕ_{gel}. The gelling concentration describes the state of a suspension in which the flocs settle on the bed and come into contact with each other. They form a structure in which the space between them

diminishes and there is a simultaneous build-up of resistance. When the gelling concentration is reached, settling is suppressed and consolidation starts. Figure 20 shows the settling velocity with hindered settling as a function of the bulk density of the mud suspension for various gelling concentrations. This indicates that the settling velocity is rather sensitive to the chosen gelling concentration. The settling velocity increases with increasing bulk density in the lower density range. Hindered settling then becomes more dominant and reduces the settling velocity with further increasing concentration of the suspension. Until the settling velocity becomes zero when the gelling concentration is reached. Afterwards the high concentrated suspension starts to consolidate.
A consolidation model is not implemented although the gelling concentration is sometimes reached in the applications of the Sections 5 and 6. The simulations cover some tide cycles or some days which is a too short time period for consolidation to take effect. In this case, neglecting the consolidation is physically not correct, but can be neglected for pragmatical reason. However, consolidation needs to be considered for simulations of longer time periods.

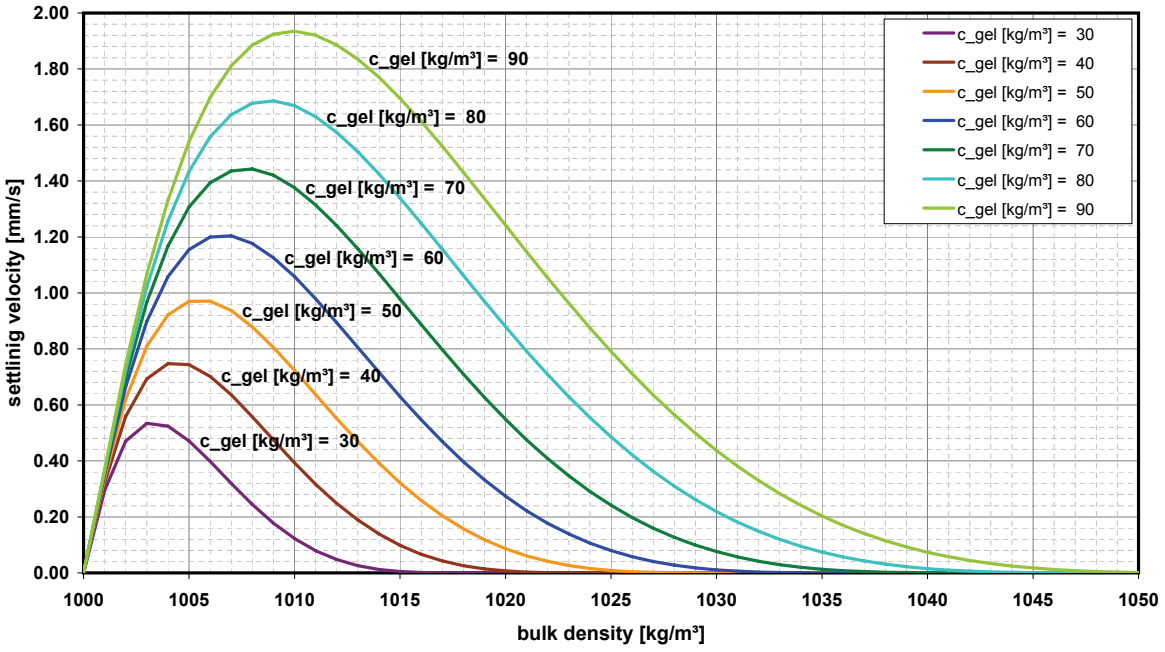

Figure 20: *Settling velocity with regard to hindered settling for different gelling concentrations according to Winterwerp and van Kesteren [2004].*
The settling velocity increases with the gelling concentration and with increasing bulk density in the low density range. In the higher density range, the settling velocity decreases with increasing density due to hindered settling. Once the suspension concentration has reached the gelling concentration the settling velocity becomes zero.

4 The Isopycnal Numerical Model

The numerical realization of the simulation of fluid mud dynamics is achieved by an isopycnal numerical method. A three-dimensional isopycnal model for the simulation of stably stratified baroclinic circulation was developed by Casulli [1997]. The fundamental property of isopycnal models is a vertical discretization by layers of constant density - the isopycnals. This is comparable to σ-models where the vertical is discretized according to geometrical characteristics instead of a physical parameter as in this case. The isopycnal model is based on the TRIM3D model [Casulli and Cheng, 1992] which is a three-dimensional hydrodynamic model for structured horizontal grid resolution with z-layers. The Reynolds-averaged shallow water equations are solved numerically by a semi-implicit method [Casulli and Cattani, 1994] and result in an efficient and stable code. The basic properties of the model are:

- calculation on a structured grid
- vertical discretization in ϱ-coordinates
- uniform density for each isopycnal layer
- momentum exchange between isopycnal layers
- no mass exchange between isopycnal layers
- stable density stratification at any time $(\varrho_1 > \varrho_2 > \ldots > \varrho_M > 0)$
- drying and wetting
- a two-dimensional model results by defining only one isopycnal layer

The 3D isopycnal approach of Casulli [1997] is extended in Appendix A to include a horizontal unstructured discretization scheme according to Casulli and Walters [2000]. An implementation of this model approach was provided by Prof. V. Casulli of the University of Trento, Italy. Moreover, the 3D isopycnal approach for unstructured grids is further developed by considering a vertical discretization with z-layers in addition to the isopycnal discretization. The combination of isopycnal and z-layer-based vertical resolution can lead to a single isopycnal layer resolved by one or more z-layers or a single z-layer resolved by one or more isopycnals. This can be advantageous for an appropriate resolution of the flow field of the entire water column. High-density gradients due to suspended sediment accumulations and fluid mud formations near the bottom can be resolved with the isopycnal layers. In this region, the isopycnal layers can become very thin so that they enable to realize the stratification. On the other hand the water body (low-concentration area with smaller density gradients) is primarily discretized by the

static z-layers. The numerical method is described for a vertical discretization scheme by a combination of z-layers and ϱ-layers in Appendix A.
The governing equations and the basic principles of the three-dimensional isopycnal model will be described in Section 4.1. It is shown how fluid mud dynamics are simulated with such a model and which extensions are needed for that purpose. The numerical method is demonstrated on a one-dimensional model vertically resolved by isopycnal layers to simplify the mathematical description. The numerical approximation and solution algorithm are then presented in Section 4.2.1 and 4.2.2 respectively. The model approach and implementation are extended to include the simulation of shear-dependent viscosity with a non-Newtonian approach (Section 4.1) and the vertical mass transfer between isopycnal layers (Section 4.3). Finally, the properties of the numerical method are summarized in Section 4.4.

4.1 Governing Equations of the Three-dimensional Isopycnal Model

The isopycnal circulation model is based on a (x, y, ϱ)-coordinate system. The system is illustrated in Figure 21. Each density layer represents a suspension of constant density which corresponds to a specific suspended sediment concentration. The bottom isopycnal layer is referred to as m_0 and the surface layer as M.

Based on the general equations of motion (2.4.10) and the continuity equation (2.4.18), three governing equations result from two assumptions. An incompressible Newtonian fluid is assumed. The density is therefore constant and can be separated from the

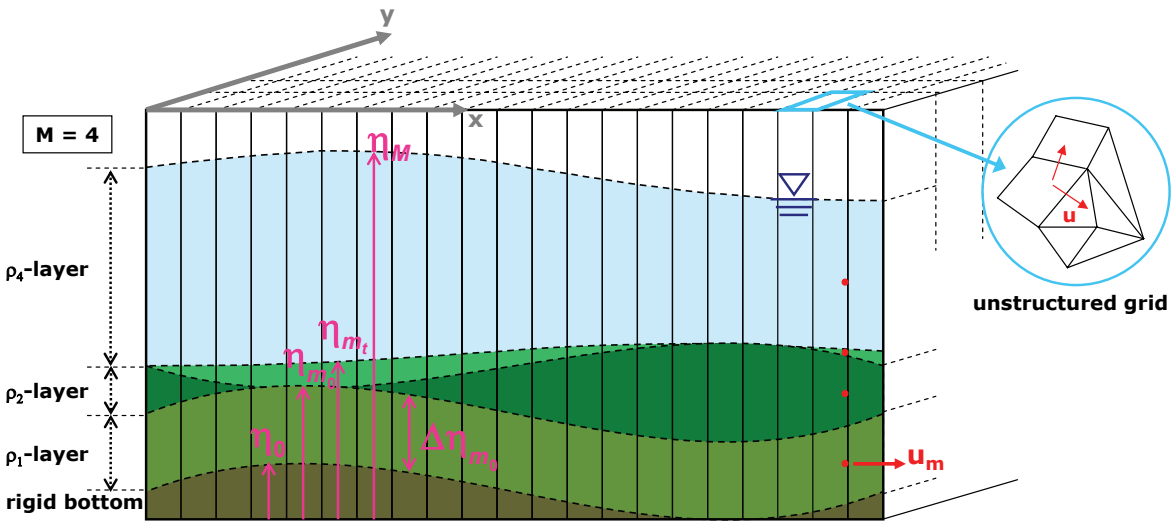

Figure 21: *Isopycnal model for three-dimensional flows.*
The vertical domain is discretized by isopycnal layers (ϱ-layer) and the horizontal domain by an unstructured grid. The layered system is stably stratified with $(\varrho_1 > \varrho_2 > \ldots > \varrho_M > 0)$. The isopycnal surfaces are denoted with η_m for the m-th isopycnal layer and the rigid bottom with η_0. The velocities u_m are layer-averaged quantities.

system of equations. The second assumption is the hydrostatic pressure approximation. Furthermore, the momentum equations are Reynolds-averaged and layer-averaged for each isopycnal layer. The density classes and the maximum number M of isopycnal layers are predefined. The isopycnal layers and their adjacent layers are specified by the following indices:

$m = m_0, \ldots, M$	isopycnal layer from bottom to surface
m_b	next active isopycnal layer below the m-th layer
m_t	next active isopycnal layer above the m-th layer

This results in a system of M two-dimensional shallow water equations for each isopycnal layer, ranging from η_{m_b} to η_m of the dimensions (x, y, ϱ). The momentum equations, which are already discretized, are given by

$$\frac{\partial u_m}{\partial t} + u_m \frac{\partial u_m}{\partial x} + v_m \frac{\partial u_m}{\partial y} = - \frac{\partial p_{h,m}}{\partial x} + \frac{\partial}{\partial x}\left(\nu_m^h \frac{\partial u_m}{\partial x}\right) + \frac{\partial}{\partial y}\left(\nu_m^h \frac{\partial u_m}{\partial y}\right) + \frac{\tau_{x,m+\frac{1}{2}} - \tau_{x,m-\frac{1}{2}}}{\varrho_m \left(\eta_m - \eta_{m_b}\right)} \tag{4.1.1a}$$

$$\frac{\partial v_m}{\partial t} + u_m \frac{\partial v_m}{\partial x} + v_m \frac{\partial v_m}{\partial y} = - \frac{\partial p_{h,m}}{\partial y} + \frac{\partial}{\partial x}\left(\nu_m^h \frac{\partial v_m}{\partial x}\right) + \frac{\partial}{\partial y}\left(\nu_m^h \frac{\partial v_m}{\partial y}\right) + \frac{\tau_{y,m+\frac{1}{2}} - \tau_{y,m-\frac{1}{2}}}{\varrho_m \left(\eta_m - \eta_{m_b}\right)} \tag{4.1.1b}$$

The second and third terms on the left side represent the **advection** terms in horizontal direction for the m-th layer. The velocities u_m and v_m are isopycnal layer-averaged quantities. The surface or subsurface elevation of the m-th isopycnal layer is given by η_m and η_0 is the bathymetric depth.

The first term on the right side represents the pressure term. The hydrostatic pressure p_h is normalized by a reference density ϱ_r and consists of the barotropic pressure and the atmospheric pressure p_a (pressure per density) at the free surface

$$p_{h,m} = g \left(\sum_{l=m}^{M} \frac{\varrho_l - \varrho_{l_t}}{\varrho_r} \eta_l \right) + p_a. \tag{4.1.2}$$

The normalized barotropic pressure considers the pressure from the surface M to the current isopycnal layer m. The density above the water surface is defined by $\varrho_{M+1} = 0$. The **gravitational transport** is determined by the pressure term. It indicates increasing gravitational forcing with increasing differences in the density of the isopycnal layers.

The second to fourth terms on the right side characterize the **internal shear stresses**. An approximation for the **non-Newtonian flow behavior** of high-concentration suspensions is derived in Sections 3.1 and 3.3. Based on this approximation, the flow behavior is described by the rheological viscosity $\nu_{r,m} = \mu_{r,m}/\varrho_m$ which is a function of space

x, time t, density ϱ which corresponds to the suspended sediment concentration and shear rate intensity $|\mathbb{II}_D|$. The horizontal and vertical viscosity components (ν_m^h and ν_m^v) are functions of the rheological viscosity ν_r and the turbulent viscosity ν_t. The detailed dependence and interaction of the two viscosity components is not yet known and has to be specified in future work. In this study, it is assumed that the horizontal and vertical viscosities can be treated as a sum of both

$$\nu_m^h = \nu_{r,m} + \nu_{t,m}^h \quad \text{and} \quad \nu_m^v = \nu_{r,m} + \nu_{t,m}^v. \tag{4.1.3}$$

The rheological viscosity has no vectorized components and its horizontal and vertical values are equal. The rheological viscosity is determined by constitutive formulations (for a further description see Sections 3.4 and 3.5). The turbulent viscosity is taken as constant for the m-th layer. It has to be ensured that the horizontal and vertical viscosities are non-negative as the viscosity terms will otherwise have an accelerating effect on the advective terms.
The interfacial shear of two adjacent isopycnals is described by the vertical shear stress term (last term on the right side). These isopycnal interfacial shear stresses for the x- and y-component are determined by

$$\frac{\tau_{x,m+\frac{1}{2}}}{\varrho_m} = \nu^v_{m+\frac{1}{2}} \frac{u_{m_t} - u_m}{(\eta_{m_t} - \eta_{m_b})}, \qquad \frac{\tau_{x,m-\frac{1}{2}}}{\varrho_m} = \nu^v_{m-\frac{1}{2}} \frac{u_m - u_{m_b}}{(\eta_{m_t} - \eta_{m_b})}, \tag{4.1.4}$$

$$\frac{\tau_{y,m+\frac{1}{2}}}{\varrho_m} = \nu^v_{m+\frac{1}{2}} \frac{v_{m_t} - v_m}{(\eta_{m_t} - \eta_{m_b})} \quad \text{and} \quad \frac{\tau_{y,m-\frac{1}{2}}}{\varrho_m} = \nu^v_{m-\frac{1}{2}} \frac{v_m - v_{m_b}}{(\eta_{m_t} - \eta_{m_b})}. \tag{4.1.5}$$

The surface boundary condition is given by

$$\frac{\tau_{x,M+\frac{1}{2}}}{\varrho_M} = \gamma_a (u_a - u_M) \quad \text{and} \quad \frac{\tau_{y,M+\frac{1}{2}}}{\varrho_M} = \gamma_a (v_a - v_M) \tag{4.1.6}$$

and the bottom boundary condition is given by

$$\frac{\tau_{x,m_0-\frac{1}{2}}}{\varrho_{m_0}} = \gamma_b u_{m_0} \quad \text{and} \quad \frac{\tau_{y,m_0-\frac{1}{2}}}{\varrho_{m_0}} = \gamma_b v_{m_0} \tag{4.1.7}$$

with the non-negative friction factors γ_a for wind friction and γ_b for bottom friction. The wind velocities are specified as u_a and v_a.

The **vertical velocity** component cancels from the momentum equations because of the depth-averaging per isopycnal layer. The vertical movement is represented by the variation of the isopycnal surfaces.

The free surface equation in (x, y, ϱ)-coordinates completes the governing equations and is given by

$$\frac{\partial \eta_m}{\partial t} + \frac{\partial}{\partial x}\left(\sum_{l=1}^{m} (\eta_l - \eta_{l-1})\, u_l\right) + \frac{\partial}{\partial y}\left(\sum_{l=1}^{m} (\eta_l - \eta_{l-1})\, v_l\right) = 0. \tag{4.1.8}$$

The development of the **isopycnal surface elevation** (surface or sub-surface) is described by the change of the elevation with time and the sum of the horizontal fluxes below the surface η_m. The thickness of the isopycnal layers can vary in time and space. The layer can disappear and reappear if drying and wetting occur.

Vertical transport processes such as settling and mixing change the degree of stratification in a suspension. In an isopycnal model approach this requires mass transfer between the isopycnal layers. Therefore, vertical fluxes are applied to the isopycnal interfaces which are determined according to parameterizations of transport rates. The layer thicknesses change according to the mass fluxes. The free surface equation then results in

$$\frac{\partial \eta_m}{\partial t} + \frac{\partial}{\partial x}\left(\sum_{l=1}^{m}\left(\eta_l - \eta_{l-1}\right) u_l\right) + \frac{\partial}{\partial y}\left(\sum_{l=1}^{m}\left(\eta_l - \eta_{l-1}\right) v_l\right) - \Phi_m^{in} + \Phi_m^{out} = 0. \quad (4.1.9)$$

where Φ_m^{in} and Φ_m^{out} are the sum of the inflow and outflow rates through the interfaces of the m-th layer. Fluxes through the rigid bottom and through the surface M are excluded. Moreover, a layer of zero thickness cannot be the origin of a transport flux, but the layer can become active due to transport flux into the layer. The mass transferred from one layer to an adjacent layer is related to the different volumes resulting from the difference in the densities of the two layers. A diapycnal mass transfer approach is therefore developed in Section 4.3 with regard to volume and mass conservation. The approach is described by a simple three-layer system in Section 4.3.1 and is then extended to consider a system of $M \geq 3$ isopycnal layers in Appendix B.

The governing equations, 4.1.1 and 4.1.9, lead to the three unknowns u_m, v_m, η_m. A semi-implicit method is applied to the governing equations to obtain a solvable system of equations as is done by Casulli [1997]. The numerical method is demonstrated in the next section by a vertical one-dimensional model with an isopycnal discretization scheme.

4.2 One-dimensional Isopycnal Model Vertically Resolved by ϱ-layers

In this section, the numerical method will be illustrated by a vertically resolved one-dimensional model approach ($1D_\varrho$) set up to simplify the discrete formulations. The extended 3D numerical method for a combined vertical discretization of ϱ- and z-layers is developed in Appendix A. In the following, the vertical domain is resolved only by ϱ-layers.

The simplifications are based on the governing equations (4.1.1) and (4.1.9) for the three-dimensional isopycnal formulations with hydrostatic assumption. Basically, an infinitely extended horizontal space is assumed and therewith the quantities do not

change in the x- and y-directions. The following assumptions lead to a $1D_\varrho$ model approach:

- The terms with horizontal velocity gradients are omitted by assuming an infinitely extended horizontal space.
- The only non-zero horizontal velocity is the longitudinal component u_m ($v_m = 0$).
- The pressure gradient remains in the governing equations representing a driving force of the flow.

This results in an one-dimensional approach with the unknown quantities: the layer-averaged velocities $u_m(t)$ and isopycnal surface elevation $\eta_m(t)$. The momentum equation is written as follows

$$\frac{\partial u_m}{\partial t} = -\frac{1}{\varrho_r}\frac{\partial p_m}{\partial x} + \frac{\tau_{x,m+\frac{1}{2}} - \tau_{x,m-\frac{1}{2}}}{\varrho_m \Delta\eta_m}. \tag{4.2.1}$$

where $\Delta\eta_m = \eta_m - \eta_{m_b}$ is the isopycnal layer thickness. The shear stress at the isopycnal interfaces is denoted by $m + 1/2$ for the upper interface and by $m - 1/2$ for the lower interface. The pressure gradient in x-direction is replaced by [Uittenbogaard, 2003]

$$\begin{aligned} \frac{1}{\varrho_r}\frac{\partial p_m}{\partial x} &= \frac{\bar{u} - \bar{u}^p}{t_r} + \frac{\tau_{x,M+\frac{1}{2}} - \tau_{x,m_0-\frac{1}{2}}}{\bar{\varrho}\left(\eta_M - \eta_0\right)} \\ &= \frac{\bar{u} - \bar{u}^p}{t_r} + \frac{\tau_a - \tau_b}{\bar{\varrho}\left(\eta_M - \eta_0\right)} \end{aligned} \tag{4.2.2}$$

where $\bar{u}^p(t)$ is the prescribed depth-averaged velocity,
$\bar{u}(t) = (\eta_M - \eta_0)^{-1} \int_{\eta_0}^{\eta_M} u_m(z,t)dz$ is the calculated depth-averaged velocity, t_r the relaxation time and $\bar{\varrho}$ is the depth-averaged density. The forcing is described by the first term. The second term balances the momentum equation because the first term can become zero when approaching a steady state. The term represents the external friction. The bed shear stress (τ_b) can be calculated, for example, according to Nikuradse by assuming a logarithmic flow profile and using the prescribed velocity $\bar{u}^p$. The surface shear stress (τ_a) can likewise be determined by applying the depth-averaged wind velocity. The rigid bottom elevation is denoted by η_0.
The free surface equation reduces according to the assumptions to

$$\frac{\partial \eta_m}{\partial t} - \Phi_m^{in} + \Phi_m^{out} = 0. \tag{4.2.3}$$

Transport fluxes between isopycnal layers due to mixing and settling are essential for the variation of the isopycnal thicknesses in the $1D_\varrho$ model. An explicit approach for diapycnal mass and volume transfer is developed for a simple three-layer system ($M = 3$) in Section 4.3.

The resulting **governing equations** of the $1D_\varrho$ model are given by

$$\frac{\partial u_m}{\partial t} = -\frac{\bar{u} - \bar{u}^p}{t_r} - \frac{\tau_a - \tau_b}{\bar{\varrho}\,(\eta_M - \eta_0)} + \frac{1}{\varrho_m\,(\Delta\eta_m)}\left[\nu^v_{m+\frac{1}{2}}\frac{u_{m_t} - u_m}{(\eta_{m_t} - \eta_{m_b})} - \nu^v_{m-\frac{1}{2}}\frac{u_m - u_{m_b}}{(\eta_{m_t} - \eta_{m_b})}\right] \tag{4.2.4a}$$

$$\frac{\partial \eta_m}{\partial t} = \Phi^{in}_m - \Phi^{out}_m \tag{4.2.4b}$$

These equations are already discrete formulations due to the isopycnal vertical discretization. The interfacial shear stresses are expressed by the vertical viscosity terms according to Equation (4.1.4). The boundary conditions for the surface and bottom are given by the first Equation of (4.1.6) and (4.1.7), respectively. In the following, the processes which can (cannot) be realized with this $1D_\varrho$ approach are summarized:

- Internal shear is described by the vertical viscosity term of Equation (4.2.4a) (third term on the right side).
- The isopycnal surface or isopycnal layer thickness varies according to the vertical mass fluxes Φ^{in}_m and Φ^{out}_m.
- The shear forces between the isopycnal layers influence the transport rates between them.
- Thus, the horizontal derivatives of the velocity components (second and third terms of Equation (4.1.1a)) are neglected, advection cannot be calculated with this model.
- Gravitational transport is not modeled, but the influence of gravitational effects can be prescribed by the pressure gradient formulation of Equation (4.2.2).

4.2.1 Numerical Approximation

The time discretization for the governing equations is realized with the semi-implicit method, which is described for an isopycnal hydrodynamic model in Casulli [1997]. The space is already vertically discretized by ϱ-coordinates and the horizontal space is extended infinitely; the time discretization is described in this section. The density layers or isopycnal layers are variable in vertical space and time. The ϱ-layers can appear and disappear or, in other words, can be dry or wet but the maximum number of M layers and their specific density are predefined. The discrete notations of the indices of the isopycnal layers are as follows

$m = m^n_0, \ldots, M^n$	isopycnal layer from bottom to surface
m^n_b	next active isopycnal layer below the m-th layer
m^n_t	next active isopycnal layer above the m-th layer
M	total number of the isopycnal layers

where n denotes the time step. An overview of the vertical structure of the model is given in the left panel of Figure 22. The thickness of an isopycnal layer m is defined by

$$\Delta\eta_m^n = \eta_m^n - \eta_{m-1}^n \begin{cases} > 0 & \text{active layer} \\ = 0 & \text{non-active layer.} \end{cases} \tag{4.2.5}$$

The **momentum equations** are divided into an implicit and an explicit part to determine the velocities of the new time step $n+1$. The vertical viscosity term is solved implicitly because the bottom and surface stresses are known quantities. This leads to the following equation for the unknown velocity of the isopycnal layer m

$$u_m^{n+1} = F\left(u_m^n\right) + \frac{\Delta t}{\Delta\eta_m^n}\left[\nu_{m+1/2}^{v,n}\frac{u_{m+1}^{n+1} - u_m^{n+1}}{\Delta\eta_{m+1/2}^n} - \nu_{m-1/2}^{v,n}\frac{u_m^{n+1} - u_{m-1}^{n+1}}{\Delta\eta_{m-1/2}^n}\right] \tag{4.2.6}$$

derived from the momentum equations (4.2.1). The horizontal velocity is calculated in the center of an isopycnal layer. The locations of the calculated quantities are indicated in the vertical structure of Figure 22 (right panel).
The boundary condition for the vertical shear at the free surface is taken as

$$\nu_{M^n+\frac{1}{2}}^{v,n}\frac{u_{M^n+1}^{n+1} - u_{M^n}^{n+1}}{\Delta\eta_{M^n+\frac{1}{2}}^n} = \gamma_a^{n+1}\left(u_a^{n+1} - u_{M^n}^{n+1}\right) \tag{4.2.7}$$

and the bottom boundary condition is described by

$$\nu_{m_0^n-\frac{1}{2}}^{v,n}\frac{u_{m_0^n}^{n+1}}{\Delta\eta_{m_0^n-\frac{1}{2}}^n} = \gamma_b^{n+1}u_{m_0^n}^{n+1}. \tag{4.2.8}$$

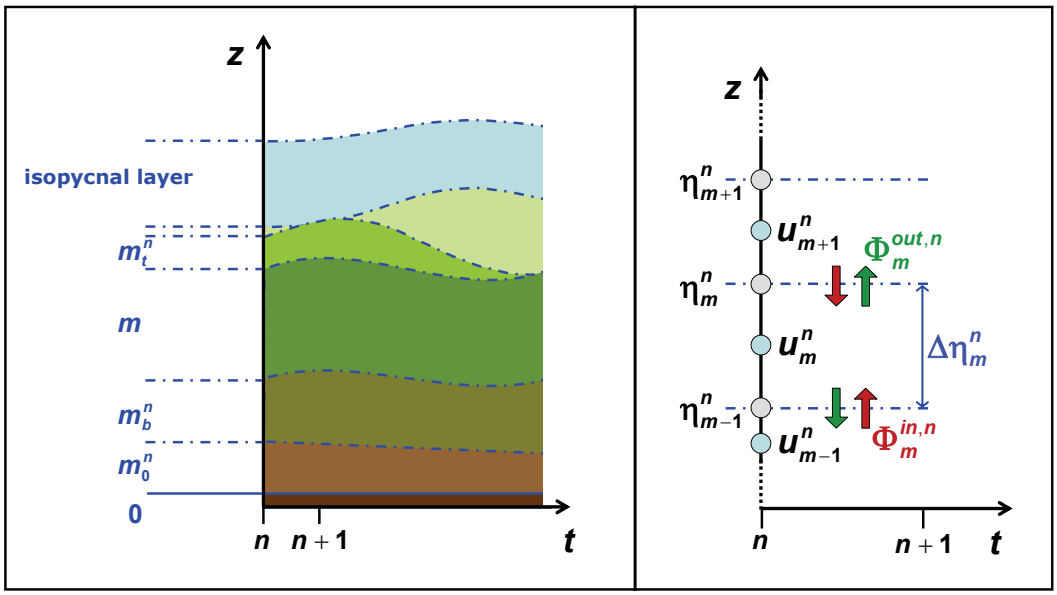

Figure 22: *Scheme of the $1D_\varrho$ isopycnal model vertically resolved by ϱ-layers.*
The left panel indicates the index notation of the vertical discretization. The isopycnals can vanish and reappear and their thickness can vary with time. The right panel shows the locations of the quantities which will be determined in the vertical structure.

The function $F\left(u_m^n\right)$ (first term of Equation (4.2.6)) contains all explicit and known terms from the momentum equations. The explicit function can be written as

$$F\left(u_{k,m}^n\right) = u_m^n - \frac{\Delta t}{t_r}\left(\bar{u}^n - \bar{u}^{p,n+1}\right) - \frac{\tau_w^{n+1} - \tau_b^{n+1}}{\bar{\varrho}\left(\eta_{M^n}^n - \eta_0^n\right)}. \tag{4.2.9}$$

The second and third terms represent the prescribed forcing.

The surface elevation of the m-th layer at time step $n+1$ can be determined from the **free surface equation** (4.2.3) by

$$\eta_m^{n+1} = \eta_m^n + \Delta t\left(\Phi_m^{in,n} - \Phi_m^{out,n}\right). \tag{4.2.10}$$

Finally, a linear system of $2M$ equations is obtained with the unknowns η_m^{n+1} and u_m^{n+1}. The way to a solvable system is described in the next section.

4.2.2 Solution Algorithm

In the previous section, the differential isopycnal Reynolds-averaged Navier-Stokes equations ($1D_\varrho$) were applied to a semi-implicit discretization scheme. The linear system of the discretized governing equations (4.2.6) and (4.2.10) is transferred to a more clearly matrix notation.

The discretized formulation of the **momentum equation** (4.2.6) needs to be manipulated by multiplying it by the layer thickness $\Delta\eta_m^n$ and moving parts of the pressure term and the viscous term to the left side

$$\Delta\eta_m^n u_m^{n+1} - \Delta t\left[\nu_{m+1/2}^{v,n}\frac{u_{m+1}^{n+1} - u_m^{n+1}}{\Delta\eta_{m+1/2}^n} - \nu_{m-1/2}^{v,n}\frac{u_m^{n+1} - u_{m-1}^{n+1}}{\Delta\eta_{m-1/2}^n}\right] = \Delta\eta_m^n F\left(u_m^n\right) \tag{4.2.11}$$

Some reorganization of the left side leads to

$$\begin{aligned}&\left(\Delta\eta_m^n + \frac{\Delta t\nu_{m+1/2}^{v,n}}{\Delta\eta_{m+1/2}^n} + \frac{\Delta t\nu_{m-1/2}^{v,n}}{\Delta\eta_{m-1/2}^n}\right)u_m^{n+1}\\ &-\frac{\Delta t\nu_{m+1/2}^{v,n}}{\Delta\eta_{m+1/2}^n}u_{m+1}^{n+1} - \frac{\Delta t\nu_{m-1/2}^{v,n}}{\Delta\eta_{m-1/2}^n}u_{m-1}^{n+1} = \Delta\eta_m^n F\left(u_m^n\right)\end{aligned} \tag{4.2.12}$$

and permits a matrix notation for the normal velocity u_m^{n+1} and the vertical viscosity components for an intermediate layer m

$$a_{m,m}^n = \Delta\eta_m^n + \frac{\Delta t\nu_{m+1/2}^{v,n}}{\Delta\eta_{m+\frac{1}{2}}^n} + \frac{\Delta t\nu_{m-\frac{1}{2}}^{v,n}}{\Delta\eta_{m-\frac{1}{2}}^n} \quad \text{and} \quad a_{m,m\pm1}^n = -\frac{\Delta t\nu_{m\pm\frac{1}{2}}^{v,n}}{\Delta\eta_{m\pm\frac{1}{2}}^n}. \tag{4.2.13}$$

The matrix formulation for the set of M^n momentum equations results in

$$\mathbf{A}^n \cdot \mathbf{U}^{n+1} = \mathbf{G}^n. \tag{4.2.14}$$

The newly-established matrices are described in the following. For simplicity, the adjacent isopycnal layers above or below the m-th layer are defined as $m \pm 1$ which indicates

- the next active layer if the matrix only considers active isopycnals $(m_0^n, \ldots, M^n)$ or
- the next layer, regardless of whether it is active or non-active, if all defined isopycnals $(1, \ldots, M)$ are considered.

The matrix for the unknown horizontal velocities is specified by

$$\mathbf{U}^{n+1} = \begin{bmatrix} \mathbf{u}_{M^n}^{n+1} \\ \vdots \\ \mathbf{u}_{m}^{n+1} \\ \vdots \\ \mathbf{u}_{m_0^n+1}^{n+1} \\ \mathbf{u}_{m_0^n}^{n+1} \end{bmatrix}. \tag{4.2.15}$$

This vector has the size M^n. The explicit terms are all combined in the vector $\mathbf{G}^n$ which has the following form

$$\mathbf{G}^n = \begin{bmatrix} \Delta\eta_{M^n}^n F\left(u_{M^n}^n\right) + \Delta t \cdot \gamma_a^{n+1} \cdot u_{a,M^n+1}^{n+1} \\ \vdots \\ \Delta\eta_m^n F\left(u_m^n\right) \\ \vdots \\ \Delta\eta_{m_0^n}^n F\left(u_{m_0^n}^n\right) \end{bmatrix}. \tag{4.2.16}$$

and has the same size as the velocity vector $\mathbf{U}^{n+1}$. The wind friction is taken into account for the free surface layer M^n.
The vertical viscosity term leads to a tridiagonal block matrix of $M^n \times M^n$ inner matrices

$$\mathbf{A}^n = \begin{bmatrix} a_{M^n,M^n}^n & a_{M^n,M^n-1}^n & & \cdots & 0 \\ a_{M^n-1,M^n}^n & a_{M^n-1,M^n-1}^n & a_{M^n-1,M^n-2}^n & & \vdots \\ & \ddots & & & \\ & a_{m,m+1}^n & a_{m,m}^n & a_{m,m-1}^n & \\ & & \ddots & & \\ \vdots & & a_{m_0^n+1,m_0^n+2}^n & a_{m_0^n+1,m_0^n+1}^n & a_{m_0^n+1,m_0^n}^n \\ 0 & \cdots & & a_{m_0^n,m_0^n+1}^n & a_{m_0^n,m_0^n}^n \end{bmatrix}. \tag{4.2.17}$$

Each row of the matrix represents a specific isopycnal layer. The component for the surface layer M^n is given by

$$a_{M^n,M^n} = \Delta\eta^n_{M^n} + \gamma_a^{n+1}\Delta t + \frac{\Delta t \nu^{v,n}_{M^n-\frac{1}{2}}}{\Delta\eta^n_{M^n-\frac{1}{2}}} \tag{4.2.18}$$

and for the bottom layer m_0^n by

$$a_{m_0^n,m_0^n} = \Delta\eta^n_{m_0^n} + \frac{\Delta t \nu^{v,n}_{m_0^n+\frac{1}{2}}}{\Delta\eta^n_{m_0^n+\frac{1}{2}}} + \gamma_b^{n+1}\Delta t. \tag{4.2.19}$$

The components $a^n_{m,m-1}$ and $a_{m,m+1}$ of the secondary diagonals of matrix $\mathbf{A}^n$ are related due to $a^n_{m\pm1,m} = a^n_{m,m\pm1}$. All components of matrix $\mathbf{A}^n$ are non-negative values. Therefore, the eigenvalues of the tridiagonal symmetric matrix which correspond to the values of the main diagonal are also non-negative. The matrix can be classified as positive definite.

The composition of M **free surface equations** (4.2.4b) can be transformed into the matrix notation by

$$\mathbf{S}^{n+1} = \mathbf{S}^n + \Delta t \mathbf{P}^n \tag{4.2.20}$$

which is a linear system of M equations. The isopycnal elevation matrix is an one-dimensional matrix

$$\mathbf{S}^{n+1} = \begin{bmatrix} \eta_M^{n+1} \\ \eta_{M-1}^{n+1} \\ \vdots \\ \eta_m^{n+1} \\ \vdots \\ \eta_1^{n+1} \end{bmatrix}. \tag{4.2.21}$$

The vector $\mathbf{P}^n$ contains the transport rates at the isopycnal interfaces

$$\mathbf{P}^n = \begin{bmatrix} \Phi_M^{in,n} - \Phi_M^{out,n} \\ \Phi_{M-1}^{in,n} - \Phi_{M-1}^{out,n} \\ \vdots \\ \Phi_m^{in,n} - \Phi_m^{out,n} \\ \vdots \\ \Phi_1^{in,n} - \Phi_1^{out,n} \end{bmatrix}. \tag{4.2.22}$$

Both vectors have the size M comprising all defined isopycnal layers because inflow enables a non-active layer to become active by diapycnal transport. By contrast, outflow can only origin from an active layer.

The matrix notation leads to two linear equations

$$\mathbf{U}^{n+1} = (\mathbf{A}^n)^{-1}\,\mathbf{G}^n \tag{4.2.23a}$$

$$\mathbf{S}^{n+1} = \mathbf{S}^n + \Delta t \mathbf{P}^n \tag{4.2.23b}$$

which can be directly solved for the horizontal velocities u_m^{n+1} (first equation) and the isopycnal elevations η_m^{n+1} (second equation) of the new time step.

4.3 Diapycnal Mass Transfer

The simulation of vertical exchange processes such as deposition, erosion, entrainment and consolidation is related to changes in the density gradient over depth. From the isopycnal point of view, this requires an adjustment of isopycnal layers and implies growth and reduction of the thickness of the density layers as well as their formation and disappearance. These mechanisms are realized due to mass and volume transfer between the isopycnal layers by simultaneous conservation of mass and volume.

The isopycnal layers are coupled through momentum exchange and interact due to internal shear stresses at their interfaces in the isopycnal model presented above. In the following, the isopycnal model approach will be extended to include mass exchange between isopycnal layers by considering a purely isopycnal approach with $N_z = 1$. Without these transfers, every isopycnal layer would act in the same way as a two-dimensional hydrodynamic model.

The concept for diapycnal mass transfer by coinstantaneous volume conservation is an adjustment of the adjacent interface. Mass transfer from one layer to the next is connected to a specific volume of suspension. For example, the mass $(P \cdot \Delta t \cdot \Phi_{m,m+1} \cdot \varrho_m)$ transferred from layer m to layer $m+1$ is connected to the volume $(P \cdot \Delta t \cdot \Phi_{m,m+1})$, where $\Phi_{m,m+1}$ is a transport rate from layer m to layer $m+1$ with the unit m/s. The position of the interface $(m, m+1)$ changes according to this volume. Because of the lower density in layer $m+1$, the volume loss of layer m is greater than the volume increase of layer $m+1$

$$P \cdot \Delta t \cdot \Phi_{m,m+1} \neq P \cdot \Delta t \cdot \Phi_{m,m+1} \cdot \frac{\varrho_m}{\varrho_{m+1}} \tag{4.3.1}$$

with continuous mass flow at the interface. To fulfill volume conservation, an adjustment of this mass difference is achieved by balancing the fluxes at the interface concerned and the next neighboring interface. In the case of downward flux from layer m to layer $m-1$, the depth of layer m decreases and layer $m-1$ increases. For mass conservation, the position of the interface above $(m, m+1)$ is adjusted and compensates the mass difference. The depth of the $(m+1)$-th layer also increases.

This concept leads to the restriction of a minimum of three defined isopycnal layers. In the following Section 4.3.1, a solution for the mass transfer in a three-layer system is

demonstrated. This solution is extended to an arbitrary number of isopycnal layers in Section B.

4.3.1 Basic Explicit Approach for Mass and Volume Balancing

A minimum of three layers is required for mass transfer. A system of a bottom layer of density ϱ_1, an intermediate suspension layer of density ϱ_2 and a clear water layer of density ϱ_3 is established. The stratification is stable with $\varrho_1 > \varrho_2 > \varrho_3$. The depth of the water column remains constant, but the interface between the free water surface and rigid bed is movable due to mass exchange, see Figure 23. This system only allows a primary mass flux from the bottom layer into the second layer and a downward mass flux from the second layer into the bottom layer. At the upper interface, only compensatory fluxes can apply because the top layer contains clear water.

Accordingly, the total depth remains constant while the layer thickness can change.

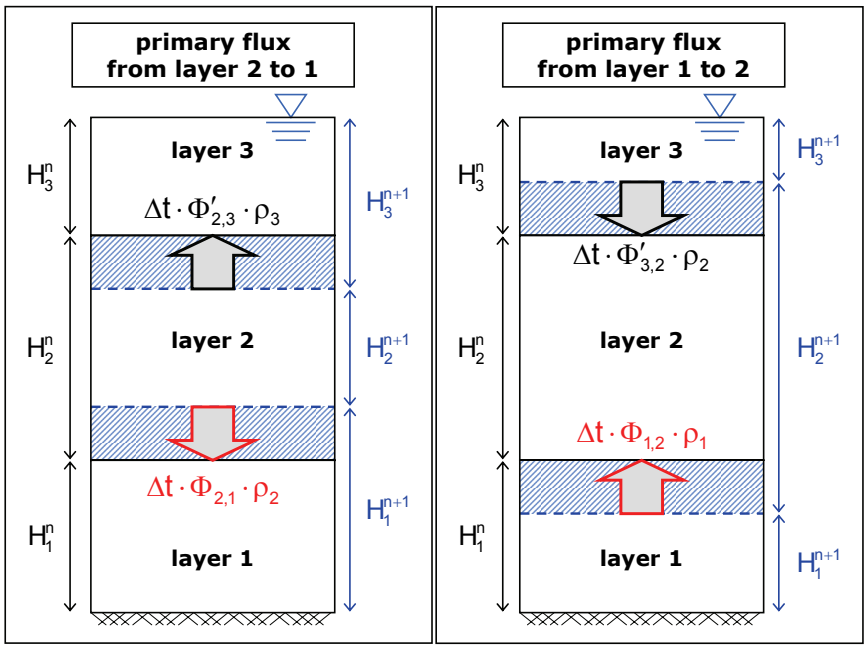

Figure 23: *Mass transfer approach for a mixed system and a stratified system based on a three-layer example with stable stratification constraint.*
Left panel: A three layer system is totally mixed when only the second layer is active. A deposition flux then leads to stratified system. This is gained by applying a flux from the second layer into the higher concentrated layer 1. At the same time, a compensatory flux is applied to the upper interface of layer 2 for volume and mass conservation. Thus, the thickness of the second layer decreases and the first and third layer increase accordingly until the layer thickness becomes zero. Right panel: A three layer system has the maximum degree of stratification when only the first and the third layer are active. The system starts to mix by applying an upward flux from the bottom layer. Then the second layer becomes active and increases with time. At the same time, the thickness of the first and third layer decreases. The compensatory flux from layer 3 into layer 2 is determined according to the volume and mass conservation demand.

This assumption guarantees volume conservation for the entire water column. The volume or layer thickness balance is

$$H_1^n + H_2^n + H_3^n = H_1^{n+1} + H_2^{n+1} + H_3^{n+1} \tag{4.3.2}$$

where the index n indicates the current time step and $n+1$ the new time step. There are two restrictions for a layer thickness. They are non-negative values ($H_m \geq 0$) and the layer thickness is not greater than the total depth of the water column

$$H_1, H_2, H_3 \leq \sum_{m=1}^{3} H_m \tag{4.3.3}$$

where H_m is the thickness of the m-th layer. Mass conservation is guaranteed by the following balance

$$P\left(H_1^n \cdot \varrho_1 + H_2^n \cdot \varrho_2 + H_3^n \cdot \varrho_3\right) = P\left(H_1^{n+1} \cdot \varrho_1 + H_2^{n+1} \cdot \varrho_2 + H_3^{n+1} \cdot \varrho_3\right) \tag{4.3.4}$$

where P is the area of the water column under consideration.

Two situations for primary fluxes are distinguished in this system. The first case starts with a fully uniform density ϱ_2 and stratifies due to downward mass transfer from layer 2 to the underlying layer 1, see left panel of Figure 23. This primary mass flux is the product of $\Phi_{2,1} \cdot \varrho_2$, where $\Phi_{2,1}$ represents the transport rate in m/s of the suspension ϱ_2. A compensatory flux $\Phi'_{2,3}$ from layer 2 to the next upper layer 3 must now be introduced for mass and volume conservation. The left side of Equation (4.3.4) is written in terms of the fluxes to determine the compensatory flux

$$\begin{aligned} \sum_{m=1}^{3} H_m^n \varrho_m &= \sum_{m=1}^{3} H_m^{n+1} \varrho_m \\ &= \left(H_1^n + \Delta t \Phi_{21}^n\right) \varrho_1 + \left(H_2^n - \Delta t \left(\Phi_{21}^n + \Phi_{23}^{\prime n}\right)\right) \varrho_2 + \left(H_3^n + \Delta t \Phi_{23}^{\prime n}\right) \varrho_3. \end{aligned} \tag{4.3.5}$$

The compensatory flux is now described

$$\Phi_{23}^{\prime n} = \Phi_{21}^n \frac{\varrho_2 - \varrho_1}{\varrho_3 - \varrho_2}. \tag{4.3.6}$$

as a function of the three layer densities concerned and the downward flux that causes it.

The second case is initially a fully stratified system, see right panel of Figure 23. For a three-layer system it means that only layer 1 and 3 are present at the beginning. When the mixing process begins, the in-between layer grows due to mass transfer from layer 1. The compensatory flux takes place at the upper interface, but goes from layer 3 to layer 2. The compensatory flux can be determined in a similar way and has the following form

$$\Phi_{32}^{\prime n} = \Phi_{12}^n \frac{\varrho_2 - \varrho_1}{\varrho_3 - \varrho_2}. \tag{4.3.7}$$

These are the compensatory fluxes for mass transfer at the interface $(1,2)$.
All the fluxes in the system under consideration have now been defined. The three layer thicknesses for the time step $n+1$ result in

$$H_1^{n+1} = H_1^n + \Delta t \left(+\Phi_{21}^n - \Phi_{12}^n\right) \tag{4.3.8a}$$

$$H_2^{n+1} = H_2^n + \Delta t \left(-\Phi_{21}^n + \Phi_{12}^n - \Phi_{21}^n \frac{\varrho_2 - \varrho_1}{\varrho_3 - \varrho_2} + \Phi_{12}^n \frac{\varrho_2 - \varrho_1}{\varrho_3 - \varrho_2}\right) \tag{4.3.8b}$$

$$H_3^{n+1} = H_3^n + \Delta t \left(+\Phi_{21}^n \frac{\varrho_2 - \varrho_1}{\varrho_3 - \varrho_2} - \Phi_{12}^n \frac{\varrho_2 - \varrho_1}{\varrho_3 - \varrho_2}\right). \tag{4.3.8c}$$

In the balance equation of the intermediate layer the first and second fluxes are located at interface $(1,2)$ and the third and fourth fluxes at interface $(2,3)$.

The example of three layers represents a special case. On the one hand, it consists of the minimum number of layers required for diapycnal mass transfer. On the other hand, the interface to be adjusted according to the primary flux can be clearly identified. The mass transfer approach is extended for the three-dimensional isopycnal model with $M \geq 3$ density layers in Appendix B.

4.4 Properties of the Numerical Method

The properties and restrictions of the $1D_\varrho$ model are as follows:

- uniform density for each isopycnal layer
- momentum exchange between isopycnal layers
- vertical mass exchange between isopycnal layers
- density stratification must always be stable
- drying and wetting of isopycnal layers
- vertical discretization with ϱ-layers
- shear dependent viscosity, which is calculated by a parameterized rheological approach
- interaction of the isopycnal layers due to interfacial shear
- no variation in horizontal direction (no advection, no horizontal internal shear stresses)
- reproduces only the vertical dynamic.

The simulation of fluid mud dynamics is realized in a similar way for the three-dimensional isopycnal model which permits investigations of the development, transport and formation of high-concentration layers in complex model domains. The numerical model is applied to verification test cases (Section 5) and to two model sections of the Ems Estuary (Section 6). This emphasizes the properties of the numerical method and the realization of the simulation of fluid mud dynamics. The applications are carried out with the 3D numerical model in x, y, ϱ-coordinates for unstructured grids. Readers interested in the details of the 3D isopycnal method are referred to Appendix A and Appendix B.

The basic properties of this three-dimensional model approach are summarized below:

- calculation on an unstructured grid
- uniform density for each isopycnal layer
- momentum exchange between isopycnal layers
- vertical mass exchange between isopycnal layers
- density stratification must always be stable
- drying and wetting of isopycnal layers
- vertical discretization with ϱ-layers
- a two-dimensional depth-averaged model results if only one isopycnal layer is defined
- shear dependent viscosity, which is calculated by a parameterized rheological approach
- interaction of the isopycnal layers due to interfacial shear

The numerical model approach presented in this thesis includes flooding and drying of the isopycnal layers. Layers, representing a suspension of a specific concentration such as fluid mud, are not necessarily active over the entire model domain.

The low-concentration isopycnal layers in particular may reach a thickness of several meters in estuaries. There, an additional z-layer discretization can support the vertical isopycnal discretization to achieve a better three-dimensional resolution. This will be worth considering in further investigations but, in the present thesis, the z-layers are negligible for high-concentration fluid dynamics. In this case, the density layer thicknesses of the highly concentrated suspensions are in the range of centimeters to decimeters where the isopycnal discretization is most effective. However, the numerical method for a three-dimensional unstructured isopycnal model vertically discretized by a combination

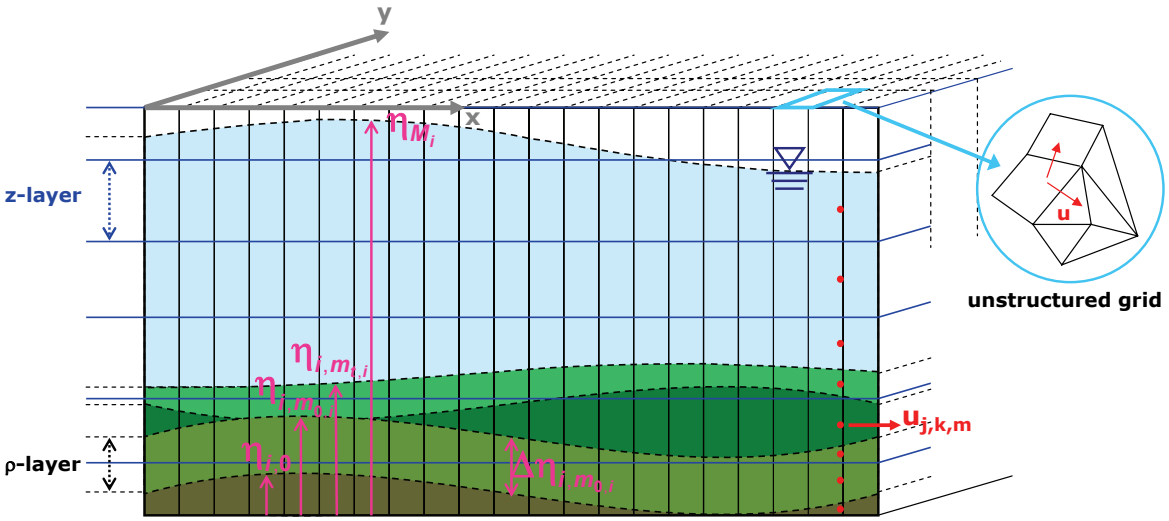

Figure 24: *Scheme of the 3D isopycnal model vertically resolved by z- and ϱ-layers.*
The vertical domain is discretized by isopycnal layers (ϱ-layer) and z-layers. An unstructured grid resolves the horizontal domain. The isopycnal surface is denoted by $\eta_{i,m}$ of the m-th layer and element i and the velocities $u_{j,k,m}$ are defined at the edge j of an element. The isopycnal layers can intersect a z-layer or vice versa. The isopycnals can vanish and reappear.

of z- layers and ϱ-layers is derived and presented in Appendix A. A scheme of this 3D numerical model is depicted in Figure 24. The 3D model in x, y, ϱ-coordinates results from this method by taking $N_z = 1$.

5 Model Verification and Performance

In this section, the functionality of the developments on the three-dimensional isopycnal numerical model is described. The numerical model is proved on the capability to reproduce particular processes, phenomena and the behavior of fluids and especially for fluid mud. Therefore, the test cases are kept as simple as possible and the model set-up is reduced to the physical process or phenomenon of interest.

The first verification test case (Section 5.1) deals with internal dynamics of stratified flows, where an analytical solution is compared to results of the numerical model. The propagation of internal waves is investigated at the boundary of two stably stratified layers in a basin. The second test case (Section 5.2) verifies the vertical transport approach. In a sedimentation tank transition from a totally mixed system to decomposition of the suspension by density dependent sedimentation is shown. Vertical and horizontal transport are considered in a stratified system of clear water and fluid mud layers with the third study (Section 5.3). In this case, entrainment is induced by movement of a fluid mud layer over a ground sill. The last two studies are more complex and focus on phenomenons of stratified and fluid mud flow. They show the different flow behavior of mud suspensions by considering the rheological viscosity. The last study (Section 5.4) demonstrates gravity-driven fluid mud flow down an inclined plane.
Some of these studies has already been presented in a former publication in Knoch and Malcherek [2011].

5.1 Interfacial internal Waves

In stratified flows with sharp vertical density gradients one expects internal waves at interfaces of density layers. The horizontal discretization scheme has to be verified for this phenomenon. The wave celerity c_w in stratified flows can be calculated analytically. Stokes developed a general approach for the propagation of waves. By considering an idealized system of two density layers, this approach can be simplified. The following assumptions are made [Lamb [1932]; Pond and Pickard [1983]]:

- an inviscid fluid, which implies shear free, turbulence free and friction free flow,
- a stable stratification,
- a sharp density gradient at the interface between the density layers (which is guaranteed due to the isopycnal approach),
- the isopycnal surface and interface are shear free, and
- the wave length must be much greater than layer-thicknesses (waves in shallow water).

The stratification has to be strong enough to damp turbulence totally and to achieve laminar flow, which is part of the assumptions for the analytical solution. This is fulfilled by a gradient Richardson number in the range of 0.1 to 0.3 and higher [Whitehouse et al., 2000], as determined from

$$Ri = \frac{g\,(\partial\varrho/\partial z)}{\varrho\,(\partial u/\partial z)^2} = \frac{g\Delta\varrho h_1}{\varrho\Delta u^2} \tag{5.1.1}$$

The density ϱ and the current velocity u are determined at depth z above the bottom. In Table 2 the gradient Ri-number is calculated for all applied test cases. It shows that the degree of stratification is high enough to reach a laminar flow state. The general solution for the wave celerity reduces now to

$$c_w = \sqrt{g h_1 h_2 \frac{|\varrho_1 - \varrho_2|}{\varrho_1 h_1 + \varrho_2 h_2}} \tag{5.1.2}$$

by regarding the assumptions above where h is the layer depth with index 1 for the lower layer and 2 for the upper layer.

Test	density of layer 1	density of layer 2	initial inclination	$\Delta\rho/\rho_1$	gradient Ri-number	analytical wave celerity	numerical wave celerity	deviation
	kg/m³	kg/m³	-	-	-	m/s	m/s	%
1	1005	1000	1/300	0.005	13.6	0.35	0.34	-3.48
2	1010	1000	1/300	0.010	18.6	0.49	0.48	-3.62
3	1030	1000	1/300	0.029	19.6	0.85	0.81	-4.34
4	1030	1000	1/600	0.029	19.6	0.85	0.83	-2.76
5	1080	1000	1/300	0.074	15.3	1.37	1.30	-5.54
6	1000.1	1000	1/300	0.0001	13.4	0.050	0.048	-3.42

Table 2: *Analytical and numerical results of the wave celerity for different test configurations.*

The model set-up for this test case consists of a basin of 600 m length and 1 m width with a horizontal discretization of 5 m. The total water depth is 10 m, and two density layers of 5 m depth each are defined. The initial interface of the two layers has a slope of 1/300; see first panel of Figure 25. With the start of the simulation, an interfacial wave propagates from right to left (second panel). After some time the wave reaches the left boundary and propagates backwards (third panel).

The wave celerity can be extracted from the time series of the interfacial movement at specific locations. This test case is performed with different density gradients at the interface; see second and third column of Table 2. Test cases 3 and 4 have the same density gradient, but case 4 starts with an interface slope of 1/600. In addition, the analytical and numerical wave celerities as well as their deviations are given in Table 2. The deviation varies between about -3 % and -5 %, so that the numerical results slightly underestimate the analytical solution.

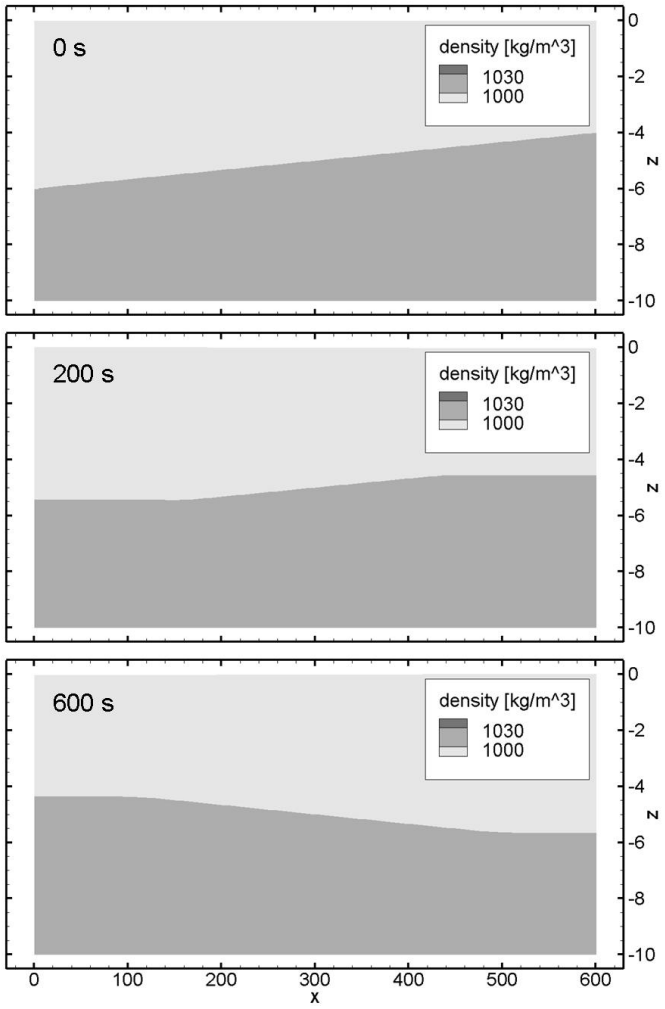

Figure 25: *Internal waves of test case 3 at initial state, 200 s and 600 s.*
The initial interface of the two fluids has a slope of 1/300. A standing wave is induced by gravitational forcing.

The time series of the interfacial elevation are shown in Figure 26. The diagrams show the interfacial movement at the left and the right boundary of the model over one wave period. A phase shift and a slightly decreasing amplitude can be observed which explains the calculated deviation. The underestimated analytical solution of the wave celerity indicates damping in the system, even though viscosity and friction were neglected. The reason for the deviations can be of geometrical origin as the width of the system is not infinite and horizontal discretization influences the numerical result. Thus, the deviations can be attributed to numerical dispersion. Mass transfer is neglected between isopycnal interfaces. Therefore numerical diffusion can be excluded for the isopycnal numerical approach. With test case 6 the stability of the system is tested by reducing the density difference to 0.1 kg/m^3. The numerical solution remains stable. The density difference could not be set to zero, because of the isopycnal approach.

The total mass and volume of the system is detected during the simulation. As an example it is drawn for test case 3 in the first panel of Figure 27. Than the accretion

and loss of them are calculated in relation to the initial total mass and volume (second panel). The model set up excludes mass exchange between the isopycnals, and there are no mass fluxes going in or out of the system. As a result there should be no change in total mass and volume. The mass losses in the order of 10^{-8} % can be attributed to computational accuracy and are small enough to be neglected.

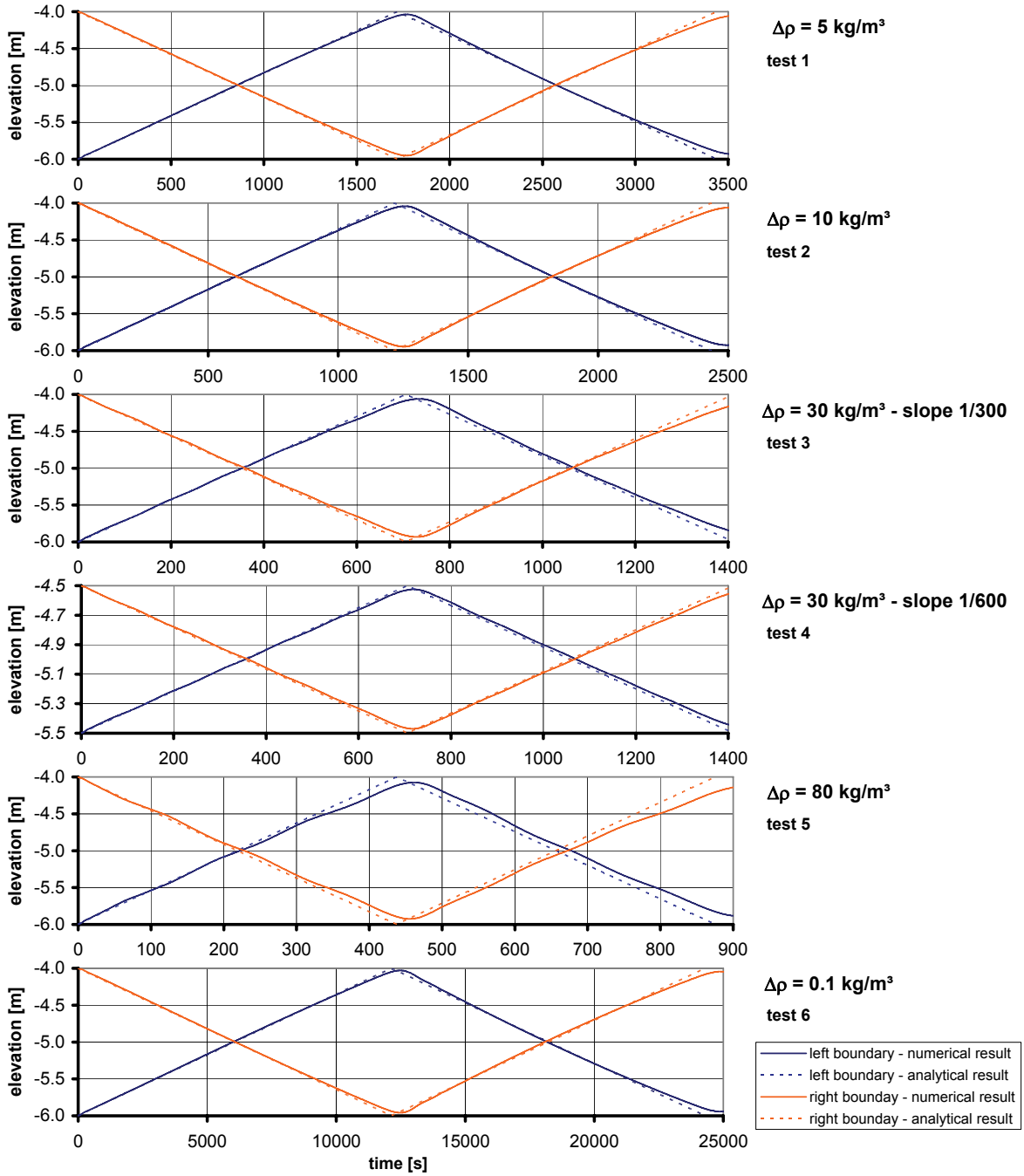

Figure 26: *Time series of the interfacial movement at the left (blue lines) and right boundary (orange lines).*
A phase shift and a decreasing amplitude can be observed in the simulation results in comparison to the analytical solution. The deviations increase with simulation time.

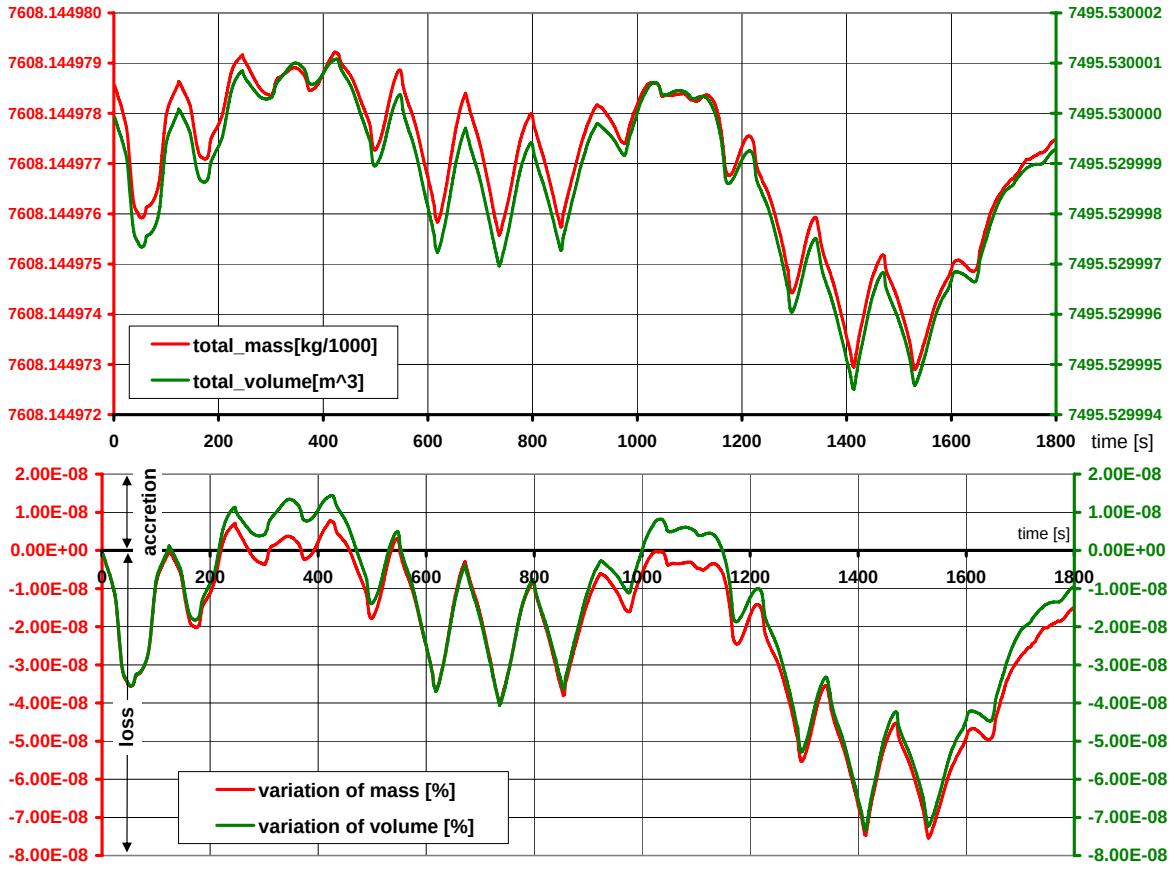

Figure 27: *Observation of the total mass and total volume during the simulation (test case 3). First panel: Changes of total mass and volume. Second panel: Variation of loss and accretion of the total mass and volume in percent. The model set up excludes mass exchange between the isopycnals, and there are no mass fluxes going in or out of the system. As a result there should be no change in total mass and volume. The deviations in the order of 10^{-8} % can be attributed to computational accuracy and are small enough to be neglected..*

5.2 Vertical Mass Transfer in a Sedimentation Tank

One class of vertical transport processes of mud suspensions are settling and deposition. Every vertical mass transport process affects the elevation of the isopycnal interfaces. In Section 4.3 a diapycnal mass transfer approach is introduced, which leads to an algorithm where layers can form, vanish or merge into each other. The performance of this algorithm is presented for a fully mixed system in a sedimentation tank. A stratification process is forced by mass fluxes which are obtained from a settling velocity approach (see Equation (3.7.3)) with hindered settling and a gelling concentration of 66.0 kg/m^3.

Although the full three-dimensional numerical approach is applied, the model set up and conditions result in a one-dimensional problem. There is only transport in z-direction considered, and the horizontal model dimension does not influence the result. So the complexity of the system is reduced to the considered process for verification of the implemented mass transfer approach.

Initially the tank of 10 m×0.5 m width, and 3 m height is filled with a suspension of 1025 kg/m^3 density. The model is set up with 35 isopycnal layers with a density range from 1000 kg/m^3 to 1050 kg/m^3. The simulation time step is 4 s. The density steps between the isopycnal layers are constant (1.5 kg/m^3). Figure 28 shows the vertical section at different times, in which every isopycnal layer has a different color. The first panel shows the initial state with a homogeneous suspension. After starting the simulation mass is transferred from top to bottom of the column. The suspension becomes more dense at the bottom and as a result new layers of increasing density are formed. At the same time the suspension dilutes at the surface by emerging layers of lower densities (compare the second to fifth panels).
The settling velocity approach (Equation (3.7.3)) which considers hindered settling produces an increase of the settling velocity up to a mud suspension density of 1008 kg/m^3. Further increase of the density, results in decreasing settling velocity. This leads to a non-uniform stratification in the water column. The clear water layer increases fast and at the bottom the denser layers increase rapidly during the first hours. But than the transport process slows down over time. Very thin emerging layers can be observed at the transition area between clear water and the intermediate layer of 1025 kg/m^3 density, see Figure 29.
The development of density distribution over time and depth is shown in Figure 30.

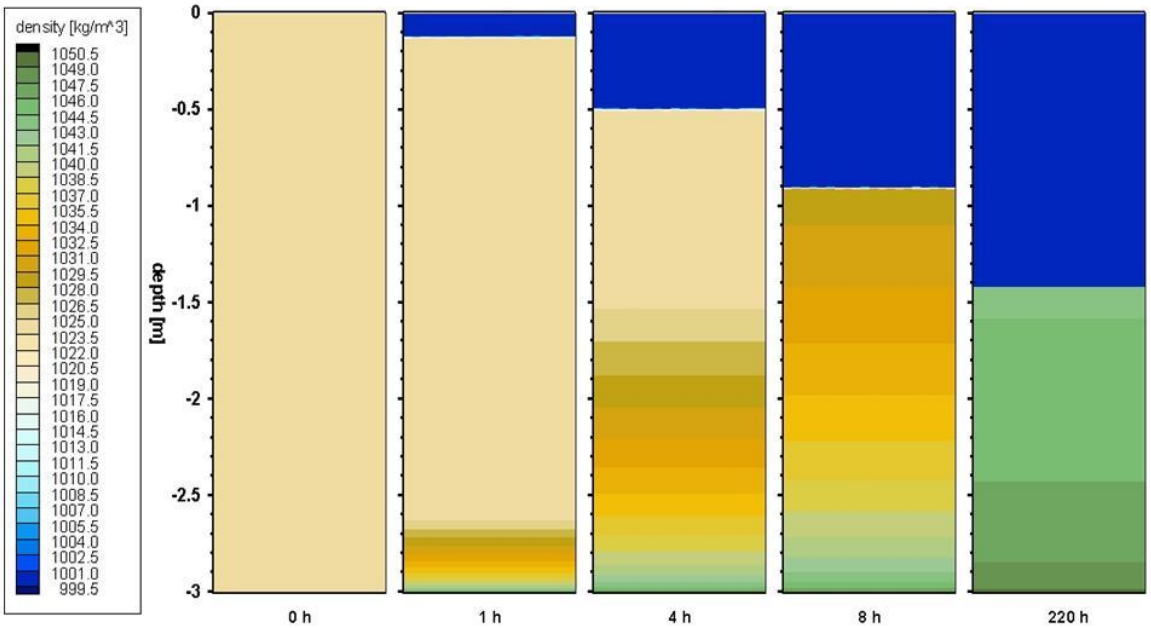

Figure 28: *Sedimentation tank at initial state and after a few hours.*
The model is set up with 35 predefined isopycnal layers with equal density differences between consecutive layers. The density classes correspond to the densities in the color scale. Initially the sedimentation tank is fully mixed. Settling starts by transferring mass into layers of higher densities near the bottom. The thickness of the clear water layer increases at the same time. The settling process slows down in the high-concentration region by virtue of hindered settling.

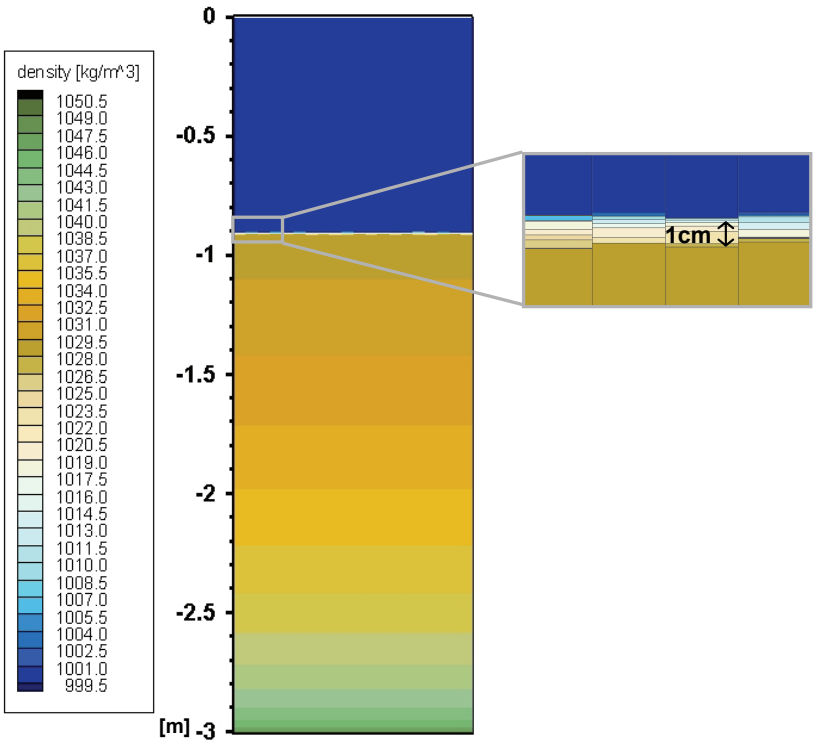

Figure 29: *Transition area between mud suspension layers and clear water layer. Very thin layer become active between the clear water layer and the higher concentration layers due to the mass exchange.*

Every step in the plots indicates a transition between density layers. Similar concentration profiles for hindered settling were gained from laboratory experiments with mud and mud-sand suspensions by Dankers [2006] and Toorman [1999]. These experiments show comparable results for sedimentation and self-weight consolidation of mud suspensions.

The presented results show, that merely by implementing a settling mechanism the isopycnal model is able to simulate a system such as a sedimentation tank. This example confirms that vertical transport processes can be reproduced by this mathematical approach in general. Mass fluxes are applied to the isopycnal interfaces and due to compensatory fluxes at the adjacent interface volume and mass conservation can be guaranteed. The mass and volume variation is analyzed by neglecting advection and the pressure term. With it the reason of deviations can be attributed to the vertical mass exchange only. The volume variation is lower than $5 \cdot 10^{-5}$ % and the mass variation is below $3 \cdot 10^{-4}$ % and tends to zero during the simulation.

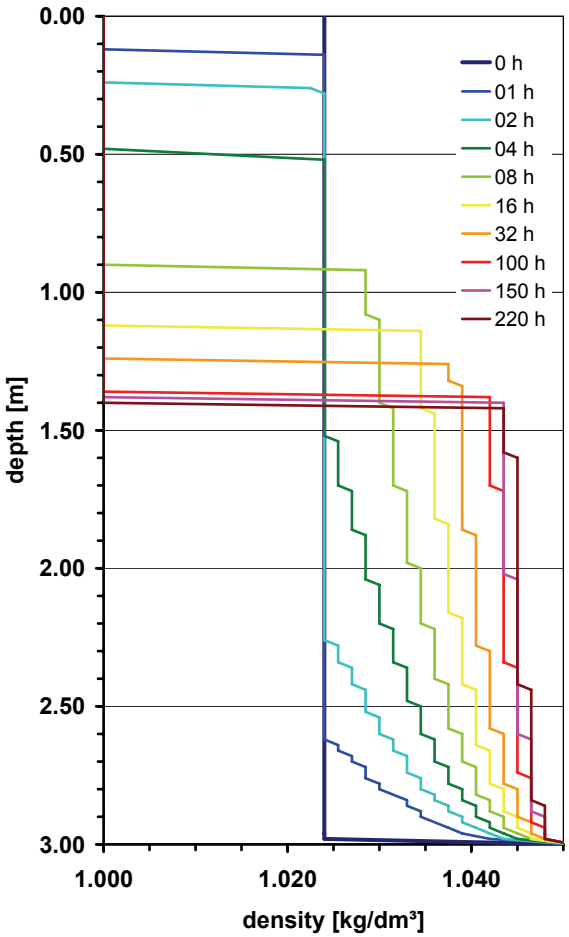

Figure 30: *Simulated density distribution over depth and time.*
Each graph indicates a new time step. The initial density distribution is constant over depth with 1025 kg/m^3. The stratification near the bottom increases with time due to the settling process. The interface between the clear water layer and the suspension layer drops down at the same time.

5.3 Flow over a Ground Sill

This test case examines the stratified flow over a ground sill by involving the physical process of entrainment. It is a two-dimensional problem in the x- and z-directions, whereas the process of the sedimentation tank (Section 5.2) was a one-dimensional problem in the z-direction. Both investigate the vertical mass transfer between isopycnals, but the present study also includes horizontal movement.

The model set-up consists of a 600 m long and 30 m wide channel. A 3 m high ground sill is located at 300 m along the length. The horizontal grid resolution is 5 m x 1.2 m. At the closed boundary on the left, a velocity is induced by the definition of a clear water source. At the open boundary on the right, the water surface and the isopycnal interfaces are kept at the initial level. This results in a flow direction from left to right, see Figure 31. Three different simulations are set up and they are described in Table 3. The initial system is defined by two density layers, these being a clear water layer and a

mud suspension layer at the bottom. The top and bottom layers are 7.5 m and 2.5 m thick respectively. This is the same in all three simulations, but the density gradients are different. The ground sill is illustrated in gray; it is not erodible.

simulation number	initial density gradient	rheological viscosity	entrainment	internal Courant number
(1)	1 kg/m^3	const. 10^{-6} m^2/s	no	0.06
(2)	80 kg/m^3	Worrall-Tuliani	no	0.55
(3)	80 kg/m^3	Worrall-Tuliani	yes	0.55

Table 3: *Simulation overview for the test case flow over a ground sill.*

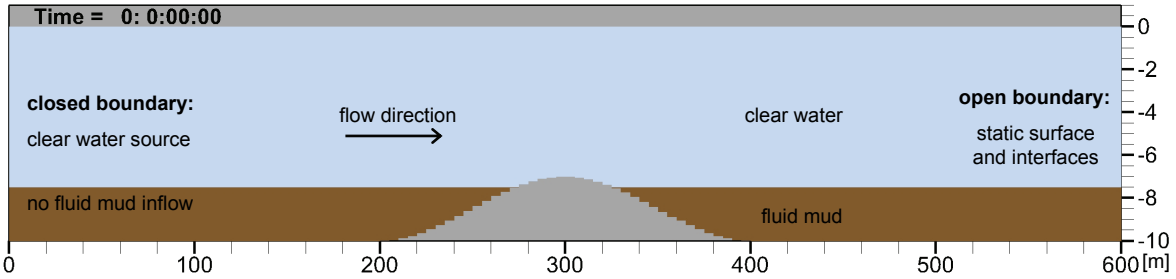

Figure 31: *Initial density distribution in a longitudinal cross-section.*
Flow is initiated by a clear water source at the right boundary whereas no fluid mud inflow occurs. The ground sill is indicated in gray.

The first simulation does not consider the rheological viscosity of mud suspensions and the density gradient is kept relatively small at 1 kg/m^3. This results in an internal Courant number of 0.06 with a time step of 1 s.
In the second simulation, a fluid mud layer is defined at the bottom with a density of 1080 kg/m^3, as shown in Figure 31. The internal Courant number increases to 0.55. The rheological properties of the fluid mud layer and the other suspension layers are now determined by the Worrall-Tuliani formulation of Equation (3.4.12). No turbulent viscosity is applied in this study.
In addition to the second simulation, the third simulation considers entrainment. There are six isopycnal layers defined by the densities 1000, 1010, 1030, 1045, 1060 and 1080 kg/m^3. Fluid mud is entrained into the overlying water layer by flowing over the ground sill. The entrainment rate is calculated by Equation (3.6.6) for the first entrainment case with a constant critical yield stress of 0.1 N/m^2 for the initiation of entrainment. Settling of fluid mud is neglected.

A low-stratified system is produced in simulation (1) by applying a density difference of 1 kg/m^3. The resulting velocity patterns are shown in Figure 32. The velocity is calculated as isopycnal layer-averaged quantity. The ground sill narrows the cross-section so that the flow accelerates in this region. Then, in simulation (2), the density

gradient is increased to 80 kg/m^3 and the viscosity is dependent on the sediment concentration and shear intensity instead of being constant. The velocity results are given in Figure 33. The movement of the bottom layer now becomes much slower and more viscous because of the higher density and rheological viscosity of that layer. It results in a strong stratified flow with high interfacial shear. The flow of the water body accelerates less above the ground sill compared with simulation (1) because the thickness of the fluid mud layer is nearly the same as the height of the ground sill. The fluid mud layer narrows the flow section over the total length and the flow increases over the total length. The velocity of the water body in simulation (2) is higher than in simulation (1) where the bottom layer moves with a velocity similar to that of the water layer.
Likewise, simulation (3) includes entrainment of the mud layer into the water layer. The density gradient and rheological viscosity approach are the same as in simulation (2) so that the velocity results are comparable, see Figure 34. At the beginning of the simulation, the fluid mud piles up in front of the ground sill (first three panels of Figure 35). The interfacial shear increases in this region in particular. Without applying the entrainment process, simulation (1) and (2), the bottom layer piles up in front of the ground sill and drops down behind it. After a while, the bottom layer overflows over the ground sill. The fluid mud layer now mixes into the water layer due to applied entrainment fluxes at the interface.

The shear rate intensity indicates the magnitude of the vertical velocity gradient between the isopycnal layers. As the shear intensity grows, the ability for entrainment and the entrainment rate itself both increase. Entrainment is realized due to mass transfer from the fluid mud layer to layers of lower concentration. This activates new isopycnal layers which emerge between the fluid mud and the clear water layer, see Figure 35. In front of the ground sill in particular the mixing process intensifies and the rheological viscosity decreases (compare last three panels of the Figures 36 and 35). Furthermore, a thin lower-concentration mud suspension layer appears along the channel. These lower-concentration layers now move with their own velocity above the fluid mud layer.

The Figures 37, 38 and 39 show the shear rate intensity of the three simulations. At the beginning of the simulation all three model set-ups show similar results for the shear intensity (first panel). The velocity gradient between the bottom and water layer is the lowest in simulation (1) where the shear rate intensity exceeds 0.009 s^{-1} in some regions only. The difference in the velocities of the water and the fluid mud body increases in simulation (2) and accordingly the shear rate intensity also increases. The magnitude hardly varies along the channel and increases temporarily in front of the ground sill. In simulation (3), fluid mud is entrained in regions where the shear rate intensity exceeds the internal resistance of the fluid mud which is dependent on the yield stress. Thin layers develop between the fluid mud and water layer due to entrainment. They produce

high shear intensities at the interface with the water layer ($>0.6\ s^{-1}$) because they move with their own velocity and have a very small thickness.

The study verifies that the implemented vertical mass transfer approach of Section 4.3 in combination with horizontal movement produces physically plausible results. However, comparison with field data is required for further validation of possible entrainment approximations.
Such ground sills of consolidated material are often found in front of harbor basins. They cause fluid mud accumulation inside the basin because of the depth difference. Moreover, they can also lead to resuspension of fluid mud as this example indicates.

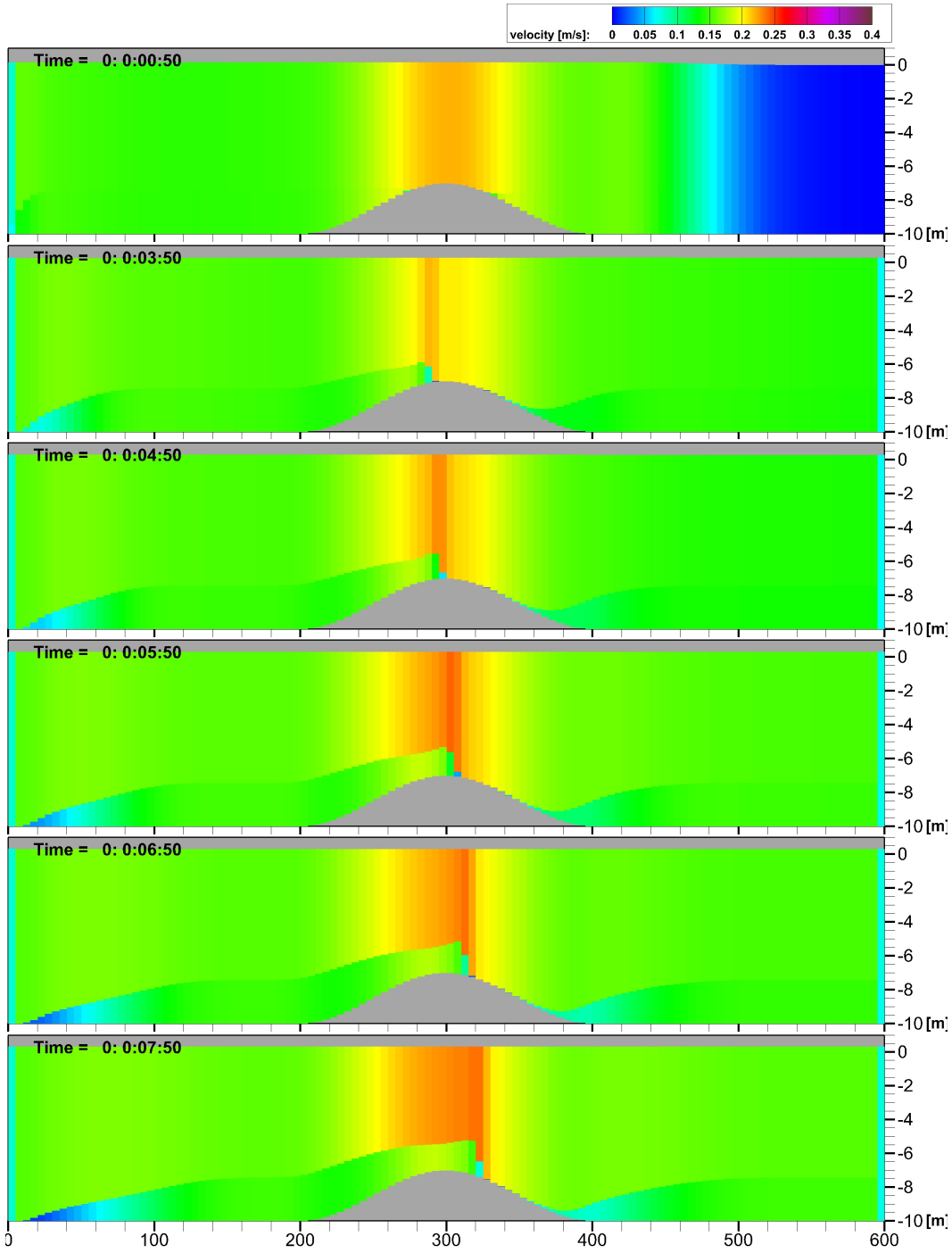

Figure 32: *Isopycnal layer-averaged velocity (absolute values) in the longitudinal cross-section of simulation (1) without constant viscosity, without entrainment and with low bottom layer density.*

The ground sill narrows the flow cross-section which accelerates the flow in this region.

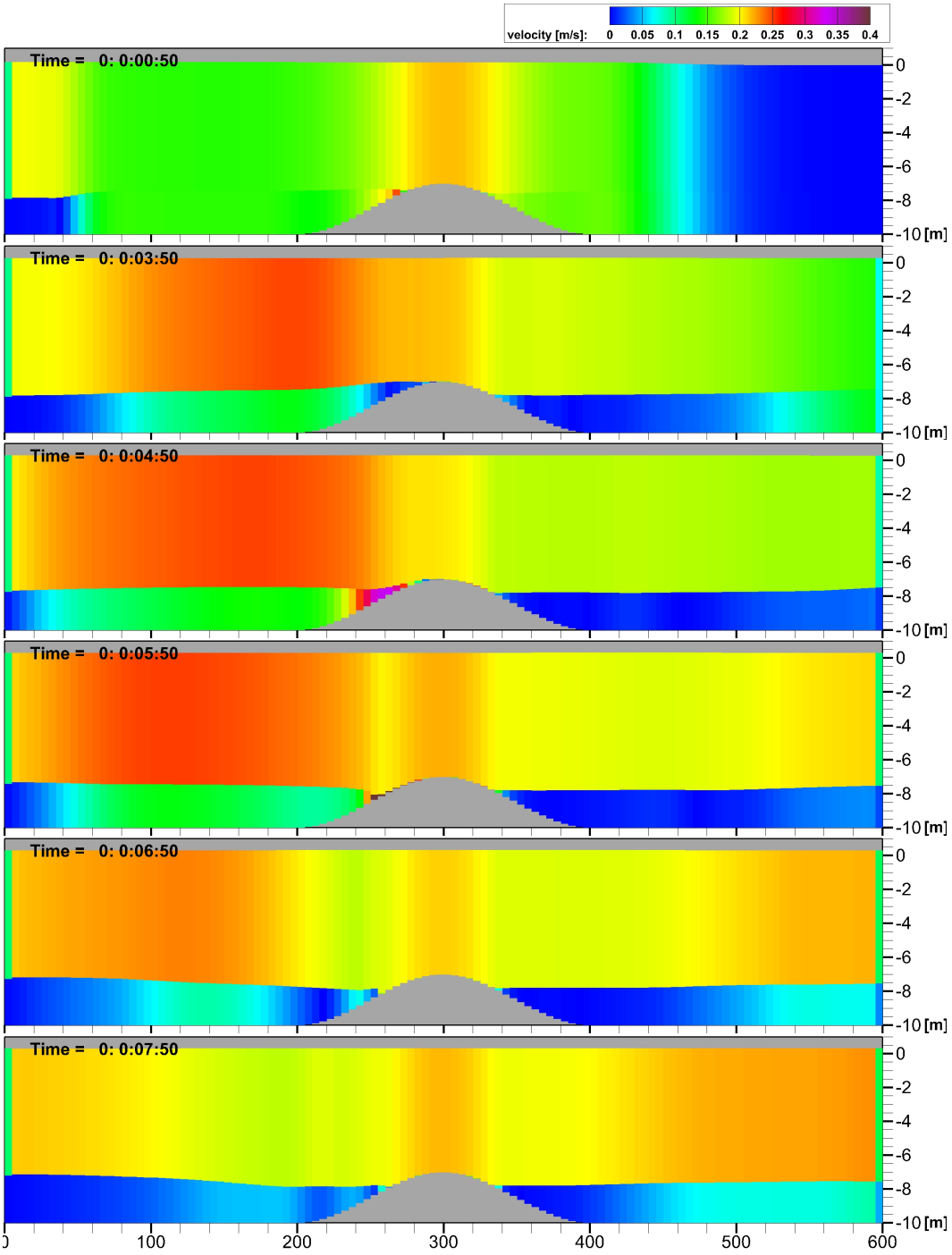

Figure 33: *Isopycnal layer-averaged velocity (absolute values) in the longitudinal cross-section of simulation (2) with rheological viscosity, without entrainment and with fluid mud as bottom layer.*

The fluid mud layer narrows the flow cross-section for the water layer over the total length of the channel. This increases the water layer velocity over the total length compared with simulation (1).

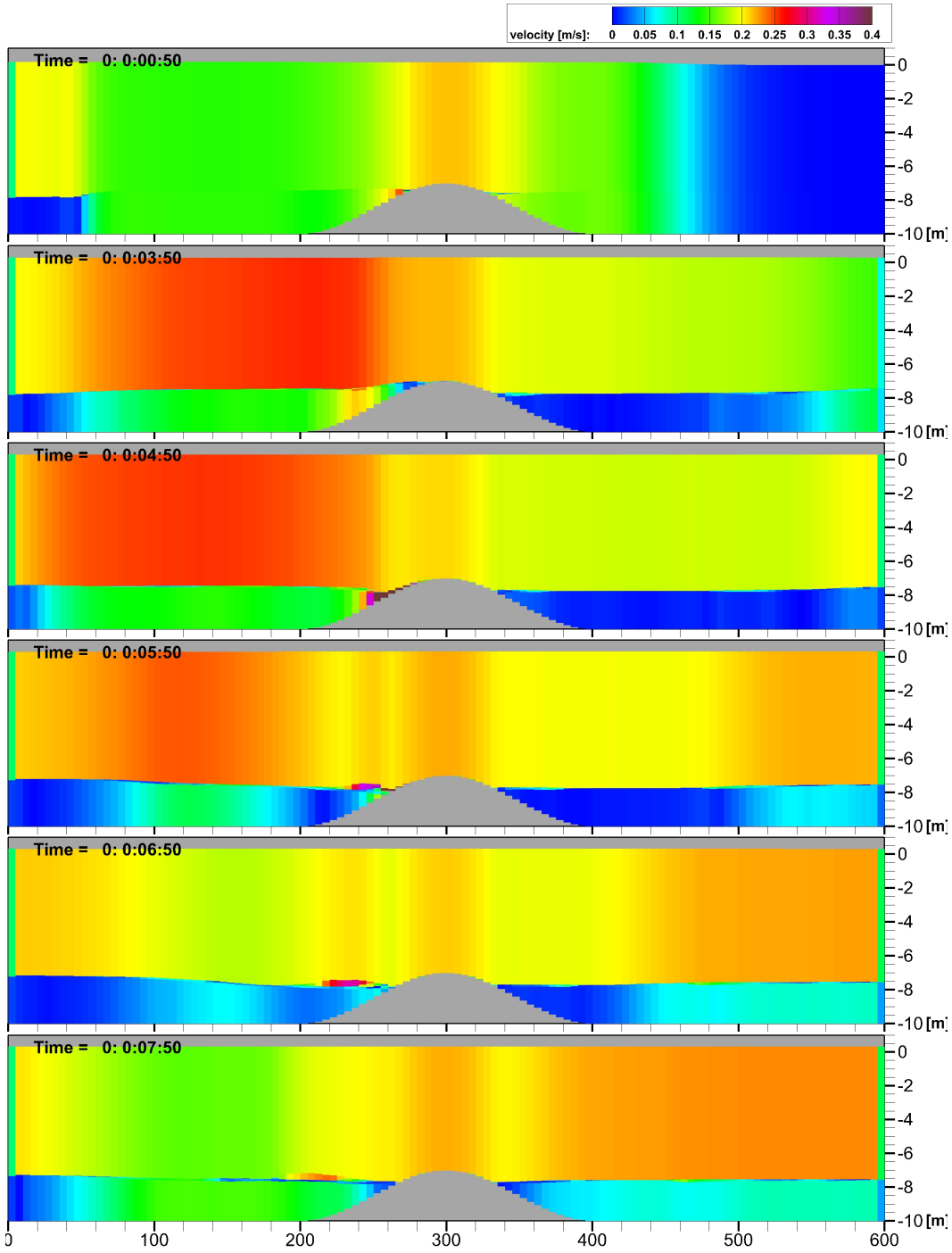

Figure 34: *Isopycnal layer-averaged velocity (absolute values) in the longitudinal cross-section of simulation (3) with rheological viscosity, with entrainment and with fluid mud as bottom layer.*

The stratified flow pattern are comparable to simulation (2), but here entrainment occurs in the region of the ground sill. New density layers appear and they move with their own velocity above the fluid mud layer.

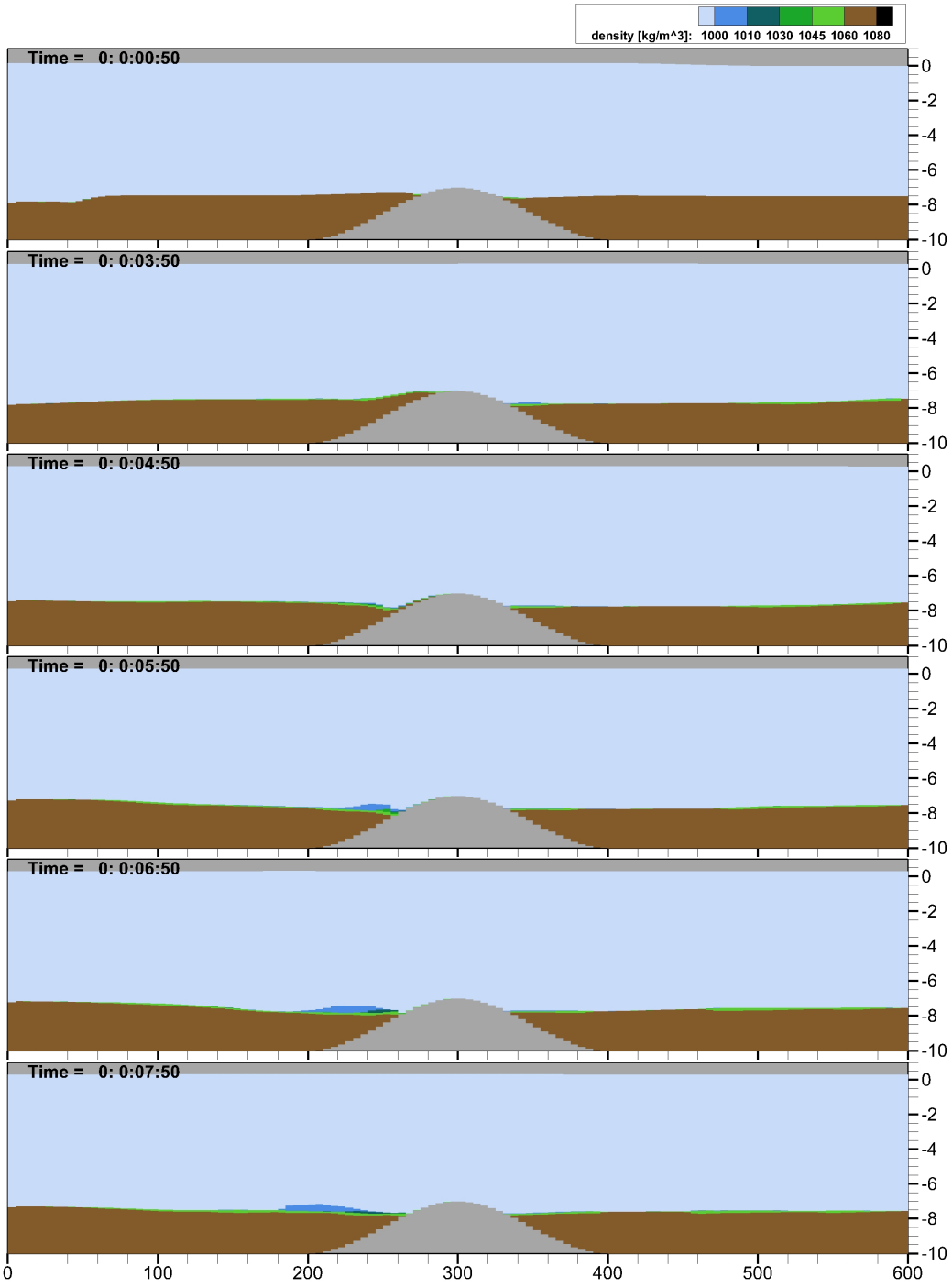

Figure 35: *Density distribution in the longitudinal cross-section of simulation (3). Increasing shear rates lead to entrainment in front of the ground sill where new isopycnal layers of lower density appear.*

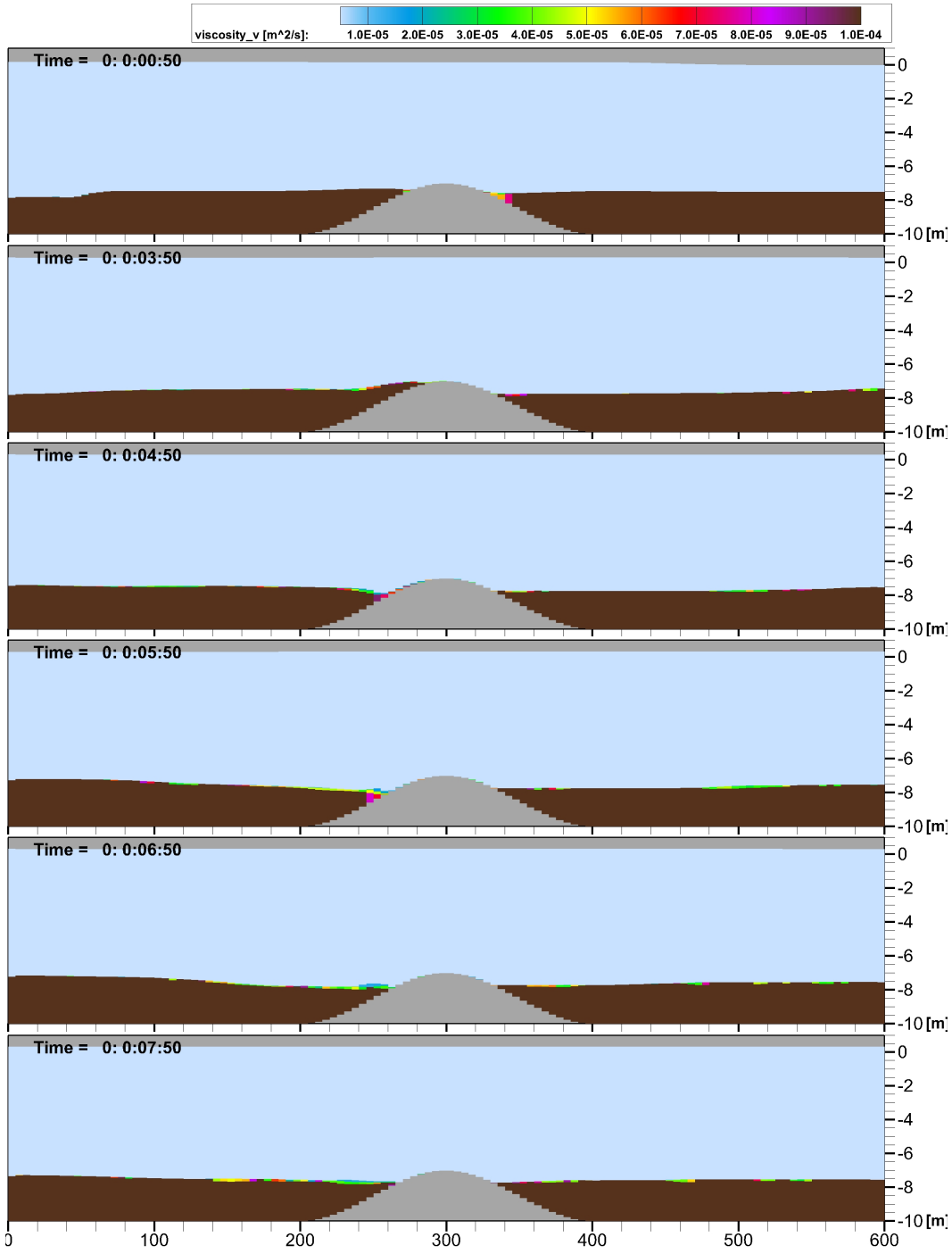

Figure 36: *Rheological viscosity in the longitudinal cross-section of simulation (3) with entrainment.*

New isopycnal layers of lower concentration appear due to entrainment with a decreased viscosity compared to the fluid mud layer.

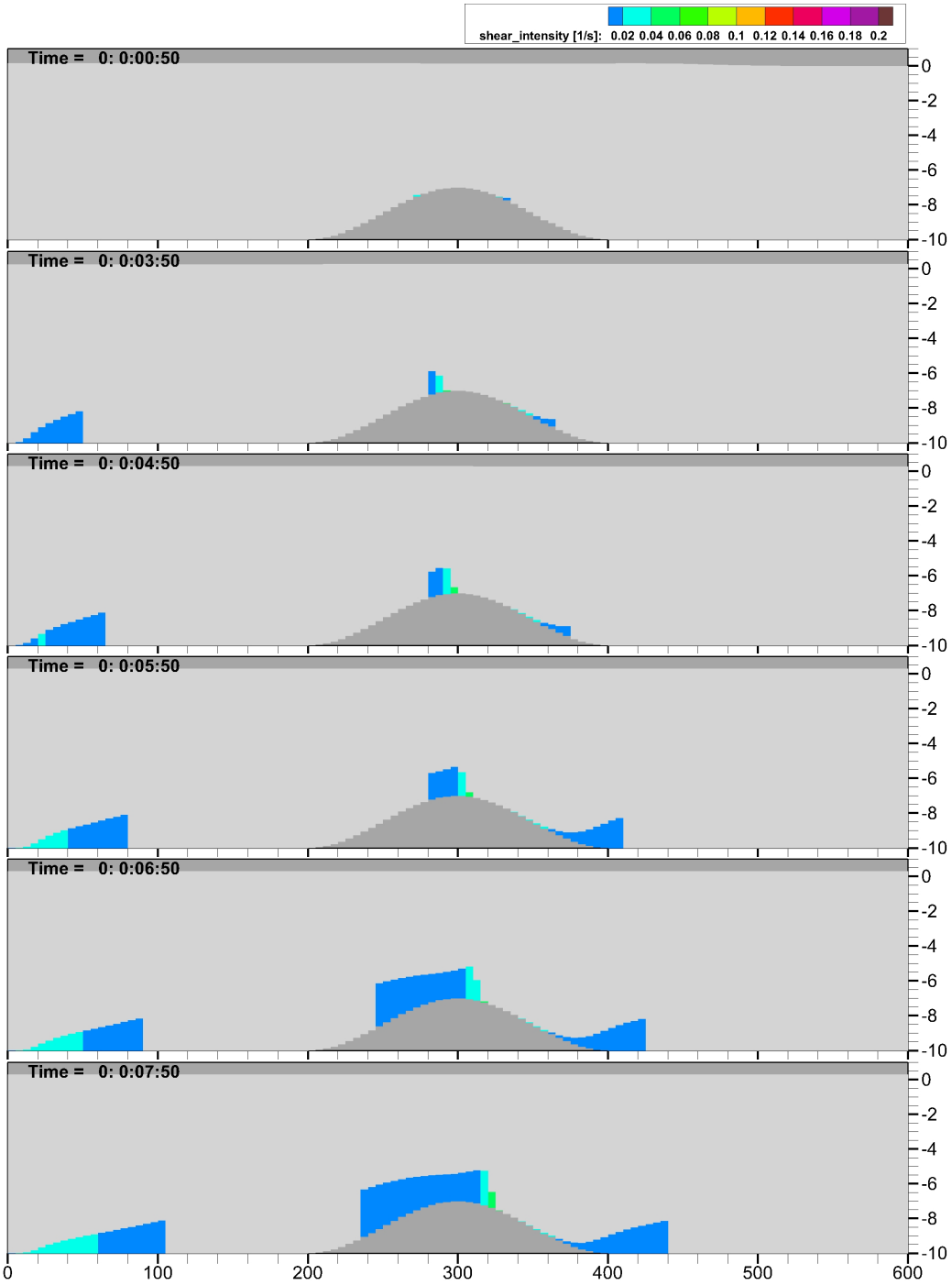

Figure 37: *Shear rate intensity in the longitudinal cross-section of simulation (1) without constant viscosity, without entrainment and with low bottom layer density.*

A small velocity gradient between bottom and top layer results in very low shear rate intensities (shear intensity lower than 0.009 s^{-1} is colored in light gray).

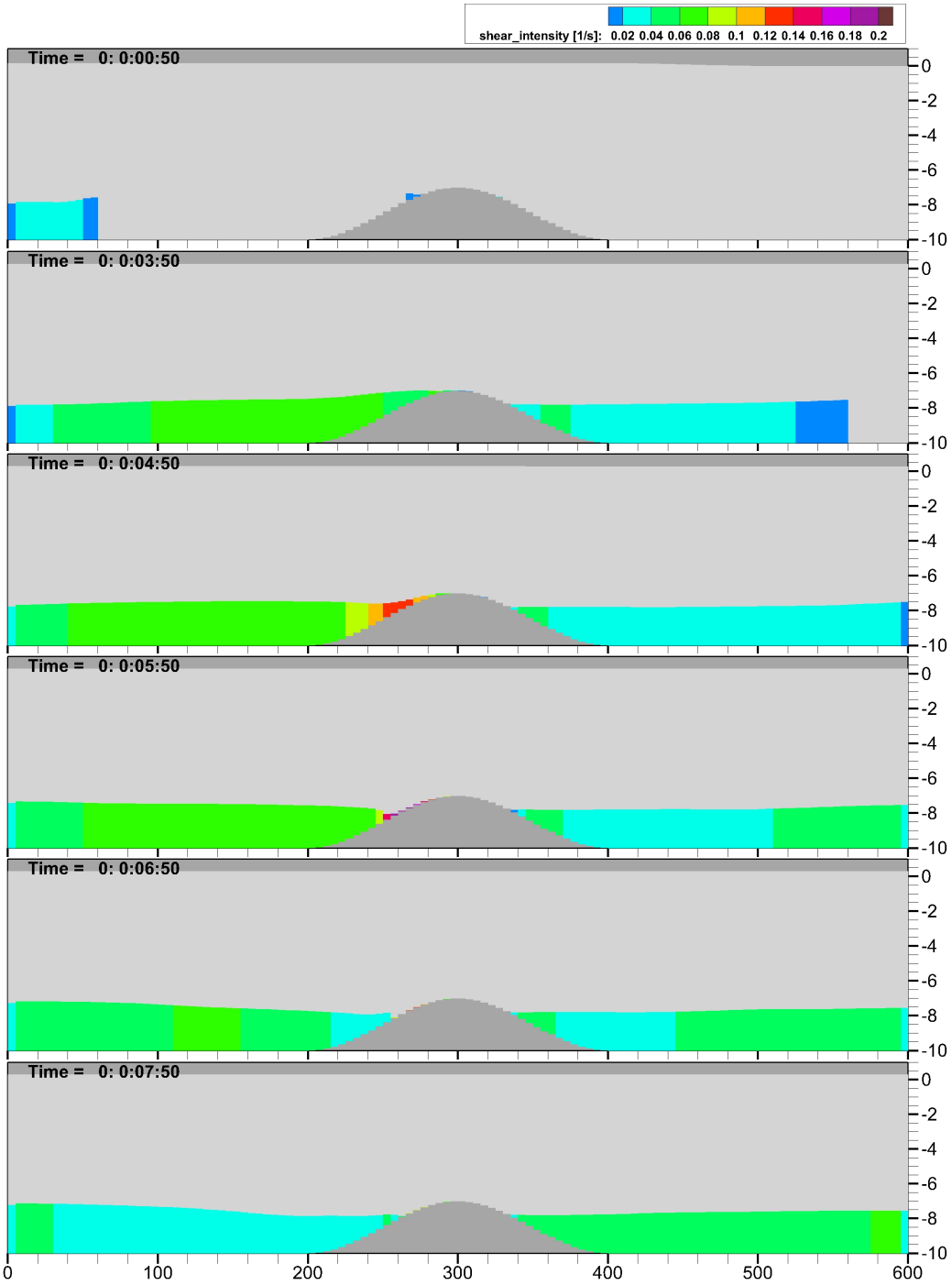

Figure 38: *Shear rate intensity in the longitudinal cross-section of simulation (2) with rheological viscosity, without entrainment and with fluid mud as bottom layer.*
The shear rate intensity increases with increasing differences in the velocities of the fluid mud and the water body, see Figure 33 (shear intensity lower than 0.009 s^{-1} is colored in light gray).

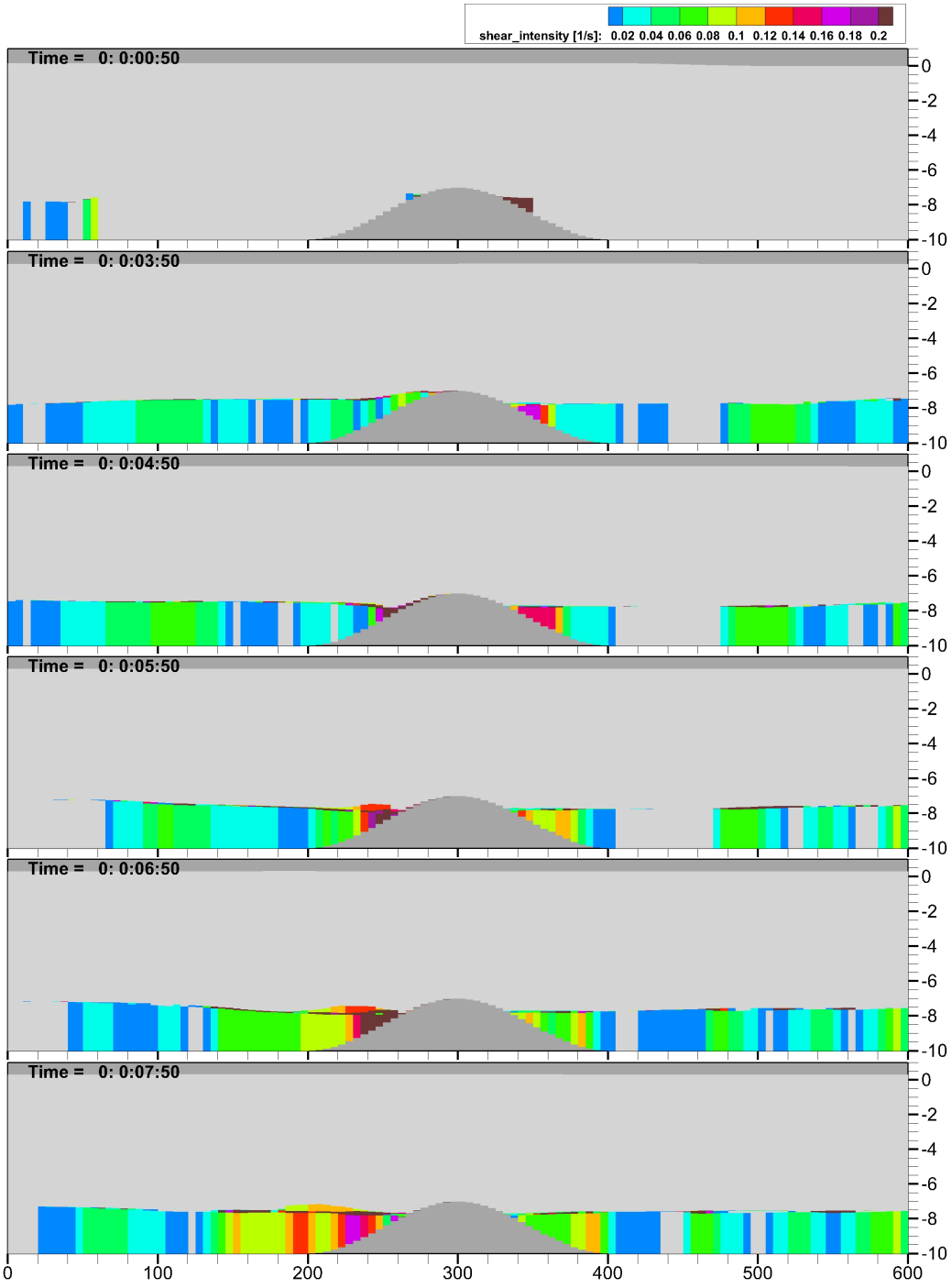

Figure 39: *Shear rate intensity in the longitudinal cross-section of simulation (3) with rheological viscosity, with entrainment and with fluid mud as bottom layer.*

Very thin density layers appear at the transition between fluid mud and clear water (shear intensity lower than 0.009 s^{-1} is colored in light gray).

5.4 Fluid Mud Movement on an Inclined Plane

In a channel with an inclined bed it will be demonstrated that the horizontal transport phenomena and the horizontal discretization scheme are capable of simulating the flow of fluid mud. The straight channel is set up with a slope of 0.1 %. Four mud suspensions of different concentrations are discharged at the left boundary and flow down the slope. The predefined densities of these isopycnal layers vary in four different model set-ups. They are given in Table 4. Gravity flow and the effects of the fluid mud rheology are studied on different scenarios of simulation (1) and on a comparison of simulations (1) to (4) with different density distributions. These processes will be observed by minimizing other effects. Therefore, mass transfer between the isopycnal layers is not considered and the turbulent viscosity is kept constant for the entire domain. The scenarios differ in including the gravitational forces due to density differences and the effect of the rheological behavior of cohesive mud suspensions. The rheological behavior is described by the parameterized Worrall-Tuliani approach of Equation (3.4.13). If the rheological behavior of fluid mud is neglected the rheological viscosity is set to 10^{-6} m^2/s for the entire system. The gravitational forcing according to density differences is modeled by the following pressure term

$$-g\frac{\partial}{\partial x}\left(\sum_{l=m}^{M}\frac{\varrho_l-\varrho_{l_t}}{\varrho_r}\eta_l\right) \tag{5.4.1}$$

for the m-th isopycnal layer of the momentum equation (x-component), see Equation (A.1.1). The term is given by

$$-g\frac{\partial}{\partial x}\eta_M \tag{5.4.2}$$

when neglecting the density differences influencing the flow. Therefore, the gravity acts on the water column as if only one isopycnal layer has been defined.

The density distribution of the highly concentrated layers is in the range of 1005 to 1080 kg/m^3 (see Table 4). The water layer has a density of 1000 kg/m^3. This applies to all scenarios of the simulation set-up (1). The simulation results are shown in Figure 40.

In the first scenario (1a) neither density differences nor rheological effects are considered. The discharged fluid mud now propagates very slowly and spreads significantly in the vertical direction. The layers flow above each other with increasing velocities. The velocity is therefore much higher near the surface and at the layer fronts. The bottom friction decelerates the movement when the different layers are in contact with the bottom.

Simulation (1b) includes the variable rheological viscosity. This does not influence the Newtonian water layer but the structural viscosity of the fluid mud layers. The rheological viscosity changes according to the density and decreases with increasing shear

simulation number	density of mud layers [kg/m^3]	isopycnal density differences [kg/m^3]	rheological viscosity approach	gravitational effects due to density differences
(1a)	1005/ 1010/ 1030/ 1080	5/ 5/ 20/ 50	const. 10^{-6} m^2/s	no
(1b)			Worrall-Tuliani app.	no
(1c)			const. 10^{-6} m^2/s	yes
(1d)			Worrall-Tuliani app.	yes
(2)	1010/ 1030/ 1080/ 1150	10/ 20/ 50/ 70	Worrall-Tuliani app.	yes
(3)	1005/ 1010/ 1020/ 1030	5/ 5/ 10/ 20	Worrall-Tuliani app.	yes
(4)	1000.1/ 1000.2/ 1000.3/ 1000.4	0.1/ 0.1/ 0.1/ 0.1	Worrall-Tuliani app.	yes

Table 4: *Simulation overview for the test case flow on an inclined plane.*

rate intensities – the shear-thinning behavior of mud suspensions. Without this structural behavior each isopycnal layer would have a constant viscosity. However, with the implemented rheological approach the viscosity varies within a certain range in an isopycnal layer. In particular, this becomes clearer in Figure 42 with a different color scale. The horizontal propagation of the two layers with lower concentrations (1005 and 1010 kg/m^3) is comparable to simulation (1a) because their rheological viscosity is only slightly higher than in simulation (1a). The viscosity of the two layers with higher concentrations is much higher and both move with a similar velocity magnitude. The vertical stratification becomes more even and stable. Accordingly, the horizontal movement now dominates over the vertical spread for the two highly concentrated layers (1030 and 1080 kg/m^3).

The third scenario (1c) includes the gravitational forces due to density differences but neglects the rheological viscosity which describes the shear-thinning and structural behavior. The results show that the gravitational flow is responsible for the downslope propagation in comparison with scenarios (1a) and (1b). Each layer moves with its own velocity due to the differences in the density of the isopycnal layers. The layers cover significantly different distances after an hour of downslope movement. Bottom friction slows down the bottom layer in particular.

The last scenario (1d) considers both gravity flow and the rheology of mud suspensions. Again, the rheological viscosity increases with the density of the isopycnal layers, but also varies inside a layer due to changes in the shear intensity. The high rheological viscosities decelerate the average downslope flow and the layer fronts are closer together. However, the fluid mud layers now appear more as a compact fluid mud body interacting due to the interfacial shear stresses. This shows that both processes are necessary to reproduce a realistic and plausible high-concentration flow on an inclined plane.

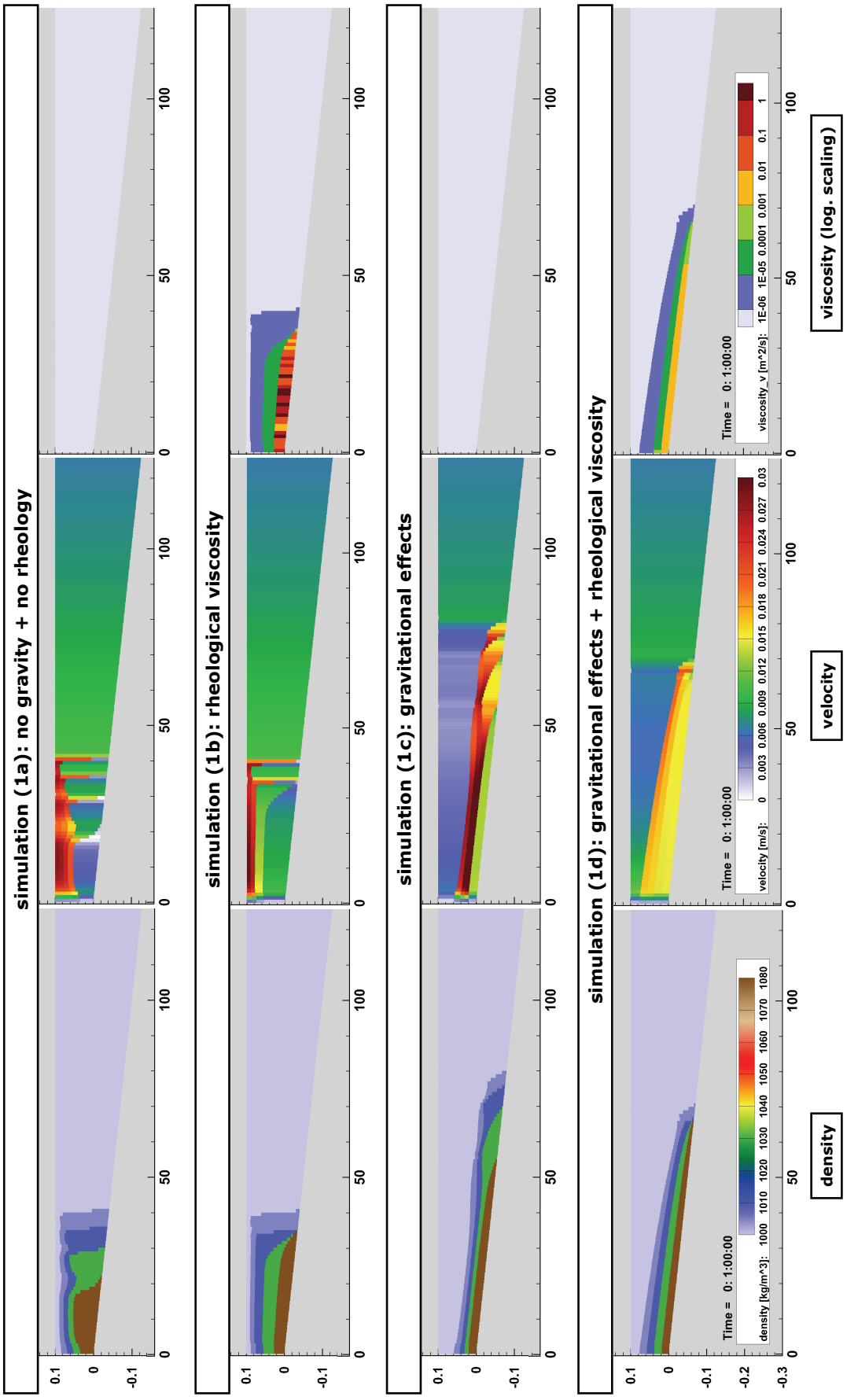

Figure 40: *Propagation of high-concentration layers - variations of simulation set-up (1) (first column: density; second column: velocity; third column: viscosity in logarithmic scaling).*

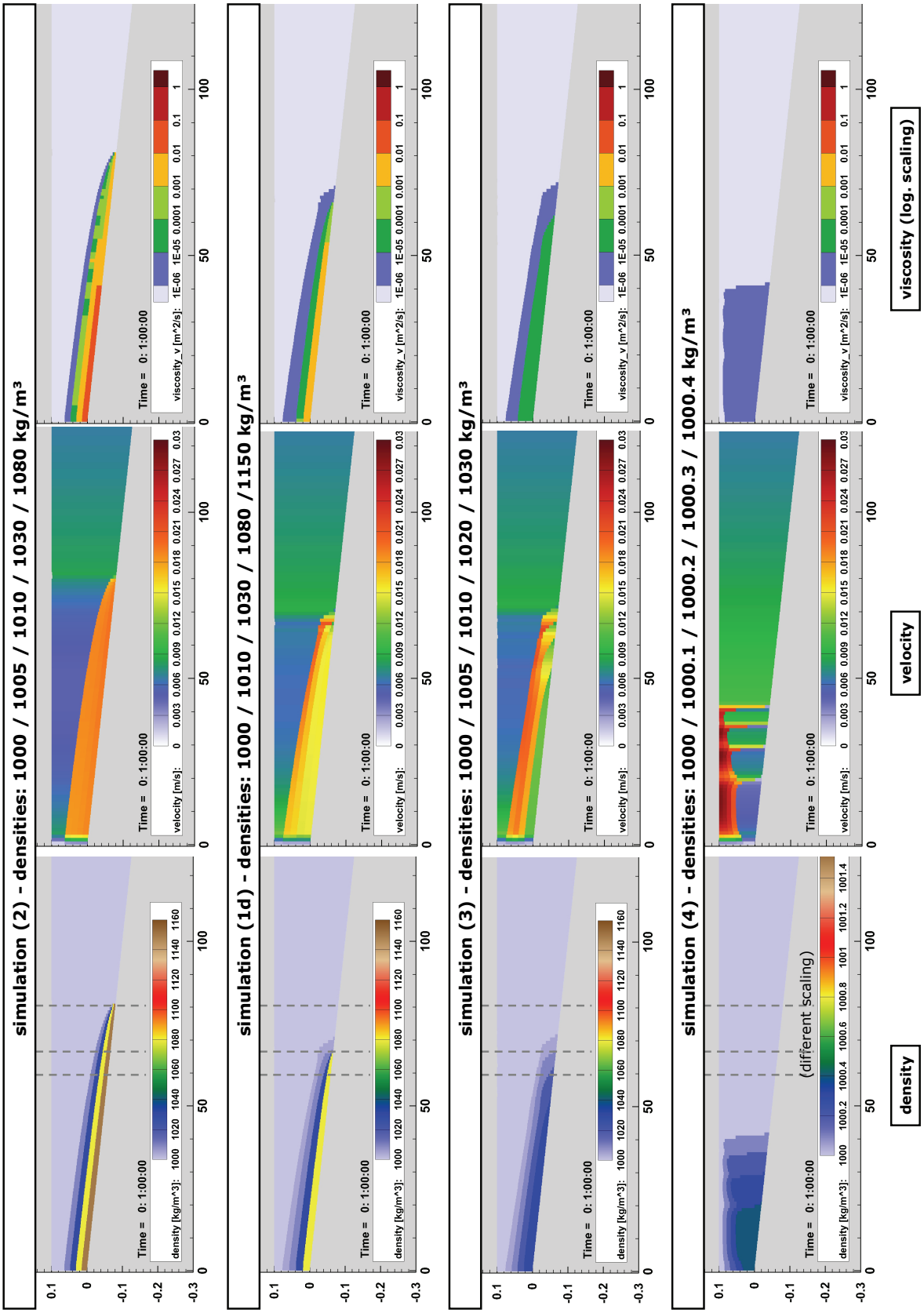

Figure 41: *Simulation results of model run (2), (1d), (3) and (4) (first column: density; second column: velocity; third column: viscosity in logarithmic scaling).*

The model set-ups of simulations (1d), (2), (3) and (4) differ in the density distribution of the four mud suspensions, see Table 4. The simulation results are given in Figure 41. The average density of the mud layers decreases from the top panel (simulation (2)) to the bottom panel (simulation (4)) of Figure 41. Moreover, the differences in the density of the isopycnal layers also decrease. The definition of the pressure term (Equation (5.4.1)) indicates increasing acceleration of the mud layers with increasing density differences. This can be observed in the varying propagation time of the fluid mud body. Accordingly, the fluid mud front advances the farthest for simulation (2) and slows down further in simulation (1), (3) to (4).
The structural viscosity counteracts the progressive movement of the fluid mud body by deceleration due to increasing viscosities with simultaneously increasing densities. Model run (4) exhibits similar results to run (1a) due to the fact that the density differences of run (4) are rather small and are omitted from the pressure term in run (1a). Moreover, the rheological viscosity is set to 10^{-6} m^2/s in simulation (1a) and the resulting viscosities differ only slightly from the magnitudes of run (4). This causes similar velocity pattern to those described for simulation (1a) above. The parameter variations of the seven model runs lead to plausible results. This is evaluated on:

- the influence of gravity and structural viscosity on the downslope flow by activating or deactivating these processes,
- the effects of the gravitational forces by varying the density differences,
- the effects of the structural (rheological) viscosity by varying the density differences.

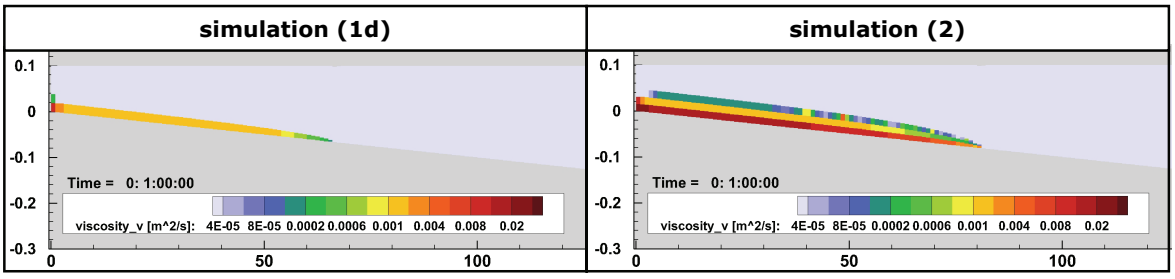

Figure 42: *Rheological viscosity illustrated with a different color scale compared to Figures 41 and 40 for simulation (1d) with lower suspension densities and simulation (2) with higher suspension densities.*
The viscosity varies inside an isopycnal layer as a function of the shear impact and it increases with increasing density according to the implemented rheological approach.

6 Application to the Ems Estuary

The Ems Estuary is located between the borders of Germany and the Netherlands. The domain and the bathymetry can be seen in Figure 43. The estuary extends from the weir at Herbrum, where the tidal signal ends, to the outer coast line with some offshore islands. This part of the Ems river is about 100 km long. A large tidal bay, the Dollard, with an area of 100 km^2 is located to the south of Emden. The Dollard and wide sections of the mouth of the estuary contain tidal flats with predominantly muddy sediment distribution. There is a deepened shipping channel between Papenburg and Borkum and the depth of the waterway is shown in Figure 44. The width of the river is 60 m at the weir, increasing to 120 m at Papenburg and 600 m at the mouth. The discharge at Herbrum weir can vary between 20 and 400 m^3/s and the most frequent discharge is about 60 m^3/s.

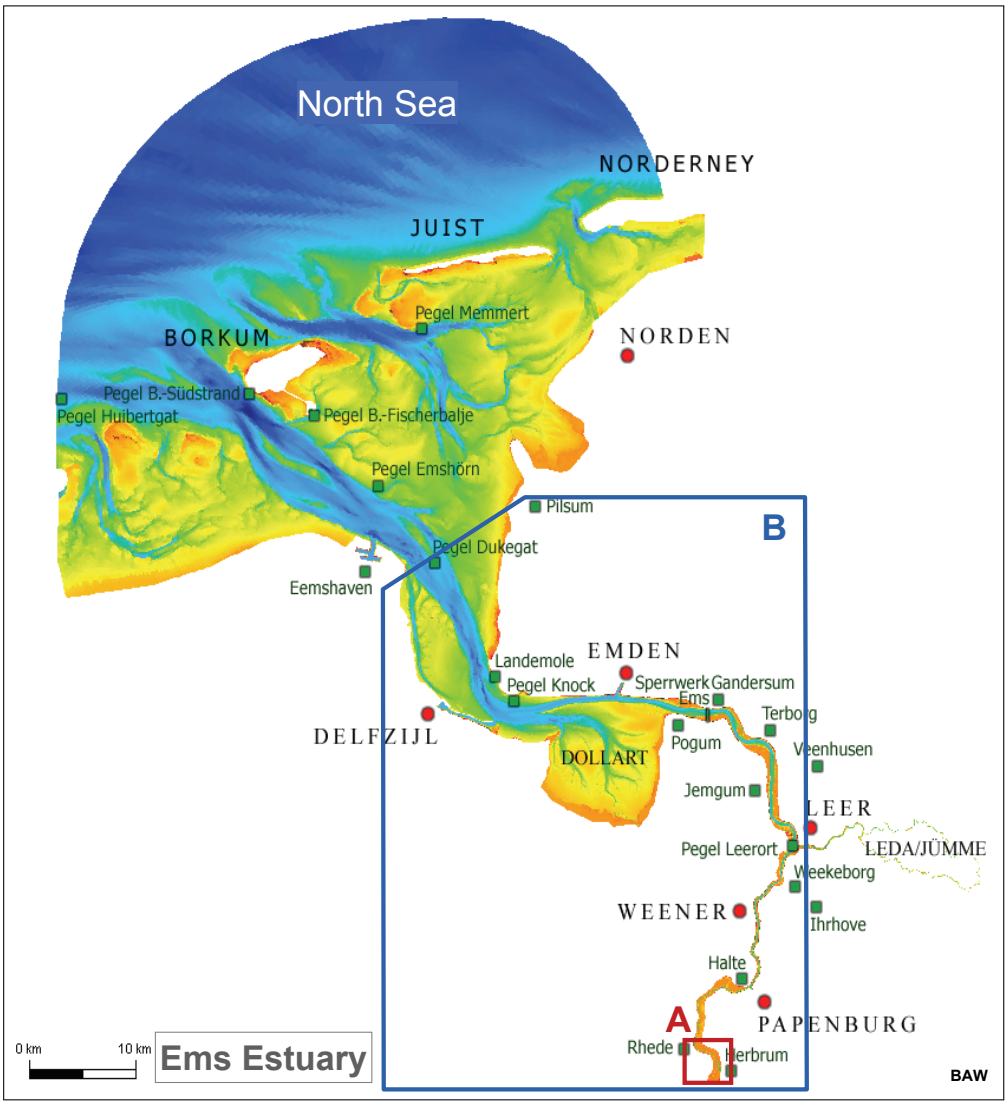

Figure 43: *Overview of the Ems Estuary (A: Region of sectional model from Rhede to Herbrum, B: Region of sectional model from Dukegat to Herbrum).*

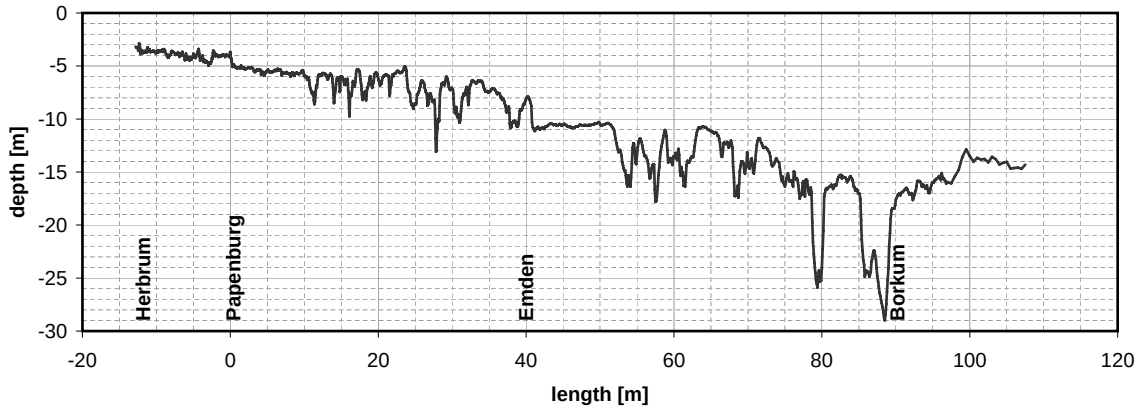

Figure 44: *Bathymetry along the center line of the Ems waterway (data according to Smile Consult [2006]).*

The tidal range increases from 2.20 m at Borkum to 3.50 m at Papenburg. The tidal curve has become highly asymmetrical in the lower Ems due to channel deepening. The asymmetry is characterized by a steep flood tide gradient and short flood phase, a long slack water period from flood to ebb and a shallower ebb tide gradient and longer ebb phase. This leads to a flood-dominated system with strong flood currents and much weaker ebb currents. Thus, suspended sediments were transported upstream due to tidal pumping. The suspended particles, mostly muddy sediments, accumulate in the wide turbidity maximum zone and form dynamic fluid mud layers. However, fluid mud layers do not occur only in the maximum turbidity zone, they can also be found in the lower Ems.
For more hydrological and morphological information see Krebs and Weilbeer [2008], Weilbeer [2005] and Winterwerp [2011]. The lower Ems Estuary has a serious occurrence of suspended mud and fluid mud. The turbidity has increased over the last decades. Schrottke [2006] showed that fluid mud layers with thicknesses of around 2 m or more can develop in the maximum turbidity zone, with concentrations up to 300 kg/m^3 or densities up to 1190 kg/m^3. Sediment echo sounder measurements (Figure 7) show a strongly stratified water body. Two to three layers of different densities were detected, each layer being around one meter in thickness.

In the following, some of the characteristic fluid mud dynamics in the Ems are investigated by system studies of sectional models. They have been chosen to focus on specific areas. Besides, the computational code is not parallelized and the computational effort is reduced in this way. The model boundaries are chosen with respect to the available boundary value data. The first model domain extends from Rhede to the Herbrum weir in order to study the effects of tidal pumping and tidal movement of the lutocline (Section 6.1). The second system study is concerned with stratified flow and siltation in a harbor basin which is studied on the Emden Outer Harbor (Section 6.2). The model domain extends from Dukegat (seaward boundary) to Herbrum.

6.1 Model Section from Rhede to Herbrum

The model section of the Ems Estuary investigated here covers the area from the tide gauge at Rhede to the weir at Herbrum. The location of the model area is indicated in Figure 45 along with the bathymetry and grid resolution of the model. The upstream section is divided into the river arm leading to the weir at Herbrum and the harbor basin of a sluice which has a ground sill at the mouth of the basin. The sediment transport in this region is dominated by mud suspensions. The fine sediments are mainly carried into this region by tidal pumping. Muddy sediments accumulate in the harbor basin.

Discharge is applied at the weir Herbrum by a source containing only clear water. The open boundary at Rhede is controlled by prescribed water levels. Suspensions of different concentrations are brought into the model domain at the open boundary. The isopycnal interfaces are triggered in the same way as the water surface. They move with the tidal signal, but with half of the tidal range.

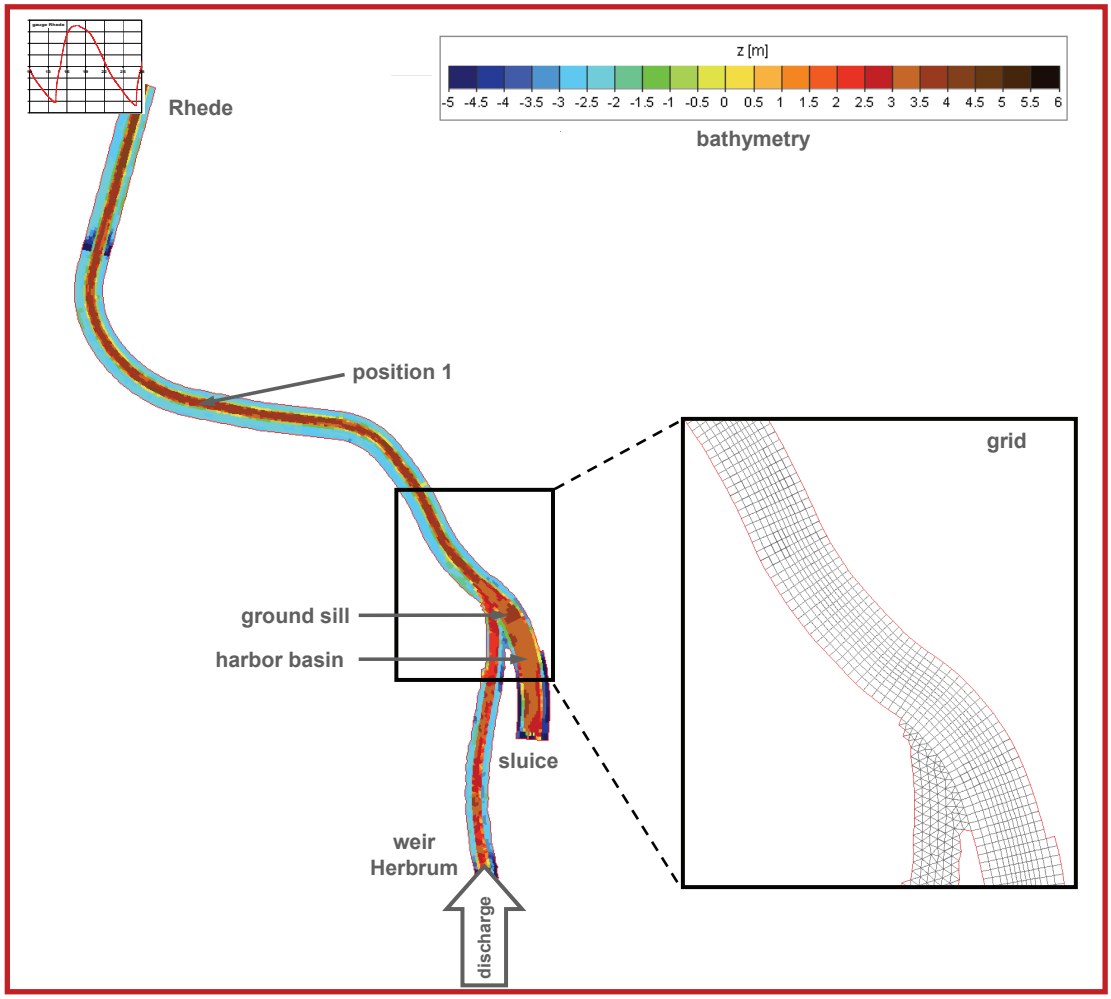

Figure 45: *Bathymetry and grid of the sectional model extending from Rhede to Herbrum. A fresh water discharge is applied at the weir at Herbrum. A tidal signal is given at the open boundary at Rhede.*

Three simulations were carried out with different boundary values, see Table 5. The first simulation (1) was forced by realistic boundary conditions. Simulation (2) differs from the first one due to reduction of the discharge. It is set at a constant 25 m^3/s. The third simulation (3) was performed with a symmetrical M2-tide instead of the real tidal signal. This enabled the effect of the asymmetrical tide wave compared with the uniform sine wave to be analyzed. The discharge is the same as in simulation (1). The initial density levels are uniformly allocated in the entire model domain and they are presented in Figure 46 and in Table 6. The density values result from the 16 predefined isopycnal layers. They range from clear water, dilute suspension, concentrated suspension, fluid mud to freshly consolidated mud.

The simulations cover several tide cycles. The simulation time step is limited due to the time step criterion of Equation (A.3.22) and the explicit solution for vertical mass transfer. Studying variations of the time step leads to a time step of 10 s which gives sufficiently accurate results.

In the following, the simulation results will be presented for a longitudinal profile following the channel center line and for selected locations. The topography of the profiles as well as the positions are illustrated in Figure 47.

The vertical transport processes considered are entrainment and settling (hindered settling). The horizontal transport is driven by currents and gravitational forces.

simulation number	**boundary value: discharge**	**boundary value: water level**	**M**
1	measured data ~50-60 m^3/s	measured data of gauge Rhede	16
2	25 m^3/s	measured data of gauge Rhede	16
3	measured data ~50-60 m^3/s	M2 tide	16

Table 5: *Simulation overview for the model Rhede to Herbrum.*

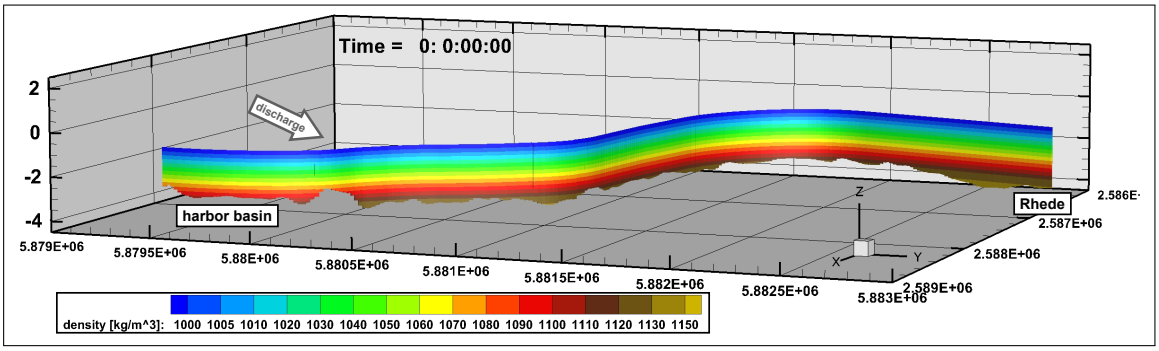

Figure 46: *Initial density distribution of the longitudinal section in the channel center line. The density increases from bottom to top. The initial distribution is constant over the entire domain.*

Entrainment is determined according the Kranenburg and Winterwerp [1997] approach

layer number	density	mud concentration	isopycnal elevation
	[kg/m^3]	[kg/m^3]	[m]
16	1000	0.00	-1.15
15	1005	8.03	-1.33
14	1010	16.06	-1.51
13	1020	32.12	-1.68
12	1030	48.18	-1.86
11	1040	64.24	-2.04
10	1050	80.30	-2.22
9	1060	96.36	-2.40
8	1070	112.42	-2.58
7	1080	128.48	-2.75
6	1090	144.55	-2.93
5	1100	160.61	-3.11
4	1110	176.67	-3.29
3	1120	192.73	-3.47
2	1130	208.79	-3.64
1	1150	240.91	-4.00

Table 6: *Initial density distribution over depth with an initial water level of -1.15 m.*

with the coefficients $C_s = 0.50$ and $C_\sigma = 0.42$ (Equation (3.6.6)). The critical shear stress for entrainment is defined by the yield strength of the mud suspensions (Equation (3.4.11)). The settling velocity with hindered settling is calculated by a formulation according to Winterwerp described in Section 3.7. The gelling concentration is set at 40 kg/m^3. Consolidation takes place in the time range of weeks and months. This process will not have effect during the simulation of a few tide cycles. Consolidation can therefore be neglected in this case.

The rheological behavior of the mud suspensions is simulated by the parameterized Worrall-Tuliani model presented in Equation (3.4.13). The fluid properties are approximated through the rheological viscosity, see Section 3.5. The rheological viscosity approach is applied to every isopycnal layer because it is valid for clear water as well as for fluid mud and soft consolidated mud. A yield stress equal to zero is obtained for clear water and increases exponentially with increasing concentrations, see Figure 15. Accordingly, the rheological viscosity decreases to the molecular viscosity of clear water. An increase in the mud concentration as well as a decrease in the shear impact leads to an increase in the rheological viscosity. This is shown in Figure 17. The horizontal turbulent viscosity is set to a constant 10^{-6} m^2/s and the vertical turbulent viscosity to 10^{-2} m^2/s.

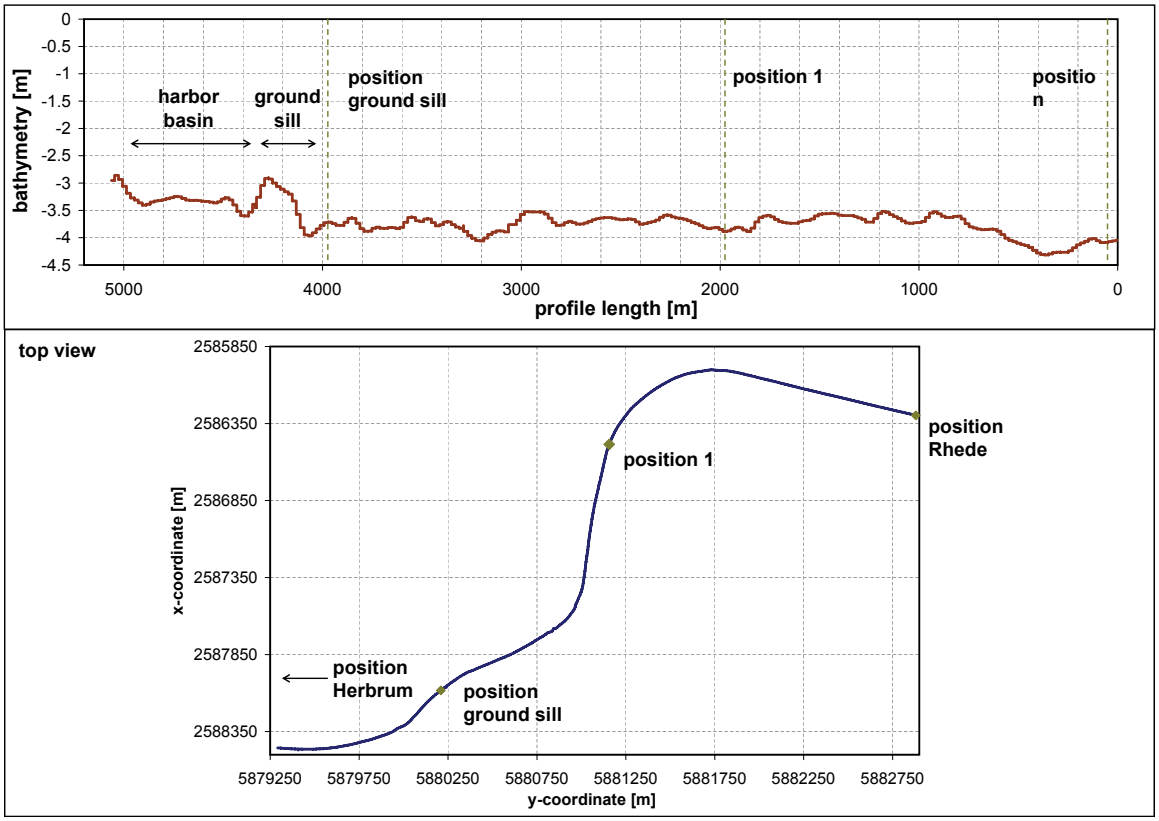

Figure 47: *Bathymetry of the longitudinal profile (upper panel) and top view of the profile with indicated positions for result output (lower panel).*

The model is calibrated by variation of the bottom roughness which compensates for turbulence damping in the system. The geometrical bottom roughness (k_s) according to Nikuradse is varied by $\sim 9.0 \cdot 10^{-2}$, $\sim 7.0 \cdot 10^{-3}$ and $\sim 2.5 \cdot 10^{-7}$ m. The model set-up corresponds to simulation (1). Figure 48 shows the simulated water levels in comparison to field data at the Herbrum position. The bottom roughness $k_s \approx 7.0 \cdot 10^{-3}$ m fits best and is applied to all simulations.

In Figure 49 the effect of the mud concentration and the rheological viscosity is analyzed on the water level elevation. The water level at the Herbrum position is compared for three simulations with the measured data. The first simulation (a) considers only one isopycnal layer of clear water ($\varrho = 1000$ kg/m^3) which results in a 2D depth-averaged simulation. Both the turbulent and the rheological viscosity are taken as constant with $\nu_t^h = 10^{-6}$m^2/s, $\nu_t^v = 10^{-2}$m^2/s and $\nu_r = 10^{-6}$m^2/s. In addition, the second simulation (b) includes transport of mud suspensions by defining 16 layers. The initial density conditions are shown in Figure 31 and Table 6. Based on simulation (b), simulation (c) takes account of the rheological viscosity which is dependent on the mud properties.

In all simulations, the up- and downstream flow during ebb and flood is slightly too strong and fast which indicates that the bottom and/or internal friction in the system is/are too low. The simulation with clear water fits well to the measured high water

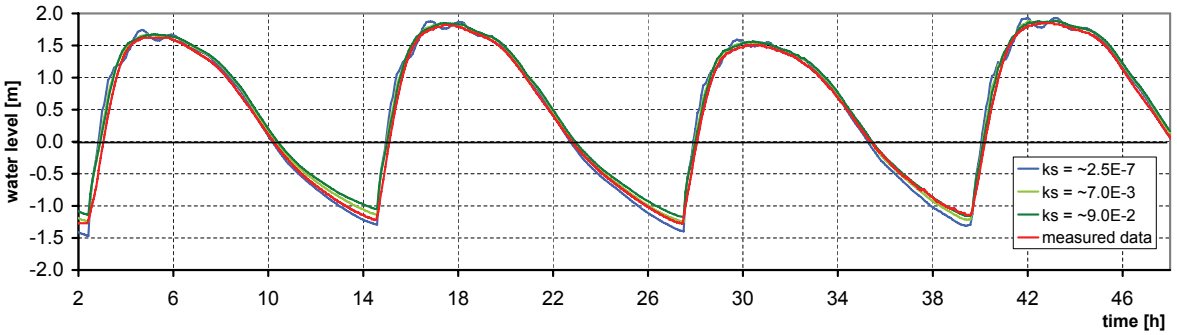

Figure 48: *Simulated water levels by variation of the bottom roughness and comparison with measured data at Herbrum.*
The model set-up with bottom roughness $k_s \approx 7.0 \cdot 10^{-3}$ m fits best and is applied to all simulations.

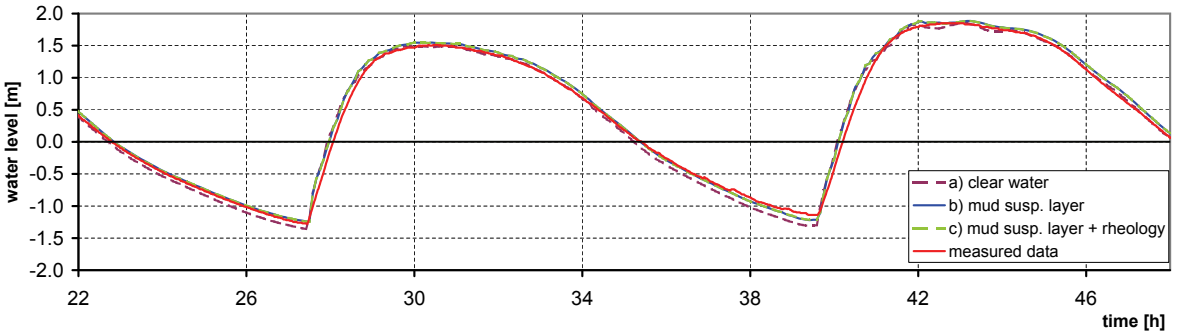

Figure 49: *Simulated water levels with variable rheological properties and comparison with measured data at Herbrum.*
The following three model set-ups are compared: (a) system with clear water (one ϱ-layer); (b) system with mud suspensions (16 ϱ-layer) with constant rheological viscosity ($10^{-6} m^2/s$); (c) system with mud suspensions (16 ϱ-layer) with rheological viscosity dependent on mud properties.

level. Both simulations with fluid mud show an increased high water level compared to simulation (a) and the measured data. The low water level is underestimated in all three simulations, whereas simulation (a) has the lowest low tide. Simulation (b) and (c) lead to very similar results for the water level although the rheological viscosity in simulation (c) is dependent on the rheology of the suspensions. Furthermore, the rheological viscosity is most effective at times of low currents. Dominating gravity current effects can cause the similar results due to the great differences in density between the layers. In addition, the density range is wide, being from 1000 to 1150 kg/m^3. Another possible reason is that the average velocity is already attenuated by the constant turbulent viscosity and the effect of the rheological viscosity is overshadowed.

The time series of the simulated **water level** are pictured in Figure 50 for the three positions Rhede, position 1 and Herbrum as well as the measured data at Herbrum. The diagram of simulation (1) illustrates the characteristic asymmetrical tide. At the Rhede position, the water level is equivalent to the input data. A comparison of simulated and measured data shows satisfying results at the downstream position at Herbrum. The tide wave deforms due to the transition from Rhede to Herbrum during ebb tide. The

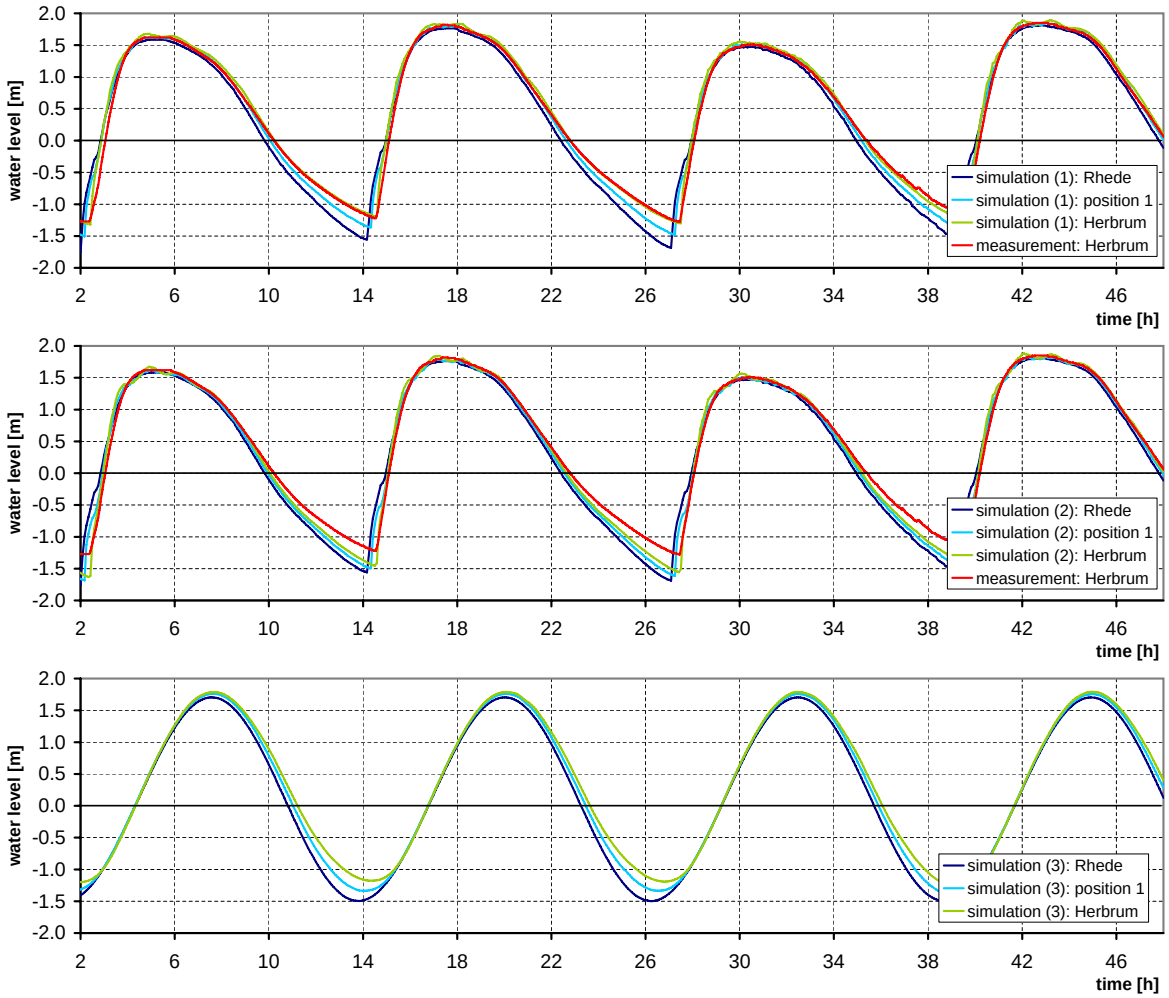

Figure 50: *Simulation results of the water level at the Herbrum position for simulations (1), (2) and (3) and comparison with measured data at Herbrum.*
The tidal wave deforms due to transition from Rhede to Herbrum. The lower fresh water discharge of simulation (2) leads to a lowering of the low tide in comparison with simulation (1). The first two simulations are dominated by an tidal asymmetry with a short flood phase and a long ebb phase, whereas simulation (3) is subject to symmetrical tide conditions.

low tide rises due to the freshwater inflow at Herbrum. Simulation (2) was run with a lower discharge of constantly 25 m^3/s, which leads to a much lesser increase in the low water. The high tide, however, nearly keeps its shape. The symmetrical M2-tide deforms in low as well as in high water through the transition from Rhede to Herbrum (simulation (3), third panel). A reason for the increase in high water is the gentler and longer flood gradient. Therefore, the water has more time to retain compared to the realistic tide curve of the simulation (1). The increase in low water from Rhede to Herbrum corresponds to the other two simulations.

The time series of the **mean velocity** and water level at position 1 are presented in Figure 51. The results give a qualitative but not quantitative impression on the flow dynamics. They are only representative of the deep channel. The influence of the symmetry of the tidal signal and discharge on tidal pumping becomes apparent when

the velocity conditions of the three simulations are compared. The simulation (1) under realistic tide conditions with a discharge of about 60 m^3/s leads to ebb and flood currents in the same range of magnitude. During the simulation, the inflow at Herbrum decreases to about 40 m^3/s. The magnitude of the flood current increases accordingly and it becomes higher than during ebb tide. The tidal pumping takes now effect and leads to a dominating upstream transport. This effect is intensified in simulation (2) because the inflow is further reduced to 25 m^3/s. In this case, the flood current is twice as high as the ebb current.
The symmetrical M2-tide in simulation (3) produces an ebb current-dominated system because the discharge intensifies the ebb current. The duration is longer and the velocity magnitude is higher than the flood currents. The flood currents become slightly stronger after 40 h due to the reduced discharge. Predominantly upstream transport due to tidal pumping is prevented by the tidal symmetry which will be shown in the following results for the mud suspension transport.

The **mud suspension transport** is represented by the density layers. Their corresponding suspended particle concentrations are listed in Table 6. Due to the isopycnal approach, a strong stratification is possible during all tide phases. The density distribution is shown in Figure 52 for simulation (1), Figure 53 for simulation (2) and Figure 54 for simulation (3). These plots represent the longitudinal section in the center line of the channel. Therefore, the results are only representative for this section. The simulation results reveal fluid mud formations comparable to the measured density gradients in Figure 7. The mud suspension layers are influenced by the tide and move with the tidal current. At flood tide, the mud suspension layers are carried in the direction of the harbor basin. The mud suspensions advance rapidly and cover a wide area in the flood-dominated conditions of simulations (1) and (2). The tidal pumping effect is more pronounced in simulation (2) because of the predominant flood currents. The tidal symmetry leads to a longer ebb phase with much higher ebb currents compared to the flood currents. Moreover, the upstream fluid mud progress is noticeably shorter which can be observed by comparing panel four of the Figures 52, 53 and 54. This indicates the noticeable effect of tidal pumping induced by the tidal asymmetry.

Internal waves can be induced by bathymetry gradients along the channel. The longitudinal section between the ground sill and position 1 is illustrated in Figure 55. The currents reverse during slack water at high tide, but this mechanism takes longer in the fluid mud body than in the water body. Internal waves are now generated due to gradients in the topography and the opposing currents. The internal waves propagate in the direction of the ebb current. Likewise, internal waves were observed during flood tides in the longitudinal section of the Ems Estuary in the area of the *Emder Fahrwasser*.

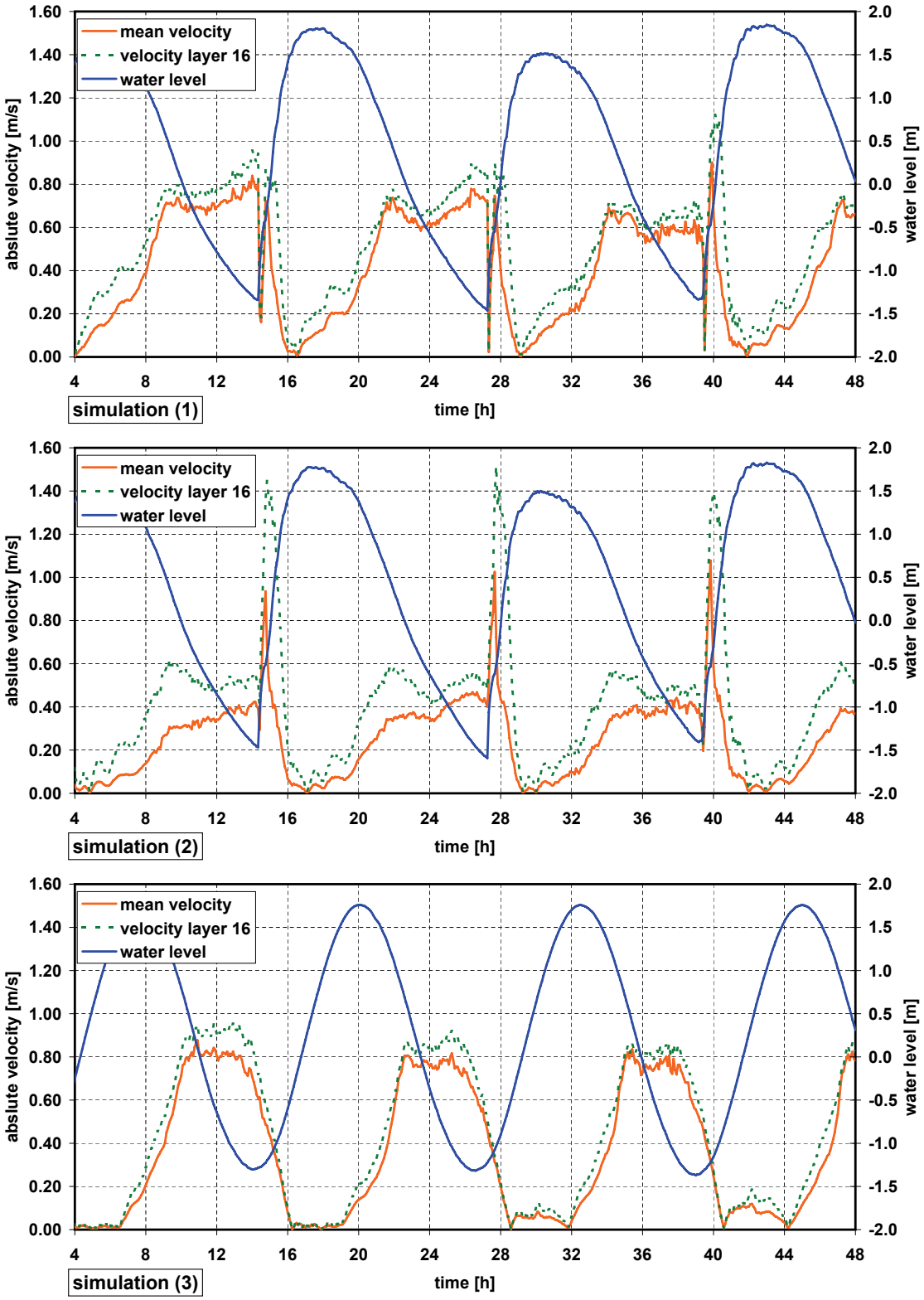

Figure 51: *Water level and mean velocity (absolute values) at position 1.*
The tidal pumping effect becomes apparent when the velocity results of simulation (1) (top panel), simulation (2) (middle panel) and simulation (1) (bottom panel) are compared. Simulation (1) and (2) show a long ebb phase and a short flood phase but with higher velocity magnitudes which results in predominantly upstream transport. This effect is intensified by reducing the upstream fresh water inflow (compare simulation (2)). The magnitude of the flood currents increases and that of the ebb currents decreases compared with simulation (1). However, the tidal symmetry results in an ebb tide-dominated system which leads to downstream-dominated transport.

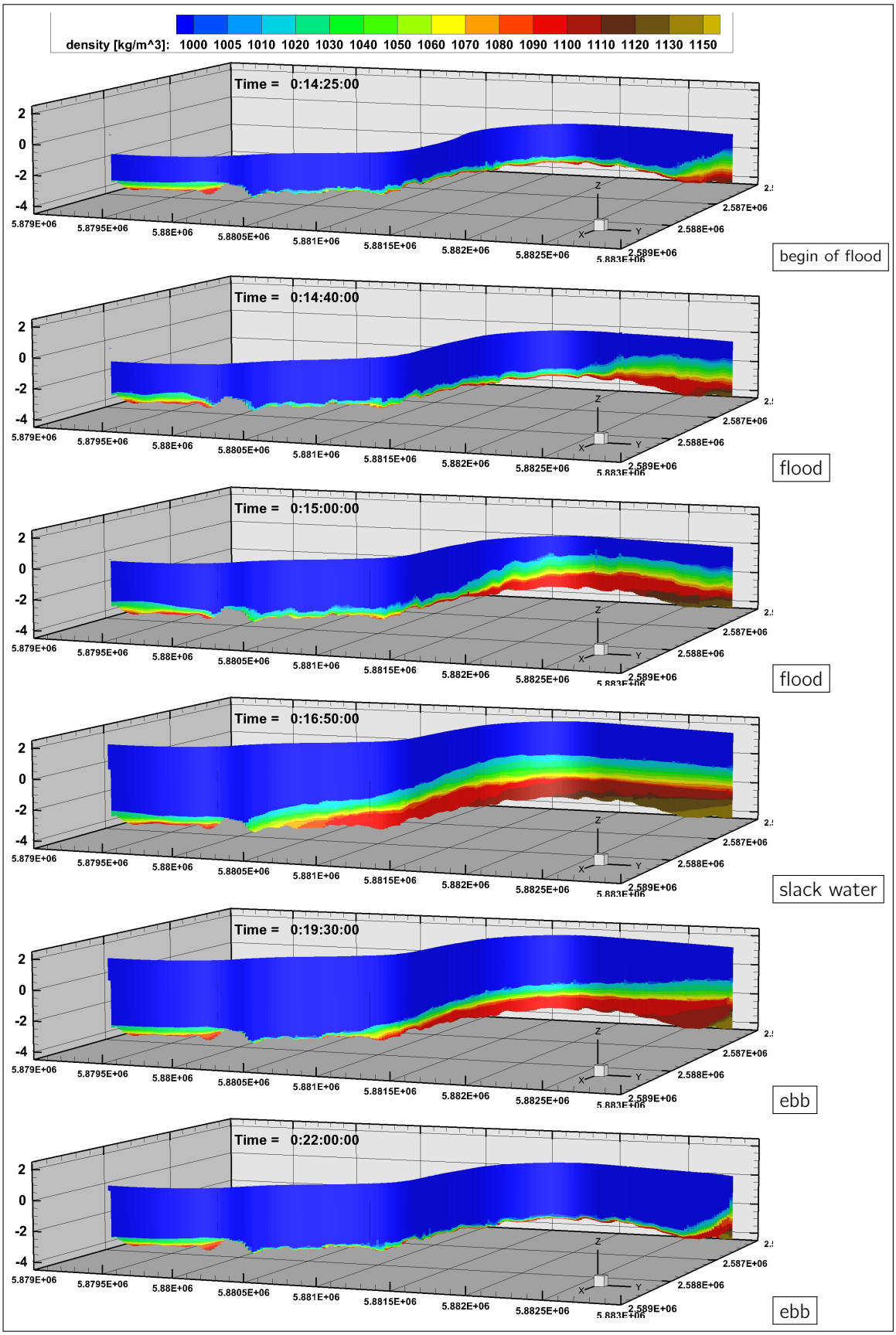

Figure 52: *Density distribution of the longitudinal section in the channel center line of simulation (1).*

Panels one to three are at flood tide, panel four at slack water and panel five and six at ebb tide. Entrainment occurs from the near bottom fluid mud layer especially during flood tide.

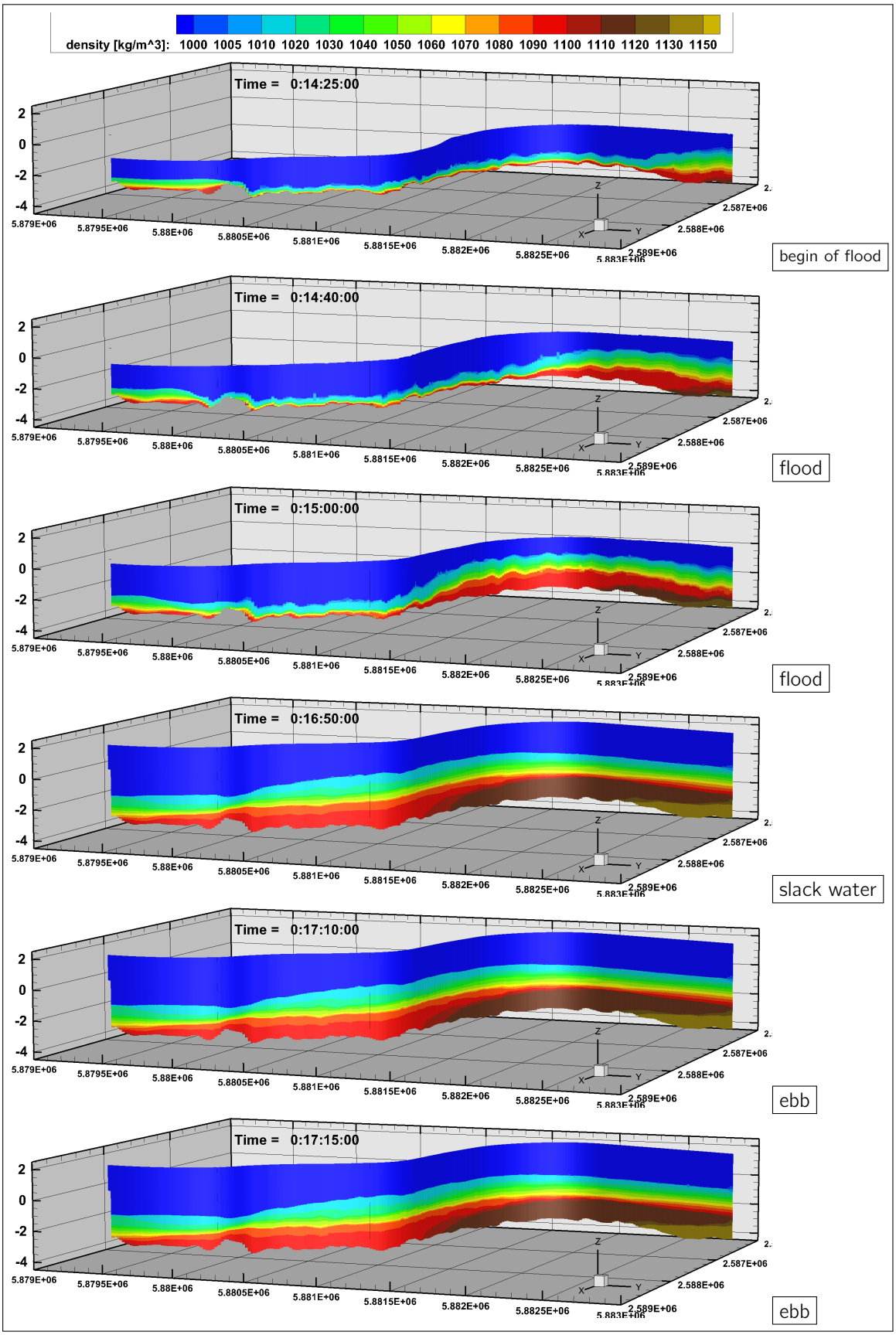

Figure 53: *Density distribution of the longitudinal section in the channel center line of simulation (2).*

The tidal pumping effect is intensified due to reduced fresh water inflow.

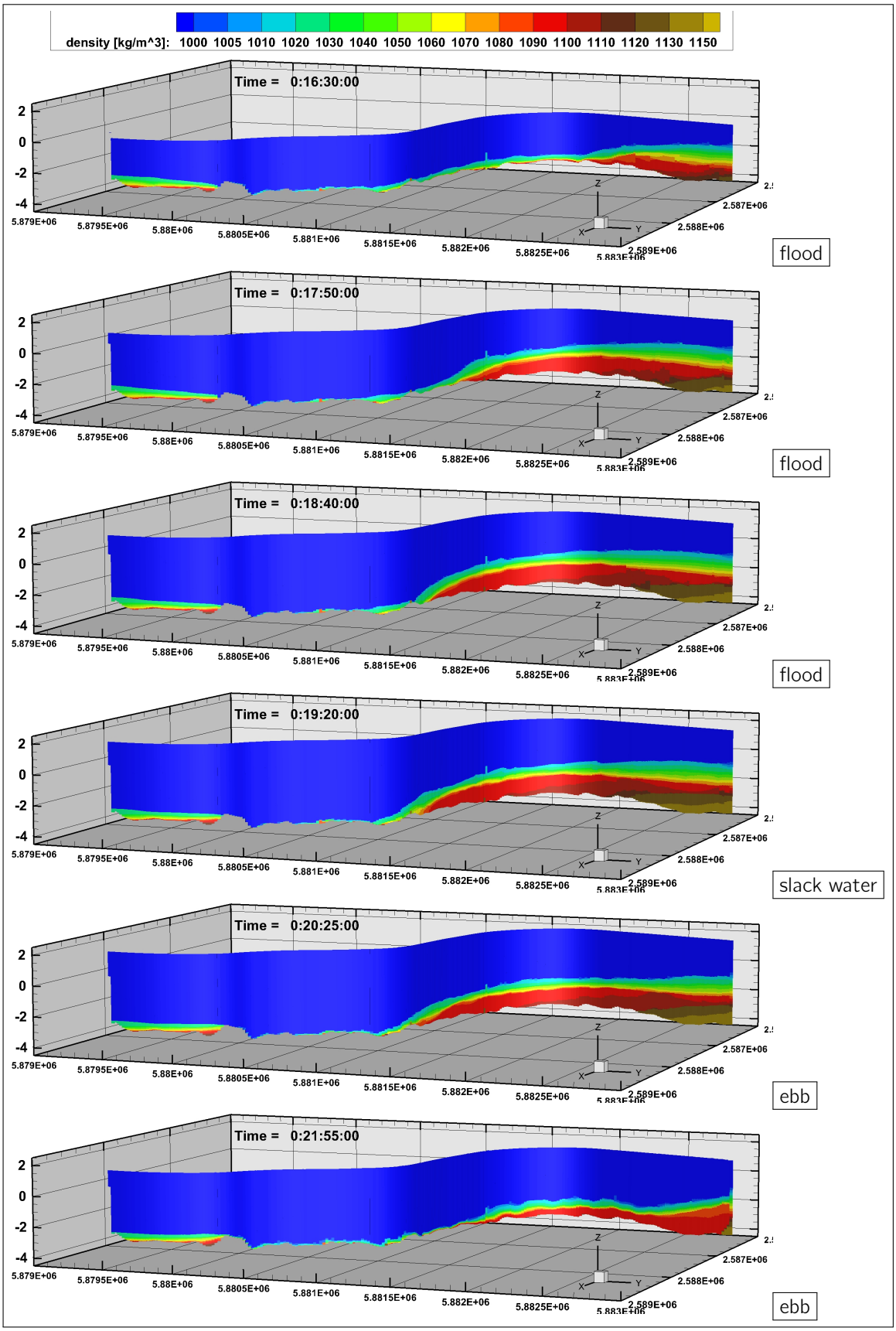

Figure 54: *Density distribution of the longitudinal section in the channel center line of simulation (3).*

The symmetrical tidal signal and a high discharge (∼40–60 m^3/s) lead to an ebb-dominated transport by contrast to simulation (2) (Figure 53).

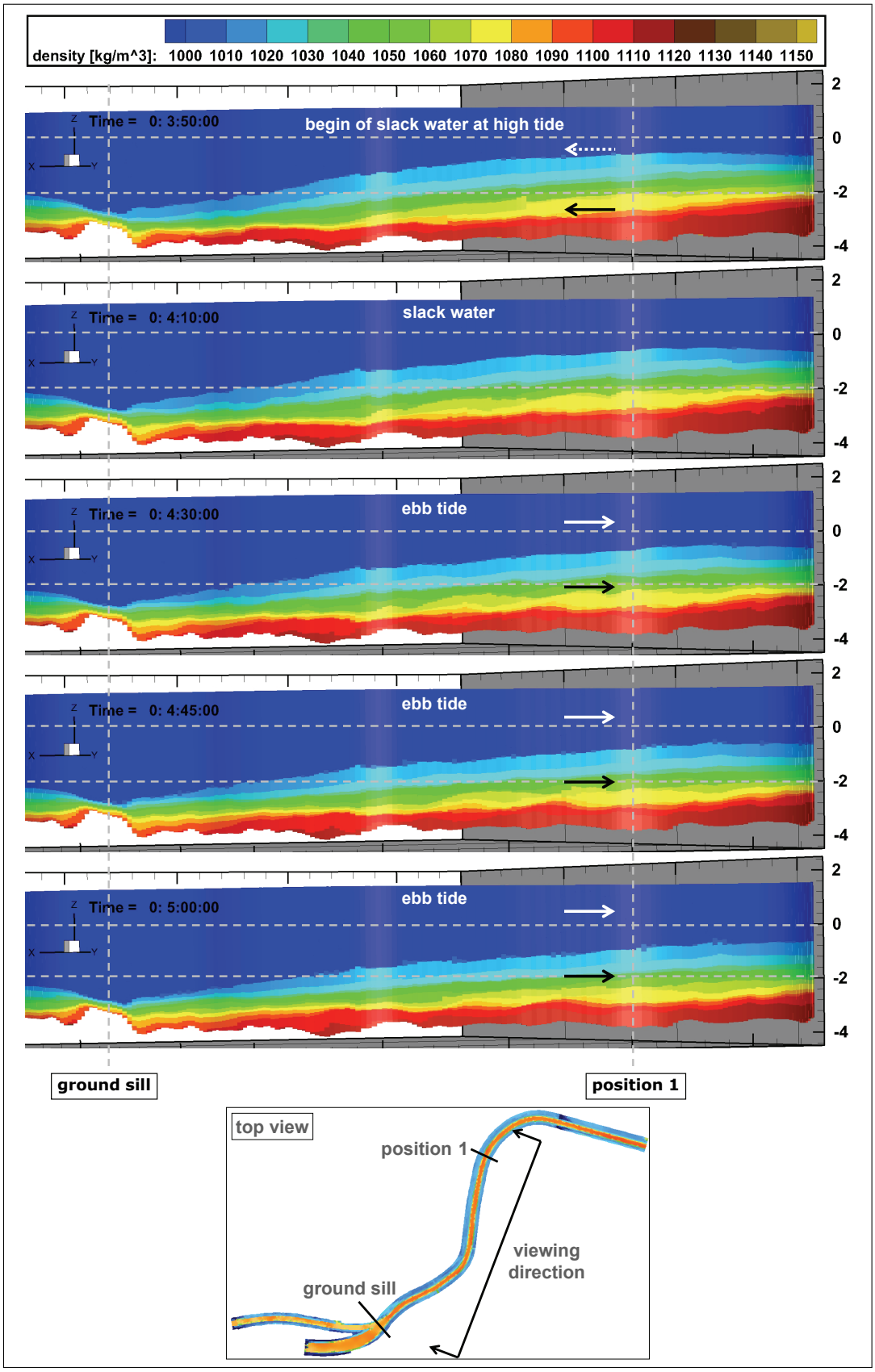

Figure 55: *Internal waves in the fluid mud layer traveling with the ebb current.*
The internal waves are induced at interfaces with high-density gradients due to gravitational effect.

The harbor basin is filled with mud during flood tides and only some of the fluid mud moves out during ebb tides. The ground sill in front of the harbor basin prevents the fluid mud being moved out of the basin entirely where it accumulates at times of low currents. The fluid mud layers become more compact after three tide cycles. Thus the thicknesses of the density layers, 1030 kg/m^3 and 1090 kg/m^3, increase and other layers either vanish or decrease in thickness. This is indicated in Figure 56 by a comparison of the results at the beginning and after three tide cycles. Further settling and consolidation will need longer simulation times and the parameterizations of the settling and entrainment approach have to be validated.

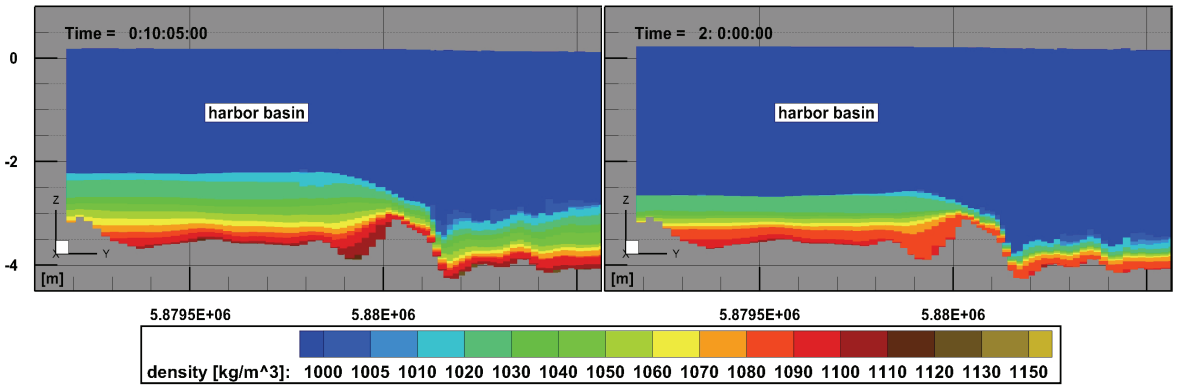

Figure 56: *Mud accumulation in the harbor basin - results of simulation (2).*
The high concentration layers at the bottom were mixed at the beginning of the simulation, but the average density of the fluid mud body increases with time.

The **velocity** and **rheological viscosity** distribution illustrate the specific rheological behavior of the mud suspensions. They are presented in Figures 57 and 58 for simulation (1), and in Figures 59 and 60 for simulation (2). The rheological behavior of fluid mud and mud suspensions is described in Sections 2.2.4 and 3.4. The parameterized Worrall-Tuliani approach is applied in the numerical model. This approach considers structural effects which lead to an increase in the rheological viscosity with an increasing suspended particle concentration and decreasing shear impact. A general impression of the viscosity as a function of density and shear rate is given in the diagram of Figure 17. In nature, the cohesive suspended particles accumulate to build up aggregates and these aggregates can form a structure due to the build-up of contacts. The internal structure is responsible for the resistance of the mud. This mechanism is parameterized by the constitutive law according to Worrall-Tuliani in the numerical model.
Therefore, high velocity gradients lead to the break-up of the particulate structure which reduces the rheological viscosity of the mud suspension. This can be observed during the flood tide and especially at the beginning of increasing flood currents, see the first and second panels of the figures. The resistance of the fluid mud increases (increase in the rheological viscosity) because of hindered settling and decreasing shear rates by reaching slack water. The higher concentrated layers maintain their movement longer

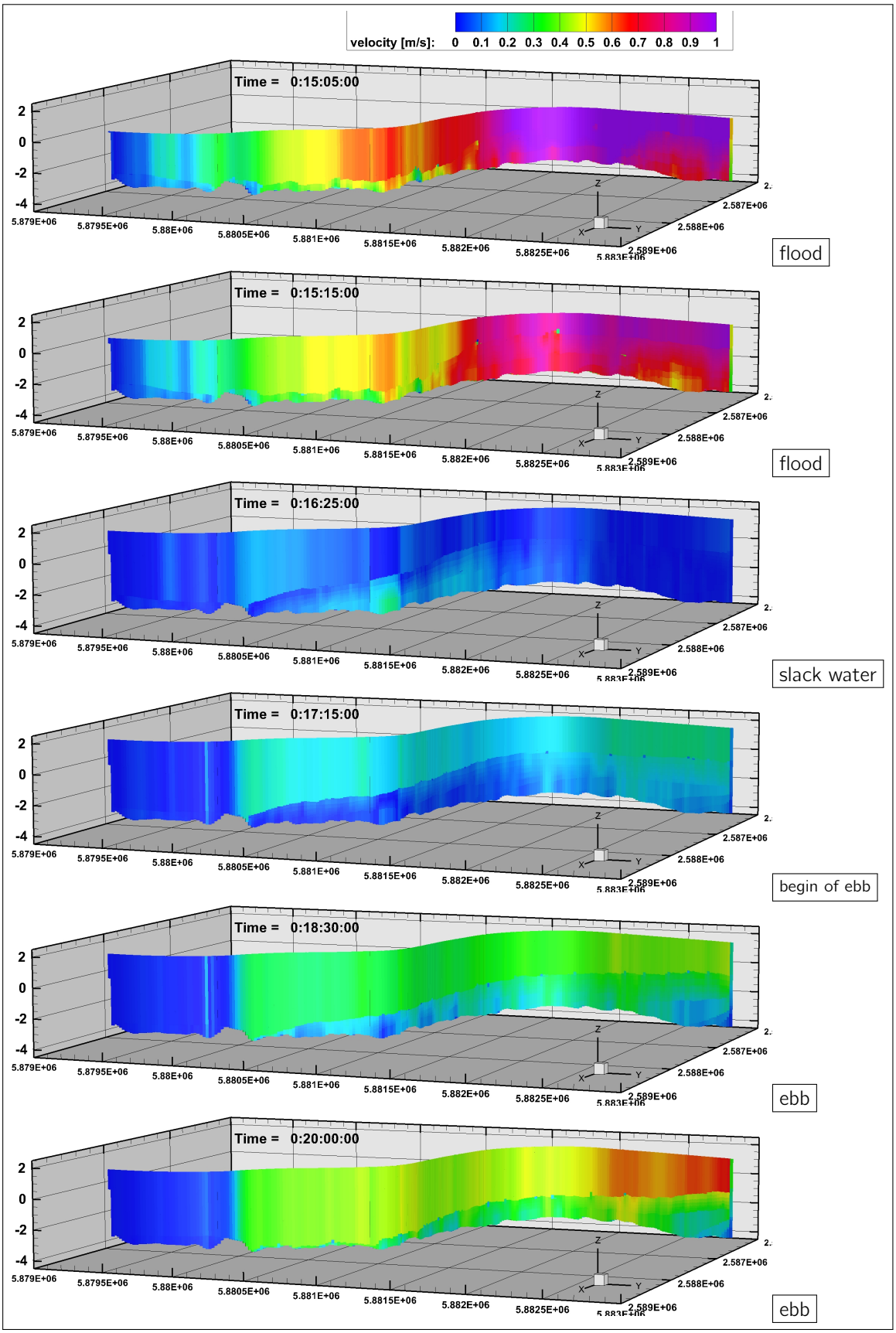

Figure 57: *Isopycnal layer-averaged velocity of the longitudinal section in the channel center line of simulation (1). Stratified flow occurs during flood and ebb tide. The inertia and resistance against the change of flow direction is stronger in the high-concentration mud suspension layers (see panels four and five).*

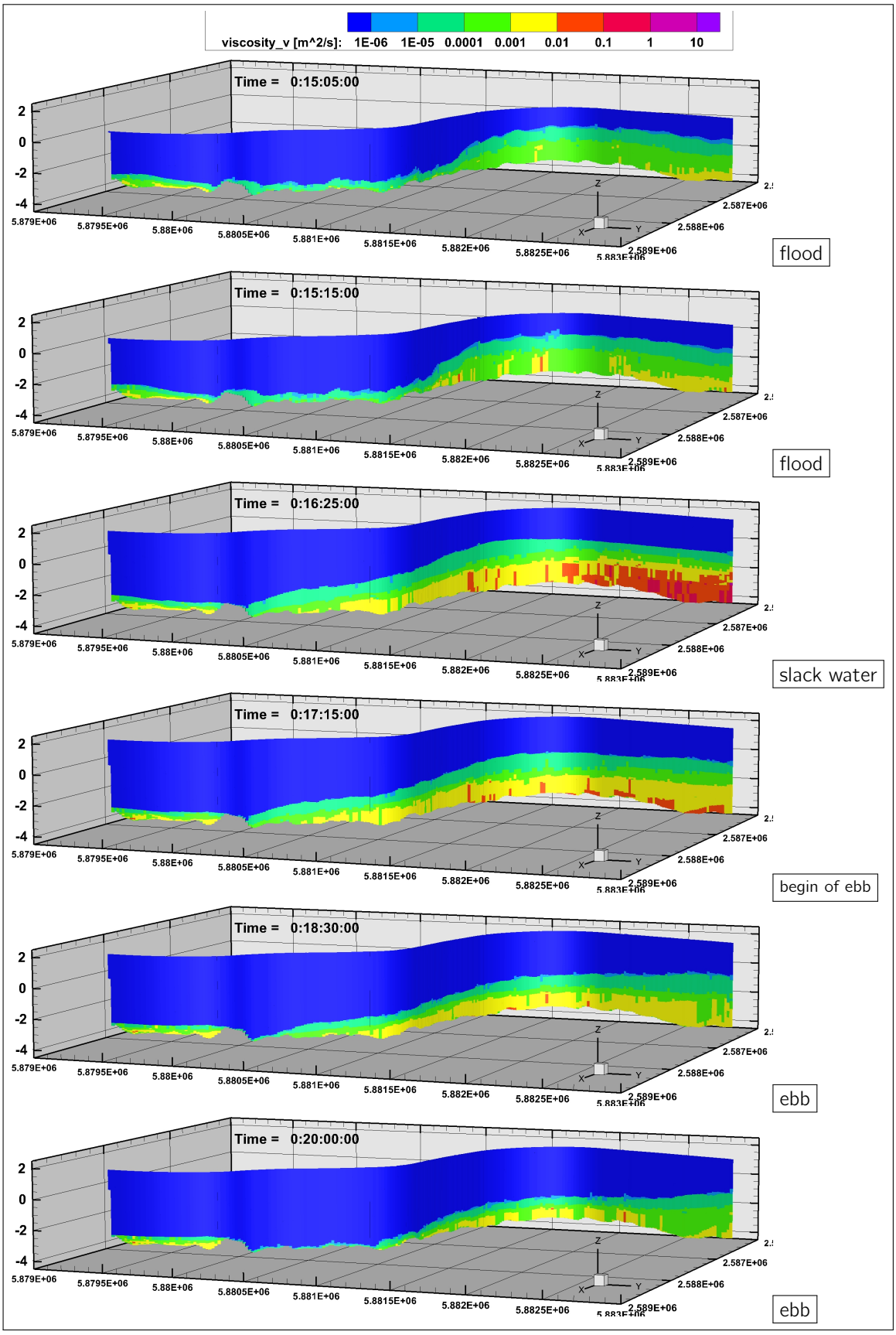

Figure 58: *Rheological viscosity of the longitudinal section in the channel center line of simulation (1). The viscosity decreases in periods of high shear forces (see panels one, two and six) whereas the internal structure can build up during slack water and the viscosity increases again (see panel three).*

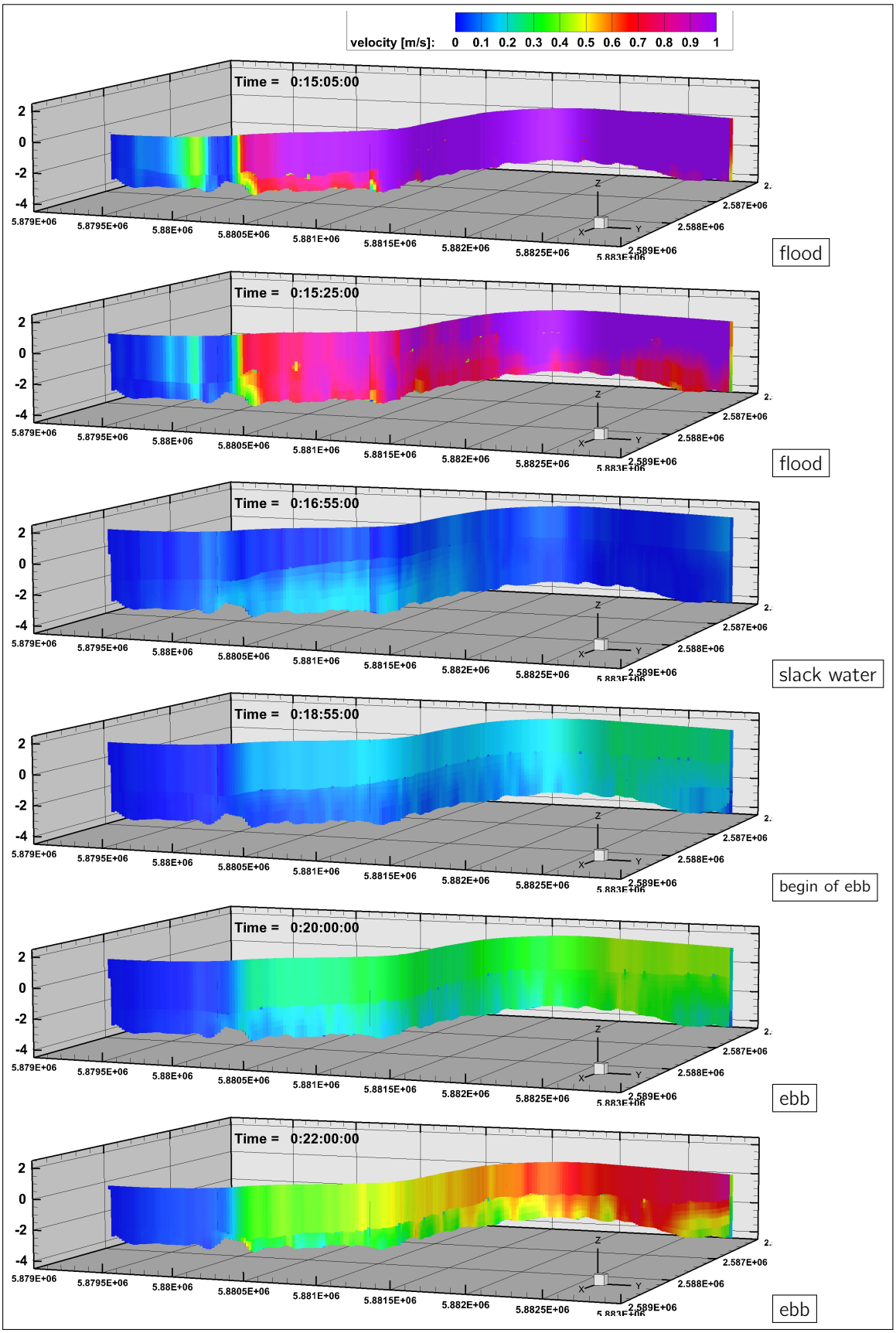

Figure 59: *Isopycnal layer-averaged velocity of the longitudinal section in the channel center line of simulation (2). Stratified flow occurs during flood and ebb tide. The inertia and resistance against the change of flow direction is stronger in the high-concentration mud suspension layers (see panels four and five).*

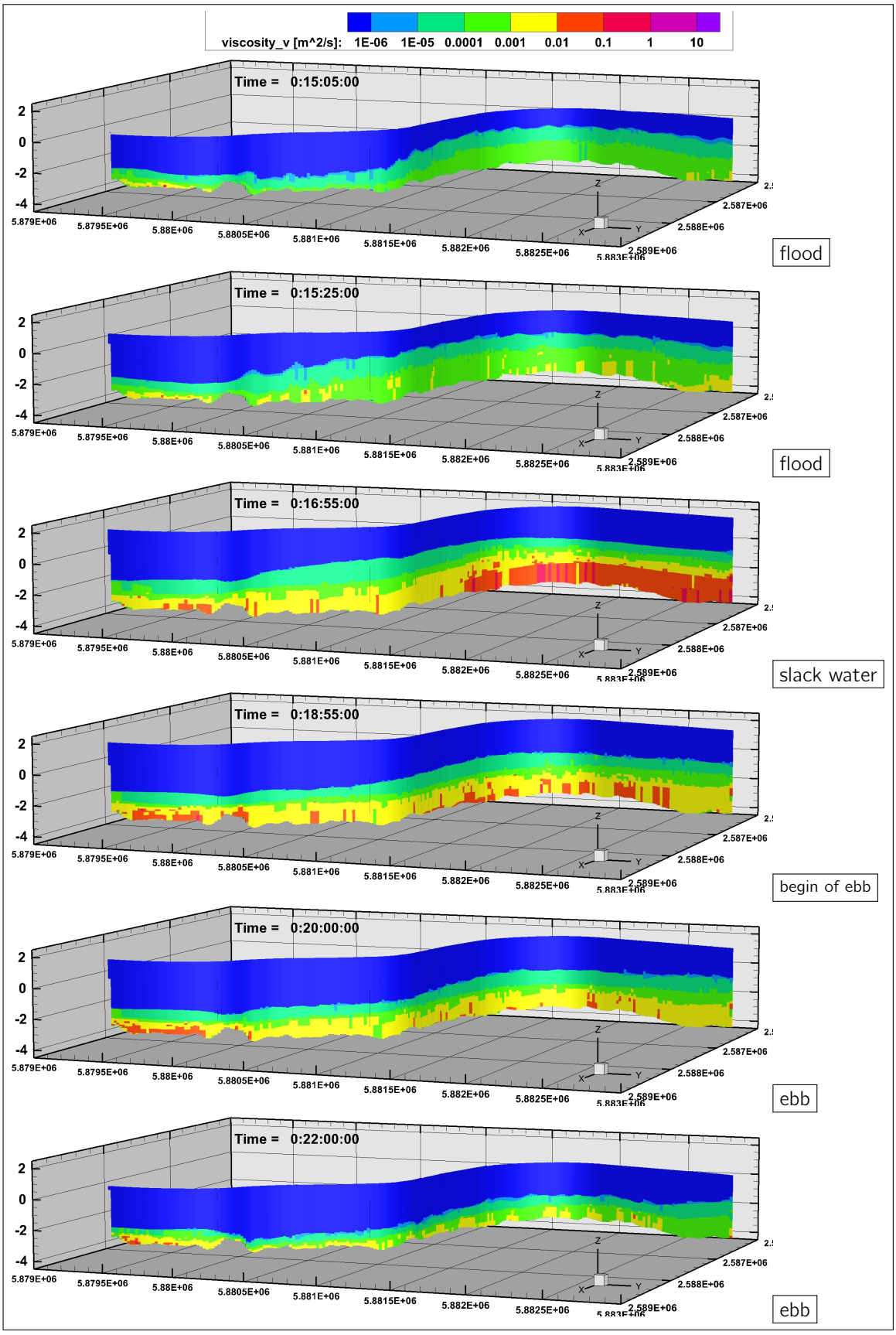

Figure 60: *Rheological viscosity of the longitudinal section in the channel center line of simulation (2). The viscosity decreases in periods of high shear forces (see panels one, two and six) whereas the internal structure can build up during slack water and the viscosity increases again (see panel three).*

than the clear water layer above due to the different viscous behavior and density effects (panel three and four).
A strongly stratified flow is formed during ebb tide. Panels five and six show the ebb currents where the velocity of the highly concentrated layers is much lower than that of the low-concentration layers. Moreover, the rheological viscosity increases with the increasing particle concentration.
Nevertheless, the gravitational effects due to the strongly stratified flow influence the system. The internal Froude number often becomes less than unity which indicates that gravitational flow predominates.

Entrainment of mud is induced due to turbulent shear forces of the overlying water layer. The isopycnal model does not yet include a sophisticated turbulence closure model so that the shear impact is underestimated. The **shear rate intensity** is determined with the formulation of Equation (3.5.19). The simulation results are shown in Figure 61. Hence, these are interfacial values; they effect the entire adjacent layer and the figures present the quantity per isopycnal layer. The shear rate intensity is an indicator of entrainment. The higher the shear rate intensity, the higher is the entrainment rate. However, the internal resistance of the suspension (the yield stress) has to be exceeded for entrainment to be initiated. The initiation of entrainment occurs particularly at the beginning of ebb tides and during flood tides where the velocities rapidly increase. Entrainment can be observed in panels two and three of Figure 52 in the area between the harbor basin and the advancing fluid mud front. In this area, the lower concentration layers (1005–1020 kg/m^3) are growing due to entrainment from the higher concentration layers below. The shear rate intensity is lowest during slack water at high tide (see panel two) but there are still velocity gradients between the layers of different mud concentration.

The fluid mud transport and development under tidal currents are evaluated qualitatively by comparing the simulation results with observations of the lutocline development according to Wang [2010]. This is illustrated in Figure 62. The observations were carried out over several tidal cycles at a specific location in the turbidity zone of the Ems Estuary (Leerort). The simulation results are taken from position 1. Apart from the different locations, the hydrodynamic conditions are not the same. Therefore, only a qualitative comparison is possible. However, both, simulation and observation, show the typical asymmetrical tide with high flood currents, long slack water at high tide as well as a long ebb phase. The different discharge conditions of the simulations emphasize the effect of variable hydrodynamic conditions. The observed lutocline was obtained from ADCP measurements by analyzing the backscatter signal. A high backscatter gradient indicates a high-density gradient in the water column. The suspended matter concentration just below the lutocline is in the range of 30 kg/m^3 (density $\approx$1020 kg/m^3) during slack water at high tide, as reported by Wang [2010]. The concentration in-

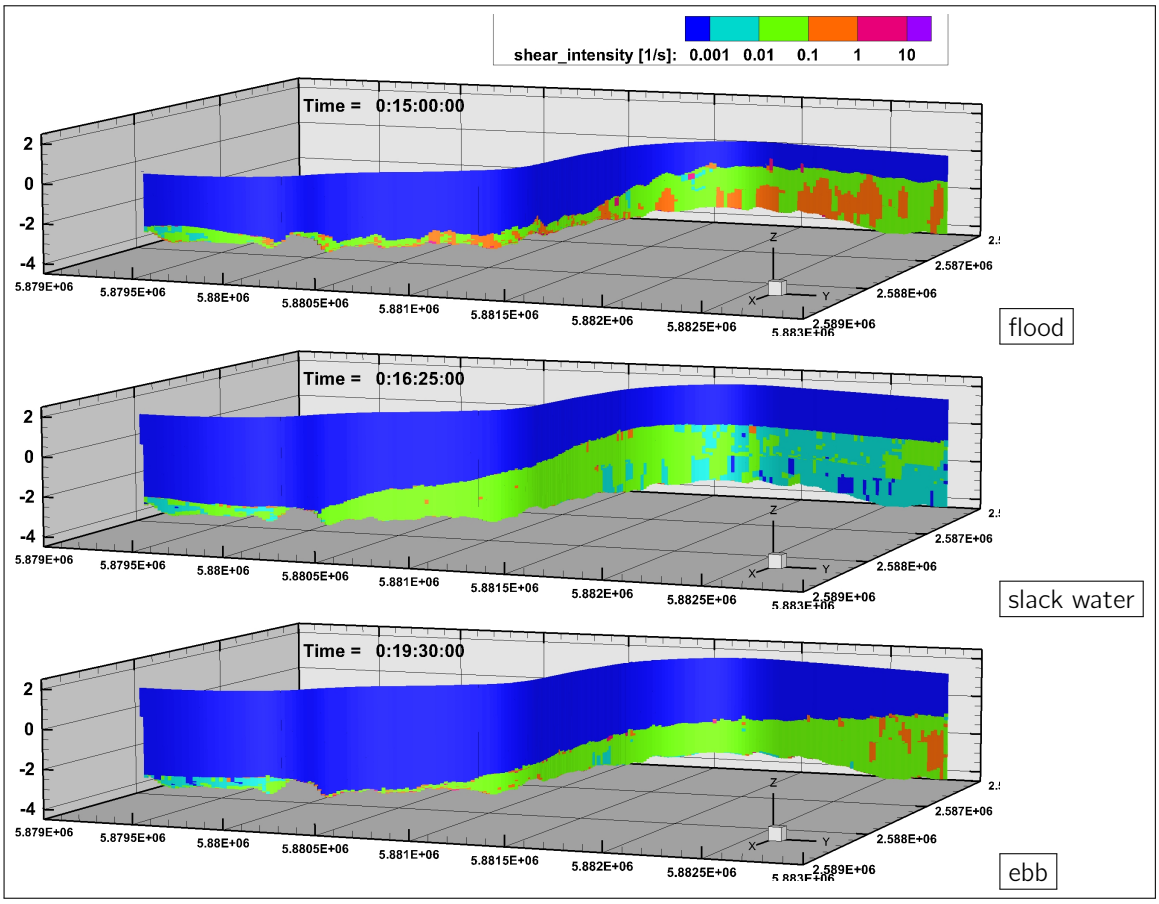

Figure 61: *Shear rate intensity of the longitudinal section in the channel center line of simulation (1).*
The shear rate intensity increases with increasing velocity gradients with respect to depth. This is the case especially during flood where fluid mud is entrained dependently on the shear rate intensity.

creases downward to the bottom. The simulated density stratification is followed by the subsurface elevation of the density layers. The lutocline is defined as the transition between Newtonian and non-Newtonian behavior which is accompanied by a sharp density gradient. This corresponds to the density layer with 1030 kg/m^3 of the simulations which is indicated in red in the graphics.

The suspended matter becomes mixed into the water column during flood tide. The observations show low backscatter gradients in the entire water column. This mixing process is represented in the model results due to the rapid increase in the layer thicknesses (subsurfaces) of the mud suspensions. The increasing layer thicknesses result from higher concentration layers being mixed with lower concentration layers due to entrainment and horizontal transport. A highly stable stratified system is then achieved in both cases during slack water. The fluid mud is carried downstream with the ebb currents which decreases the lutocline elevation. The intensifying ebb velocities progressively lower the lutocline level which is reproduced both in the simulations and in the observations. At the same time, the sharp transition between fluid mud and water body vanishes. The shapes of the simulated and observed lutoclines are very similar

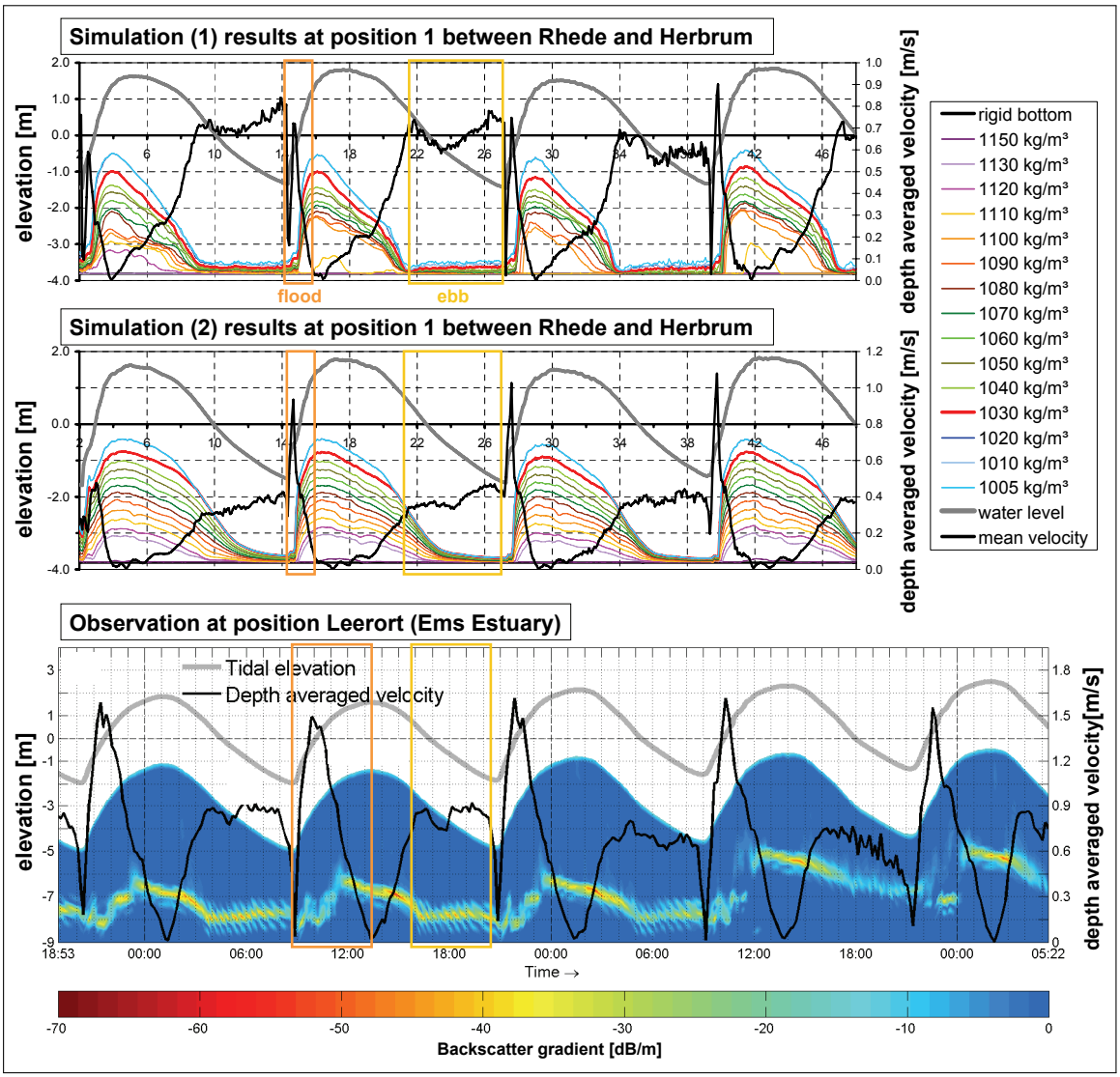

Figure 62: *Tidal dynamic of the lutocline - comparison between simulation results (upper two panels) and observations which result from 300 kHz ADCP measurements (lower panel). The density corresponding to the lutocline is 1030 kg/m^3 for the simulations. The lutocline is indicated by a high backscatter gradient in the measurements. It should be noted that the simulated and measured data are related to different locations and different hydrological situations. However, the characteristic development of the lutocline is very similar. (illustration of observations used with permission of Wang [2010]).*

and reveal comparable reactions to the tidal flow although the mixing process should be intensified in the simulations.

Concluding Remarks

The numerical model is able to simulate tidal-influenced fluid mud dynamics in a more complex topographic domain. The rheological viscosity approach predicts plausible results with respect to the velocity and density distribution. The comparison of the simulated and observed development of the lutocline leads to satisfying results. Owing to

the isopycnal approach, a highly stratified multi-layered flow is achieved during ebb tide and slack water. The density layers interact due to interfacial shear stresses, momentum transfer and mass transfer which enables formation, development and movement of the stratified fluid mud flow to take place. The density-driven flow is induced by the differences in the densities of the isopycnal layers which influence the flow at slack water in particular and results in internal waves caused by bottom gradients. The shear rate intensities increase during ebb and flood currents because the velocity differences are highest in that period. However, the shear intensities may be much higher when considering a turbulence closure model which would lead to higher entrainment rates. Further validation of the parameterized entrainment approach is needed for this matter.

The interfaces of the density layers are controlled at the open boundary at Rhede. They move with half of the water-surface amplitude. This steering assumption should be replaced by measured data for the dynamic movement of the lutocline in more advanced and realistic studies. These measurements should investigate the movement as well as the density gradient of the lutocline. In addition, the detection of more density horizons between the lutocline and the cohesive bed is needed for data input and validation of the model.

6.2 Model of Emden Harbor

Flow regimes of estuarine harbor basins are influenced by tidal currents, density effects due to salinity and suspended particle concentrations, the geometry of the harbor and the tidal conditions (in particular, the tidal range). Large-scale vortices are initiated depending on the flow direction of the river at the harbor entrance, see Figure 63. The tidal currents induce water exchange between the basin and the river depending on the tidal range. Additionally, density effects induce near-bottom inflow of the denser fluid and near-surface outflow of the low-density fluid (low suspended particle concentration and low salinity) during the flood tide. The flow directions reverse during ebb tide. The actual flow patterns are a superposition of all three effects. Nasner [2004] reports from observations in different German brackish harbors that the intensity of the velocity is lower during ebb tide than during flood tide which increases the tendency for siltation to occur in the harbor basins. Once the suspended sediment has been transported into the harbor basin, the probability of it being deposited is quite high owing to the very low currents.

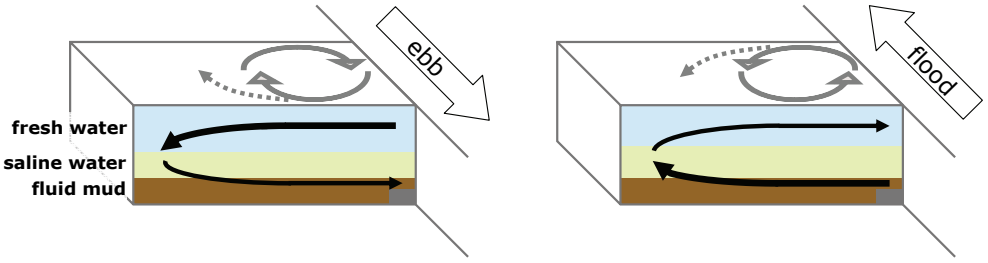

Figure 63: *Scheme of basic flow pattern in a harbor basin located in the brackish zone of an estuary.*
Flow regimes of estuarine harbor basins are influenced by tidal currents, density effects due to salinity and suspended particle concentration, the geometry of the harbor and the tidal conditions.

In this section, a system study is carried out on the Emden Outer Harbor with the fluid mud model. The harbor is located in the brackish water zone of the Ems Estuary, see Figure 64. The model domain extends from Dukegat, the open seaward boundary, to the weir at Herbrum, the closed boundary.
The boundary values are prescribed by measured data for the discharge at the weir at Herbrum and the water level at the open boundary. The model runs on a unstructured grid with increasing grid refinement in the harbor basin. Its vertical domain is discretized with eight isopycnal layers.

Nasner and Pieper [2009] carried out measurements in the Emden Outer Harbor to improve the knowledge of siltation mechanisms in harbor basins. Fluid mud samples were taken in the Emden Outer Harbor at four different depths and at six different positions. The results were averaged over the six positions and give information on the

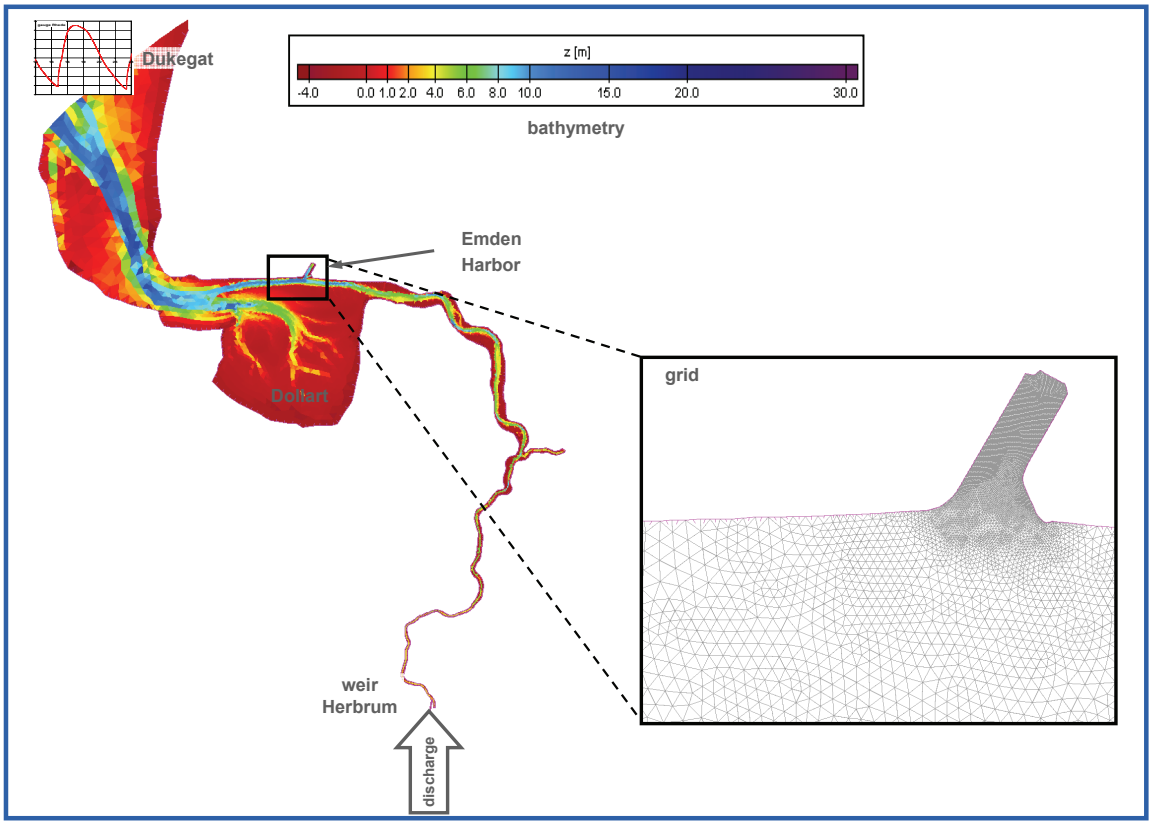

Figure 64: *Bathymetry and grid of the sectional model from Dukegat to Herbrum. A fresh water discharge is applied at the weir at Herbrum. A tidal signal is given at the seaward open boundary.*

density over depth. The range of the measured densities at four different horizons is as follows:

- high-frequency horizon - lutocline: 1020 to 1070 kg/m^3
- middle of fluid mud layer: 1060 to 1110 kg/m^3
- above low-frequency horizon: 1090 to 1140 kg/m^3
- below low-frequency horizon - consolidated mud layer: $>$ 1200 kg/m^3

The densities of the isopycnal layers are based on these measurements and are given in Table 7. Moreover, Table 7 and Figure 65 show the initial elevation of the isopycnal surfaces. The following parameters and processes specific to fluid mud are considered in the numerical simulations: the rheological viscosity varying with time and space, described by Equation (3.4.13), entrainment according to Equation (3.6.10) with the coefficient $C_f = 0.01$ and the settling velocity is determined by Equation (3.7.3) with regard to hindered settling and a gelling concentration of 40 kg/m^3. The simulation covers a period of two days, therefore consolidation is negligible in this simulation. Density currents are induced by differences in the density of the isopycnal layers. The density of the isopycnals is related to suspended sediment concentrations according to

layer number	density	mud concentration	isopycnal elevation
	[kg/m^3]	[kg/m^3]	[m]
8	1000	0.0	-0.47
7	1002	3.2	-7.00
6	1010	16.1	-8.50
5	1020	32.1	-8.75
4	1040	64.2	-9.00
3	1050	80.3	-9.30
2	1070	112.4	-10.50
1	1100	160.6	-11.00

Table 7: *Initial density distribution over depth with an initial water level of -0.47 m.*

the conceptual model (Section 3). Therefore, salinity effects are not considered in this study.

Simulation results of the velocities for the water body (-5 mNN horizon) and for the fluid mud body (-10mNN horizon) are presented in Figure 66. The results show the horizontal large-scale vortices at the entrance of the harbor during flood and ebb tide as they are described above. These vortices develop in the water layer as well as in the fluid mud body. The vortex in the fluid mud body is retained for longer than in the water body during slack water. This occurs on account of the viscous behavior and the barrier at the entrance of the harbor.
The water volume in the harbor adjusts to the tidal range. Thus, the basin empties after high tide and refills after low tide. This can be observed at the end of slack water where either inflow or outflow dominate and the vortex at the entrance has not yet built up. The barrier inhibits the near-bottom inflow and outflow which can be observed in the slice through the fluid mud body at a depth of -10 m.

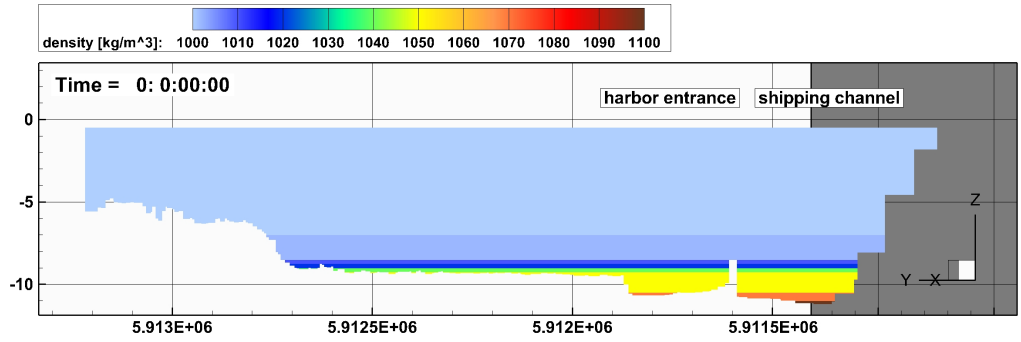

Figure 65: *Initial vertical density distribution in the center line of the harbor basin.*

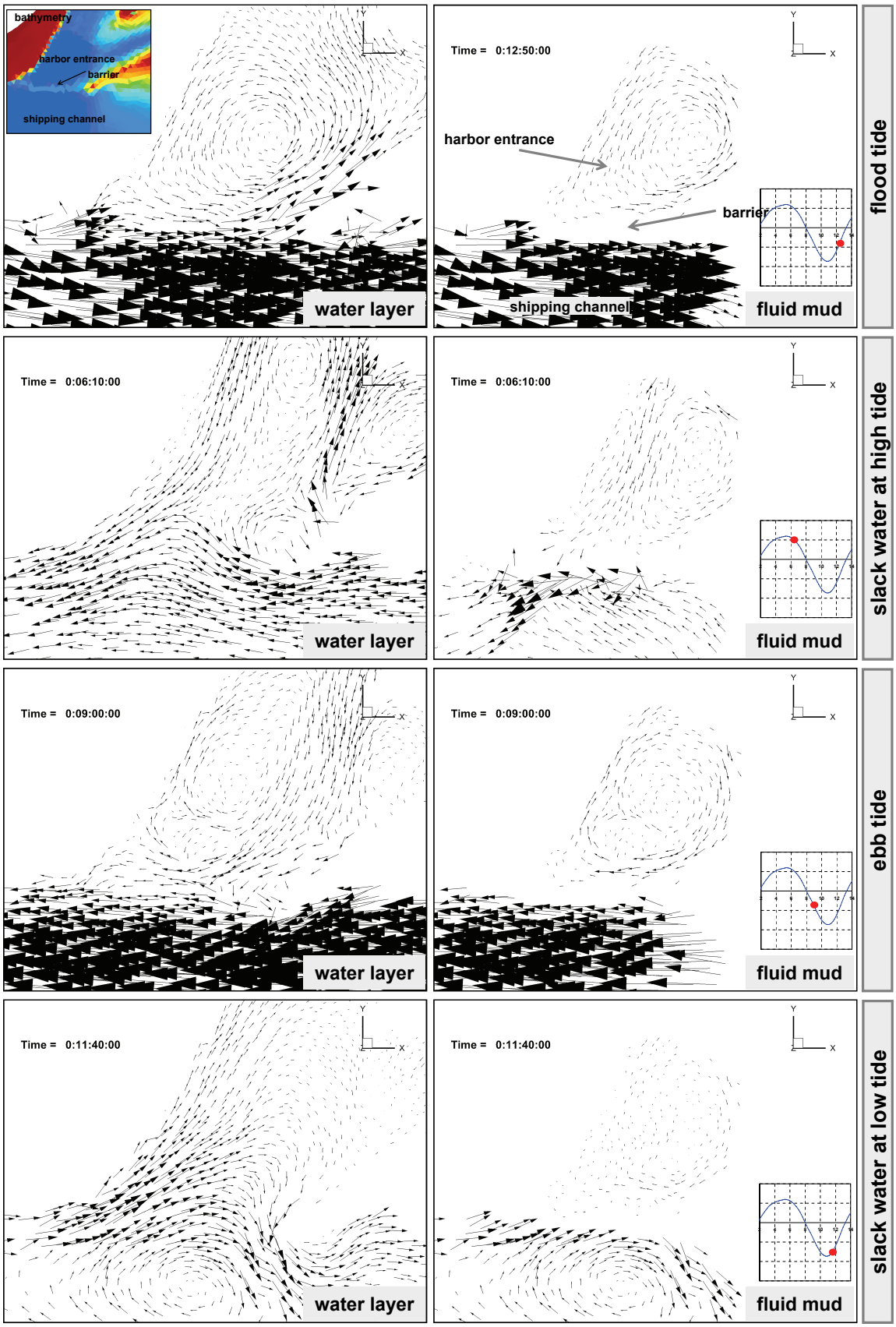

Figure 66: *Simulated velocity pattern in the entrance to the Emden harbor basin. (left side: z-slice through water body, right side: z-slice through fluid mud body near the bottom; the size of the vectors indicates the intensity)*

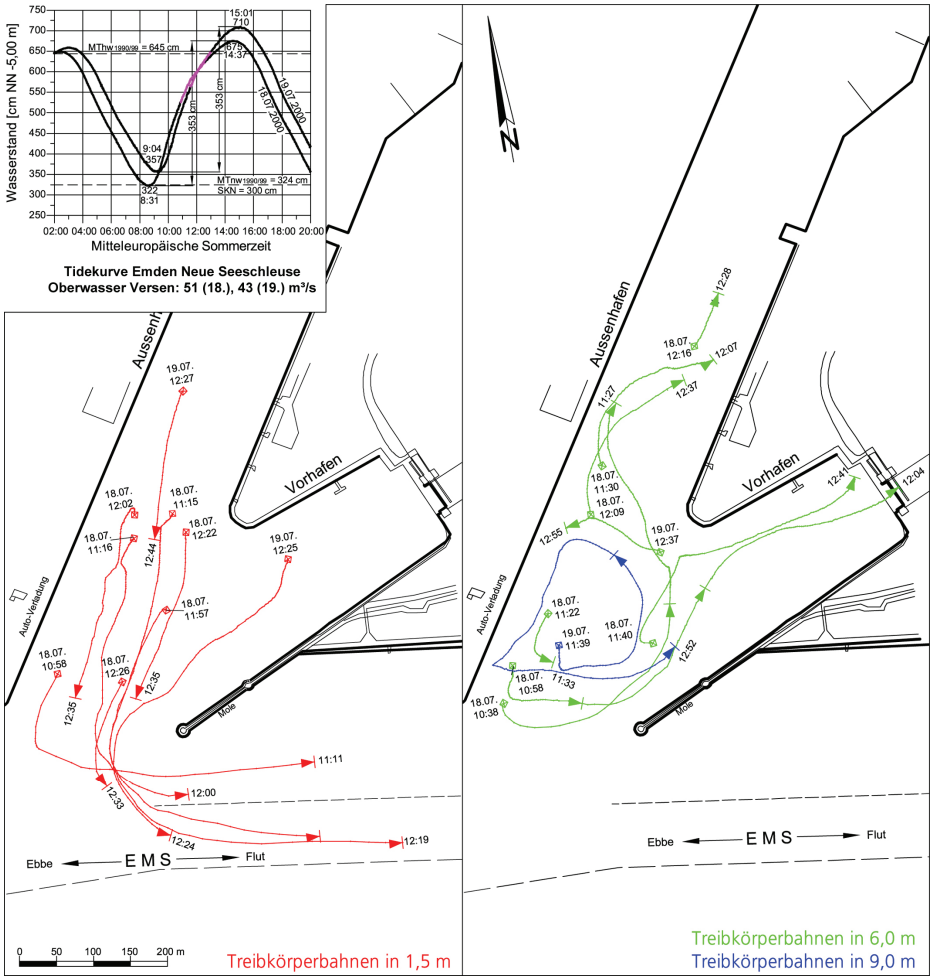

Figure 67: *Observed drift paths during flood currents.*
(in red: drift path at a depth of 1.5 m below the water surface; in green: at a depth of 6.0 m below the water surface; in blue: at a depth of 9.0 m below the water surface) (from Nasner [2004], with permission of the editor KFKI)

Investigations on tracking drift paths in the Emden Outer Harbor were carried out by Nasner [2004, 1997]. The observed drift paths of tracers show near-surface outflow and a near-bottom vortex which transports denser water into the harbor during flood tide (left panel of Figure 67). Thus, the simulated and observed near-bottom flow patterns are comparable whereas the near-surface results differ. Similar flow patterns were observed during a second period at the end of the flood phase, see the bottom panel of Figure 68. However, the observations at the beginning of the flood phase reveal a vortex over the entire water column (top panel of Figure 68) which are comparable to the simulated flow patterns (top panel of Figure 66).

Nasner and Pieper [2009] indicated the importance of a barrier forming at the entrance to a harbor basin. Such barriers prevent fluid mud from flowing out of the harbor basin. The height of the barrier is reduced in a second simulation run to study these effects. The velocity results are given in Figure 69 where the right panel shows the results with an increased barrier height and the left panel shows the results with a reduced

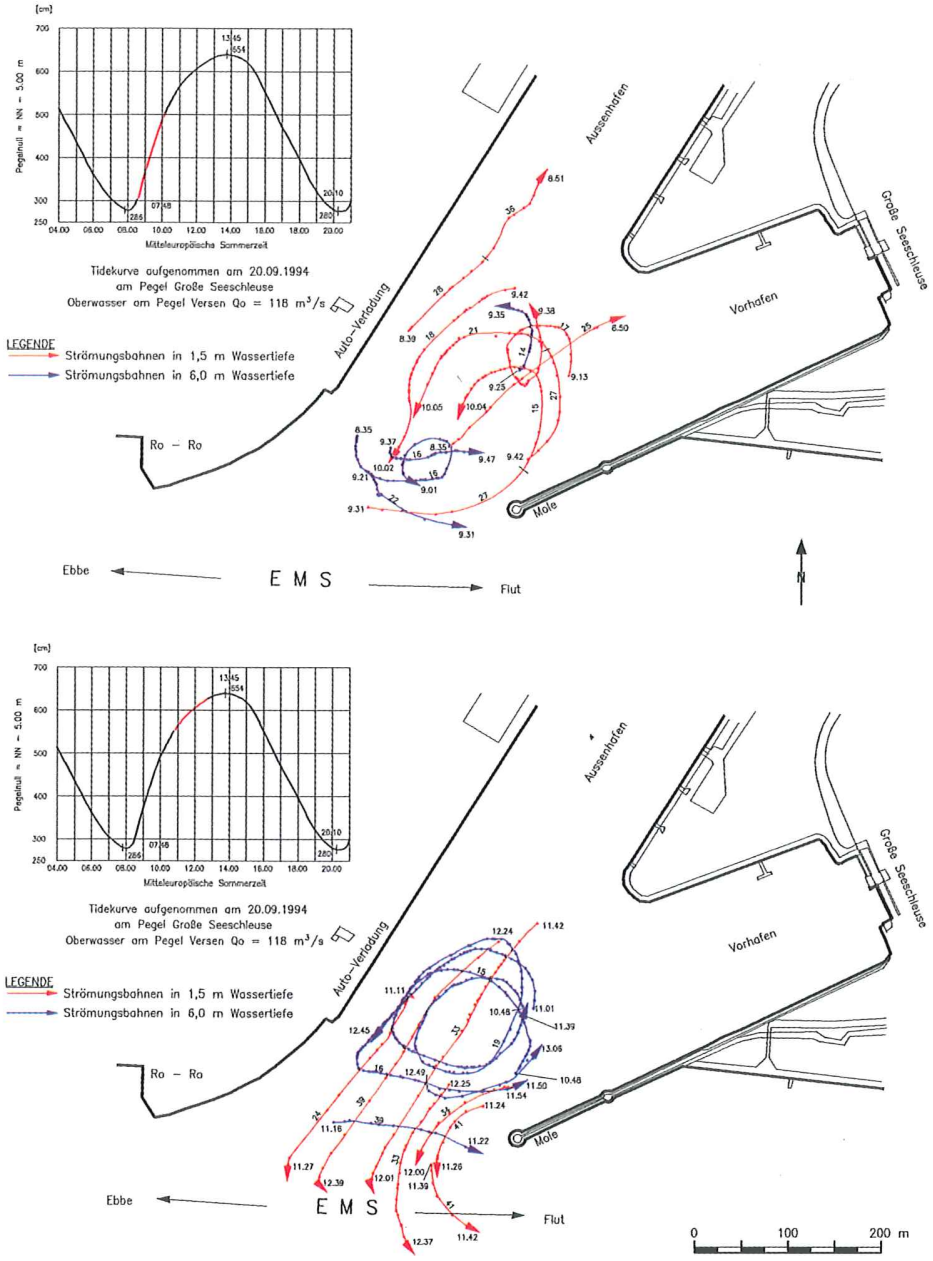

Figure 68: *Observed drift paths during flood currents.*
(in red: drift path at a depth of 1.5 m below the water surface; in blue: at a depth of 6.0 m below the water surface) (from Nasner [1997], with permission of the editor KFKI)

barrier height. The reduced barrier height intensifies near-bottom fluid (mud) exchange between the harbor basin and the river. Moreover, the flow increases at the rear of the basin during ebb as well as during flood tide. Further analysis of the residual transport over several tide cycles would be required to ascertain whether the imbalance changes between the inflow and outflow of suspended sediments and whether it influences the siltation in the harbor.

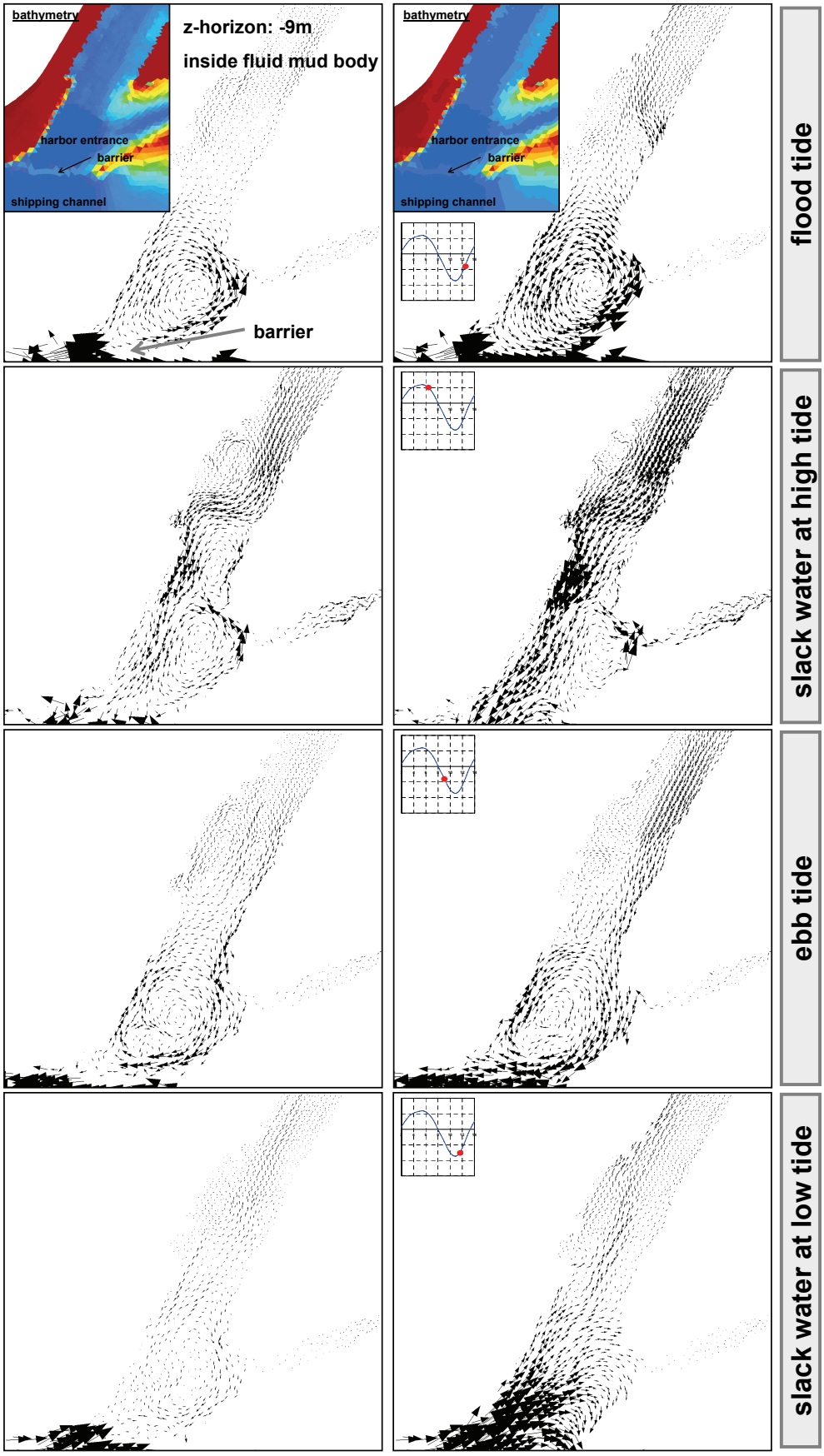

Figure 69: *Comparison of simulated velocity patterns in the fluid mud body at a depth of -9m with different ground sill heights at the entrance to the Emden harbor basin.*
(left side: increased barrier height, right side: reduced barrier height; the size of the vectors indicates the intensity)

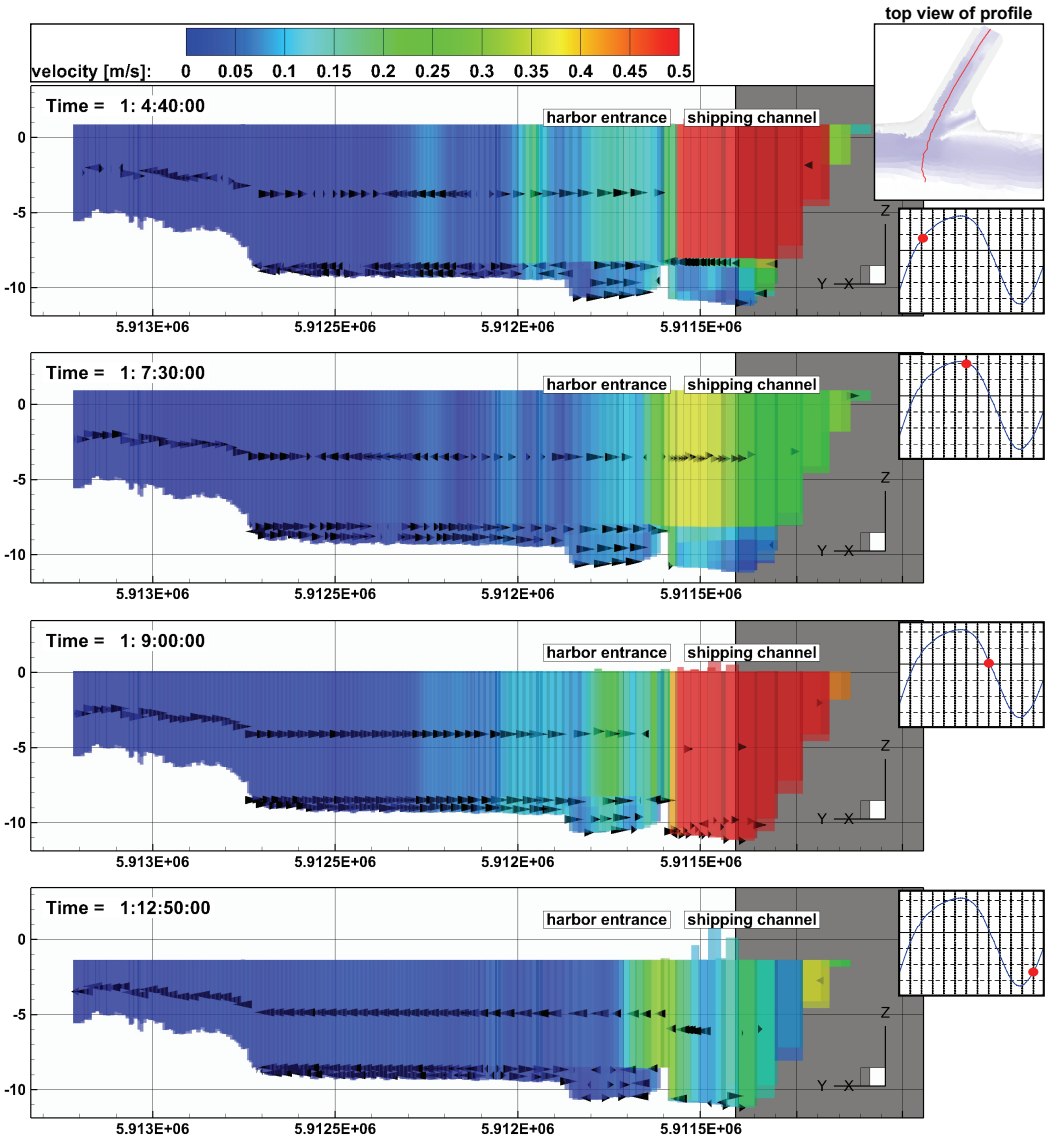

Figure 70: *Isopycnal layer-averaged velocities in the profile along the harbor basin with increased barrier height. (The vectors indicate the direction of the velocity but not the magnitude.)*

In addition, the velocity distribution is shown in a profile along the harbor basin with an increased barrier height in Figure 70 and a reduced barrier height in Figure 71. These results are only representative for this section. The water body is represented by two isopycnal layers and the fluid mud body by six layers, but not all layers are active all along. Their velocities are determined as layer-averaged values. The horizontal vortex develops in the region of the harbor entrance (indicated in the figure). Therefore, the flow directions become ambiguous in the profile view. Although the absolute velocities are rather small in the region behind the horizontal vortex, the flow directions become apparent. Fluid mud flows further into the harbor basin during flood tide (first panel) which corresponds to the observed drift paths in Figure 67 (left panel). At the beginning of the ebb tide, the fluid mud flows in the direction of the river while the water layer still fills up the basin (second panel). A further decrease in the water level then leads

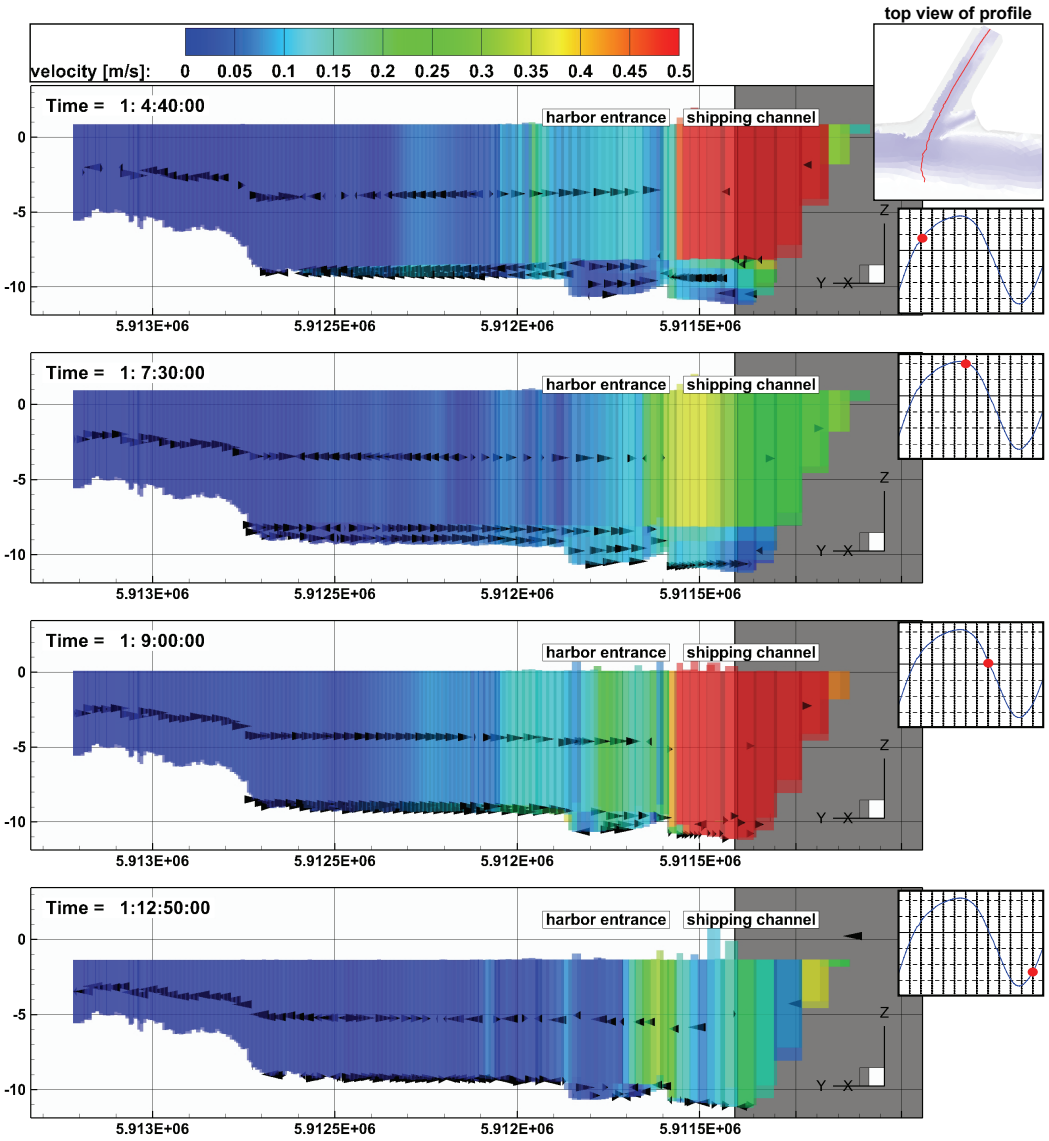

Figure 71: *Isopycnal layer-averaged velocities in the profile along the harbor basin with reduced barrier height. (The vectors indicate the direction of the velocity but not the magnitude.)*

to outflow over the entire water column. The change from outflow to inflow can be observed after slack water at low tide. Stratified flow becomes apparent not only in the different flow directions but also in the differences in the magnitude of the velocity. The near-bottom velocities increase in the harbor basin when the height of the barrier is reduced (see Figures 70 and 71). This effect can also be observed in the horizontal flow pattern of Figure 69.

The density distribution in particular shows the effect of changes in the height of the barrier, see Figure 72. The fluid mud layer maintains a specific thickness during the entire tidal cycle owing to the barrier (left panel). The fluid mud exchange between harbor basin and river is intensified by reducing the barrier height as described above. During ebb tide, the mud flows almost completely out of the harbor, apart from the deeper region at the harbor entrance. By contrast, the fluid mud thickness is similar in

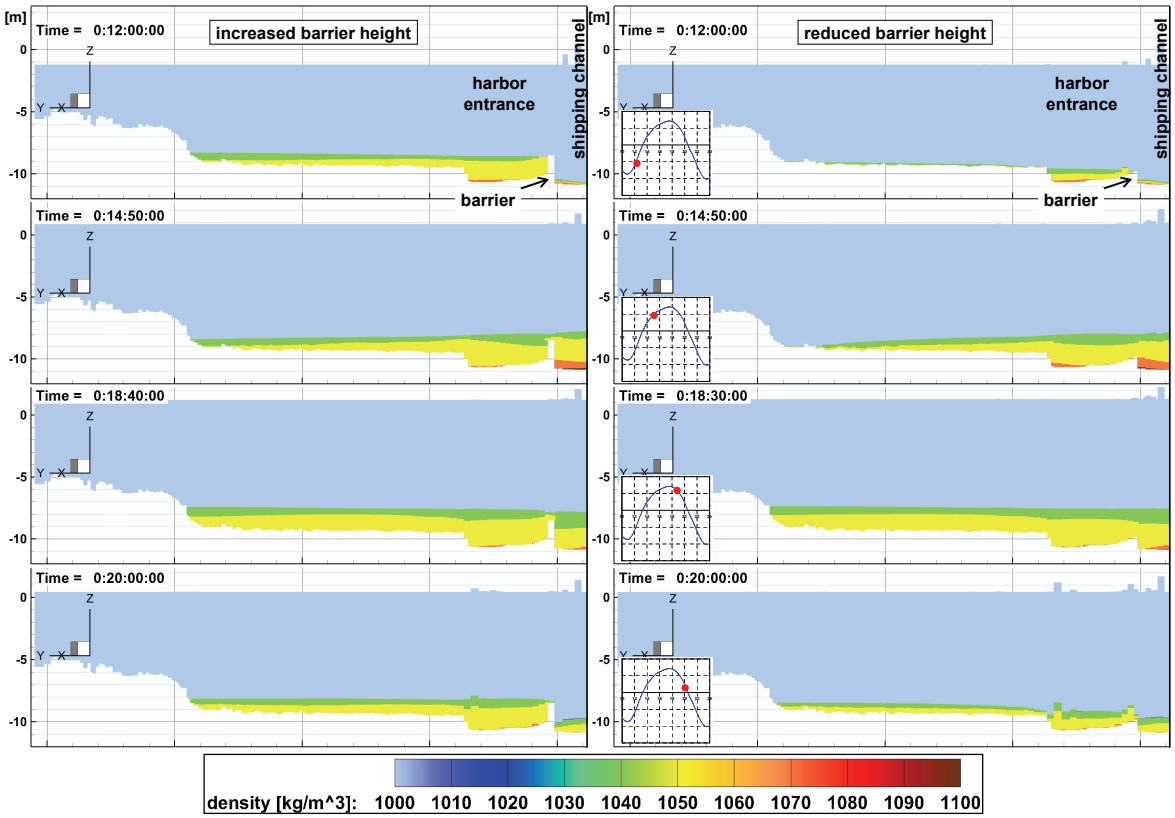

Figure 72: *Simulated density distribution in the profile along the harbor basin. The thickness of the fluid mud body decreases during ebb tide due to the reduced barrier height (right panel) compared with the results with a greater barrier height (left panel).*

both simulated scenarios at high tide (third panel). Observations show higher fluid mud thicknesses compared with the modeled thicknesses and the fluid mud reaches into the rear of the harbor, see Figure 73. This may result from long-term mud accumulations and consolidation processes which could not be achieved by the simulation of two tidal cycles. Moreover, the simulation shows shortcomings concerning the suspended sediment transport with the upper water body by which cohesive material can be transported into the rear of the basin.

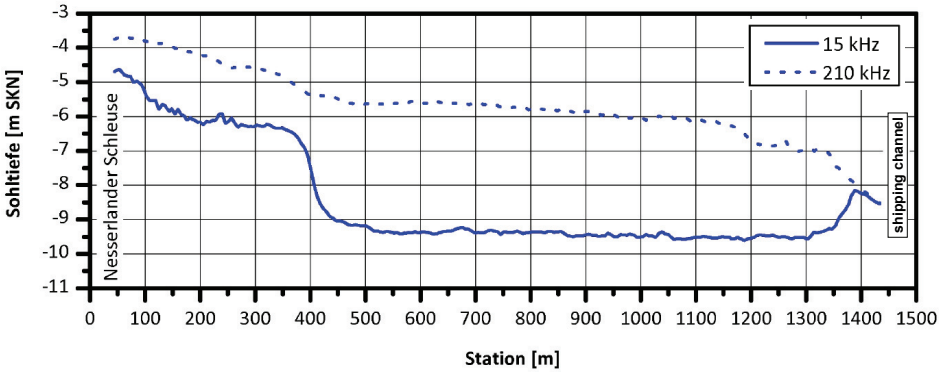

Figure 73: *Observed fluid mud layer thicknesses in the Emden Outer Harbor by echo sounder measurements with different frequencies (provided by Nasner [2004], modified figure).*

Concluding Remarks

It can be demonstrated that this system study can contribute to improving the understanding of constructional effects on fluid mud dynamics by using such a model.

The differences between the simulated and observed velocities can result from different discharge situations, differences in the actual tidal range, the thickness of the fluid mud body in the simulations being lower than the observed thickness and certainly from neglecting salinity in the numerical simulation. The harbor is located in the brackish zone which leads to additional stratification due to salinity. The simulated density-induced flow pattern results only from the suspended particle concentration. These near-bottom and near-surface flow patterns in opposite directions remain longer in the observations which may indicate that the contribution of the salinity to the density effect is greater than that of the suspended particle concentration. Further investigations with a better representation of the water body would be required to improve the density effects. Nevertheless, the simulation results are plausible and explainable with respect to these aspects.

The development of fluid mud is triggered by the initial conditions and by the boundary conditions of the model run. Therefore, improvement of the simulated formation and occurrence of fluid mud in the model domain can be achieved, for example, by:

- improvement of the initial conditions based on observations of the occurrence and the layer thicknesses of fluid mud
- simulation of a longer period of time to achieve an equilibrium and a realistic situation based on a model set-up not necessarily based on observations

The current implementation of the numerical model has the status of a research code. It will require additional work on serial optimization and parallelization to achieve more efficient simulation times. The simulations presented give an impression of the computational effort: the model (13433 vertices, 25269 polygons and 38701 sides) runs with a real time to run time relationship of 1:1.7 to 1:7 on a computer with a xeon processor using one CPU of a node. The range of the run time period depends on the output data and output intervals and on the parameterized physical processes under consideration.

7 Conclusions and Perspective

The aim of this thesis is the numerical simulation of the flow behavior, transport, formation and resuspension of fluid mud to enhance the understanding of fluid mud dynamics. This has been realized by a hydrodynamic model in isopycnal coordinates. The extension of an existing numerical model contributes to achieving a better understanding of fluid mud dynamics in coastal areas, estuaries and harbors.
This section summarizes the achievements of this thesis and gives recommendations for future research.

Achievements of this thesis

The occurrence of fluid mud is observed in single layer as well as in multi-layer systems. The fluid mud body can vary from a few decimeters to several meters in thickness. These high concentration layers lead to stable stratified flow in a low-concentration suspension when mixing is insignificant. Then strong density gradients exist between the water body and the fluid mud body. For this reason, an isopycnal numerical approach becomes promising. The developments for the simulation of fluid mud dynamics are therefore based on a three-dimensional hydrodynamic isopycnal model approach. The characteristics of the **numerical method** are as follows (Section 4, Appendix A and B):

- isopycnal discretization enables a three-dimensional resolution of the fluid mud body with a low degree of discretization and little computational effort
- the isopycnal approach resolves the density stratification and the velocity profile within the fluid mud body
- layer thicknesses vary with the transition to different states of suspension, the formation, resuspension, settling and advective and gravitational transport of fluid mud
- the numerical implementation is based on a numerical discretization in vertical direction by z- and ϱ-layers, in horizontal direction by unstructured grids and in time
- communication of the isopycnal layers is realized due to momentum transfer, vertical mass transfer and interfacial shear stresses

The implementation of the three-dimensional discretization scheme has been verified by a comparison between simulated and analytically determined propagation of an internal standing wave (Section 5.1).

The vertical transport processes, which lead to formation and resuspension of fluid mud, are predominated by hindered settling and entrainment. This requires the thickness of the density layers to vary with time and in accordance with the actual mass transport rates. Vertical mass transfer between isopycnal layers was derived for a three-dimensional system (x, y, ϱ) by conserving volume and mass (Section 4.3 and Appendix B). The functionality of the extended numerical model was evaluated as follows:

- By applying a settling velocity formulation with hindered settling (Section 5.2), the mass transfer approach has lead to reasonable results for a sedimentation tank in which the transition from a well-mixed system to a stratified system was reproduced.
- The mixing of a stratified system has been studied in the stratified flow over a ground sill (Section 5.3). The interfacial shear intensity increases near the ground sill, initiating the entrainment of fluid mud into the water body above.

A method was presented for the integration of **non-Newtonian flow behavior** in a numerical model based on the Reynolds-averaged Navier-Stokes equations. The model has the capability to simulate the non-Newtonian flow of fluid mud by introducing a rheological viscosity to parameterize the rheology depending on shear impact and particle concentration. The rheological model describes the structural break-up and recovery of aggregates in a mud suspension (Section 3.4). Furthermore, only the relevant internal stress terms of the stress tensor are taken into account in the momentum equation. The rheological viscosity is no longer a constant such as the molecular viscosity but is now a time-dependent and process-descriptive parameter. It is possible to apply different rheological models in this way. Such rheological parameterizations can also be used for the transport of mud in pipelines or the determination of the nautical depth.
The isopycnal numerical model described above was extended by using the rheological viscosity in the same way as the turbulent viscosity in the Reynolds-averaged Navier-Stokes equations. Although the rheological viscosity determines both the Newtonian and non-Newtonian flow behavior of suspensions, the character of the differential momentum equations remains unchanged. Internal friction and interfacial shear stresses are now related to the rheological behavior of the mud suspension and are taken into account in the numerical solution.
The rheology of fluid mud is described as a viscoplastic shear-thinning fluid by applying a parameterized Worrall-Tuliani model (Section 3.4.2). The model considers a yield stress and the break-up and recovery of the microscopic structure (aggregates of cohesive sediments). These parameters are calculated as a function of the shear impact and solid volume concentration. The entire water column is modeled with this approach as it not only covers the non-Newtonian behavior of high-concentration suspensions

but also the Newtonian behavior of low-concentration suspensions and of clear water. The shear-thinning behavior has been studied phenomenologically and it was feasible to reproduce the shear-thinning behavior in the study of the Ems river section from Rhede to the weir at Herbrum in which stratified flow in a tidal influenced system was investigated (Section 6.1). The influence of the rheological behavior on high-concentration flow was analyzed by a study of flow on an inclined plane (Section 5.4). This effect was compared to the influence of gravitational forcing due to density differences which has shown to be the dominant process for this test case.

Fluid mud dynamics under the influence of tidal currents have been investigated on two model domains of the Ems Estuary (Section 6):

- Fluid mud formation, advective and gravitational transport and resuspension are periodic processes in tidal systems.
- Strong stratified flow develops during slack water at high tide and during ebb tide in the fairway.
- The rheological viscosities determined as a function of the shear rate and density show plausible results and influence the velocities of the stratified flow.
- A qualitative comparison of the simulated fluid mud formations and the observed development of the lutocline shows similar results (Section 6.1).
- Simulation of tidal and density-induced currents result in similarly stratified flow patterns observed by measurements in the Emden Outer Harbor (Section 6.2).

These applications demonstrate that the developed numerical model approach enables the simulation of three-dimensional fluid mud dynamics.

Recommendations for Future Research

The developed numerical model is capable to simulate fluid mud dynamics in systems such as harbor basins and river sections where high-concentration flow and fluid mud formations predominate the system.
The numerical model applies an appropriate resolution of the fluid mud body according to isopycnal layers which is presented in Sections 5 and 6. Each isopycnal layer represents a single phase fluid/suspension with a specific particle concentration and specific rheological properties. The isopycnal layer may become very thin or even reach zero thickness depending on the transport and development of the cohesive mud suspensions. The three-dimensional isopycnal model is applied to the entire water column from the consolidated bed to the free surface in the model applications of this thesis. The simulation of the dynamics of highly concentrated mud suspensions shows reasonable

results. However, the numerical approach limits the flow to a stable stratification. This assumption does not always applies in highly turbulent flows with suspended sediments. In particular, the presence of suspended sediment transport and baroclinic processes may result in an **unstable stratification** in estuaries. It will need further investigations on the simulation of the low concentrated water body to enable the comprehensive modeling of estuarine systems. Basically, there are three possible solutions to obtain a more sophisticated model of the water body.

- The first solution can be obtained by implementing the approach for non-Newtonian shear stresses in an established hydrodynamic model with Cartesian coordinates with z- or σ-layers. The flow behavior of fluid mud is then described by parameterizations of the rheological viscosity such as it is done in this thesis. In this case, the main issue will be the realization of strong stratifications which directly influences the internal shear stresses. This will require very fine vertical resolutions (centimeters to decimeters) in regions where high-concentration suspensions can occur in the model domain.

- The second solution can be achieved by coupling the isopycnal model with an existing and established hydrodynamic model such as UnTRIM [Casulli and Walters, 2000; Casulli and Lang, 2004], Telemac [Hervouet and Bates, 2000; Electricité de France, 2000] or Delft3D [Lesser et al., 2004; Gerritsen et al., 2007]. The isopycnal numerical model functions then as a module representing the fluid mud body. The suspended sediment and salt transport simulation is performed by the hydrodynamic model. The isopycnal fluid mud module would become active in case of fluid mud formation by exceeding the threshold from Newtonian to non-Newtonian flow or a specific mud concentration. The module will only be activated in model domains with cohesive sediment accumulations which reduces the computational effort for large model domains with different transport regimes such as those in estuaries.

- The third concept comprises a holistic model approach by modeling the domain from consolidated bet to water surface in once. In Section A, the conceptual model was derived for a three-dimensional method with a vertical discretization by z- and ϱ-layers. This method can be used to resolve the water body with the addition of a z-layer-based discretization inside an isopycnal layer. The z-layer resolution is usually in the range of 0.5 m to 2.0 m. This resolution is too coarse to permit discretization of the fluid mud body. The additional density layers therefore enable the thin and highly variable high-concentration suspensions to be simulated as it is presented in this thesis (see Figure 24). Following this approach, further developments are required to simulate suspended sediment transport and salt transport by solving the advection-diffusion equation. This transport will

also affect the density distribution. A possible solution is to allow small density differences within an isopycnal layer as long as the average densities of the adjacent isopycnal layers guarantee stable stratification. Accordingly, the 3D vertical mass transfer approach (Appendix B) has to be extended for a vertically resolved system by z- and ϱ-layers.

All three concepts will require further developments, research and software engineering work for comprehensive modeling of estuarine systems.
The first concept is the most pragmatical solution of the three concepts and requires limited work on further developments. However, strong stratified flow is difficult to maintain in z- and σ-layer based models [Rennau and Burchard, 2009]. These discretization schemes can lead to unwanted numerical mixing. In case of σ-layers, a numerical, baroclinic pressure gradient error occurs which can produce wrong velocities [Mellor et al., 1998] (work on improvements e.g. Liu and Huang [2008]). Hence, it has to be proven that the high vertical resolutions are sufficient to reach and preserve strong stratifications. In addition, the computational effort can rapidly increase as a consequence of the high resolutions. The practicability depends therefore not only on the realization of strong stratifications but also on the available computer capacities.
The third concept (scalar transport by allowing small density differences inside isopycnals and combined vertical resolution by z- and ϱ-layers) has the highest complexity and uncertainties from the current perspective. The advantage of this concept is the holistic approach by modeling the water body and fluid mud body in one system which means being independent from effects of model coupling. At the same time, it is taken advantage of the properties of the z- and ϱ-layer discretization. This model concept will need a lot of additional developments and implementations for the simulation of low-concentration hydrodynamics to reach a comparable state such as the advanced 3D hydrodynamic models mentioned above.
Coupling of the isopycnal fluid mud model with an advanced hydrodynamic model (second concept) appears to be a promising and practicable solution for modeling fluid mud dynamics in practical applications of estuarine environments. This enables still to utilize the optimal vertical discretization for each problem – isopycnals for fluid mud dynamics and z- or σ-layers for low-concentration hydrodynamics – but independently applied. In this case, the communication of the models will require further investigations on both software engineering and description of physical processes. One aspect thereof is described in the next paragraph.
Following the second concept, further investigations into an **implicit mass transfer approach** may be advantageous. The explicit approach, derived in Section 4.3 and Appendix B, requires rather small time steps to be accurate.

This thesis focuses on the interfacial and internal friction resulting from the rheological behavior. However, the internal shear stresses are also influenced by turbulence.

In nature, fluid mud flows become laminar as the turbulence is destroyed due to density stratification. On the other hand, rheology changes from non-Newtonian to Newtonian behavior as the mud concentration decreases in the water body and turbulence may arise at the same time. Turbulence interacts with the suspended particles due to turbulence damping and buoyancy effects which influence the settling velocity. Thus, in the highly concentrated, stratified areas, the flow behavior is characterized by the rheological viscosity whereas the turbulent viscosity is dominant in low-concentration, mixed areas. Both **rheology and turbulence** are modeled with a similar conceptual model as described above. They are taken into account through a viscosity and result in a deceleration of the average velocity with increasing viscosities (internal friction). However, their physical effect is contradictory. Whereas the rheological viscosity leads to laminar and stratified flow as its magnitude increases, increasing turbulent viscosity, on the other hand, intensifies turbulent mixing and may cause unstable stratifications. Accordingly, research on the interaction between rheological and turbulent viscosity will be important for progressive fluid mud and suspended sediment transport modeling. The focus should be on the transitional area between fluid mud and dilute suspension as well as on the formation process and the resuspension of fluid mud as both quantities may reach considerable magnitudes during resuspension or entrainment. A general approach using the viscosity should combine rheology and turbulence modeling and take account of the solids concentration, shear conditions and structural mechanisms (e.g. flocculation) for the overall water body.
The improvement of the turbulence model will also affect the entrainment of fluid mud which is basically induced by turbulent interfacial shear stresses. Another aspect worth investigating is the influence of fluid mud formation in large areas and of sizable thickness on the internal friction in estuarine systems. Turbulence will be damped during periods of high stratification and internal friction is built up by the rheological viscosity. The shear-thinning behavior of fluid mud may then lead to relatively small rheological viscosities once the fluid mud moves with the tidal currents. Compared to the magnitudes of the rheological viscosities, the turbulent viscosities can reach much higher magnitudes in a turbulence-dominated system. This aspect and the reduced bottom friction of the water body flowing above the fluid mud body may lead to a larger tidal range in estuaries (see description of tidal dynamics in Malcherek [2010]).

Further process-based improvements and validation of the fluid mud model will require additional comparisons with laboratory studies and **field measurements**. Observation of the development of fluid mud involves measurements not only of the lutocline movement but also of the density stratification below the lutocline and the velocity distribution inside the fluid mud body. These types of measurement are subject of ongoing research into highly dynamic systems as it is difficult to perform measurements in a highly concentrated medium. These measurements should allow to relate specific

observed phenomena to physical processes. In tidal systems, the physical processes are strongly related to the tidal cycle. Therefore, it is necessary to obtain continuous information in tidal systems (e.g. at least one tidal cycle).

An additional impact on fluid mud or consolidated mud, in particular, is induced by **waves** which become important in shallow areas such as tidal flats. Waves can initiate the fluidization of consolidated mud so that the mud reverts to a fluid state. This means that further investigations into the quantitative description of the rheological viscosity in relationship to the oscillatory wave impact are required. The rheology can be characterized by viscoelastic behavior which may be measured under oscillating shear conditions. In this case, the consolidated mud bed exhibits elastic behavior on exposure to short and periodic shear impact whereas the mud behaves as a viscous fluid once it has been fluidized. Modeling the wave impact will additionally require the coupling with a spectral wave model. The impact of the waves can be described by the relationship between shear stress and the wave amplitude and wave period in a similar way as it is applied for wave-induced sediment transport [Malcherek and Knoch, 2006].

The characteristic flow behavior of fluid mud can be reproduced by considering a mud suspension comprising only cohesive sediments and water. However, there are several aspects from which we can learn and gain a better understanding of the flow behavior under different conditions. Some of these aspects are **biology**, **dissolved oxygen** and **mud-sand mixtures** (considering grains larger than 63 μm).

Appendices

A 3D Unstructured Isopycnal Model with Combined Vertical Discretization of z-layers and ϱ-layers

A.1 Governing Equations

In this section, the numerical method is presented for a (x, y, z, ϱ)-coordinate model on an unstructured horizontal grid resolution. A scheme of this model is shown in Figure 24 of Section 4.4. The governing equations and the basic principle of the isopycnal model are described in Section 4.1. The isopycnal approach is combined with the concept for a vertical z-layer-based discretization scheme according to Casulli and Walters [2000]. In the following, the resulting numerical approximation and solution algorithm are derived. The combination of isopycnal and z-layer-based vertical resolution can lead to a single isopycnal layer resolved by one or more z-layers or a single z-layer resolved by one or more isopycnals. An implementation of this model approach was provided by Prof. V. Casulli of the University of Trento, Italy. Furthermore, the model approach and implementation are extended for the simulation of shear-dependent viscosity with a non-Newtonian approach and for vertical mass transfer between isopycnal layers which is introduced for an unstructured 3D approach in (x, y, ϱ)-coordinates. According to Section 4.1, a definite number M of isopycnal layers with a specific density is predefined. The governing equations are discretized for the parameter ϱ. Now the momentum equations of the four parameters (x, y, z, ϱ) result in

$$\frac{\partial u_m}{\partial t} + u_m\frac{\partial u_m}{\partial x} + v_m\frac{\partial u_m}{\partial y} + w_m\frac{\partial u_m}{\partial z} = -g\frac{\partial}{\partial x}\left(\sum_{l=m}^{M}\frac{\varrho_l - \varrho_{l_t}}{\varrho_r}\eta_l\right) + \nu^h\left(\frac{\partial^2 u_m}{\partial x^2} + \frac{\partial^2 u_m}{\partial y^2}\right) + \frac{\partial}{\partial z}\left(\nu^v\frac{\partial u_m}{\partial z}\right) \tag{A.1.1a}$$

$$\frac{\partial v_m}{\partial t} + u_m\frac{\partial v_m}{\partial x} + v_m\frac{\partial v_m}{\partial y} + w_m\frac{\partial v_m}{\partial z} = -g\frac{\partial}{\partial y}\left(\sum_{l=m}^{M}\frac{\varrho_l - \varrho_{l_t}}{\varrho_r}\eta_l\right) + \nu^h\left(\frac{\partial^2 v_m}{\partial x^2} + \frac{\partial^2 v_m}{\partial y^2}\right) + \frac{\partial}{\partial z}\left(\nu^v\frac{\partial v_m}{\partial z}\right) \tag{A.1.1b}$$

where z ranges from η_{m_b} to η_m. These are the isopycnal, Reynolds-averaged momentum equations after applying the hydrostatic pressure assumption and assuming an incompressible Newtonian fluid. The last two terms represent the internal stresses of a Newtonian fluid (see Section 2.4.4) which is indicated by treating the viscosity, in this case the horizontal component, as a constant. However, in the following, the

viscosity is considered as variable in space and time and dependent on the shear rate. The viscosity consists of two components, these being the function of the rheological viscosity $\nu_r = f\left(\mathbf{x}, t, \varrho, |\mathbb{II}_D|, ...\right)$ determined by rheological constitutive formulations (for a further description see Section 3.4 and 3.5), and the turbulent viscosity ν_t, which is set constant for the m-th layer. The dependence and interaction of the two viscosity components is not yet known and has to be specified in future. In this thesis t is assumed that the horizontal and vertical viscosities can be treated as a sum of both

$$\nu_m^h = \nu_{r,m} + \nu_{t,m}^h \quad \text{and} \quad \nu_m^v = \nu_{r,m} + \nu_{t,m}^v. \tag{A.1.2}$$

The rheological viscosity has no vectorized components and its horizontal and vertical values are equal.

The stress terms need to be adapted for the simulation of the behavior of high-concentration suspensions, which is non-Newtonian. The non-Newtonian fluid behavior is approximated by means of the rheological viscosity and the most important internal stress components, identified by dimensional analysis in Section 3.3. With this approximation, the solution algorithm is still applicable. This leads to a reformulation of the viscosity terms of Equation (A.1.1)

$$\ldots + \frac{\partial}{\partial x}\left(\nu_m^h \frac{\partial u_m}{\partial x}\right) + \frac{\partial}{\partial y}\left(\nu_m^h \frac{\partial u_m}{\partial y}\right) + \frac{\partial}{\partial z}\left(\nu_m^v \frac{\partial u_m}{\partial z}\right) \tag{A.1.3a}$$

$$\ldots + \frac{\partial}{\partial x}\left(\nu_m^h \frac{\partial v_m}{\partial x}\right) + \frac{\partial}{\partial y}\left(\nu_m^h \frac{\partial v_m}{\partial y}\right) + \frac{\partial}{\partial z}\left(\nu_m^v \frac{\partial v_m}{\partial z}\right). \tag{A.1.3b}$$

The free surface equation is derived by integrating the continuity equation

$$\frac{\partial u_m}{\partial x} + \frac{\partial v_m}{\partial y} + \frac{\partial w_m}{\partial z} = 0 \tag{A.1.4}$$

with respect to the m-th layer thickness. As the sum of the spatial velocity derivatives is taken to be zero, its integral is also zero. The integral covers the thickness $\Delta\eta_m = \eta_m - \eta_{m_b}$ of the current isopycnal layer m and results in

$$\begin{aligned} 0 &= \int_{\eta_{m_b}}^{\eta_m} \left(\frac{\partial u_m}{\partial x} + \frac{\partial v_m}{\partial y} + \frac{\partial w_m}{\partial z}\right) dz \\ &= \int_{\eta_{m_b}}^{\eta_m} \frac{\partial u_m}{\partial x} dz + \int_{\eta_{m_b}}^{\eta_m} \frac{\partial v_m}{\partial y} dz + \int_{\eta_{m_b}}^{\eta_m} \frac{\partial w_m}{\partial z} dz. \end{aligned} \tag{A.1.5}$$

By considering the Leibniz-Law the equation is modified to [Malcherek, 2001]

$$\begin{aligned} 0 &= \frac{\partial}{\partial x}\left[\int_{\eta_{m_b}}^{\eta_m} u_m dz\right] - u_m \frac{\partial \eta_m}{\partial x} + u_{m_b} \frac{\partial \eta_{m_b}}{\partial x} \\ &+ \frac{\partial}{\partial y}\left[\int_{\eta_{m_b}}^{\eta_m} v_m dz\right] - v_m \frac{\partial \eta_m}{\partial x} + v_{m_b} \frac{\partial \eta_{m_b}}{\partial x} \\ &+ w_m - w_{m_b}. \end{aligned} \tag{A.1.6}$$

The kinematic conditions for the surface and bottom of the m-th layer are

$$w_m = \frac{d\eta_m}{dt} = \frac{\partial \eta_m}{\partial t} + u_m \frac{\partial \eta_m}{\partial x} + v_m \frac{\partial \eta_m}{\partial y} \tag{A.1.7a}$$

$$w_{m_b} = \frac{d\eta_{m_b}}{dt} = \frac{\partial \eta_{m_b}}{\partial t} + u_{m_b} \frac{\partial \eta_{m_b}}{\partial x} + v_{m_b} \frac{\partial \eta_{m_b}}{\partial y}. \tag{A.1.7b}$$

They can be extracted from Equation (A.1.6)

$$\begin{aligned} 0 \;=\; & \frac{\partial}{\partial x}\left[\int_{\eta_{m_b}}^{\eta_m} u_m \, dz\right] + \frac{\partial}{\partial y}\left[\int_{\eta_{m_b}}^{\eta_m} v_m \, dz\right] \\ - \; & \underbrace{u_m \frac{\partial \eta_m}{\partial x} - v_m \frac{\partial \eta_m}{\partial x} + w_m}_{\text{free surface condition for the m-th layer}} \\ + \; & \underbrace{u_{m_b} \frac{\partial \eta_{m_b}}{\partial x} + v_{m_b} \frac{\partial \eta_{m_b}}{\partial x} - w_{m_b}}_{\text{bottom condition for the m-th layer}} . \end{aligned} \tag{A.1.8}$$

This results in the conservative form of the free surface equation for the m-th layer

$$0 = \frac{\partial \eta_m}{\partial t} - \frac{\partial \eta_{m_b}}{\partial t} + \frac{\partial}{\partial x}\left[\int_{\eta_{m_b}}^{\eta_m} u_m \, dz\right] + \frac{\partial}{\partial y}\left[\int_{\eta_{m_b}}^{\eta_m} v_m \, dz\right]. \tag{A.1.9}$$

Considering the total depth from the rigid bottom η_0 to the m-th surface η_m it leads to

$$0 = \frac{\partial \eta_m}{\partial t} + \frac{\partial}{\partial x} \sum_{l=m_0}^{m} \left[\int_{\eta_{l_b}}^{\eta_l} u_l \, dz\right] + \frac{\partial}{\partial y} \sum_{l=m_0}^{m} \left[\int_{\eta_{l_b}}^{\eta_l} v_l \, dz\right]. \tag{A.1.10}$$

This expression describes the surface movement of an isopycnal layer m by considering the fluxes through the fluid column.

To complete the governing equations, the boundary condition at the free surface is defined by

$$\nu_M^v \frac{\partial u_M}{\partial z} = \gamma_a \left(u_a - u_M\right) \qquad \text{and} \qquad \nu_M^v \frac{\partial v_M}{\partial z} = \gamma_a \left(v_a - v_M\right) \tag{A.1.11}$$

where u_a and v_a are the horizontal wind velocity components. The boundary condition at the bottom is given by

$$\nu_{m_0}^v \frac{\partial u_{m_0}}{\partial z} = \gamma_b u_{m_0} \qquad \text{and} \qquad \nu_{m_0}^v \frac{\partial v_{m_0}}{\partial z} = \gamma_b v_{m_0} \tag{A.1.12}$$

with the current isopycnal bottom layer m_0. The friction factors of the unit m/s are defined as follows

$$\gamma_a = f_a \sqrt{\left(u_a - u_M\right)^2 + \left(v_a - v_M\right)^2} \qquad \text{and} \qquad \gamma_b = f_b \sqrt{u_{m_0}^2 + v_{m_0}^2} \tag{A.1.13}$$

where f_a and f_b are dimensionless friction coefficients.
The interfacial shear stresses for the upper $(m + 1/2)$ and lower boundary $(m - 1/2)$ of the m-th layer are

$$\nu_m^v \frac{\partial u_m}{\partial z} = \gamma_{m+\frac{1}{2}} \left(u_{m_t} - u_m\right) - \gamma_{m-\frac{1}{2}} \left(u_m - u_{m_b}\right) \text{ and} \tag{A.1.14a}$$

$$\nu_m^v \frac{\partial v_m}{\partial z} = \gamma_{m+\frac{1}{2}} \left(v_{m_t} - v_m\right) - \gamma_{m-\frac{1}{2}} \left(v_m - v_{m_b}\right) \tag{A.1.14b}$$

with the interfacial non-negative friction factor $\gamma_{m\pm\frac{1}{2}}$.

A.2 Numerical Approximation

The time discretization for the governing equations is realized with the semi-implicit method, which is described for the isopycnal hydrodynamic model on structured grids in Casulli [1997] and for the unstructured, z-layer-based and hydrodynamic model UnTRIM in Casulli and Walters [2000]. The numerical approximation and solution algorithm for the unstructured isopycnal model can be developed by combining the isopycnal and unstructured methods. The space is discretized in three dimensions by four parameters. The space is horizontally defined by the coordinates (x, y) and vertically by z and ϱ-coordinates. The z-layers are static and predefined. The density layers or isopycnal layers are variable in space and time and by intersection of a z-layer they can divide the z-layer into two or more than two z-layers according to the intersections. The ϱ-layers can appear and disappear or, in other words, can be dry or wet but the maximum number of M layers and their specific density are predefined. The discrete notations of the indices of the isopycnal layers and z-layers and their relationship are as follows

$m = m^n_{0,i}, \ldots, M^n_i$	isopycnal layer from bottom to surface
$m^n_{b,i}$	next active isopycnal layer below the m-th layer
$m^n_{t,i}$	next active isopycnal layer above the m-th layer
M	total number of the isopycnal layers
$k = k^n_{0,i}, \ldots, N^n_i$	z-layers from bottom to surface
$k^n_{b,i,m}, \ldots, k^n_{t,i,m}$	range of the z-layers inside an isopycnal layer
	with $k^n_{0,i} = k^n_{b,i,m^n_{0,i}}$ and $N^n_i = k^n_{t,i,M^n_i}$
N_z	total number of z-layers

where i indicates the polygon and n the time step.
An overview of the vertical structure of the model is given in Figure 74 and Figure 75. The thickness of an isopycnal layer of the i-th polygon is specified by $\Delta\eta^n_{i,m} = \eta^n_{i,m} - \eta^n_{i,m^n_{b,i}}$. The z-layer thickness $\Delta z^n_{j,k,m}$ is defined for each isopycnal layer m from $k = 1, \ldots, N_z$ by considering intersecting isopycnal layers and non-active layers. This leads to the following definition

$$\Delta z^n_{j,k,m} = \begin{cases} z^n_{j,k,m} - z^n_{j,k-1,m} & \text{if} \quad k^n_{b,j,m} \le k \le k^n_{t,j,m} \quad \text{active layer} \\ 0 & \text{if} \quad k < k^n_{b,j,m} \quad \text{non-active layer} \\ 0 & \text{if} \quad k > k^n_{t,j,m} \quad \text{non-active layer .} \end{cases} \tag{A.2.1}$$

At an isopycnal interface $(m, m^n_{t,j})$ the depth difference is determined by

$$\Delta z^n_{j,k^n_{b,j,m^n_{t,j}},m^n_{t,j}} = z^n_{j,k^n_{b,j,m^n_{t,j}},m^n_{t,j}} - z^n_{j,k^n_{t,j,m},m}. \tag{A.2.2}$$

The horizontal domain is defined by an unstructured orthogonal grid with

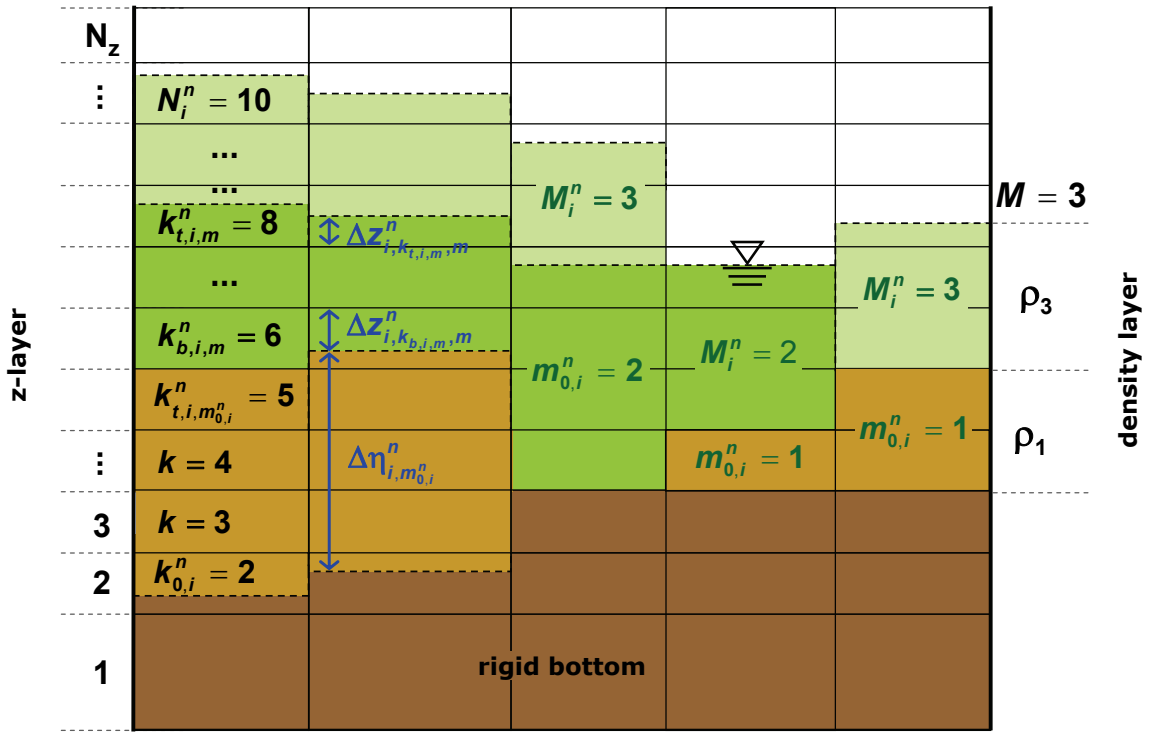

Figure 74: *Vertical structure of isopycnals combined with z-layers.*
The bottom layer is defined by the indices $k_{0,i}$ indicating the z-layer and $m^n_{0,i}$ indicating the active isopycnal layer at the bottom of the i-th polygon and at time step n. The surface layer is described accordingly by the indices N_i and M^n_i. The bottom and top z-layer of the m-th layer are $k^n_{b,i,m}$ and $k^n_{t,i,m}$, respectively. The z-layer thickness is described by $\Delta z^n_{i,k,m}$ and the isopycnal layer thickness by $\Delta\eta^n_{i,m}$.

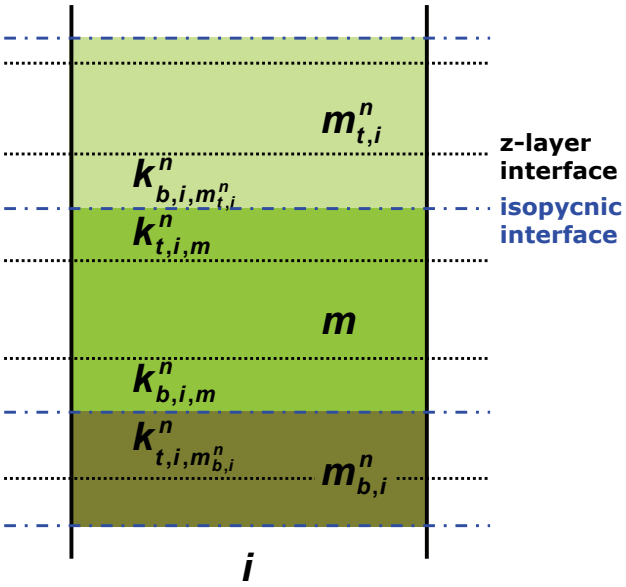

Figure 75: *Definition of the z-layer and ϱ-layer at isopycnal interfaces.*
The next active isopycnal layer above the m-th layer is $m^n_{t,i}$ for the i-th polygon and at time step n and the next active layer below the m-th layer is $m^n_{b,i}$, respectively. The top most z-layer inside the m-th layer is $k^n_{t,i,m}$ and the bottom z-layer is $k^n_{b,i,m}$, respectively.

$i = 1, 2, 3, \ldots, N_p$ polygons and $j = 1, 2, 3, \ldots, N_s$ sides. Each polygon has $e = 1, 2, \ldots, E_i$ sides and at least three sides ($E_i = 3$). The horizontal velocity components u and v are obsolete for the unstructured grid and a velocity component $u_{j,k,m}$ normal to side j, of the k-th z-layer and the m-th isopycnal layer is introduced instead, see Figure 76.

A.2.1 Momentum Equation

The momentum equations are divided into an implicit and an explicit part to determine the velocity of the new time step $n+1$. By reason the isopycnal definition, the density of every prism (volume element) is known. Therefore, the barotropic pressure is calculated implicitly. The vertical viscosity term can also be determined implicitly because the interfacial bottom and surface stresses are known quantities. This leads to the following equation for the unknown velocity of the j-th side, the z-layer k and the isopycnal layer m

$$
\begin{aligned}
u^{n+1}_{j,k,m} = {} & F\left(u^{n}_{j,k,m}\right) \\
& \underbrace{- g\frac{\Delta t}{\delta_j}\sum_{l=m}^{M^n_j}\left(\left[\frac{\varrho_l - \varrho_{l^n_{t,j}}}{\varrho_{r,j}}\right]\left[\Theta\left(\eta^{n+1}_{i(j,2),l} - \eta^{n+1}_{i(j,1),l}\right) + (1-\Theta)\left(\eta^{n}_{i(j,2),l} - \eta^{n}_{i(j,1),l}\right)\right]\right)}_{\text{hydrostatic barotropic pressure}} \\
& + \frac{\Delta t}{\Delta z^n_{j,k,m}}\left[\underbrace{\nu^{v,n}_{j,k+1/2,m}\frac{u^{n+1}_{j,k+1,m} - u^{n+1}_{j,k,m}}{\Delta z^n_{j,k+1/2,m}}}_{\text{shear at upper interface}}\underbrace{-\nu^{v,n}_{j,k-1/2,m}\frac{u^{n+1}_{j,k,m} - u^{n+1}_{j,k-1,m}}{\Delta z^n_{j,k-1/2,m}}}_{\text{shear at lower interface}}\right]
\end{aligned}
\tag{A.2.3}
$$

derived from the momentum equations (A.1.1). The shear stresses at an isopycnal interface result from Equation (A.1.14). They are specified for the upper interface $(m, m^n_{t,j})$ by

$$
\nu^{v,n}_{j,k^n_{t,j,m}+\frac{1}{2},m}\frac{u^{n+1}_{j,k^n_{b,j,m^n_{t,j}},m^n_{t,j}} - u^{n+1}_{j,k^n_{t,j,m},m}}{\Delta z^n_{j,k^n_{t,j,m}+\frac{1}{2},m}} \tag{A.2.4}
$$

and for the lower interface $(m, m^n_{b,j})$ by

$$
\nu^{v,n}_{j,k^n_{b,j,m}-\frac{1}{2},m}\frac{u^{n+1}_{j,k^n_{b,j,m},m} - u^{n+1}_{j,k^n_{t,j,m^n_{b,j}},m^n_{b,j}}}{\Delta z^n_{j,k^n_{b,j,m}-\frac{1}{2},m}} \tag{A.2.5}
$$

The boundary condition for the vertical shear at the free surface is set to

$$
\nu^{v,n}_{j,N^n_j+\frac{1}{2},M^n_j}\frac{u^{n+1}_{j,N^n_j+1,M^n_j} - u^{n+1}_{j,N^n_j,M^n_j}}{\Delta z^n_{j,N^n_j+\frac{1}{2},M^n_j}} = \gamma^{n+1}_{a,j}\left(u^{n+1}_{a,j} - u^{n+1}_{j,N^n_j,M^n_j}\right) \tag{A.2.6}
$$

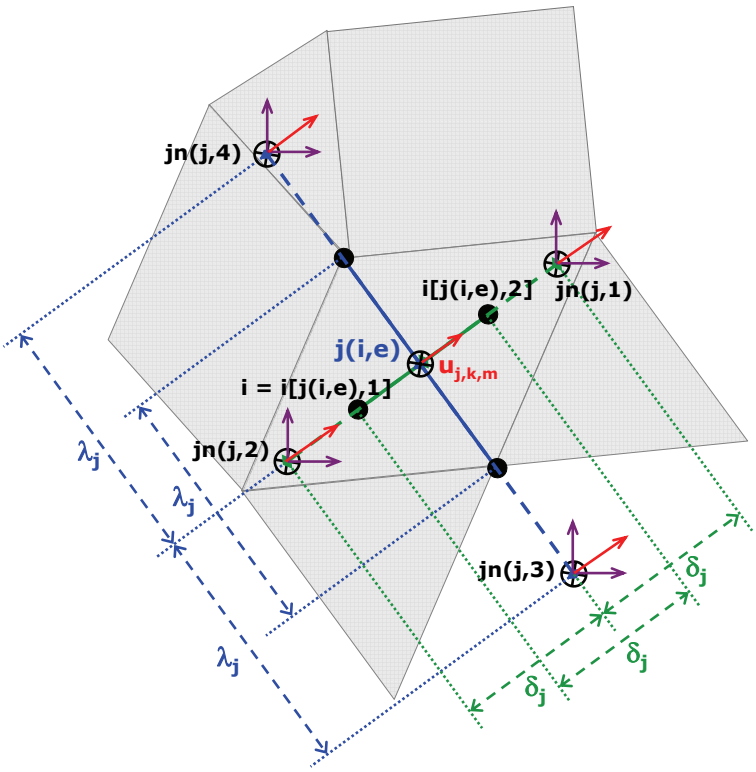

Figure 76: *Location, indices and interpolation of the horizontal velocity.*
The velocity of the j-th side is defined at position $j\,(i,e)$. There are four velocity neighbors given for each side. Two neighbors, $jn\,(j,1)$ and $jn\,(j,2)$, are located perpendicular to side j in $\pm\delta_j$ distance. The other two neighbors, $jn\,(j,3)$ and $jn\,(j,4)$, are located in $\pm\lambda_j$ distance. The adjacent polygons of side j are defined with $i\,[j\,(i,e)\,,1]$ and $i\,[j\,(i,e)\,,2]$.

and the bottom boundary condition is described by

$$\nu^{v,n}_{j,k^n_{0,j}-\frac{1}{2},m^n_{0,j}} \frac{u^{n+1}_{j,k^n_{0,j},m^n_{0,j}}}{\Delta z^n_{j,k^n_{0,j}-\frac{1}{2},m^n_{0,j}}} = \gamma^{n+1}_{b,j}\, u^{n+1}_{j,k^n_{0,j},m^n_{0,j}}. \tag{A.2.7}$$

F is an explicit function of $u^n_{j,k,m}$ and can be determined by different formulations, the simplest being to set F equal to $u^n_{j,k,m}$. In this case, the function is solved with the Eulerian-Lagrangian method for the advective terms [Cheng et al., 1993] and contains the explicit terms from the momentum equations

$$\begin{aligned} F\left(u^n_{j,k,m}\right) = {} & \underbrace{u^{*n}_{j,k,m}}_{\text{advection}} + \underbrace{\Delta t f_c v^{*n}_{j,k,m}}_{\text{Coriolis term}} - \underbrace{\frac{\Delta t}{\delta_j}\left(p^n_{a,i(j,2)} - p^n_{a,i(j,1)}\right)}_{\text{atmospheric pressure}} \\ & + \frac{\Delta t \nu^h}{\delta_j^2}\left(u^{*n}_{jn(j,1),k,m} - 2u^{*n}_{j,k,m} + u^{*n}_{jn(j,2),k,m}\right) \\ & + \underbrace{\frac{\Delta t \nu^h}{\lambda_j^2}\left(u^{*n}_{jn(j,3),k,m} - 2u^{*n}_{j,k,m} + u^{*n}_{jn(j,4),k,m}\right)}_{\text{horizontal viscosity terms}} \end{aligned} \tag{A.2.8}$$

where $u^{*n}_{j,k,m}$ is the horizontal velocity normal to side j at the end of the Lagrangian trajectory and its tangential component $v^{*n}_{j,k,m}$. The horizontal viscosity terms are discretized in the direction normal to side j by considering distance δ_j and tangential to side j by considering the distance λ_j. Further details are shown in Figure 76 as well as the positions of the neighboring velocities $u_{jn(j,e),k,m}$.
These are the discretized equations with constant viscosity formulation. They have to be reformulated by considering the viscosity as a function (the rheological viscosity). The viscosity will now be discretized in space and time, too. The vertical viscosity is defined at the center of a prism and is derived over the vertical z-layer distance $\Delta z^n_{j,k,m}$. The interpolation of the vertical viscosity to position $k \pm 1/2$ can be done with

$$\nu^{v,n}_{j,k\pm1/2,m} = \frac{1}{4}\left(\nu^{v,n}_{je(j,1),k,m} + \nu^{v,n}_{je(j,2),k,m} + \nu^{v,n}_{je(j,1),k\pm1,m} + \nu^{v,n}_{je(j,2),k\pm1,m}\right), \quad \text{(A.2.9)}$$

and the location is illustrated in three-dimensions in Figure 77. The indices $je\,(j,1)$ and $je\,(j,2)$ indicate the adjacent polygons of side j. Accordingly, the explicit expression $F\left(u^n_{j,k,m}\right)$ changes to

$$\begin{aligned} F\left(u^n_{j,k,m}\right) &= u^{*n}_{j,k,m} + \Delta t f_c v^{*n}_{j,k,m} - \frac{\Delta t}{\delta_j}\left(p^n_{a,i(j,2)} - p^n_{a,i(j,1)}\right) \\ &+ \frac{\Delta t}{\delta_j^2}\nu^{*h,n}_{je(j,1),k,m}\left(u^{*n}_{jn(j,1),k,m} - u^{*n}_{j,k,m}\right) \\ &- \frac{\Delta t}{\delta_j^2}\nu^{*h,n}_{je(j,2),k,m}\left(u^{*n}_{j,k,m} - u^{*n}_{jn(j,2),k,m}\right) \\ &+ \frac{\Delta t}{\lambda_j^2}\nu^{*h,n}_{jt(j),k,m}\left(u^{n}_{jn(j,3),k,m} - u^{*n}_{j,k,m}\right) \\ &- \frac{\Delta t}{\lambda_j^2}\nu^{*h,n}_{jb(j),k,m}\left(u^{*n}_{j,k,m} - u^{*n}_{jn(j,4),k,m}\right) \end{aligned} \quad \text{(A.2.10)}$$

with the horizontal viscosity $\nu^{*h,n}_{i,k,m}$ being determined at the end of the Lagrangian trajectory at time step n.

A.2.2 Free Surface Equation

The surface elevation of the m-th layer at time step $n+1$ can be determined from the free surface Equation (A.1.10). A semi-implicit volume discretization is applied by introducing the implicitness factor Θ which ranges from zero to one. The discretized formulation results in

$$\begin{aligned} P_i\frac{\eta^{n+1}_{i,m} - \eta^n_{i,m}}{\Delta t} &= -\Theta\sum_{e=1}^{E_i}\left[s_{i,e}\lambda_{j(i,e)}\sum_{l=1}^{m}\sum_{k=1}^{N^n_j}\Delta z^n_{j(i,e),k,l}u^{n+1}_{j(i,e),k,l}\right] \\ &- (1-\Theta)\sum_{e=1}^{E_i}\left[s_{i,e}\lambda_{j(i,e)}\sum_{l=1}^{m}\sum_{k=1}^{N^n_j}\Delta z^n_{j(i,e),k,l}u^{n}_{j(i,e),k,l}\right] \end{aligned} \quad \text{(A.2.11)}$$

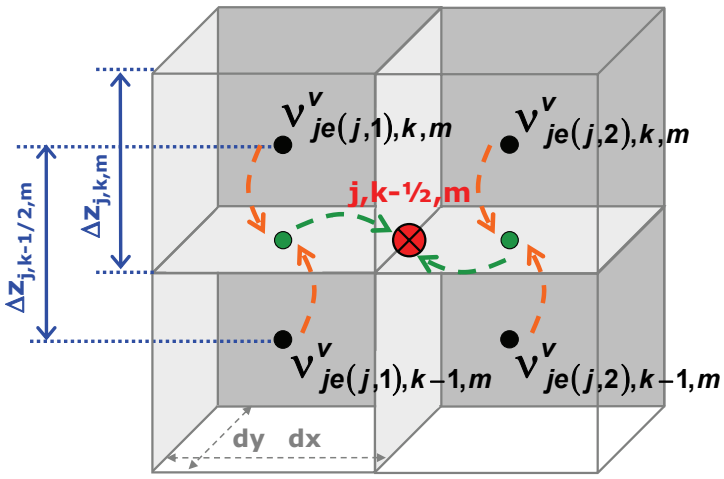

Figure 77: *Locations and interpolation of the vertical viscosity.*
The viscosity is defined at the center of a prism. The adjacent viscosities of side j in the layer k of the isopycnal layer m are given with $\nu^v_{je(j,1),k,m}$ and $\nu^v_{je(j,2),k,m}$. The viscosity $\nu^v_{j,k-1/2,m}$ is interpolated from these components and the adjacent components of the $(k-1)$-layer.

and some transformation leads to the formulation of the prism volume of the new time step or the isopycnal elevation of the new time step, respectively

$$\begin{aligned} P_i\eta^{n+1}_{i,m} &= P_i\eta^{n}_{i,m} - \Theta\Delta t \sum_{e=1}^{E_i}\left[s_{i,e}\lambda_{j(i,e)} \sum_{l=1}^{m}\sum_{k=1}^{N^n_j} \Delta z^n_{j(i,e),k,l} u^{n+1}_{j(i,e),k,l} \right] \\ &- (1-\Theta)\,\Delta t \sum_{e=1}^{E_i}\left[s_{i,e}\lambda_{j(i,e)} \sum_{l=1}^{m}\sum_{k=1}^{N^n_j} \Delta z^n_{j(i,e),k,l} u^{n}_{j(i,e),k,l} \right]. \end{aligned} \quad \text{(A.2.12)}$$

The second and third terms of the free surface equation denote the volume fluxes over the polygon edges $j\,(i,e)$, where E gives the maximum number of edges of element i and for all active layers from bottom to surface of the m-th layer. If a layer is non-active the flux will be zero because the thickness $\Delta z^n_{j,k,m}$ is zero. The index $j\,(i,e)$ indicates the side e of polygon i. The sign function $s_{i,e}$ is given by

$$s_{i,e} = \frac{i\left[j\,(i,e)\,,2\right] - 2i + i\left[j\,(i,e)\,,1\right]}{i\left[j\,(i,e)\,,2\right] - i\left[j\,(i,e)\,,1\right]}. \quad \text{(A.2.13)}$$

The neighboring element of i is defined as a function of the velocity at side $j\,(i,e)$. The neighboring element results in $i\left[j\,(i,e)\,,1\right]$ for outflow and in $i\left[j\,(i,e)\,,2\right]$ for inflow. Consequently, the result of the sign-function is given by

$$s_{i,e} = \begin{cases} 1 & \text{if} \quad i = i\left[j\,(i,e)\,,1\right] \quad \text{outflow} \\ -1 & \text{if} \quad i = i\left[j\,(i,e)\,,2\right] \quad \text{inflow} \end{cases} \quad \text{(A.2.14)}$$

which is indicated in Figure 76.

Finally, a linear system of $\left[(M+N_z-1)\times N_s + M\times N_p\right]$ equations is obtained with the unknowns $\eta^{n+1}_{i,m}$ and $u^{n+1}_{j,k,m}$. The system of equations can be reduced by decreasing the dimension of the model. Three cases can be considered:

- a pure isopycnal model by setting $N_z = 1$:
  - a vertically layer-averaged, three-dimensional model in isopycnal coordinates according to Casulli [1997] and Section 4.1
  - the depth difference $\Delta z^n_{j,k^n_{0,j},m} = \Delta\eta^n_{j,m} = \eta^n_{j,m} - \eta^n_{j,m^n_{b,j}}$ represents the isopycnal layer thickness
  - the linear system of equations has the size $[M \times (N_s + N_p)]$
  - the vertical movement is only described by the movement of the interfaces
- a classical three-dimensional model considering only one isopycnal layer with $M = 1$:
  - three-dimensional z-layer-based model for unstructured grids, as described in Casulli and Walters [2000]
  - with the z-layer thickness $\Delta z^n_{j,k,m^n_{0,j}} = \Delta z^n_{j,k,M^n_j}$
  - the linear system of equations has the size $[N_z \times N_s + N_p]$
- a two-dimensional numerical model is obtained by defining $N_z = 1$ and $M = 1$:
  - a depth-averaged model
  - the total water depth is represented by $\Delta eta^n_{j,M^n_j}$
  - the linear system of equations has the size $[N_s + N_p]$

The linear system of equations has to be solved for the velocity and the surface elevation for each new time step $n + 1$. The way to a solvable system is described in the next section with the aim of reducing the computational effort.

A.3 Solution Algorithm

In the previous section, the differential isopycnal Reynolds-averaged Navier-Stokes equations were applied to a semi-implicit discretization scheme. The two concepts for the unstructured, three-dimensional, z-layer-based approach [Casulli and Walters, 2000] and the isopycnal approach for structured grids [Casulli, 1997] are also combined for the solution algorithm.

A.3.1 Momentum Equation in Matrix Notation

The discretized formulation of the momentum Equation (A.2.3) needs to be manipulated by multiplying it by the layer thickness $\Delta z^n_{j,k,m}$, changing the order of the pressure

term and moving the viscous term to the left side

$$\begin{aligned}
&\Delta z^n_{j,k,m} u^{n+1}_{j,k,m} - \Delta t \left[\nu^{v,n}_{j,k+1/2,m} \frac{u^{n+1}_{j,k+1,m} - u^{n+1}_{j,k,m}}{\Delta z^n_{j,k+1/2,m}} - \nu^{v,n}_{j,k-1/2,m} \frac{u^{n+1}_{j,k,m} - u^{n+1}_{j,k-1,m}}{\Delta z^n_{j,k-1/2,m}} \right] \\
= \;& \Delta z^n_{j,k,m} F\left(u^n_{j,k,m}\right) - \frac{\Delta z^n_{j,k,m} g \Delta t}{\delta_j \varrho_{r,j}} (1-\Theta) \sum_{l=m}^{M^n_j} \left[\left(\varrho_l - \varrho_{l^n_{t,j}} \right) \eta^n_{j,l} \right] \\
- \;& \frac{\Delta z^n_{j,k,m} g \Delta t}{\delta_j \varrho_{r,j}} \Theta \sum_{l=m}^{M^n_j} \left[\left(\varrho_l - \varrho_{l^n_{t,j}} \right) \eta^{n+1}_{j,l} \right]
\end{aligned} \tag{A.3.1}$$

where the elevation $\eta_{j,m} = \frac{1}{2}\left(\eta_{i(j,1),m} + \eta_{i(j,2),m}\right)$ is the average between two neighboring elements. Some reorganization of the left side

$$\begin{aligned}
&\left(\Delta z^n_{j,k,m} + \frac{\Delta t \nu^{v,n}_{j,k+1/2,m}}{\Delta z^n_{j,k+1/2,m}} + \frac{\Delta t \nu^{v,n}_{j,k-1/2,m}}{\Delta z^n_{j,k-1/2,m}} \right) u^{n+1}_{j,k,m} \\
&- \frac{\Delta t \nu^{v,n}_{j,k+1/2,m}}{\Delta z^n_{j,k+1/2,m}} u^{n+1}_{j,k+1,m} - \frac{\Delta t \nu^{v,n}_{j,k-1/2,m}}{\Delta z^n_{j,k-1/2,m}} u^{n+1}_{j,k-1,m} \quad = \quad \dots
\end{aligned} \tag{A.3.2}$$

permits a matrix notation for the normal velocity $u^{n+1}_{j,k,m}$ and the vertical viscosity components $a^n_{j,m,k,k}$ and $a^n_{j,m,k,k\pm1}$. The matrix notation is introduced to show the entire system of equations and their characteristics. The matrix formulation for the set of M^n_j momentum equations results in

$$\mathbf{A}^n_j \cdot \mathbf{U}^{n+1}_j = \mathbf{G}^n_j - \frac{\Theta g \Delta t}{\delta_j \, \varrho_{r,j}} \Delta \mathbf{Z}^n_j \left(\mathbf{D}_j \cdot \mathbf{S}^{n+1}_j \right) \tag{A.3.3}$$

for the j-th side. The newly-established matrices are described in the following. For simplicity, the adjacent isopycnal layers above or below the m-th layer are defined as $m \pm 1$ which indicates

- the next active layer if the matrix considers only active isopycnals $(m^n_{0,j}, \dots, M^n_j)$ or
- the next layer, regardless of whether it is active or non-active, if all defined isopycnals $(1, \dots, M)$ are considered.

The layer thickness is set up by a block matrix

$$\Delta \mathbf{Z}^n_j = \begin{bmatrix}
\Delta \hat{\mathbf{Z}}^n_{j,M^n_j} & & \cdots & 0 \\
\Delta \hat{\mathbf{Z}}^n_{j,M^n_j-1} & \Delta \hat{\mathbf{Z}}^n_{j,M^n_j-1} & & \vdots \\
\vdots & & \ddots & \\
\Delta \hat{\mathbf{Z}}^n_{j,m^n_{0,j}+1} & \cdots & \Delta \hat{\mathbf{Z}}^n_{j,m^n_{0,j}+1} & \\
\Delta \hat{\mathbf{Z}}^n_{j,m^n_{0,j}} & \cdots & & \Delta \hat{\mathbf{Z}}^n_{j,m^n_{0,j}}
\end{bmatrix} \tag{A.3.4}$$

with $M_j^n \times M$ inner matrices. The number of rows of this matrix results from the number of active layers at the time step n, whereas the number of columns is static and equal to the total number of isopycnal layers. Their inner matrices contain the z-layer thicknesses of the m-th layer

$$\Delta\hat{\mathbf{Z}}_{j,m}^n = \begin{bmatrix} \Delta z_{j,k_{t,j,m}^n,m}^n \\ \Delta z_{j,k_{t,j,m}^n-1,m}^n \\ \vdots \\ \Delta z_{j,k,m}^n \\ \vdots \\ \Delta z_{j,k_{b,j,m}^n,m}^n \end{bmatrix} \tag{A.3.5}$$

and they are vectors of the size $\left(k_{b,j,m}^n, \ldots, k_{t,j,m}^n\right)$. Altogether, the matrix size of $\Delta\mathbf{Z}_j^n$ is $\left(M_j^n + N_{j,M_j^n}^n\right) \times M$. The isopycnal elevation matrix is an one-dimensional vector

$$\mathbf{S}_i^{n+1} = \begin{bmatrix} \eta_{i,M}^{n+1} \\ \eta_{i,M-1}^{n+1} \\ \vdots \\ \eta_{i,m}^{n+1} \\ \vdots \\ \eta_{i,1}^{n+1} \end{bmatrix} \text{ and } \mathbf{S}_j^{n+1} = \begin{bmatrix} \eta_{i(j,2),M}^{n+1} - \eta_{i(j,1),M}^{n+1} \\ \eta_{i(j,2),M-1}^{n+1} - \eta_{i(j,1),M-1}^{n+1} \\ \vdots \\ \eta_{i(j,2),m}^{n+1} - \eta_{i(j,1),m}^{n+1} \\ \vdots \\ \eta_{i(j,2),1}^{n+1} - \eta_{i(j,1),1}^{n+1} \end{bmatrix} \tag{A.3.6}$$

which is defined either element-wise S_i^{n+1} or side-wise S_j^{n+1}. The vector has the size M. The matrix for the unknown velocities normal to side j is specified by

$$\mathbf{U}_j^{n+1} = \begin{bmatrix} \hat{\mathbf{U}}_{j,M_j^n}^{n+1} \\ \vdots \\ \hat{\mathbf{U}}_{j,m}^{n+1} \\ \vdots \\ \hat{\mathbf{U}}_{j,m_{0,j}^n+1}^{n+1} \\ \hat{\mathbf{U}}_{j,m_{0,j}^n}^{n+1} \end{bmatrix} \text{ with } \hat{\mathbf{U}}_{j,m}^{n+1} = \begin{bmatrix} u_{j,k_{t,j,m}^n,m}^{n+1} \\ \vdots \\ u_{j,k,m}^{n+1} \\ \vdots \\ u_{j,k_{b,j,m}^n+1,m}^{n+1} \\ u_{j,k_{b,j,m}^n,m}^{n+1} \end{bmatrix}. \tag{A.3.7}$$

This block vector has the size $M_j^n + N_{j,M_j^n}^n$. The density matrix is given by

$$\mathbf{D}_j = \begin{bmatrix} \varrho_{j,M^n-1} - \varrho_{j,M} & \cdots & 0 \\ & \ddots & \\ \vdots & \varrho_{j,m-1} - \varrho_{j,m} & \vdots \\ & & \ddots \\ 0 & \cdots & \varrho_{j,0} - \varrho_{j,1} \end{bmatrix} \tag{A.3.8}$$

which is a diagonal matrix of $M \times M$ elements. The explicit terms are all combined in the block vector $\mathbf{G}_j^n$ which has the following form

$$\mathbf{G}_j^n = \begin{bmatrix} \hat{\mathbf{G}}^n_{j,M_j^n} \\ \vdots \\ \hat{\mathbf{G}}^n_{j,m} \\ \vdots \\ \hat{\mathbf{G}}^n_{j,m^n_{0,j}+1} \\ \hat{\mathbf{G}}^n_{j,m^n_{0,j}} \end{bmatrix} \text{ with}$$

$$\hat{\mathbf{G}}^n_{j,m} = \begin{bmatrix} \Delta z^n_{j,k^n_{t,j,m},m}\left[F\left(u^n_{j,k^n_{t,j,m},m}\right) - g\frac{\Delta t}{\delta_j}(1-\Theta)\sum_{l=m}^{M_j^n}\left(\frac{\varrho_{j,l}-\varrho_{j,l^n_{t,j}}}{\varrho_{r,j}}\eta^n_{j,l}\right)\right] \\ \vdots \\ \Delta z^n_{j,k,m}\left[F\left(u^n_{j,k,m}\right) - g\frac{\Delta t}{\delta_j}(1-\Theta)\sum_{l=m}^{M_j^n}\left(\frac{\varrho_{j,l}-\varrho_{j,l^n_{t,j}}}{\varrho_{r,j}}\eta^n_{j,l}\right)\right] \\ \vdots \\ \Delta z^n_{j,k^n_{b,j,m},m}\left[F\left(u^n_{j,k^n_{b,j,m},m}\right) - g\frac{\Delta t}{\delta_j}(1-\Theta)\sum_{l=m}^{M_j^n}\left(\frac{\varrho_{j,l}-\varrho_{j,l^n_{t,j}}}{\varrho_{r,j}}\eta^n_{j,l}\right)\right] \end{bmatrix}. \tag{A.3.9}$$

The block matrix has the same size as the velocity matrix $\mathbf{U}_j^{n+1}$. The wind friction is taken into account for the free surface layer M_j^n which results in

$$\hat{\mathbf{G}}^n_{j,M_j^n} =$$

$$\begin{bmatrix} \Delta z^n_{j,N_j^n,M_j^n}\left[F\left(u^n_{j,N_j^n,M_j^n}\right) - g\frac{\Delta t}{\delta_j}(1-\Theta)\left(\Delta\varrho_{j,M_j^n}\cdot\eta^n_{j,M_j^n}\right)\right] + \Delta t\cdot\gamma^{n+1}_{a,j}\cdot u^{n+1}_{a,j,N_j^n,M_j^n+1} \\ \vdots \\ \Delta z^n_{j,k,M_j^n}\left[F\left(u^n_{j,k,M_j^n}\right) - g\frac{\Delta t}{\delta_j}(1-\Theta)\left(\Delta\varrho_{j,M_j^n}\cdot\eta^n_{j,M_j^n}\right)\right] \\ \vdots \\ \Delta z^n_{j,k^n_{b,j,M_j^n},M_j^n}\left[F\left(u^n_{j,k^n_{b,j,M_j^n},M_j^n}\right) - g\frac{\Delta t}{\delta_j}(1-\Theta)\left(\Delta\varrho_{j,M_j^n}\cdot\eta^n_{j,M_j^n}\right)\right] \end{bmatrix} \tag{A.3.10}$$

with the normalized density gradient $\Delta\varrho_{j,M_j^n} = \frac{\varrho_{j,M_j^n}}{\varrho_{r,0}}$.

The vertical viscosity term leads to a tridiagonal block matrix of $M_j^n \times M_j^n$ inner matrices

$$\mathbf{A}_j^n = \begin{bmatrix} \hat{\mathbf{A}}^n_{j,M_j^n,M_j^n} & \hat{\mathbf{A}}^n_{j,M_j^n,M_j^n-1} & & \cdots & 0 \\ \hat{\mathbf{A}}^n_{j,M_j^n-1,M_j^n} & \hat{\mathbf{A}}^n_{j,M_j^n-1,M_j^n-1} & \hat{\mathbf{A}}^n_{j,M_j^n-1,M_j^n-2} & & \vdots \\ & \ddots & & & \\ & \hat{\mathbf{A}}^n_{j,m,m+1} & \hat{\mathbf{A}}^n_{j,m,m} & \hat{\mathbf{A}}^n_{j,m,m-1} & \\ & & \ddots & & \\ \vdots & & \hat{\mathbf{A}}^n_{j,m^n_{0,j}+1,m^n_{0,j}+2} & \hat{\mathbf{A}}^n_{j,m^n_{0,j}+1,m^n_{0,j}+1} & \hat{\mathbf{A}}^n_{j,m^n_{0,j}+1,m^n_{0,j}} \\ 0 & \cdots & & \hat{\mathbf{A}}^n_{j,m^n_{0,j},m^n_{0,j}+1} & \hat{\mathbf{A}}^n_{j,m^n_{0,j},m^n_{0,j}} \end{bmatrix}. \tag{A.3.11}$$

A scheme of the matrix $\mathbf{A}_j^n$ is shown in Figure 78. Each row of the matrix represents a specific isopycnal layer m. The diagonal inner matrices contain the components from inside the layer m. The matrices of the secondary diagonals represent the lower and upper interfaces of the current isopycnal layer. They describe the shear between two adjacent isopycnals which act such as coupling between the adjacent isopycnals. The diagonal components $\hat{\mathbf{A}}^n_{j,m,m}$ are diagonal, symmetric, square matrices with $\left(k^n_{b,j,m},\ldots,k^n_{t,j,m}\right) \times \left(k^n_{b,j,m},\ldots,k^n_{t,j,m}\right)$ elements

$$\hat{\mathbf{A}}^n_{j,m,m} = \begin{bmatrix} a_{j,m,k_{t,j,m},k_{t,j,m}} & a_{j,m,k_{t,j,m},k_{t,j,m}-1} & \cdots & 0 \\ a_{j,m,k_{t,j,m}-1,k_{t,j,m}} & a_{j,m,k_{t,j,m}-1,k_{t,j,m}-1} & a_{j,m,k_{t,j,m}-1,k_{t,j,m}-2} & \vdots \\ & \ddots & & \\ & & & \\ \vdots & & \ddots & \\ 0 & \cdots & a_{j,m,k^n_{b,j,m},k^n_{b,j,m}+1} & a_{j,m,k^n_{b,j,m},k^n_{b,j,m}} \end{bmatrix}. \tag{A.3.12}$$

Their components for an intermediate layer m are given by

$$a_{j,m,k,k} = \Delta z^n_{j,k,m} + \frac{\Delta t \nu^{v,n}_{j,k+1/2,m}}{\Delta z^n_{j,k+\frac{1}{2},m}} + \frac{\Delta t \nu^{v,n}_{j,k-\frac{1}{2},m}}{\Delta z^n_{j,k-\frac{1}{2},m}} \quad \text{and} \tag{A.3.13a}$$

$$a_{j,m,k,k\pm1} = -\frac{\Delta t \nu^{v,n}_{j,k\pm\frac{1}{2},m}}{\Delta z^n_{j,k\pm\frac{1}{2},m}}, \tag{A.3.13b}$$

for the surface boundary by

$$a_{j,M_j^n,N_j^n,N_j^n} = \Delta z^n_{j,N_j^n,M_j^n} + \gamma^{n+1}_{a,j}\Delta t + \frac{\Delta t \nu^{v,n}_{j,N_j^n-\frac{1}{2},M_j^n}}{\Delta z^n_{j,N_j^n-\frac{1}{2},M_j^n}} \tag{A.3.14}$$

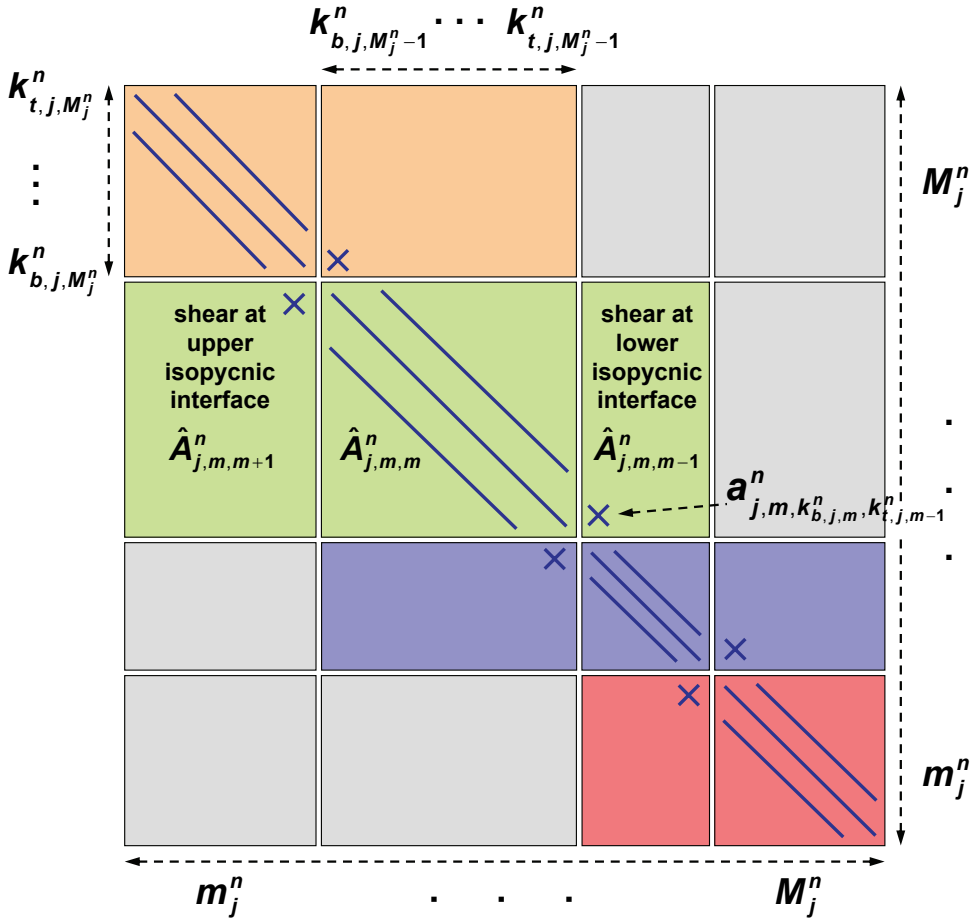

Figure 78: *Scheme of the tridiagonal block matrix* $\mathbf{A}^n_j$ *for the j-th side at time step n which represents the vertical viscosity terms.*
Each row of the block matrix represents a specific isopycnal layer m. The diagonal inner matrices contain the components from inside the layer m (indicated by blue lines). The matrices of the secondary diagonals represent the lower and upper interfaces of the current isopycnal layer. They describe the shear between two adjacent isopycnals due to the only component indicated with a blue cross. The size of the block matrix and the inner matrices can vary with time and space. (The coloring corresponds to Equation (A.3.11)*.)*

and for the bottom boundary by

$$a_{j,m^n_{0,j},k^n_{0,j},k^n_{0,j}} = \Delta z^n_{j,k^n_{0,j},m^n_{0,j}} + \frac{\Delta t \nu^{v,n}_{j,k^n_{0,j}+\frac{1}{2},m^n_{0,j}}}{\Delta z^n_{j,k^n_{0,j}+\frac{1}{2},m^n_{0,j}}} + \gamma^{n+1}_{b,j}\Delta t. \tag{A.3.15}$$

The eigenvalues of the matrix $\hat{\mathbf{A}}^n_{j,m,m}$ correspond to the values of the diagonal which are non-negative values. Therefore, the matrix is positive definite.
The matrices $\hat{\mathbf{A}}^n_{j,m,m-1}$ and $\hat{\mathbf{A}}^n_{j,m,m+1}$ of the secondary diagonals of matrix $\mathbf{A}^n_j$ are rectangular matrices of the size $\left(k^n_{b,j,m},\ldots,k^n_{t,j,m}\right) \times \left(k^n_{b,j,m-1},\ldots,k^n_{t,j,m-1}\right)$ and $\left(k^n_{b,j,m},\ldots,k^n_{t,j,m}\right) \times \left(k^n_{b,j,m+1},\ldots,k^n_{t,j,m+1}\right)$. They are related due to $\hat{\mathbf{A}}^n_{j,m+1,m} =$

$\left(\hat{\mathbf{A}}^n_{j,m,m+1}\right)^T$ and are described by

$$\begin{aligned}
\hat{\mathbf{A}}^n_{j,m,m-1} &= \begin{bmatrix} 0 & & \cdots & 0 \\ \vdots & & & \vdots \\ -a^n_{j,m,k^n_{b,j,m},k^n_{t,j,m-1}} & & \cdots & 0 \end{bmatrix} \quad \text{and} \\
\hat{\mathbf{A}}^n_{j,m,m+1} &= \begin{bmatrix} 0 & \cdots & -a^n_{j,m,k^n_{t,j,m},k^n_{b,j,m+1}} \\ \vdots & & \vdots \\ 0 & \cdots & 0 \end{bmatrix}
\end{aligned} \tag{A.3.16}$$

with only one non-zero and negative element. In this case, the adjacent isopycnal layers $m \pm 1$ are the next active layers.
All block components of matrix $\mathbf{A}^n_j$ are non-negative values. Therefore, the eigenvalues of the tridiagonal symmetric matrix are also non-negative, and the matrix can be classified as positive definite.

A.3.2 Free Surface Equation in Matrix Notation

The composition of M free surface equations (A.2.12) can be transformed into the matrix notation

$$\begin{aligned}
P_i \mathbf{S}^{n+1}_i = P_i \mathbf{S}^n_i &- \Theta \Delta t \sum_{e=1}^{E_i} \left(s_{i,e} \lambda_{j(i,e)} \left[\Delta \mathbf{Z}^n_{j(i,e)} \right]^T \mathbf{U}^{n+1}_{j(i,e)} \right) \\
&- (1-\Theta) \Delta t \sum_{e=1}^{E_i} \left(s_{i,e} \lambda_{j(i,e)} \left[\Delta \mathbf{Z}^n_{j(i,e)} \right]^T \mathbf{U}^{n}_{j(i,e)} \right).
\end{aligned} \tag{A.3.17}$$

Volumetric discretization is applied to the equation and is defined element-wise. If the block matrix $\Delta \mathbf{Z}^n_j$ (A.3.4) is transposed, its inner matrix $\Delta \hat{\mathbf{Z}}^n_{j,m}$ must also be transposed.

A.3.3 Substitution

After developing the matrix notation for the isopycnal linear system, the system of equations is solved by substitution of the horizontal velocity of Equation (A.3.3)

$$\mathbf{U}^{n+1}_j = \left(\mathbf{A}^n_j\right)^{-1} \mathbf{G}^n_j - \frac{\Theta g \Delta t}{\delta_j \varrho_{r,j}} \left(\mathbf{A}^n_j\right)^{-1} \Delta \mathbf{Z}^n_j \left(\mathbf{D}_j \mathbf{S}^{n+1}_j \right) \tag{A.3.18}$$

into the free surface Equation (A.3.17). This results in the discrete wave equation for isopycnal surface elevations for the new time step $n+1$

$$
\begin{aligned}
&P_i \mathbf{S}_i^{n+1} - \frac{\Theta^2 g \Delta t^2}{\delta_j \varrho_{r,j}} \sum_{e=1}^{E_i} \left(s_{i,e} \lambda_{j(i,e)} \left(\left[\Delta \mathbf{Z}_{j(i,e)}^n \right]^T \left[\mathbf{A}_{j(i,e)}^n \right]^{-1} \Delta \mathbf{Z}_{j(i,e)}^n \right) \left(\mathbf{D}_{j(i,e)} \mathbf{S}_{j(i,e)}^{n+1} \right) \right) \\
&= P_i \mathbf{S}_i^n - \Theta \Delta t \sum_{e=1}^{E_i} \left(s_{i,e} \lambda_{j(i,e)} \left[\Delta \mathbf{Z}_{j(i,e)}^n \right]^T \left[\mathbf{A}_{j(i,e)}^n \right]^{-1} \mathbf{G}_{j(i,e)}^n \right) \\
&\qquad - (1-\Theta) \Delta t \sum_{e=1}^{E_i} \left(s_{i,e} \lambda_{j(i,e)} \left[\Delta \mathbf{Z}_{j(i,e)}^n \right]^T \mathbf{U}_{j(i,e)}^n \right). \qquad \text{(A.3.19)}
\end{aligned}
$$

The matrix product $\mathbf{D}_j \mathbf{S}_j^{n+1} = \check{\mathbf{S}}_j^{n+1}$ is redefined in order to obtain a symmetric expression. Now the reformulated balance results in

$$
\begin{aligned}
&P_i \mathbf{D}_i^{-1} \check{\mathbf{S}}_i^{n+1} - \frac{\Theta^2 g \Delta t^2}{\delta_j \varrho_{r,j}} \sum_{e=1}^{E_i} \left(s_{i,e} \lambda_{j(i,e)} \left(\left[\Delta \mathbf{Z}_{j(i,e)}^n \right]^T \left[\mathbf{A}_{j(i,e)}^n \right]^{-1} \Delta \mathbf{Z}_{j(i,e)}^n \right) \check{\mathbf{S}}_{j(i,e)}^{n+1} \right) \\
&= P_i \mathbf{S}_i^n - \Theta \Delta t \sum_{e=1}^{E_i} \left(s_{i,e} \lambda_{j(i,e)} \left[\Delta \mathbf{Z}_{j(i,e)}^n \right]^T \left[\mathbf{A}_{j(i,e)}^n \right]^{-1} \mathbf{G}_{j(i,e)}^n \right) \\
&\qquad - (1-\Theta) \Delta t \sum_{e=1}^{E_i} \left(s_{i,e} \lambda_{j(i,e)} \left[\Delta \mathbf{Z}_{j(i,e)}^n \right]^T \mathbf{U}_{j(i,e)}^n \right). \qquad \text{(A.3.20)}
\end{aligned}
$$

The terms on the left contain the isopycnal elevations for the new time step, while the explicit terms are on the right. The expression $\left(\left[\Delta \mathbf{Z}_j^n \right]^T \cdot \left[\mathbf{A}_j^n \right]^{-1} \cdot \Delta \mathbf{Z}_j^n \right)$ is a non-negative vector of the size M_j^n because of the positive definiteness of matrix $\mathbf{A}_j^n$. A linear system of N_p block-wise equations now has to be solved for $\check{\mathbf{S}}_i^{n+1}$ of the parameter $\eta_{i,m}^{n+1}$. That is done by a conjugate gradient method. The new velocities are subsequently determined by the linear, block tridiagonal system of N_s equations (A.3.18). Both equation systems are symmetric and positive definite.

The wave equation (A.3.20) contains no volume fluxes between isopycnal layers, which will be inevitable for modeling processes such as deposition and mixing of mud suspensions. Section 4.3 deals with this problem and an explicit approach for mass and volume fluxes between isopycnal layers is developed.

A.3.4 Vertical Velocity

The last unknown parameter for the new time step is the vertical velocity which is determined by finite volume discretization of the continuity equation (A.1.4). The vertical velocity is defined element-wise at the top of every z-layer $w_{i,k+1/2}$. The calculation is done by adding up all out- and in-going volume fluxes through the prisms

below the upper face $\left(i, k+\frac{1}{2}\right)$, see Figure 79. The vertical velocity balance results in

$$w_{i,k+\frac{1}{2}}^{n+1} = \frac{1}{P_i} \sum_{e=1}^{E_i} \left[s_{i,e} \lambda_{j(i,e)} \sum_{l=1}^{k} \sum_{m=1}^{M} \left(\Delta z_{j(i,e),l,m}^{n} u_{j(i,e),l,m}^{n+1} \right) \right] \quad \text{or} \tag{A.3.21a}$$

$$w_{i,k+\frac{1}{2}}^{n+1} = w_{i,k-\frac{1}{2}}^{n+1} - \frac{1}{P_i} \sum_{e=1}^{E_i} \left[s_{i,e} \lambda_{j(i,e)} \sum_{m=1}^{M} \left(\Delta z_{j(i,e),k,m}^{n} u_{j(i,e),k,m}^{n+1} \right) \right]. \tag{A.3.21b}$$

The fluxes are summed up over all isopycnal layers and z-layers. The thickness $\Delta z_{j,k,m}^{n}$ of non-active layers is zero, therefore their fluxes are zero. An implicit solution is possible by solving the system from the bottom to the top of a water column because the vertical velocity $w_{i,-1/2}^{n+1}$ is zero at the bottom boundary.

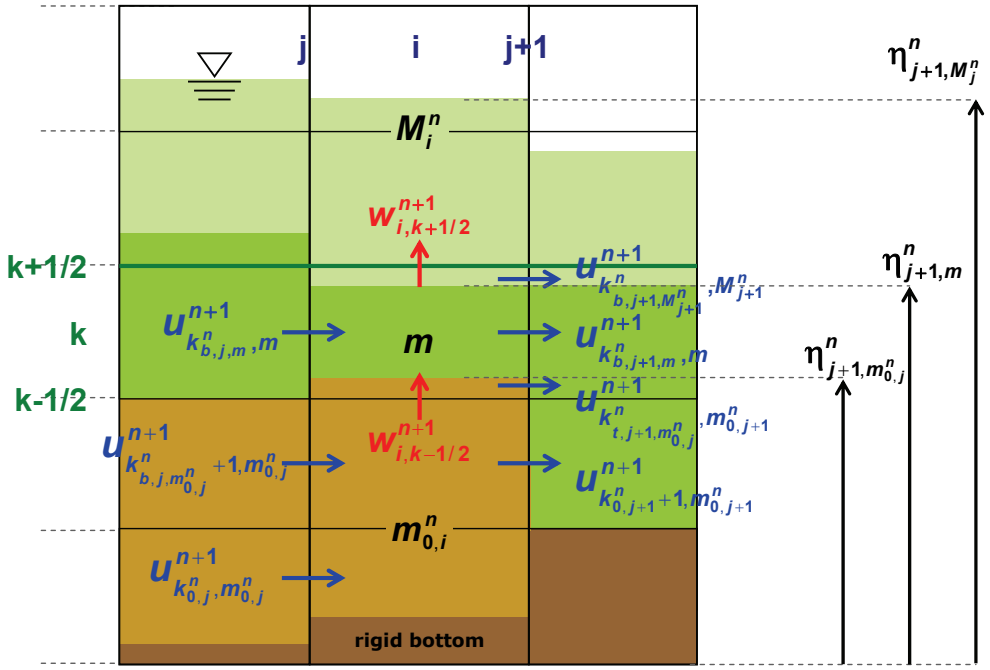

Figure 79: *Calculation of the vertical velocity by considering the horizontal fluxes from bottom to top.*

The vertical velocity $w_{i,k+\frac{1}{2}}^{n+1}$ at the surface of the k-th layer is determined by summation of the in- and out-going fluxes of the water column i below. In this case, this includes the horizontal fluxes from layer $m_{0,i}^n$ of the k-th layer to layer M_i^n of the k-th layer and the vertical velocity $w_{i,k-\frac{1}{2}}^{n+1}$ at the bottom of the k-th layer.

A.3.5 Time Step Limitation

The time step limitation for the isopycnal model results from the explicitly solved terms of the solution system

$$\Delta t \leq \frac{1}{2\nu^h \left(\frac{1}{\Delta x^2} + \frac{1}{\Delta y^2} \right)}. \tag{A.3.22}$$

It will lead to very small time steps if high viscosities are considered or simulation takes place on a very fine horizontal grid resolution. If the viscosity represents the rheological

viscosity of fluid mud, it could rapidly increase during periods of low shear rates or at high solid concentrations 3.4. Simulation of fluid mud characteristics could therefore lead to a reduction in the time step.

A.4 Properties of the Numerical Method

The basic properties of the three-dimensional, unstructured isopycnal model approach with a vertical z-layer and ϱ-layer discretization are:

- calculation on an unstructured grid
- uniform density for each isopycnal layer
- momentum exchange between isopycnal layers
- vertical mass exchange between isopycnal layers
- density stratification has always to be stable
- drying and wetting
- vertical discretization in ϱ- and z-coordinates
- a two-dimensional depth-averaged model results if only one isopycnal layer and one z-layer are defined
- a three-dimensional model results if only one isopycnal layer or one z-layer is defined
- shear dependent viscosity, which is calculated by a parameterized rheological approach
- interaction of the isopycnal layers due to interfacial shear

The numerical model approach presented in this thesis includes flooding and drying of the isopycnal layers. Layers, representing a suspension of a specific concentration such as fluid mud, are not necessarily active over the entire model domain.

The low-concentration isopycnal layers in particular may reach a thickness of several meters in estuaries. There, the z-layers can support the vertical isopycnal discretization for a better three-dimensional resolution. This will be worth considering in further investigations but, in the present thesis, the z-layers are negligible for high-concentration fluid dynamics. In this case, the layer thicknesses of the highly concentrated suspensions are in the range of centimeters to decimeters where the isopycnal discretization is more effective.

The mass exchange between isopycnal layers is applied to the isopycnal system by assuming $N_z = 1$ and $M \geq 3$ (Appendix B). Therefore, the model applications of the Sections 5 and 6 are also applied to this three-dimensional numerical approach in x, y, ϱ-coordinates.

B General Solution for Diapycnal Mass Transfer

A solution for mass transfer in a three-layer system is derived in Section 4.3. In this section, the approach will be extended to the following system:

- the number of isopycnal layers is defined as $M \geq 3$,
- the water column is discretized in the three-dimensions x, y and ϱ,
- stable stratification applies with $\varrho_m > \varrho_{m+1} > 0$
- both the surface $\eta^n_{i,M}$ and the bottom $\eta^n_{i,0}$ of the water column are static,
- no flux is allowed to pass through the bottom or surface,
- the surface layer M is defined as clear water in which there is no suspended matter to be transferred.

A primary mass flux of arbitrary direction originates in layer m and flows into the next adjacent layer $m \pm 1$. If layer m is active with a definite thickness, the mass flux also has a definite value. Otherwise, for a non-active layer, the primary flux is zero. Therefore, the primary fluxes are defined as follows:

$$\begin{aligned} &\text{active layer:} && \Delta\eta^n_{i,m} > 0 && \Rightarrow && \Phi^n_{i,m,m\pm1} \geq 0 \\ &\text{non-active layer:} && \Delta\eta^n_{i,m} = 0 && \Rightarrow && \Phi^n_{i,m,m\pm1} = 0. \end{aligned} \tag{B.0.1}$$

The thickness of the adjacent layer $(m \pm 1)$ then increases by $\Delta t \Phi^n_{i,m,m\pm1}$ due to the primary flux.

In a system of more than three isopycnal layers, the adjacent interface for the mass balance has to be predefined. The definition of the adjusted interfaces is illustrated in Figure 80. The next adjacent interface above is adjusted for both a primary downward and a primary upward flux.

Two cases of compensatory fluxes are considered according to their origin. The first case: a compensatory flux resulting from a downward primary flux originates in the same layer as the flux that causes it (see panel first of Figure 80). Hence, as both fluxes originate in the same layer, either the layer is non-active and both fluxes become zero or the layer is active and both fluxes become greater than zero. The second case is a compensatory flux resulting from an upward primary flux (see panel second of Figure 80). In this case, both fluxes originate in different layers and terminate in the same layer m. Therefore, the origin of the compensatory flux is defined as the next active layer above the m-th layer. This is not necessarily the $(m+1)$-th layer but may be the $\left(m^n_{t,i}\right)$-th layer. Thus, the index for the next active layer above the m-th layer will be specified as $t^n_{i,m}$ to simplify the notation in the following.

The third panel of Figure 80 shows an exception for the interface $(M, M-1)$ below the free surface. Primary fluxes are not applied at this interface as the layer M consists of clear water by definition.

A general formulation of the layer thickness is derived from Equation (4.3.8) by assuming a system with internal vertical fluxes but without horizontal fluxes. The layer thickness $H_{i,m}^{n+1}$ for the m-th layer and the i-th polygon at the time step $n+1$ is given by

$$
\begin{aligned}
H_{i,m}^{n+1} &= H_{i,m}^{n} \\
&+\Delta t \underbrace{\left(-\Phi_{i,m,m-1}^{n} + \Phi_{i,m-1,m}^{n} + \Phi_{i,m-1,m-2}^{n} R_{m-1} - \Phi_{i,m-2,m-1}^{n} \frac{\varrho_{m-1} - \varrho_{m-2}}{\varrho_{t_{i,m-1}^{n}} - \varrho_{m-1}} \right)}_{\text{fluxes through the bottom of the m-th layer}} \\
&+\Delta t \underbrace{\left(\Phi_{i,m+1,m}^{n} - \Phi_{i,m,m+1}^{n} - \Phi_{i,m,m-1}^{n} R_{m} + \Phi_{i,m-1,m}^{n} \frac{\varrho_{m} - \varrho_{m-1}}{\varrho_{t_{i,m}^{n}} - \varrho_{m}} \right)}_{\text{fluxes through the top of the m-th layer}}
\end{aligned}
\tag{B.0.2}
$$

with the density factor $R_m = (\varrho_m - \varrho_{m-1}) \,/\, (\varrho_{m+1} - \varrho_m)$. The layer thickness of the surface layer M is given by

$$
H_{i,M}^{n+1} = H_{i,M}^{n} + \Delta t \left(\Phi_{i,M-1,M-2}^{n} R_{M-1} - \Phi_{i,M-2,M-1}^{n} \frac{\varrho_{M-1} - \varrho_{M-2}}{\varrho_{t_{i,M-1}^{n}} - \varrho_{M-1}} \right) \tag{B.0.3}
$$

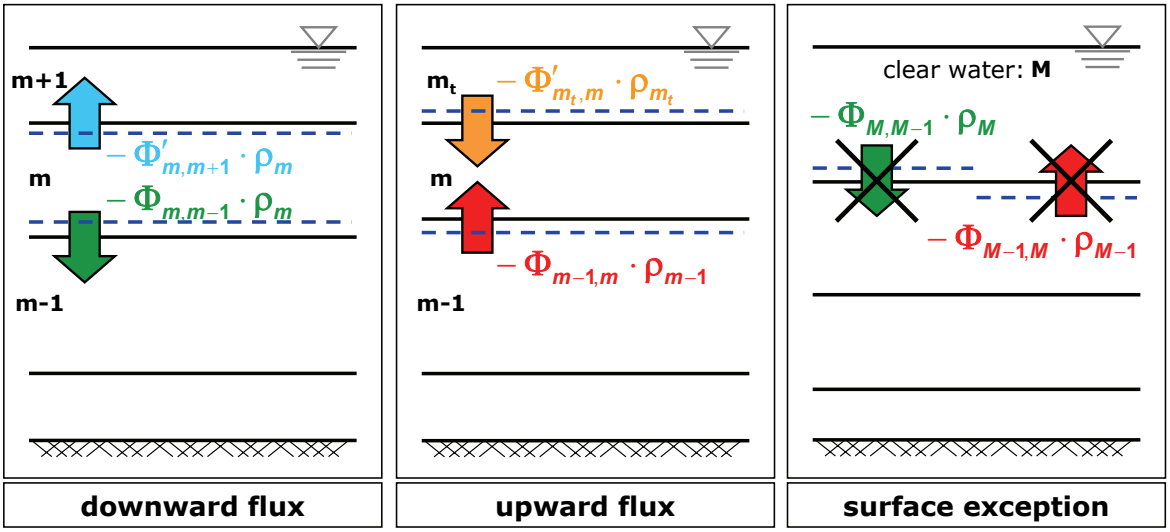

Figure 80: *Definition of the neighboring interface for the mass balance.*
First panel: The correspondent compensatory flux of a downward primary flux (from layer m to layer $m-1$) is applied to the upper interface of layer m. The compensatory flux transfers mass from layer m to the next layer above, regardless if the layer is active or non-active. Second panel: The correspondent compensatory flux of an upward primary flux (from layer $m-1$ to layer m) is located at the upper interface of layer m. The compensatory flux transfers mass from the next active layer above to layer m. Third panel: Primary fluxes cannot be applied at the top most isopycnal interface $(M, M-1)$ by taking into account the surface layer M as clear water.
(red and green: primary fluxes, orange and blue: compensatory fluxes; coloring correspondent to the equations of this section)

and for the bottom layer $(m = 1)$ by

$$H_{i,1}^{n+1} = H_{i,1}^{n} + \Delta t \left(\Phi_{i,2,1}^{n} - \Phi_{i,1,2}^{n} \right). \tag{B.0.4}$$

The volume balances for layers M and $M-1$ are exceptions because only compensatory fluxes are allowed at the top most interface. This results in the following volume balance formulation for layer $M-1$

$$\begin{aligned} H_{i,M-1}^{n+1} &= H_{i,M-1}^{n} + \Delta t \underbrace{\left(-\Phi_{i,M-1,M-2}^{n} + \Phi_{i,M-2,M-1}^{n} \right)}_{\text{fluxes through the bottom of the (M-1)-th layer}} \\ &+ \Delta t \underbrace{\left(\Phi_{i,M-2,M-3}^{n} R_{M-2} - \Phi_{i,M-3,M-2}^{n} \frac{\varrho_{M-2} - \varrho_{M-3}}{\varrho_{t_{i,M-2}^{n}} - \varrho_{M-2}} \right)}_{\text{fluxes through the bottom of the (M-1)-th layer}} \\ &+ \Delta t \underbrace{\left(-\Phi_{i,M-1,M-2}^{n} R_{M-1} + \Phi_{i,M-2,M-1}^{n} \frac{\varrho_{M-1} - \varrho_{M-2}}{\varrho_{t_{i,M-1}^{n}} - \varrho_{M-1}} \right)}_{\text{fluxes through the top of the (M-1)-th layer}}. \end{aligned} \tag{B.0.5}$$

These formulations are now adapted to the three-dimensional unstructured numerical approach described in Section 4.1. The vertical z-layer-based discretization is neglected by defining $N_z = 1$. The free surface equation, corresponding to Equation (A.2.12), takes the following form by considering diapycnal volume transfer

$$\begin{aligned} P_i \, \eta_{i,m}^{n+1} &= P_i \, \eta_{i,m}^{n} - \Theta \, \Delta t \sum_{e=1}^{E_i} \left[s_{i,e} \, \lambda_{j(i,e)} \sum_{l=1}^{m} \Delta\eta_{j(i,e),l}^{n} \, u_{j(i,e),l}^{n+1} \right] \\ &- (1-\Theta) \, \Delta t \sum_{e=1}^{E_i} \left[s_{i,e} \, \lambda_{j(i,e)} \sum_{l=1}^{m} \Delta\eta_{j(i,e),l}^{n} \, u_{j(i,e),l}^{n} \right] \\ &+ P_i \Delta t \left[\Phi_{i,m+1,m}^{n} - \Phi_{i,m,m+1}^{n} - \Phi_{i,m,m-1}^{n} R_m + \Phi_{i,m-1,m}^{n} \frac{\varrho_m - \varrho_{m-1}}{\varrho_{t_{i,m}^{n}} - \varrho_m} \right]. \end{aligned} \tag{B.0.6}$$

with the isopycnals thickness $\Delta\eta_{j(i,e),m}^{n} = \eta_{j(i,e),m}^{n} - \eta_{j(i,e),m_{b,i}^{n}}^{n}$. The volume balance is valid for $m = m_j^n, \ldots, M_j^n$ with $m_j^n > 1$ and $M_j^n \leq M-1$. The isopycnal elevation $\eta_{i,m}^{n+1}$ is affected by the fluxes through the prism sides of column i and by the volume fluxes at the interface $(m, m+1)$, but not by the fluxes at the lower interface $(m, m-1)$. Boundary conditions have to be taken into account for the bottom interface $(1, 0)$ and for the surface $(M, M+1)$ through which no fluxes are allowed to pass. This results in the mass balance of the first layer

$$\begin{aligned} P_i \, \eta_{i,1}^{n+1} &= P_i \, \eta_{i,1}^{n} - \Theta \, \Delta t \sum_{e=1}^{E_i} \left[s_{i,e} \, \lambda_{j(i,e)} \Delta\eta_{j(i,e),1}^{n} \, u_{j(i,e),1}^{n+1} \right] \\ &- (1-\Theta) \, \Delta t \sum_{e=1}^{E_i} \left[s_{i,e} \, \lambda_{j(i,e)} \Delta\eta_{j(i,e),1}^{n} \, u_{j(i,e),1}^{n} \right] \\ &+ P_i \Delta t \left[+\Phi_{i,2,1}^{n} - \Phi_{i,1,2}^{n} \right] \end{aligned} \tag{B.0.7}$$

and the $(M-1)$-th layer

$$\begin{aligned} P_i\,\eta_{i,M-1}^{n+1} &= P_i\,\eta_{i,M-1}^{n} - \Theta\,\Delta t \sum_{e=1}^{E_i}\left[s_{i,e}\,\lambda_{j(i,e)}\sum_{l=1}^{M-1}\Delta\eta_{j(i,e),l}^{n}\,u_{j(i,e),l}^{n+1}\right] \\ &- (1-\Theta)\,\Delta t \sum_{e=1}^{E_i}\left[s_{i,e}\,\lambda_{j(i,e)}\sum_{l=1}^{M-1}\Delta\eta_{j(i,e),l}^{n}\,u_{j(i,e),l}^{n}\right] \\ &+ P_i\Delta t\left[-\Phi_{i,M-1,M-2}^{n}R_{M-1} + \Phi_{i,M-2,M-1}^{n}\frac{\varrho_{M-1}-\varrho_{M-2}}{\varrho_{t_{i,M-1}^{n}}-\varrho_{M-1}}\right]. \end{aligned} \tag{B.0.8}$$

As negative volume may be produced by taking more volume out of a layer than is possible, two correction factors are introduced. The correction factor for the downward fluxes $\zeta_{i,m}$ is determined by

$$\zeta_{i,m} = \frac{\Phi_{i,m}^{n,in} + \frac{\Delta\eta_{i,m}^{n}}{\Delta t}}{\Phi_{i,m}^{n,out}} \tag{B.0.9}$$

and for the upward fluxes by

$$\psi_{i,m} = \frac{\Phi_{i,m}^{n,in} + \frac{\Delta\eta_{i,m}^{n}}{\Delta t}}{\Phi_{i,m}^{n,out}} \tag{B.0.10}$$

where the total inflow flux of the m-th layer and the i-th polygon is $\Phi_{i,m}^{n,in}$ and the total outflow flux is $\Phi_{i,m}^{n,out}$. The range of the factors is $0 < \zeta_{i,m} \leq 1$ and $0 < \psi_{i,m} \leq 1$. These factors are smaller than 1.0 if the outgoing flux of a volume element is greater than the present volume (incoming flux in addition to the prism volume). Physically, the downward mass fluxes represent deposition and settling. The upward fluxes represent processes such as erosion, entrainment and resuspension. The two types of vertical transport process do not occur at the same time at the same interface. Therefore, the correction factors for the different kinds of flux are independent of each other.

The solution algorithm presented in Section A.3 only modifies the isopycnal surface elevation matrix S_i^n of Equation (A.3.6). In the case of three predefined isopycnal layers with $M = 3$ the matrix S_i^n takes the following form

$$\mathbf{S}_i^n = \begin{bmatrix} \eta_{i,3}^{n} \\ \eta_{i,2}^{n} + \Delta t\left[-\zeta_{i,2}\Phi_{i,2,1}^{n}R_2 + \psi_{i,1}\psi_{i,3}\Phi_{i,1,2}^{n}\frac{\varrho_2-\varrho_1}{\varrho_{t_{i,2}^{n}}-\varrho_2}\right] \\ \eta_{i,1}^{n} + \Delta t\left[\zeta_{i,2}\Phi_{i,2,1}^{n} - \psi_{i,1}\psi_{i,3}\Phi_{1,2}^{n}\right] \end{bmatrix}. \tag{B.0.11}$$

Finally, the matrix of the isopycnal surface elevation for an arbitrary number of layers $M \geq 3$ results in

$$\mathbf{S}_i^n = \begin{bmatrix} \eta_{i,M}^n \\ \\ \eta_{i,M-1}^n + \Delta t \left[-\zeta_{i,M-1} \Phi_{i,M-1,M-2}^n R_{M-1} \right] \\ +\Delta t \left[\psi_{i,M} \psi_{i,M-2} \Phi_{i,M-2,M-1}^n \frac{\varrho_{M-1} - \varrho_{M-2}}{\varrho_{t_{i,M-1}^n} - \varrho_{M-1}} \right] \\ \vdots \\ \eta_{i,m}^n + \Delta t \left[\zeta_{i,m+1} \Phi_{i,m+1,m}^n - \zeta_{i,m} \Phi_{i,m,m-1}^n R_m \right] \\ +\Delta t \left[-\psi_{i,m} \psi_{i,m+2} \Phi_{i,m,m+1}^n + \psi_{i,m-1} \psi_{i,m+1} \Phi_{i,m-1,m}^n \frac{\varrho_m - \varrho_{m-1}}{\varrho_{t_{i,m}^n} - \varrho_m} \right] \\ \vdots \\ \eta_{i,2}^n + \Delta t \left[\zeta_{i,3} \Phi_{i,3,2}^n - \zeta_{i,2} \Phi_{i,2,1}^n R_2 \right] \\ +\Delta t \left[-\psi_{i,2} \psi_{i,4} \Phi_{i,2,3}^n + \psi_{i,1} \psi_{i,3} \Phi_{i,1,2}^n \frac{\varrho_2 - \varrho_1}{\varrho_{t_{i,2}^n} - \varrho_2} \right] \\ \\ \eta_{i,1}^n + \Delta t \left[\zeta_{i,2} \Phi_{i,2,1}^n - \psi_{i,1} \psi_{i,3} \Phi_{i,1,2}^n \right] \end{bmatrix}. \tag{B.0.12}$$

The present vertical mass transfer approach is applied and verified in a study of a sedimentation tank and by entrainment induced by flow over a ground sill. This is presented in Section 5.

Nomenclature

List of Abbreviations

Abbreviation	Full Name
ADCP	Acoustic Doppler Current Profiler
BAW	The Federal Waterways Engineering and Research Institute / *Bundesanstalt für Wasserbau*
CPU	central processing unit
KFKI	German Coastal Engineering Research Council / Kuratorium für Forschung im Küsteningenieurwesen
1D	one-dimensional; one-dimension
1DV	one-dimensional and vertically resolved
$1D_\varrho$	one-dimensional and vertically resolved by isopycnals
2D	two-dimensional; two-dimension
2DV	two-dimensional and laterally averaged
3D	three-dimensional; three-dimension

List of Variables

Name	Unit	Description
a	–	empirical parameter
$a_{j,m,k,k}$	m	diagonal component of matrix $\hat{\mathbf{A}}_{j,m,m}$
$a_{j,k,m\pm\frac{1}{2}}$	m	components of the secondary diagonals of matrix $\hat{\mathbf{A}}^n_{j,m\pm1,m}$
b	–	empirical parameter
b_{ij}	–	component of the symmetric, 2nd-order tensor $\mathbf{B}$
c	m/s	wave celerity
c_{aggr}	–	empirical parameter for build-up of aggregates
c_{break}	–	empirical parameter for break-up of aggregates
c_{mud}	kg/m^3	concentration of fluid mud suspension
c_s	kg/m^3	solid (mass) concentration
c_{struc}	–	empirical parameter of the Worral-Tuliani model
c_w	kg/m^3	concentration of water suspension

List of Variables (continued)

Name	Unit	Description
c_{wm}	kg/m^3	concentration at the interface of fluid mud and water suspension
c_λ	–	structural parameter for the degree of aggregation
C	–	empirical constant
C_f	–	empirical parameter for entrainment
C_z	$m^{1/2}/s$	Chezy coeffiecient
E	–	entrainment coefficient
E_i	–	maximum number of edges of the i-th element
f_a	–	wind friction coefficient at the free surface
f_b	–	bottom friction coefficient
f_c	$1/s$	Coriolis parameter
f_s	–	sidewall friction coefficient
f_x, f_y, f_z	m/s^2	force components in Cartesian coordinates, normalized with density
f_{wm}	–	friction coefficient at the water-fluid mud interface
g	m/s^2	gravitational acceleration
G	$1/s$	dissipation parameter
H_m	m	depth of m-th isopycnal layer
H_{mud}	m	depth of the fluid mud layer
H_w	m	depth of the water layer
H	m	characteristic vertical length
$\mathbb{I}_B, \mathbb{II}_B, \mathbb{III}_B$	–	first,second and third invariant of tensor $\mathbf{B}$
L	m	characteristic horizontal length
K	–	empirical parameter for the flow consistency index
n_i	–	i-th component of the normal vector
p	m^2/s^2	total pressure
p_a	m^2/s^2	atmospheric pressure normalized by a reference density ϱ_r
p_h	m^2/s^2	hydrostatic pressure
P_i	m^2	area of the i-th polygon
R_m	–	density factor $R_m = (\varrho_m - \varrho_{m-1}) \,/\, (\varrho_{m+1} - \varrho_m)$
Ri	–	gradient Richardson number

List of Variables (continued)

Name	Unit	Description
Ri_*	–	bulk Richardson number
s_i	N/m^2	i-th component of force per surface
$s_{i,e}$	–	sign function ± 1 for i-th polygon and e-th side
S	m^2	specific surface
t	s	time
Δt	s	numerical time step
u	m/s	velocity in x-direction
$\hat{u}$	–	dimensionless velocity in x-direction
$\bar{u}$	m/s	depth-averaged velocity
u_a	m/s	wind velocity in x-direction
u^b	m/s	velocity in x-direction at the bottom
$\bar{u}^p$	m/s	depth-averaged prescribed velocity
u^s	m/s	velocity in x-direction at the surface
$u_{j,k,m}$	m/s	normal velocity component for j-th side, k-th z-layer and m-th isopycnal layer
$u^*_{j,k,m}$	m/s	normal velocity component $u_{j,k,m}$ at the end of the Lagrangian trajectory
u_*	m/s	shear velocity of the main flow
$u_{*,wm}$	m/s	shear velocity at the interface of water and fluid mud
U	m/s	characteristic horizontal velocity
v	m/s	velocity in y-direction
v^b	m/s	velocity in y-direction at the bottom
v^s	m/s	velocity in y-direction at the surface
$v_{j,k,m}$	m/s	velocity component orthogonal to $u_{j,k,m}$
$v^*_{j,k,m}$	m/s	velocity component $v_{j,k,m}$ at the end of the Lagrangian trajectory
v_a	m/s	wind velocity in y-direction
$\hat{v}$	-	dimensionless velocity in y-direction
V	m^3	specific mass Volume
w	m/s	vertical velocity in z-direction
w_s	m/s	settling velocity of particles

List of Variables (continued)

Name	Unit	Description
$w_{i,k\pm\frac{1}{2},m}$	m/s	w for i-th polygon at top/bottom of k-th z-layer and for m-th isopycnal layer
$\hat{w}$	–	dimensionless velocity in z-direction
W	m; m/s	flume width; or characteristic vertical velocity
x, y, z	m	Cartesian coordinates
$\hat{x}, \hat{y}, \hat{z}$	-	dimensionless Cartesian coordinates
$z_{i,k,m}$	m	z-coordinate of the i-th polygon, the k-th z-layer and the m-th isopycnal layer
$z_{j,k,m}$	m	z-coordinate of the j-th side, the k-th z-layer and the m-th isopycnal layer
$\Delta z_{i,k,m}$	m	thickness of k-th vertical layer for i-th polygon and m-th isopycnal layer $\Delta z_{i,k,m} = z_{i,k,m} - z_{i,k-1,m}$
δ_j	m	distance between adjacent polygon centers for the j-th side
$\gamma_{j,k,m}$	m/s	friction factor for the j-th side, k-th z-layer and m-th isopycnal layer
γ_a	m/s	wind friction factor
γ_b	m/s	bottom friction factor
$\dot{\gamma}$	1/s	one-dimensional shear rate
$\dot{\gamma}_{i,j}$	1/s	component of the shear rate tensor
$\zeta_{i,m}$	–	correction factor for incoming fluxes
ϵ	m^2/s^3	turbulent dissipation rate
$\eta_{i,m}$	m	surface elevation for the i-th polygon and m-th isopycnal layer
$\Delta\eta_{i,m}$	m	isopycnal layer thickness for the i-th polygon and m-th layer $\Delta\eta_{i,m} = \eta_{i,m} - \eta_{i,m-1}$
η_m	m	surface elevation of m-th isopycnal layer
η_0	m	bathymetric depth / rigid bottom
Θ	–	implicitness factor
λ_j	m	polygons edge length for the j-th side
μ	kg/(ms)	dynamic viscosity
μ_r	kg/(ms)	rheological dynamic viscosity

List of Variables (continued)

Name	Unit	Description
μ_B	kg/(ms)	Bingham dynamic viscosity
μ_t	kg/(ms)	turbulent dynamic viscosity
$\Delta\mu$	kg/(ms)	difference of dynamic viscosity dependent on flocculation
μ_0	kg/(ms)	dynamic viscosity of clear water
μ_∞	kg/(ms)	dynamic viscosity at fully broken structure
ν	m^2/s	kinetic viscosity $\nu = \mu/\varrho$
$\nu_{r,wm}$	m^2/s	rheological viscosity at the water fluid mud interface
ν^h	m^2/s	horizontal kinetic viscosity
$\nu^h_{i,k,m}$	m^2/s	ν^h for i-th polygon, k-th z-layer and m-th isopycnal layer
$\nu^{*h}_{i,k,m}$	m^2/s	ν^h at the end of the Lagrangian trajectory
$\nu^h_{j,k\pm\frac{1}{2},m}$	m^2/s	ν^h for j-th side at top/bottom of k-th z-layer and m-th isopycnal layer
ν^v	m^2/s	vertical kinetic viscosity
$\nu^v_{i,k,m}$	m^2/s	ν^v for i-th polygon, k-th z-layer and m-th isopycnal layer
$\nu^{*v}_{i,k,m}$	m^2/s	ν^v at the end of the Lagrangian trajectory
$\nu^v_{j,k\pm\frac{1}{2},m}$	m^2/s	ν^v for j-th side at top/bottom of k-th z-layer and m-th isopycnal layer
ϱ	kg/m^3	density of a suspension, bulk density
ϱ_m	kg/m^3	ϱ for the m-th isopycnal layer
ϱ_r	kg/m^3	reference density
τ_a	N/m^2	surface / wind shear stress
τ_b	N/m^2	bottom shear stress
$\tau_{i,j}$	N/m^2	component of the shear stress tensor
τ_y	N/m^2	yield stress
$\tau_{y,B}$	N/m^2	Bingham yield stress
ϕ_s	–	solid volume concentration / solid particle content
$\Phi_{m,m\pm1}$	m/s	transport rate from layer m to layer $m \pm 1$
$\Phi^{in}_{i,m}$	m/s	transport rate into layer m
$\Phi^{out}_{i,m}$	m/s	transport rate outgoing of layer m
$\psi_{i,m}$	–	correction factor for outgoing fluxes

List of Vectors and Matrices

Name	Unit	Description
$\mathbf{A}_j$	m	tri-diagonal block matrix for the vertical viscosity terms for j-th side; size: $M_j^n \times M_j^n$
$\hat{\mathbf{A}}_{j,m,m}$	m	inner matrix of the diagonal of $\mathbf{A}_j$ for the j-th side; size: $\left(k_{b,j,m}^n, \ldots, k_{t,j,m}^n\right) \times \left(k_{b,j,m}^n, \ldots, k_{t,j,m}^n\right)$
$\hat{\mathbf{A}}_{j,m,m\pm1}^n$	m	inner matrix of the secondary diagonals of $\mathbf{A}_j$; size $\left(k_{b,j,m}^n, \ldots, k_{t,j,m}^n\right) \times \left(k_{b,j,m\pm1}^n, \ldots, k_{t,j,m\pm1}^n\right)$
$\mathbf{b}$	N/kg	body force per mass
$\mathbf{B}$	–	symmetric, 2nd-order tensor
$\mathbf{D}$	1/s	deformation rate or shear rate tensor
$\mathbf{D}_j$	kg/m^3	matrix of isopycnal densities at the j-th side; size: $M \times M$
$\mathbf{E}$	–	unit matrix
$\mathbf{f}$	m/s^2	external forces normalized with density
$\mathbf{G}_j$	m^2/s	block vector containing the explicit terms for the j-th side; size: M_j^n
$\hat{\mathbf{G}}_{j,m}$	m^2/s	inner vector of $\mathbf{G}_j$ of the j-th side and m-th isopycnal layer; size: $k_{b,j,m}^n, \ldots, k_{t,j,m}^n$
$\mathbf{P}$	m/s	vector of inflow and outflow transport rates per isopycnal layer; size: M
$\mathbf{s}$	N/m^2	external force per surface
$\mathbf{S}_i$	m	vector of isopycnal elevations $\eta_{i,m}^n$ of the i-th polygon; size: M
$\mathbf{u}$	m/s	velocity vector
$\mathbf{U}_j$	m/s	block vector of horizontal velocities for j-th side; size: M_j^n
$\hat{\mathbf{U}}_{j,m}$	m/s	vector of horizontal velocities $u_{j,k,m}$ for the j-th side, the k-th layer and m-th layer; size: $k_{b,j,m}^n, \ldots, k_{t,j,m}^n$
$\mathbf{x}$	m	vector of the Cartesian coordinates
$\Delta\mathbf{Z}_j$	m	block matrix of z-layer thicknesses for the j-th side; size: $M_j^n \times M$
$\Delta\hat{\mathbf{Z}}_{j,m}$	m	vector of z-layer thicknesses $\Delta z_{j,k,m}$ for the j-th side; size: $k_{b,j,m}^n, \ldots, k_{t,j,m}^n$
$\boldsymbol{\sigma}$	N/m^2	total stress tensor
$\boldsymbol{\tau}$	N/m^2	shear stress tensor

List of Indices

Name	Description
a	index for wind
$aggr$	abbreviation for aggregation
b	index for bottom or empirical exponent
$break$	abbreviation for break-up of aggregates
B	abbreviation for Bingham
e	index for the sides of the i-th polygon
E_i	index for the maximum number of sides of the i-th polygon
i	index for the i-th polygon of a grid
$i(j,1)$	index for *left* polygon of the j-th side
$i(j,2)$	index for *right* polygon of the j-th side
j	index for the j-th side of the computational grid
$j(i,e)$	side index for e-th side of the i-th polygon
k	index for the k-th z-layer of a grid
$k_{0,i,m}$	index for first active z-layer above the rigid bottom of the i-th polygon and the m-th isopycnal layer
$k_{b,i,m}$	index for the bottom of the m-th isopycnal layer of the i-th polygon
$k_{t,i,m}$	index for the top z-layer of the m-th isopycnal layer of the i-th polygon
m	index for the m-th isopycnal layer
m_0	index for the first active isopycnal layer above the rigid bottom
$m_{b,i}$	index for the next active layer below the m-th isopycnal layer of i-th polygon
$m_{t,i}$	index for the next active layer above the m-th isopycnal layer of i-th polygon
mol	abbreviation for molecular, index for viscosity
mud	abbreviation for fluid mud, index for different variables
M	index for the maximum number of isopycnal layer
M_j	index for the maximum number of layers of the j-th side
n	index for the n-th time step
$N_{j,m}$	index for the top most active z-layer of the j-th side and the m-th isopycnal layer
N_s	index for the maximum number of sides

List of Indices (continued)

Name	Description
N_p	index for the maximum number of polygons
N_z	index for the maximum number of z-layer
r	abbreviation for rheological or reference, index for the viscosity or density respectively
s	index for surface or settling
t	abbreviation for turbulence, index for viscosity
$t_{i,m}$	index for the next active layer above the m-th isopycnal layer of i-th polygon
y	index for yield
w	index for water
wm	index for the interface of fluid mud and water

List of Operators

Name	Description
∂	partial differential operator
Δ	difference
$F\left(u_{j,k,m}^{n}\right)$	explicit finite difference operator
$F\left(II_D\right)$	continuous function of the second shear rate tensor's invariant
∇	Nabla operator

References

Banfill, P.F.G. (2003). The rheology of fresh cement and concrete - a review. In *Proc. 11'th International Cement Chemistry Congress*. 1, 3

Barnes, H.A. (2000). *A Handbook of Elementary Rheology*. University of Wales, Institute of Non-Newtonian Fluid Mechanics, Aberystwyth, UK. 42

Berlamont, J., Ockenden, M., Toorman, E., and Winterwerp, J. (1993). The characterization of cohesive sediment properties. *Coastal Eng.*, 21(1–3):105–128. 33, 42, 45

Bronstein, I.N, Semendjajew, K.A., Musiol, G., and Mühlig, H. (1997). *Taschenbuch der Mathematik*. Harri Deutsch, Frankfurt am Main, 3rd edition. 48

Brummer, R. (2006). *Rheology Essentials of Cosmetic and Food Emulsions*. Springer, Berlin, Heidelberg, New York. 13

Casulli, V. (1997). Numerical simulation of three-dimensional free surface flow in isopycnal co-ordinates. *Int. J. Numer. Meth. Fluids*, 25:645–658. 61, 65, 67, 150, 156

Casulli, V. and Cattani, E. (1994). Stability, accuracy and efficiency of a semi-implicit method for three-dimensional shallow water flow. *Computers Math. Applic.*, 27(4):99–112. 61

Casulli, V. and Cheng, R.T. (1992). Semi-implicit finite difference methods for three-dimensional shallow water flow. *Int. J. Numer. Meth. Fluids*, 15:629–648. 61

Casulli, V. and Lang, G. (2004). Mathematical model UnTRIM. Validation Document, The Federal Waterways Engineering and Research Institute (BAW), Hamburg. www.baw.de/downloads/wasserbau/mathematische_verfahren/pdf/vd-untrim-2004.pdf. 142

Casulli, V. and Walters, R.A. (2000). An unstructured three-dimensional model based on the shallow water equations. *Int. J. Numer. Meth. Fluids*, 32:331–348. 61, 142, 147, 150, 156

Cheng, R.T., Casulli, V., and Gartner, J.W. (1993). Tidal, residual, internal mudflat (TRIM) model and its applications to San Francisco Bay, California. *Estuarine Coastal Shelf Sci.*, 36(3):235–280. 153

Chhabra, R.P. and Richardson, J.F. (2008). *Non-Newtonian Flow and Applied Rheology: Engineering Applications*. Elsevier, 2nd edition. 10, 26, 42

Coussot, P. (1997). *Mudflow Rheology and Dynamics*. A.A. Balkema, Rotterdam, The Netherlands. 7, 8, 10, 12, 33

Crapper, M. and Ali, K.H.M. (1997). A laboratory study of cohesive sediment transport. In N. Burt, R. Parker and Watts, J., editors, *Cohesive Sediments*, pages 149–174, London, UK. John Wiley. 31

Dankers, P.J.T. (2006). *On the Hindered Settling of Suspensions of Mud and Mud-Sand Mixtures*. PhD thesis, Delft University of Technology, The Netherlands. 8, 85

Deltares (2010). Delft3D-FLOW - simulation of multi-dimensional hydrodynamic and transport phenomena, including sediments. User Manual 3.14, Deltares. 31

Electricité de France (2000). TELEMAC-2D validation document version 5.0. Note technique, Electricité de France, Direction des Etudes et Recherches, Chatou Cedex, France. 142

Foda, M.A. and Hunt, J.R. (1993). A nonlinear model for the fluidization of marine mud by waves. *J. Geophys. Res.*, 98(C4):7039–7047. 20

Fredrickson, A.G. (1964). *Principles and Applications of Rheology*. Prentice Hall, Englewood Cliffs, USA. 48

Gerritsen, H., de Goede, E.D., Platzek, F.W., Genseberger, M., van Kester, J.A.Th.M., and Uittenbogaard, R.E. (2007). Validation document Delft3D-FLOW - a software system for 3D flow simulations. Report, Delft Hydraulics, The Netherlands. X0356, M3470. 142

Graebel, W.P. (2007). *Advanced Fluid Mechanics*. Academic Press, Burlington, San Diego, London. 49, 50

Guan, W.B., Kot, S.C., and Wolanski, E. (2005). 3-D fluid mud dynamics in the Jiaojiang Estuary, China. *Estuarine Coastal Shelf Sci.*, 65:747–762. 30, 53

Heinz, A. (2006). *Modifizierte Bentonitsuspensionen für geotechnische Bauverfahren in Böden hoher Durchlässigkeit*. Band 229, PhD thesis, Swiss Federal Institute of Technology Zurich (ETH), Switzerland. 1, 3

Hervouet, J.M and Bates, P. (2000). The TELEMAC modelling system. *Hydrol. Processes*, 14(13):2209–2210. 142

Hsu, T.-J., Traykovski, P.A., and Kineke, G.C. (2007). On modeling boundary layer and gravity-driven fluid mud transport. *J. Geophys. Res.*, 112(C04011). 30

Jain, M. and Mehta, A.J. (2009). Role of basic rheological models in determination of wave attenuation over muddy seabeds. *Cont. Shelf Res.*, 29(3):642–651. 20

Knoch, D. and Malcherek, A. (2011). A numerical model for simulation of fluid mud with different rheological behaviors. *Ocean Dynamics*, 61(2):245–256. 45, 79

Kranenburg, C. (1994). An entrainment model for fluid mud. Communications on Hydraulic and Geotechnical Engineering Report 93-10, Delft University of Technology, Faculty of Civil Engineering, The Netherlands. 17, 52

Kranenburg, C. and Winterwerp, J.C. (1997). Erosion of fluid mud layers. i: Entrainment model. *J. Hydraul. Eng.*, 123(6):504–511. 54, 55, 106

Krebs, M. and Weilbeer, H. (2008). Ems-Dollart Estuary. *Die Küste*, 74:252–262. 104

Lamb, H. (1932). *Hydrodynamics*. Cambridge University Press, New York, USA, 6th edition. 25, 79

Le Hir, P., Bassoullet, P., and Jestin, H. (2001). Application of the continuous modeling concept to simulate high-concentration suspended sediment in a macrotidal estuary. In McAnally, W.H. and Mehta, A.J., editors, *Coastal and Estuarine Fine Sediment Processes*, volume 3 of *Proceedings in Marine Science*, pages 229–247. Elsevier Science. 30

Lesser, G.R., Roelvink, J.A., van Kester, J.A.T.M., and Stelling, G.S. (2004). Development and validation of a three-dimensional morphological model. *Coastal Eng.*, 51(8-9):883–915. 142

Lick, W. and McNeil, J. (2001). Effects of sediment bulk properties on erosion rates. *The Science of the Total Environment*, 266(1-3):41–48. 20

Liu, X. and Huang, W. (2008). An effective algorithm to reduce horizontal pressure gradient errors in σ-coordinate in EFDC hydrodynamic model. *J. Coast. Res.*, 52:193–204. 143

Malcherek, A. (1995). *Mathematische Modellierung von Strömungen und Stofftransportprozessen in Ästuaren*. Bericht 44, PhD thesis, Institut für Strömungsmechanik und Elektron. Rechnen im Bauwesen der Universität Hannover, University of Hannover, Germany. 59

Malcherek, A. (2001). *Hydromechanik der Fließgewässer*. Bericht 61, Institut für Strömungsmechanik und Elektronisches Rechnen im Bauwesen der Universität Hannover, University of Hannover, Germany. 25, 38, 52, 148

Malcherek, A. (2010). *Gezeiten und Wellen - Die Hydrodynamik der Küstengewässer*. Praxis. Vieweg + Teubner, Wiesbaden, Germany. 144

Malcherek, A. and Cha, H. (2011). Zur Rheologie von Flüssigschlicken: Experimentelle Untersuchungen und theoretische Ansätze - Projektbericht. Mitteilungen Heft 111, University of the German Armed Forces, Institute of Hydro Science, Munich, Germany. 39, 41, 42, 43, 44

Malcherek, A. and Knoch, D. (2006). The influence of waves on the sediment composition in a tidal bay. In Spaulding, M.L., editor, *Estuarine and Coastal Modelling - Proceedings of the 9'th International Conference in Charleston, South Carolina*, pages 842–859, Reston. ASCE. 145

Malvern, L.E. (1969). *Introduction to the Mechanics of a Continuous Medium*. Prentice-Hall Series in Engineering of the Physical Sciences. Prentice-Hall, Englewood Cliffs, USA. 23, 26, 48, 50, 51

McAnally, W.H., Friedrichs, C., Hamilton, D., Hayter, E., Shrestha, P., Rodriguez, H., Sheremet, A., and Teeter, A. (2007a). Management of fluid mud in estuaries, bays, and lakes. I: Present state of understanding on character and behavior. *J. Hydraul. Eng.*, 133(1):9–22. 13, 16, 17, 32, 52, 53, 54

McAnally, W.H. and Mehta, A.J. (2001). Collisional aggregation of fine estuarial sediment. In McAnally, W.H. and Mehta, A.J., editors, *Coastal and Estuarine Fine Sediment Processes*, Proceedings in Marine Science. Elsevier Science. 8

McAnally, W.H., Teeter, A., Schoellhamer, D., Friedrichs, C., Hamilton, D., Hayter, E., Shrestha, P., Rodriguez, H., Sheremet, A., and Kirby, R. (2007b). Management of fluid mud in estuaries, bays, and lakes. II: Measurement, modeling, and management. *J. Hydraul. Eng.*, 133(1):23–38. 13, 15

Mehta, A.J. (1991). Understanding fluid mud in a dynamic environment. *Geo-Mar. Lett.*, 11(3-4):113–118. 33

Mehta, A.J. (1996). Interaction between fluid mud and water waves. In Singh, P.V. and Hager, W.H., editors, *Environmental Hydraulics*, Water Science and Technology, chapter 5, pages 153–187. Kluwer Academic Publishers, Kluwer, Dordrecht, The Netherlands. 20

Mehta, A.J., Hayter, E.J., Parker, W.R., Krone, R.B., and Teeter, A.M. (1989). Cohesive sediment transport. I: Process description. *J. Hydraul. Eng.*, 115(8):1076–1093. 13, 16, 17, 52

Mellor, G.L., Oey, L.-Y., and Ezer, T. (1998). Sigma coordinate pressure gradient errors and the seamount problem. *J. Atmos. Oceanic Technol.*, 15:1122–1131. 143

Merckelbach, L. (2000). *Consolidation and Strength Evolution of Soft Mud Layers*. PhD thesis, Technical University Delft, The Netherlands. 20

Migniot, C. (1989). Tassement et rhéologie des vases. 2ième partie. *La Houille Blanche*, 2:95–111. 43

Mori, M., Seyssiecq, I., and Roche, N. (2006). Rheological measurements of sewage sludge for various solids concentrations and geometry. *Process Biochem.*, 41(7):1656–1662. 1, 3

Nasner, H. (1997). Sedimentation in Tidehäfen, Phase 2. *Die Küste*, 59:63–114. 131, 132

Nasner, H. (2004). Hydrodynamische und morphologische Vorgänge in brackwasserbeeinflussten Vorhäfen -In situ Messungen. *Die Küste*, 68:1–65. 127, 131, 136

Nasner, H. and Pieper, R. (2009). Eigenschaften und Verhalten von Fluid Mud in Brackwasserhäfen. Abschlussbericht 03KIS051, Institut für Wasserbau, Hochschule Bremen. 127, 131

Novarino, D., Santagata, E., Dalmazzo, D., and Zanetti, M. (2010). Rheological characterization of sludge coming from a wastewater treatment plant. *Am. J. Environ. Sci.*, 6(4):329–337. 1, 3

Oliveira, P.J. and Pinho, F.T. (1998). A qualitative assessment of the role of a viscosity depending on the third invariant of the rate-of-deformation tensor upon turbulent non-Newtonian flow. *J. Non-Newtonian Fluid Mech.*, 78:1–25. 48, 50

Oswald, P. (2009). *Rheophysics - The Deformation and Flow of Matter*. Cambridge university Press, New York, USA. 9

Pond, S. and Pickard, G. (1983). *Introductory Dynamical Oceanography*. Pergamon Press, 2nd edition. 79

Prager, W. (1961). *Einführung in die Kontinuumsmechanik*. Lehr- und Handbücher der Ingenieurwissenschaften. Birkhäuser, Basel, Stuttgart. Band 20. 48, 50, 51

Rennau, H. and Burchard, H. (2009). Quantitative analysis of numerically induced mixing in a coastal model application. *Ocean Dynamics*, 59(5):671–687. 143

Robertson, A.M. (2008). Review of relevant continuum mechanics. In Galdi, G.P., Robertson, A.M., Rannacher, R., and Turek, S., editors, *Hemodynamical Flows: Modeling, Analysis and Simulation*, volume 37 of *Oberwolfach Seminars*, pages 1–62. Birkhäuser Basel. 48, 49, 50

Ross, M.A. (1988). *Vertical Structure of Estuarine Fine Sediments Suspensions*. PhD thesis, University of Florida, Gainesville, USA. 8

Ross, M.A. and Mehta, A.J. (1989). On the mechanics of lutoclines and fluid mud. *J. Coast. Res.*, 5:51–62. Special Issue on Physics of High Concentration Suspensions in Estuaries. 8

Ross, M.A. and Mehta, A.J. (1990). Fluidization of soft estuarine mud by waves. In Bennet, R.H., editor, *Microstructure of Fine-grained Sediments: From Mud to Shale*, chapter 19, pages 185–191. Springer, New York. 19

Roussel, N. (2007). Rheology of fresh concrete: from measurements to predictions of casting processes. *Mater. Struct.*, 40(10):1001–1012. 1, 3

Schlichting, H. and Gersten, K. (1997). *Grenzschicht-Theorie*. Springer, Berlin, Heidelberg, New York, 9th edition. 52

Schrottke, K. (2006). Dynamik fluider Schlicke im Weser und Ems Ästuar - Untersuchungen und Analysen zum Prozessverständnis. In *Erfahrungsaustausch zur Untersuchung und Einschätzung von Transportprozessen in Ästuaren und Wattgebieten und zum Sedimentmanagement in Tidegewässern*. BAW/BfG-Kolloquium Nov.2006. 104

Schrottke, K., Becker, M., Bartholomä, A., Flemming, B.W., and Hebbeln, D. (2006). Fluid mud dynamics in the Weser Estuary turbidity zone tracked by high-resolution side-scan sonar and parametric sub-bottom profiler. *Geo-Mar. Lett.*, 26(3):185–198. 21

Schulze, M. (1990). *Zur Dynamik des Schwebstoffhaushaltes in Brackwassergebieten am Beispiel des Ems-Ästuars*. Heft 108, PhD thesis, Leichtweiss-Institut für Wasserbau der Technischen Universität Braunschweig, Germany. 59

Scully, M.E., Friedrichs, C.T., and Wright, L.D. (2002). Application of an analytical model of critically stratified gravity-driven sediment transport and deposition to observations from the Eel River Continental Shelf, Northern California. *Cont. Shelf Res.*, 22(14):1951–1974. 16

Smile Consult (2006). Erstellung einer konsistenten digitalen Bathymetrie (KoDiBa) des Emsästuares sowie des Dollarts. Abschlussbericht, smile consult GmbH, Vahrenwalder Str. 7, 30165 Hannover. 104

Soltanpour, M. and Haghshenas, S.A. (2009). Fluidization and representative wave transformation on muddy beds. *Cont. Shelf Res.*, 29(3):666–675. 20

Son, M. and Hsu, T.-J. (2009). The effect of variable yield strength and variable fractal dimensional on flocculation of cohesive sediment. *Water Res.*, 43(14):3582–3592. 31

Teeter, A.M. and Johnson, B.H. (2005a). Atchafalaya bar channel numerical hydrodynamic and fluid / settled mud modeling. Report Ms 39066, U.S. Army Corps of Engineers, New Orleans District, Computational Hydraulics and Transport LLC, Edwards. 30

Teeter, A.M. and Johnson, B.H. (2005b). Sediment and fluid mud modeling of Atchafalaya Pro-Delta Channel. In Spaulding, Malcolm L., editor, *Estuarine and Coastal Modeling*, 9th International Conference, pages 714–733. ASCE. 30

Toorman, E.A. (1994). An analytical solution for the velocity and shear rate distribution of non-ideal Bingham fluids in concentric cylinder viscometers. *Rheol. Acta*, 33(3):193–202. 39

Toorman, E.A. (1997). Modelling the thixotropic behaviour of dense cohesive sediment suspensions. *Rheol. Acta*, 36(1):56–65. 12, 32, 39, 40

Toorman, E.A. (1999). Sedimentation and self-weight consolidation: Constitutive equations and numerical modelling. *Geotechnique*, 49(6):709–726. 85

Toorman, E.A. and Berlamont, J.E. (1993). Mathematical modeling of cohesive sediment settling and consolidation. In Metha, A.J., editor, *Nearshore and Estuarine Cohesive Sediment Transport*, volume 42 of *Coastal Estuarine Studies*, pages 167–184. American Geophysical Union. 20

Uittenbogaard, R. (2003). Modelling turbulence in vegetated aquatic flows. *International Workshop on Riparian Forest Vegetated Channels: Hydraulic, Morphological and Ecological Aspects*. Trento, Italy. 66

van Kessel, T. (1997). *Generation and Transport of Subaqueous Fluid Mud Layers*. PhD thesis, Dept. of Civil Engineering, Delft University of Technology, The Netherlands. 13

van Leussen, W. (1994). *Estuarine Macroflocs and their Role in Fine-Grained Sediment Transport*. PhD thesis, University of Utrecht, The Netherlands. 59

van Rijn, L.C. (2005). *Principles of Sedimentation and Erosion Engineering in Rivers, Estuaries and Coastal Seas*. Aqua Publications, The Netherlands. 8

Wan, Z. and Wang, Z. (1994). *Hyperconcentrated Flow*. IAHR Monograph. A.A. Balkema, Rotterdam, The Netherlands. 13

Wang, L. (2010). *Tide Driven Dynamics of Subaqueous Fluid Mud Layers in Turbidity Maximum Zones of German Estuaries*. PhD thesis, University of Bremen, Germany. 122, 124

Weilbeer, H. (2005). Numerical simulation and analyses of the sediment transport processes in the Ems-Dollard Estuary with a three-dimensional model. In Kusuda, T., Yamanishi, H., Spearman, J., and Gailani, J.Z., editors, *Sediment and Eco-Hydraulics: INTERCOH 2005*, number 9 in Proceedings in Marine Science, pages 447–462. Elsevier. 104

Whitehouse, R., Soulsby, R., Roberts, W., and Mitchener, H. (2000). *Dynamics of Estuarine Muds*. HR Wallingford. Thomas Telford Ltd., London. XVII, 8, 13, 18, 56, 58, 80

Winterwerp, J.C. (1999). *On the dynamics of high-concentrated mud suspensions*. PhD thesis, Delft University of Technology, The Netherlands. 8

Winterwerp, J.C. (2011). Fine sediment transport by tidal asymmetry in the high-concentrated Ems River: indications for a regime shift in response to channel deepening. *Ocean Dynamics*, 61(2-3):203–215. 15, 104

Winterwerp, J.C. and Kranenburg, C. (1997). Erosion of fluid mud layers. ii: Experiments and model validation. *J. Hydraul. Eng.*, 123(6):512–519. 55

Winterwerp, J.C. and van Kesteren, W.G.M. (2004). *Introduction to the Physics of Cohesive Sediment in the Marine Environment*, volume 56 of *Developments in Sedimentology*. Elsevier. 8, 13, 59, 60

Winterwerp, J.C., Wang, Z.B., van Kester, J.A.Th.M., and Verweij, J.F. (2002). Far-field impact of water injection in the Crouch River. In *Proceedings of the ICE - Water and Maritime Engineering*, volume 154, pages 285–296. XVII, 31, 55, 57

Worrall, W.E. and Tuliani, S. (1964). Viscosity changes during the ageing of clay-water suspensions. *Trans Brit. Ceramic Soc.*, 63:167–185. 12, 39

Wright, L.D., Friedrichs, C.T., Kim, S.C., and M.E., Scully (2001). Effects of ambient currents and waves on gravity-driven sediment transport on continental shelves. *Mar. Geol.*, 175(1-4):25–45. 16

Wurpts, R. (2005). Hyperconcentrated flow. *HANSA Int. Marit. J.*, 142(9):75–88. 1, 3, 12, 21

Yan, Y. and Hayter, E.J. (1994). Numerical modeling of fluid mud transport in estuaries. In Cotroneo, G.V. and Rumer, R.R., editors, *Hydraulic Engineering*, National Conference on Hydraulic Engineering 1994, pages 1070–1074. ASCE. 29